Novel ion-exchange materials derived from poly(styrene-*co*-maleimide) and a study of the extraction and recovery of gold (III) chloride from acidic solutions

By

Eugene Marlin Lakay

Thesis presented for the degree of Doctor of Philosophy

at the

University of Stellenbosch

Promoter: Professor Klaus R. Koch

Co-promoter: Professor Bert Klumperman

March 2013

Declaration

By submitting this thesis/dissertation electronically, I declare that the entirety of the work contained therein is my own, original work, that I am the sole author thereof (save to the extent explicitly otherwise stated), that reproduction and publication thereof by Stellenbosch University will not infringe any third party rights and that I have not previously in its entirety or in part submitted it for obtaining any qualification.

Date: March 2013

"Challenges are what make life interesting, overcoming them is what makes life meaningful"

Joshua J. Marine

Acknowledgements

I would sincerely like to thank:

- First of all I am indebted to my academic father and mentor, Professor Klaus Koch for his guidance, encouragement and support throughout my studies.
- Professor Bert Klumperman for his "open-door policy" and willingness to share his knowledge on polymer chemistry.
- Professor Sophie Hermans of the Catholic University of Louvain in Belgium for XPS analysis and her generous input into my work.
- Ann Conolly of the University College Dublin in Ireland for elemental analyses.
- Mohamed Jaffer, Franscious Cumming and Miranda Waldron of the University of Cape Town for the TEM and SEM analysis and for stimulating discussions.
- Dr. Jaco Brand and Mrs. Elsa Malherbe of the Central Analytical Facility at the University of Stellenbosch for NMR analysis.
- Mrs. Hanlie Both for surface area and porosity analysis
- Shafiek, Roger, Ursula and Deidre for technical assistance and support.
- The PGM research group members, especially James, Izak and Pieter with whom I have become close friends with over the years.
- The Free Radical Research group members for creating a friendly environment to work in.
- To my parents, sisters, brother, nieces and especially Ancret and her parents for being there for me always. Your invaluable support, understanding and prayers, especially towards the end of my Ph.D. study have carried me through.
- The University of Stellenbosch and the National Research Foundation for financial support.
- To my Heavenly Father, Praise, Honour and Glory be unto your Name. You've been the wind beneath my wings.

Conference proceedings

RSC SACI-Inorganic Conference 2007, Club Mykonos, Western Cape, South Africa.
Poster presentation and best poster prize

SACI Young Chemists Mini Symposium 2008, Stellenbosch, South Africa.

RSC 39th SACI Convention 2008, Stellenbosch, South Africa
Poster presentation

RSC SACI Inorganic Conference 2009, Bloemfontein, South Africa.
Poster presentation and best poster prize

RSC 40th SACI Convention 2011, WITS University, Johannesburg, South Africa.

Poster presentation

Outputs

PCT International patent application

Title: Modified poly(styrene-*co*-maleic anhydride) and uses thereof

Authors: E. Lakay, B. Klumperman, K.R. Koch

Publication No: WO/2012/098459

International Application No: PCT/IB2012/000078

Manuscripts are being prepared for publication under the titles:

- *The extraction and recovery of anionic complexes of gold (III) chloride using modified poly(styrene-co-maleic anhydride)*

  E. Lakay, B. Klumperman, S. Hermans, K.R. Koch

- *The extraction of precious metal complexes from aqueous acidic solutions using novel micro- to millimeter size poly(styrene-co-maleimide) resin beads*

  E. Lakay, A. Willemse, B. Klumperman, K.R. Koch

Abstract

In this study an economical, environmentally friendly, selective and efficient process for the extraction and recovery of $[AuCl_4]^-$ from aqueous acidic chloride-rich solutions, particularly those aqueous solutions having low concentrations of the precious metal complexes has been investigated. Functionalized poly(styrene-*co*-maleimide) (PSMI) nanoparticles were synthesized by thermal imidization of the poly(styrene-*co*-maleic anhydride) (PSMA) copolymer with 3-*N*,*N*-dimethylaminopropylamine. Stable water-based dispersions were obtained containing spherical, monodisperse PSMI nanoparticles with a narrow size-distribution and average diameters of 50 ± 5 nm. The specific surface area of the bulk PSMI nanoparticles is 88.1 ± 2.2 m^2/g with an average pore diameter of 82.3 Å. ^{13}C NMR, FTIR and elemental analyses confirmed the successful and complete conversion of PSMA into the PSMI derivative.

The functionalized PSMI nanoparticles synthesized were investigated as a novel anion-exchange material for the extraction of $[AuCl_4]^-$ ions from aqueous acidic solutions. Batch sorption studies were carried out as a function of various parameters, such as initial gold concentration, PSMI mass, contact time and agitation rate. The $[AuCl_4]^-$ extraction occurred with extremely fast sorption kinetics and is dependent on the rate of agitation during the batch sorption process. The functionalized PSMI nanoparticles show a maximum gold loading capacity of 1.76 mmol/g (347.7 mg/g). Langmuir and Freundlich isotherm models were applied to analyze the experimental sorption data. The best model describing the sorption process is given by the Langmuir model. Desorption efficiencies of about 80 % and 93 % were obtained using acidified thiourea (0.25 M thiourea/2 M HCl) and a mixture of 10 M HNO_3/0.5 HCl as elutant solutions, respectively. X-ray photoelectron spectroscopy (XPS) analysis unambiguously confirms that the immobilized gold species exists in several oxidation states of 0, +I and +III on the PSMI nanoparticles. This proves that the $[AuCl_4]^-$ ions initially present in the gold feed solutions unfortunately are subject to a reduction phenomenon on the surface of the functionalized PSMI nanoparticles. The existence of the various gold species contributed significantly to poor desorption efficiencies.

In addition to PSMI nanoparticles, micro- to millimeter size PSMI resin beads was prepared by an electrospray methodology. This allows for a wide range of PSMI spherical and quasi-

spherical bead diameters of shape to be prepared by manipulation of the experimental conditions employed during the electrospray process, such as the concentration of the PSMI in solution, the capillary tip-to-collector distance, flow rate and the applied voltage. ^{13}C NMR and FTIR spectroscopy analyses show that the electrospray methodology allows PSMI resin beads preparation without any change in chemical composition of the PSMI material. Surface area and porosity analysis shows that 450 µm and 1620 µm PSMI beads selected for use in the gold extraction experiments are microporous and have BET specific surface areas of 2.8 ± 0.4 m^2/g and 2.0 ± 0.1 m^2/g, respectively.

Micro- to millimeter size PSMI resin beads of 450 µm and 1620 µm diameter were tested as potential anion-exchange resins for the extraction of $[AuCl_4]^-$ from aqueous acidic solutions. The time-dependent studies reveal that the extent of gold uptake increases with an increase in contact time and is dependent on the gold concentration in the $[AuCl_4]^-$ feed solutions. A maximum loading capacity of 120.7 mg/g and 98.16 mg/g was attained for the 450 µm and 1620 µm resin beads, respectively. The experimental sorption data followed a linear trend consistent with a Freundlich sorption model. This sorption trend for $[AuCl_4]^-$ suggests that a multi-layer sorption process predominates. Desorption of immobilized gold species from the loaded PSMI resin beads was investigated using various elutants such as HCl, HNO_3, thiourea, NaCN and NaOH solutions. The best results were obtained using a mixture of 10 M HNO_3/0.5 M HCl as elutant with a desorption efficiency of about 97%.

Finally, superparamagnetic magnetite (Fe_3O_4) nanoparticles with a high degree of crystallinity and phase purity were synthesized by a chemical co-precipitation of Fe^{2+} and Fe^{3+} salts. The average diameters of the obtained Fe_3O_4 nanoparticles were about 7 – 8 nm. The Fe_3O_4 nanoparticles were coated with oleic acid surfactant molecules and used as seed particles for the preparation of 50 nm diameter magnetic PSMI nanoparticles *via* an *in situ* imidization reaction. TEM analysis confirmed that the magnetically responsive PSMI nanoparticles consist of magnetite core-polymer shell structure, although more work is required to perfect such materials.

Opsomming

In hierdie studie is ‘n ekonomiese, omgewings vriendelike, seleketiewe en effektiewe proses vir die ekstraksie en herwinning van $[AuCl_4]^-$ uit suur chloried-ryke oplossings, spesifiek oplossings van lae konsentrasies van edel metal komplekse was bestudeer. Gefunksionaliseerde poli(stireen-ko-maleïmied) (PSMI) nanopartikels was gesintetiseer deur middel van termiese imidisasie van die poli(stireen-ko-maleïk anhidried) kopolimeer met 3-*N*,*N*-dimetielaminopropielamien. Stabiele dispersies in water was gevind wat soos sweriese mono-disperse PSMI nanopartikels met ‘n noue partikel-grootte verspreiding met ‘n gemiddelde deursnee van 50 ± 5 nm. Die spesifieke oppervlak area van die massa PSMI nanopartikels is 88.1 ± 2.2 m^2/g met ‘n gemiddelde porie-grootte van 82.3 Å. ^{13}C NMR, FTIR en elementêre analiese bevestig die suksesvolle en volledige omskakeling van PSMA na PSMI.

Die gefunksionaliseerde PSMI nanopartikels was bestudeer as ‘n nuwe anion-uitruil material vir die ekstraksie van $[AuCl_4]^-$ ione uit suur oplossings. Stel sorpsie studies was uitgevoer as ‘n funksie van verskeie parameters soos onder andere die goud konentrasie in oplossing, PSMI massa, kontak tyd en ‘n mengings tempo. Die $[AuCl_4]^-$ ekstraksie gebeur met ‘n geweldige sorpsie kinetika en is afhanklik van die mengings tempo gedurende die stel sorpsie proses. Die gefunksionaliseerde PSMI nanopartikels het ‘n maksimum goud sorpsie kapsiteit van 1.76 mmol/g (347.7 mg/g). Langmuir en Freundlich isoterm modelle was gepas en geanaliseer op die experimentele sorpsie data waarvan die Langmuir isoterm model die data die beste gepas het. De-sorpsie effektiwiteit van ongeveer 80 % en 93% was vekry vir die aangesuurde thiourea (0.25 M thiourea/2 M HCl) en ‘n mengsel van 10 M HNO_3/0.5 M HCl as elueer oplossings, onderskeidelik. X-straal foto-elektron spektroskopie (XPS) analiese bevestig ongetwydeld die geimmobileerde goud spesies in oksidasietoestande van 0, +I, en +III op die PSMI nanopartikels. Hierdie is bewyse dat die $[AuCl_4]^-$ oorspronklik teenwoordig in die goud oplossings is onderhewe auto-reduksie fenomeen op die oppervlak van die gefunksionalieerde PSMI nanopartikels. Die bestaan van verskeie goud spesies dra by tot die power de-sorpsie effektiwiteit van ge-immobiliseerde goud.

Bykomend tot die nanopartikels is mikro- tot millimeter grootte PSMI partikels voorberei met ‘n elektro-sproei proses. Hierdie metode stel ons instaat om ‘n wye reeks sferiese en quasi-sferiese PSMI partikel se deersnee voorteberei. Deur die manupulasie van die eksperimentele kondisies gedurende die elektro-sproei proses, soos die konsentrasie van die PSMI in

oplossing, die kapilêre punt-tot-ontvanger afstant, vloeispoed en die toegepasde potensiaal. ^{13}C KMR en FTIR spectroskopiese analiese wys dat die elektro-sproei proses die PSMI partikel bereiding toelaat sonder enige veranderinge in die chemiese samestelling van die PSMI materiaal. Oppervlak area en porie-grootte analise wys dat 450lksdfhld en dskl jmm partikels gebruik in die goud ekstraksie eksperimente is mikro-porieës en het spesifieke oppervlak-areas van 2.8 ± 0.4 m^2/g en 2.0 ± 0.1 m^2/g onderskeidelik.

Mikro- tot millimeter grootte poli(stireen-ko-maleimied) (PSMI) partikels van 450 µm en 1620 µm deursnee was getoets as potensieele anion-uitruilings-hars vir die ekstraksie van $[AuCl_4]^-$ vanuit suur oplossings. Die tyd afhanklike studies gee aanduiding dat die mate van goud opname toeneem met ‘n toename in kontak-tyd en is afhanklik van die goud konsentrasie in die $[AuCl_4]^-$ oplossings. ‘n Maksimum opname-kapasiteit van 120.7 mg/g en 98.2 mg/g was verkry vir die 450 µm en 1620 µm hars partikels onderskeidelik. Die eksperimentele sorpsie-data volg ‘n lineêre neiging in ooreenstemming met die Freundlich model. Die sorpsie neiging van $[AuCl_4]^-$ dui aan dat ‘n meervuldige laag sorpsie proses domineer. De-sorpsie van die geimobiliseerde goud spesies vanaf die PSMI hars partikels was bestudeer deur gebruik te maak van verskeie elueermiddels soos HCl, HNO_3, thiourea, NaCN en NaOH oplossings. Die beste resultate is verkry deur ‘n mengsel te gebruik van 10M HNO_3/0.5M HCl as elueermiddel met n de-sorpsie effektiviteit van ongeveer 97%.

Superparamagnetiese magnetiet (Fe_3O_4) nanopartikels met ‘n hoë graad van kristaliniteit en fase-reinheid was voorberei deur ‘n chemiese ko-neerslagvorming van Fe^{2+} en Fe^{3+} soute. Die gemiddelde deursnee van die Fe_3O_4 nanopartikels was ongeveer 7 – 8 nm. Die Fe_3O_4 nanopartikels was omhul met oleic suur benatter molekules wat gebruik word as saadjies vir voorbereiding van 50 nm deursnee-magnetiese PSMI nanopartikels deur middel van ‘n imidisasie reaksie. TEM analiese bevestig dat die magnetiese PSMI partikels nanopartikels bestaan uit ‘n magnetiet-kern polimeer-skil struktuur.

Table of contents

List of Figures

List of Tables

List of Schemes

1 General introduction

1.1 History, occurrence, properties and uses of gold

Gold appears to be the first metal known and used by man. It is not exactly clear how, where and by whom gold was discovered but it seems to have been mined by early civilizations directly from streams and rivers. [1,2] A variety of objects made of gold dating back to 6200 years ago has been found in Bulgaria and Egypt. [2,3] The word "gold" has been connected with the Sanscrit word "*jvalita*", which is derived from the verb "*jval*", which means to shine. The symbol derives from the Latin word Aurum, which is related to the goddess of dawn, Aurora. [4] Since the prehistoric times, humans almost intuitively attributed a high value to gold, associating it with power, beauty, and the cultural elite. Undoubtedly, the most famous and well documented stories about gold and its discovery occurred in the late 1840s. [5,6] Thousands of people flocked to California in the United States of America, Johannesburg in South Africa and New South Wales, Australia in search of gold. This era was called the Gold Rush. The search for gold has been an important factor in world exploration and the development of world trade. [7]

Due to its relative chemical inertness, in nature gold is found in its native state (as the free metal occasionally as nuggets but most often as fine grains) and in gold containing compounds called tellurides ($AuTe_2$). [8,9] It is widely distributed all over the world and almost always associated with quartz and sulfide minerals. The most common sulfide associations are pyrite, chalcopyrite, galena, sphalerite, arsenopyrite, stib nite and pyrrhotite. It is found in veins and in alluvial deposits. [1,8,9] Gold is one of the rarest elements and is widely distributed in the Earth's crust at a

background level of 3 mg per ton (0.03 ppm by weight). Gold also occurs in seawater in concentrations of 0.1 – 2 mg per ton, depending on the location of the sample. [10] However, no sustainable means of gold recovery from seawater has been established thus far. In the solid state bulk, gold is a yellow-colored metal, although it may be black, ruby, or purple when finely divided, while colloidal solutions containing nanoparticles of gold are intensely coloured from red to purple. [1,9] The latter is referred to by some scientists as the "Purple of Cassius".

Currently, the world's largest gold reef deposit (gold bearing sedimentary rock) which stretches through approximately 400 km with over 50 % of all gold reserves is found on the Archaean Witwatersrand basin, South Africa. [11,12] The Witwatersrand basin, which has been mined for over 100 years and has produced more than 41 000 tons of gold, remains the greatest unmind source of gold in the world. According the US Geological Survey, South Africa is estimated to have 6000 metric tons of gold reserves, currently the most of any gold producing country. [13] This arises not only from the fact that South Africa has an extremely high natural abundance in gold mineral wealth but also due to the fact that the gold mines reach unprecedented depths – the deepest being 3.8 km underground. [11] Up until a few years ago, South Africa was the world's largest gold producer. However, by 2009, China surpassed South Africa with a production of 324 tonnes, followed by Australia at 222.8 and South Africa with 219.8 tonnes. [13] Illustrated in Figure 1.1, is South Africa's gold production between 1980 and 2009.

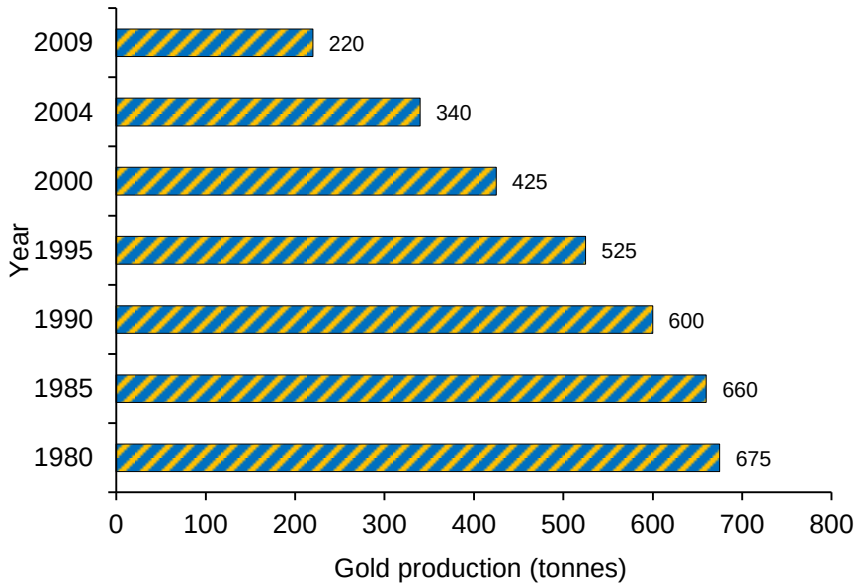

Figure 1.1 Gold production in South Africa between 1980 – 2009. [31]

The steady fall in production over the years is a consequence of a number of factors including declining ore grades, increased depth of mining and thus higher costs involved in the mining operations. Although the supply of gold by South Africa has fallen significantly, the world-wide demand for this precious metal has risen over the last couple of years due to the enduring physical and chemical properties of gold and its widespread use in a range of important and technologically advanced applications. [14]

Some of the most important characteristics of gold are ductility, malleability and sectility, meaning it can be stretched into a wire, pounded into other shapes, and cut into slices. Gold is the most ductile and malleable element on our planet. It is a great metal for jewellery because it never tarnishes. Gold is a good conductor of electricity and heat. It is not affected by exposure to air or to most reagents. It is inert and a good reflector of infrared radiation. Gold has an electrochemical potential which is the lowest of any metal. This means that gold in any cationic form will accept electrons from virtually any reducing agent to form metallic gold. It is the most electronegative of all metals, which once again confirms its noble character. Gold is usually alloyed to increase its strength. Pure gold is measured in troy weight, but when gold is alloyed with other metals the term ‘karat’ is used to express the amount of gold present. [1,15-18]

Gold has been historically important as currency and remains important as an investment metal. The color and luster of gold are what make this metal so attractive and desirable. For this reason it has found use in jewelry, coins, medals, and artwork for thousands of years. Due to its properties, gold also has a number of uses in industry such as a wide range of electronic manufacturing equipment, dentistry and medicine. [1,16,17,19] For example, one radioactive isotope of gold (^{198}Au, with a half-life of 2.7 days) is commonly used to treat cancer. [15] Gold is also an outstanding element for use as a heterogeneous catalyst operating at ambient temperature because it is catalytically active at low temperature (200 – 350 K compared with Pd and Pt at 400 – 800 K). [19] In the last few years several uses in homogeneous catalysis have been reported. [20]

1.2 Recovery of gold from ore

Gold recovery operations consist of three major steps: extraction, beneficiation, and processing. [1,21-24] Extraction is analogous to mining and is defined as removing ore material from a deposit. These include open-pit and underground mining. Beneficiation is the process in which gold is concentrated after it has been extracted from the gold-containing ores and following comminution (crushing and grinding). Four main techniques are used in the beneficiation of gold ore: gravity concentration, amalgamation (with mercury), flotation, and cyanidation. The method used varies with mining operations and depends on the characteristics of the ore and on economic considerations. A basic flow chart for the recovery of gold from its ore and converted into a gold concentrate (before processing) is provided in Scheme 1.1. Processing includes purification of the gold concentrate and subsequent refining steps.

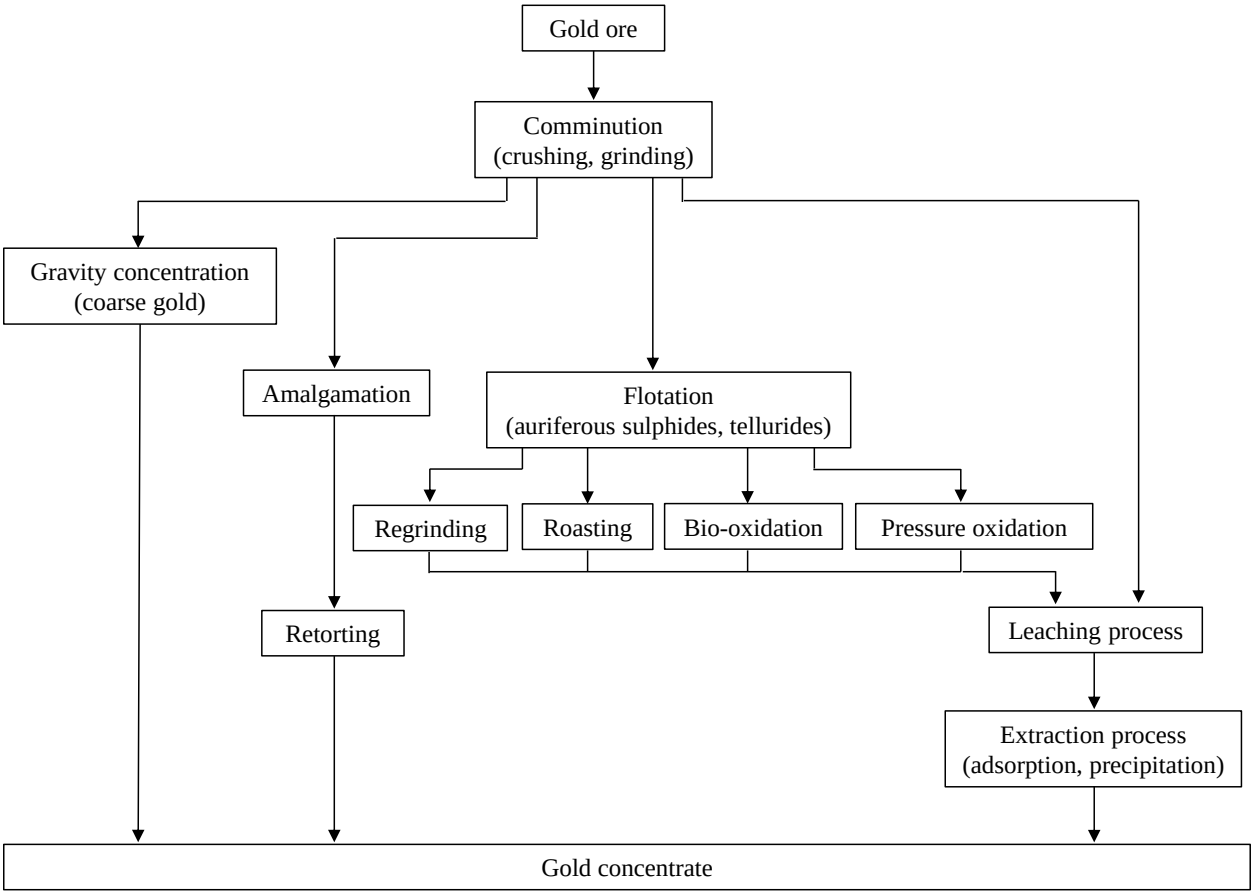

Scheme 1.1 Basic flowchart for gold recovery from gold-containing ores. [1,21-24]

The most important and widely used technique in gold mining is cyanidation (cyanide leaching). Cyanidation is a process in which the gold-containing ores are treated with potassium cyanide (or some other salt of cyanide) in the presence of lime and oxygen in order to dissolve the gold from the crushed ores. The oxidized gold combines with the cyanide ions to form a new compound, gold (I) cyanide, $Au(CN_2)^-$ in the leachate. The chemical reactions illustrating the dissolution of gold and the formation of gold (I) cyanide complexes are given by Equations 1.1 to 1.3. (The overall reaction is given by Elsner's equation, Equation 1.3.).

$$2\ Au + 4\ KCN + O_2 + 2\ H_2O \rightleftharpoons 2\ K[Au(CN)_2] + 2\ KOH + H_2O_2 \qquad (1.1)$$

$$2\ Au + 4\ KCN + H_2O_2 \rightleftharpoons 2\ K[Au(CN)_2] + 2\ KOH \qquad (1.2)$$

$$4\ Au_{(s)} + 8\ CN^-_{(aq)} + O_{2(g)} + 2\ H_2O_{(l)} \rightleftharpoons 4\ Au(CN)_2^-{}_{(aq)} + 4\ OH^-_{(aq)} \qquad (1.3)$$

There are two basic types of cyanidation operations, tank leaching and heap leaching. In addition, tank leaching involves one of two distinct types of operations for recovery of $Au(CN_2)^-$ complexes, Carbon-in-Pulp (CIP) or Carbon-in-Leach (CIL). In CIP operations, the ore pulp is leached in an initial set of tanks followed by sorption on carbon occurring in a second set of tanks. In CIL operations, leaching and carbon recovery of the gold values occur simultaneously in the same set of tanks. High grade quality ores yield their gold under cyanidation in what is called vat leaching.

Heap leaching was introduced in the 1970's as a means to drastically reduce gold recovery costs and specifically to recover gold and silver from lower grade ores. A typical gold heap leaching operation consists of placing crushed ore on an impervious pad. A dilute cyanide solution is delivered to the top of the heap (pile of ore), usually by sprinkling or drip irrigation. The solution trickles through the heap, dissolving out the gold in the ore. The pregnant (gold bearing) solution drains from the bottom of the heap and is collected in a large plastic-lined pond for gold recovery by either carbon sorption or zinc precipitation. The barren solution is then recycled to the pile. Heap leaching generally requires 60 to 90 days for processing ore that could be leached in 24 hours in a conventional agitated leach process. Gold recovery is typically 60 – 80 % as compared with 85 – 95 % in an agitated leach plant. [1,10,21,22,25]

Cyanide is still universally used in gold extraction processes because of its relatively low cost and great effectiveness for gold dissolution due to the extreme stability of the $[Au(CN)_2]^-$ complexes ($K \sim 10^{39}$). [26] The recovery of the soluble $[Au(CN)_2]^-$ from the leachates is well established. However, cyanide can pose a high risk to health and the environment. Due to the potential toxicity of cyanide, the recovery of gold from cyanide-free containing solutions is an important consideration in the development of possible alternative gold leaching systems. Non-cyanide reagents/lixiviants such as aqua regia, thiourea, thiosulphate and thiocyanate have several potential advantages over the use of cyanide. The most important advantages include faster gold leaching kinetics and a higher degree of selectivity than cyanide for gold over other metals. [27] In addition, a lixiviant such as thiourea can also be applied in acidic media, which may be more suitable for refractory ore treatment. Of the several substitutes that have been proposed, generally, thiourea and thiosulfate are regarded as being the most realistic and promising substitutes and have been used in some applications. [28,29]

Gold halogenation and subsequent recovery from acidic solutions has attracted considerable attention during the last two decades. The use of halide (fluorine, chlorine, bromine and iodine) systems for gold dissolution pre-dates the cyanidation process. [21,30] However, of the halides, only chlorine/chloride has been applied industrially on a significant scale. Chlorination rates are favored by low pH, high chloride and chlorine levels, increased temperatures, and high ore surface areas. [22,31,32] A good example of such a method is the recovery of gold from ores and concentrates containing platinum group metals (Pt, Pd, Ir, Os, Rh, Ru) (PGMs) and silver which is also a common occurrence in the mining industry in South Africa as shown by Scheme 1.2. [33] The refining processes of the precious metal (Au, Ag and the PGMs) concentrate (after precious metal extraction from ore body and separation from base metals) consist of total leaching (complete dissolution) in hydrochloric acid solution containing chlorine gas or hypochlorite. This process, which is less hazardous than cyanidation, results in the formation of dissolved gold in the tetrachloroaurate complex form, $[AuCl_4]^-$ in addition to amongst others, relatively stable anionic PGM complexes. This lixiviation process illustrating the dissolution of gold to form $[AuCl_4]^-$ in solution is given by Equation 1.4. [34]

$$2\ Au_{(s)} + 3\ Cl_{2(g)} + 2\ Cl^-_{(aq)} \rightarrow 2\ AuCl_4^-{}_{(aq)} \qquad (1.4)$$

Following the dissolution, ion-exchange and solvent extraction techniques are used in the preconcentration of $[AuCl_4]^-$ from the precious metal containing solution.

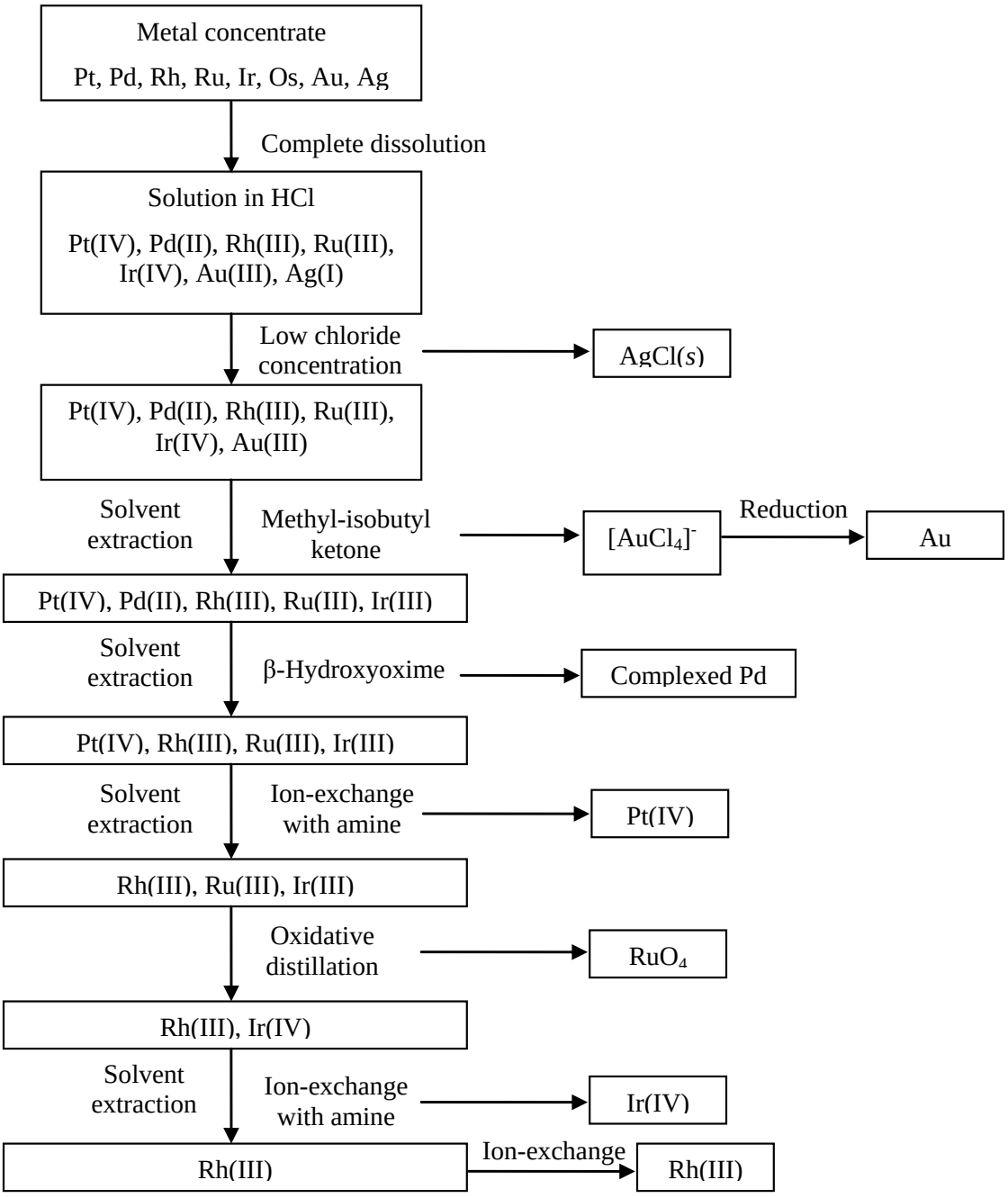

Scheme 1.2 Basic flowchart for gold recovery from a PGM-containing concentrate. [33]

1.3 Industrial processes for the recovery and extraction of dissolved gold (I/III) ions from aqueous solutions

Commercially, dissolved gold is recovered from cyanide solutions as the gold (I) cyanide, $Au(CN)_2^-$ or from acidic solutions as the gold (III) chloride, $[AuCl_4]^-$ complexes. The anionic gold complexes can be recovered from their respective pregnant (gold-bearing) solutions by one (or a combination) of the following four processes: [1,10,22,24,32]

1) Zinc 'cementation' (reduction of gold ions to metallic state)
2) Activated carbon sorption (as $[Au(CN)_2]^-$ complexes)
3) Ion-exchange (as $[Au(CN)_2]^-$ and $[AuCl_4]^-$ complexes)
4) Solvent extraction (as $[AuCl_4]^-$ complexes)

1.3.1 Zinc cementation

The use of base metals to precipitate gold or other precious metals by reduction is called cementation. Usually, it is used to recover precious metals from a solution without regard to their resultant purity. Normally, the product of cementation would be subject to further separation and purification. With only one or two types of metal ions in solution, this system can be of advantage. By adding zinc to an acidic or basic solution, the precious metals are readily reduced and precipitate, and then separated from each other and from the undissolved zinc by selective digestion and precipitation. However, this system is slow and inefficient at best. Having a sizable number of different types of metal ions in solution, the end product of cementation will be a complex of metals all mixed together, which should be refined fully. In addition, for an efficient recovery of dissolved gold by cementation, the following conditions must be established: The pregnant solution should be clarified to less than 5 ppm solids, be de-oxygenated to less than 1 ppm oxygen and adequate amount of high-purity zinc dust must be added (5 to 12 parts of zinc per part of gold). Low concentrations of copper, antimony or arsenic will stop the cementation. Even at concentration of 10^{-6} M, these ions will significantly reduce the gold recovery.

1.3.2 Activated carbon sorption

Activated carbon sorption is the most used process for recovery of dissolved gold in the form of $[Au(CN)_2]^-$ complexes from cyanide solutions. This process has three steps:

1) Loading: Sorption of $[Au(CN)_2]^-$ from solution onto the carbon;
2) Elution: Desorption of $[Au(CN)_2]^-$ from carbon into a more concentrated solution;
3) Regeneration of the carbon after elution.

Loading of the $[Au(CN)_2]^-$ is the most important step of the process. The average concentrations of $[Au(CN)_2]^-$ in pregnant solutions are generally less than 5 ppm, usually 1 to 3 ppm. The sorption circuit is a cascade of six to eight large (e.g. 9 m diameter and 9.25 m height) agitated tanks. The average time for loading differs from 12 to 24 h. Only 3 to 4 kg of gold in the form of $[Au(CN)_2]^-$ is sorbed per ton of carbon. The loading step is followed by a stripping process. The activated carbon, being an excellent sorbent for $[Au(CN)_2]^-$, does not relinquish the sorbed $[Au(CN)_2]^-$ easily. This process performs by addition of hot dilute acid (3 % HCl at 90°C) in more than 2 h. The last step of this process is regeneration of the used carbon. The process involves heating the wet carbon to 650 – 700 °C, in the absence of air, for up to 30 min.

1.3.3 Solvent extraction

In the case of conventional solvent extraction techniques for the recovery of $[AuCl_4]^-$ from hydrochloric acid solutions, several types of extractants such as basic extractants like amines, solvating extractants such as neutral organophosphorus compounds and other extractants containing S as the donor atom have been used. [35,36] As shown in Scheme 1.2, Au(III) in the form of $[AuCl_4]^-$ is efficiently and selectively extracted from acidic solutions containing other precious metals (PGMs and Ag) using methyl-isobutyl ketone (MIBK) in a solvent extraction process. [33] This has been the preferred choice of $[AuCl_4]^-$ extraction and separation from the aqueous acidic mixed-metal solutions for many years now by some refineries. The solubility problems of liquid extractants resulting in solvent and gold losses to the aqueous phase, along with mixing and settling requirements are serious drawbacks in solvent extraction. [11] Due to highly expensive selective solvents for $[AuCl_4]^-$, the extraction of $[AuCl_4]^-$ using solvent extraction is not always economical, especially when applied to aqueous solutions containing low gold concentration.

1.3.4 Ion-exchange

Use of ion-exchange resins for recovery of dissolved gold from solutions was introduced in 1951. [37] The process of recovery of a suitable anionic gold complex, e.g. $[Au(CN)_2]^-$ or $[AuCl_4]^-$ is very similar to the activated carbon sorption process. Some of the disadvantages cited for presently available ion-exchange resins are as follows: [21,37,38]

1) Poor selectivity
2) Small particle size
3) Poor physical strength
4) Low bead density
5) High cost

The stripping/desorption of $[AuCl_4]^-$ or $[Au(CN)_2]^-$ from the loaded ion-exchange resins is generally incomplete and, after a number of cycles, the resins must be incinerated to reclaim the contained gold value. The incomplete desorption may be attributed to the strong coulombic interaction between the positively charged functional groups of the ion-exchange resins and the negatively charged anionic gold complexes. [39] This was also a problem encountered in the work presented in this thesis. With the high cost of resins, their incineration makes the ion-exchange process unattractive. [32,40,41] Irrespective of this, ion-exchange and sorption methods are still the most widely used for metal ions extraction from aqueous solutions. [40]

1.4 Literature overview of ion-exchange/sorbent materials investigated for the extraction and recovery of gold (I) and gold (III) ions from aqueous solutions

The recovery of gold (I/III) complex anions from solutions gained the attention of many researchers over the years and has been actively studied for industrial purposes. Mining, mineral processing, and metallurgical industries generate billions of tons of metal containing waste solutions such as industrial effluents every year which still contains some quantities of precious metals. [21,40] The increase in the industrial demand for gold accompanied with a decline in production corresponds to an increase in the need for gold recovery from such waste solutions and also gold recycling. In recent years, an important means to obtain and recycle gold is to reclaim them from other secondary sources such as spent catalysts, recycled jewelry and

electronic scrap (e.g. printed circuit boards which contain a substantial amount of precious metals) and even their waste solutions used during the manufacturing processes. [42-46] The recovery of gold from these precious metal-rich scrap materials is by an initial treatment with aqua regia (1:3 ratio of HNO_3/HCl). Under such conditions, gold is oxidized to gold (III) and forms the anionic chlorido-complexes with predominant species being $[AuCl_4]^-$ ions. [47] The recovery of gold (I/III) anions from waste solution is usually carried out by conventional hydrometallurgical methods such as chemical precipitation, [48] electrowinning, [49] solvent extraction with dibutyl carbitol (DBC) [50,51] or methyl isobutyl ketone (MIBK), [50-52] carbon sorption, [53] and ion-exchange. [54] Because these processes are extremely expensive, energy and time consuming, there is continued interest in the development for alternative, more efficient and cost-effective methods and materials for recovering gold from waste solutions and precious metal containing effluents.

Numerous ion-exchange/sorbent materials have been proposed for gold recovery from solution. No attempt will be made here to cover all of these materials. An overview of some of the literature follows. Reported loading capacities are noted when possible to give some idea of sorbent effectiveness. Sorption depends heavily on experimental conditions such as solution pH, metal concentration, ligand concentration, competing ions, particle size and the nature of the sorbent material. However, the literature often fails to report specific test conditions and sufficient space is not available to incorporate conditions here. It is recommended that the reported loading capacities be taken as an example of values that can be achieved under a specific set of conditions rather than as maximum loading capacities. The reader is, therefore, encouraged to refer to the original articles for information on experimental conditions.

1.4.1 Carbon based sorbents

Mansooreh et al. used activated carbon of hard shell of apricot stones to adsorb $[Au(CN)_2]^-$ from industrial wastewater. [55] The results showed that under the optimal operating conditions, more than 98 % of $[Au(CN)_2]^-$ was adsorbed onto activated carbon after only 3 h. The equilibrium adsorption data were well described by the Langmuir and Freundlich isotherms. Gold desorption studies were performed with aqueous solution mixture of sodium hydroxide and organic solvents at ambient temperatures. Quantitative recovery of gold is possible by this method. [55] Porous

carbon of rice husk and barley straw adsorbed Au(III) ions in the form of $[AuCl_4]^-$ from gold containing solutions. Rice husk carbon was found to be highly selective for $[AuCl_4]^-$. The maximum adsorption capacity of the rice husk and barley straw carbon for $[AuCl_4]^-$ was found to be 0.76 mol/kg and 1.47 mol/kg, respectively. The extraction efficiency of $[AuCl_4]^-$ from industrial spent solution was also tested and barley straw carbon was found to be highly efficient and selective for the targeted metal ions in the presence of excess of other metal ions. [56]

A carbonaceous sorbent prepared from flax shive adsorbed $[AuCl_4]^-$ ions from gold bearing spent solution. The results showed that the rate of sorption followed a first-order relationship with the initial rate described largely by pore diffusion. The sorption of the $[AuCl_4]^-$ followed the Langmuir equation with the correlated monolayer capacities. The sorption process was shown to occur by ion-exchange reactions with functional groups on the sorbent. Once the $[AuCl_4]^-$ had been loaded onto the sorbent, and reduced by the sorbent to the metal further ion-exchange sites was generated for sorption of the $[AuCl_4]^-$ to occur. This allowed the possibility of sorbent recycling until significant amounts of $[AuCl_4]^-$ had been accumulated, thus simplifying the recovery of the gold by combustion of the residual sorbent. [57]

Recent research has focused on modification of the activated carbon surface for creation of specific functional groups to enhance extraction of Au(III) ions from solution. The new sorbents prepared by immobilization of 1-amino-2-naphtol-4-sulfonate, [58] 2,6-diaminopyridine [59] and ethyl-3-(2-aminoethylamino)-2-chlorobut-2-enoate [60] on activated carbon have been proposed for preconcentration of traces of gold. The loading capacity of these materials is 32, 202.7 and 305 mg/g, respectively. Acidic solution of thiourea was used in all cases for elution of adsorbed metal ions.

1.4.2 Polymeric sorbents

For the extraction of Au(I/III) ions from waste solution, many studies have made use of functionalized anion-exchange resins. Several authors have reported the adsorption of $[AuCl_4]^-$ by anion-exchange resins such as Lewatit MP-64. [61] Among the available anion-exchange resins, Amberlite resin is considered a good choice for the adsorption of gold (I/III) ions. Some studies have been carried out on the adsorption of Au(III) in the form of $[AuCl_4]^-$ from waste

solution using Amberlite XAD 2000, [62] XAD-4, XAD-7, and XAD-8 resins. [63,64] Because of the good adsorption properties including the large specific surface area and hydrophobic nature, Amberlite XAD-7 has been used effectively for the extraction of gold from waste solution. [65] Some strong anion-exchange resins, such as purolite A-500, [66] Dowex 21K, [67] and Dowex G-55, [67] have been used for the adsorption of $[Au(CN_2)]^-$ and $[Au(S_2O_3)_2]^{3-}$ due to their fast loading rates and high capacity. However, the difficulty is in the elution step due to the great strength of Au(I/III) complex anion adsorption by the anion-exchange resin such as reported by Alguacil et al. [61] Also, common strong base anion-exchange resins do not selectively adsorb anionic precious metal chlorido-complexes.

For this reason, chelating resins have been developed, taking advantage of the intrinsic selectivity provided by the grafted functional groups. In conformity with the hard and soft acids and bases theory (HSAB), functional groups containing S and N donor atoms interact strongly with the soft acids like the precious metals. [68,69] This led to the development of chelating resins containing S or N atoms. In particular, a great effort has been made in the modification of different polymeric matrices with such chelating groups. The chelating groups are either impregnated into the pores of the solid polymeric matrix of the resin or covalently bonded to the polymeric surface. Among those groups, thiol, [70,71] thiosemicarbazide, [72] dithiocarbamate, [73] dithizone [74,75] and tributylphosphine sulfide [76] are of particular interest. There is a large body of literature on this topic that has recently been reviewed by Qu. [77]

1.4.3 Bio-sorbents

Bio-sorption along with bio-oxidation are the two main areas of bio-hydrometallurgy for the recovery of gold. Bio-oxidation has been successfully applied for the recovery of gold from metallic sulfides (Scheme 1.1), which are the major bearing minerals of gold, and spent electronic materials, by the use of bacterially assisted reactions. In some parts of the world, the recovery of gold is industrially produced in significant proportions this way, especially from low grade marginal ores. [78] The bio-sorption process is a passive physico-chemical interaction between the charged surface groups of micro-organisms and biomass with ions in solution, in which living as well as dead organisms can be used. Numerous micro-organisms including algae, fungi, bacteria and yeasts are known to accumulate Au(I/III) ions actively. Summarized in Table

1.1, is a list of micro-organisms that have been used for this purpose as well as the reported gold loading capacities for each of them. [79-85]

Table 1.1 Bio-sorption of gold (III) ions from aqueous solutions using different micro-organisms as sorbent materials.

Adsorbents	pH	q_{max} (mmol/g)	Reference
Algae			
Fucus vesiculosus	7.0	0.35	Mata et al. [79]
Dealginated seaweed waste	3.0	0.4	Gonz'alez et al. [80]
Sargassum natanss	2.5	2.1	Kuyucak et al. [81]
Ascophyllum nodosum	2.5	0.15	Kuyucak et al. [81]
Chlorella vulgaris	2.0	0.5	Darnall et al. [82]
Fungi			
C. cladosporioides Strain 1	4.0	0.4	Pethkar et al. [83]
C. cladosporioides Strain 2	4.0	0.5	Pethkar et al. [83]
Aspergillus niger	2.5	1.0	Kuyucak et al. [81]
Rhizopus arrhizus	2.5	0.8	Kuyucak et al. [81]
Bacteria			
Streptomyces erythraeus	4.0	0.03	Savvaidis [84]
Spirulina platensis	4.0	0.026	Savvaidis [84]
Thiobacillus novelus IFO 12443	-	-	Takehiko et al. [85]
Yeasts	-	-	
Cryptococcus albidus AHU 3812	-	-	Takehiko et al. [85]
Cryptococcus laurentii AHU 3671	-	-	Takehiko et al. [85]
Kluyveromyces marxianus IAM 4985	-	-	Takehiko et al. [85]

More recently, interest has been focused on the use of materials of biological origin extracted from agriculture wastes or seafood by-products. [86-88] Some of these materials exhibit very high loading capacities, which make the use of these products competitive despite their slightly higher cost compared with traditional bio-sorbents, especially in the case of strategic and precious metals. [86,89,90]

A biomass that shows promise to adsorb metals is chitin. Chitin is the most abundant biopolymer available in nature after cellulose and is found in the exoskeletons of crabs and other arthropods and in the cell walls of some fungi. [91,92] Chitin is also a waste product of the crab meat canning industry. Onsøyen and Skaugrud estimated that more than 40,000 tons of chitin is available from the fisheries of crustaceans annually. [93] However, more important than chitin is its deacetylated derivative, glucosamine, or chitosan. Chitosan is produced by the alkaline deacetylation of chitin. Chitosan is characterized by its high percentage of nitrogen, present in the form of amine moieties that are responsible for metal ion binding through chelation (coordination) mechanisms. However, due to its pK_a that ranges between 6.2 and 7 (depending on the degree of deacetylation of chitosan), it is protonated in acidic solutions. [94] Thus, it is also possible to adsorb metal ions through anion-exchange mechanisms. Yang and Zall report that chitosan chelates five to six times greater amounts of metal ions than chitin due to the free amino groups exposed during deacetylation. [95] Glutaraldehyde has been frequently used to cross-link chitosan and to stabilize it in acidic solutions. [87,96] Chitosan was successfully modified and used for Au(III) adsorption, [97,98] and the 4-amino-4'-nitroazobenzene modified chitosan adsorbed only Au(III) and Pd(II) in the presence of Fe(II), Co(II), Ni(II), Cu(II) and Zn(II) in the solution. [99] The capability of chitosan was further illustrated by Chen et al., who interestingly utilized a chitosan-coated magnetic nano-adsorbent for the recovery of Au(III) ions from solution. [100] It was found that the Au(III) ions could be fast and efficiently adsorbed, and the adsorption capacity increased with the decrease in pH due to the protonation of the amino groups of chitosan. A maximum loading capacity of 59.52 mg/g was reported. Even though chitosan is highly sorptive in its natural state, its adsorption capacity could also be improved by the substitution of various functional groups onto the chitosan backbone. Besides the excellent natural properties offered by chitosan, it is soluble in solution with high acidic content. Another limitation of chitosan is that it is non-porous. Hsien and Rorrer suggest N-acylation as a means of increasing porosity. [101] Another

interesting naturally occurring biomaterial is lignin. Lignin is one of the main components of wood, furnishing 10 – 30 % of its total structure. Lignin is an anomalous type of complicated polymeric material that consists of dissimilar repeating units with different functional groups such as hydroxyl, ether, and carbonyl. [102] The effective separation of lignin without disturbing its three-dimensional matrix which was previously a difficult process is now possible because of the landmark contribution of Funaoka. [103] Three novel lignin-based adsorption gels, viz., cross-linked lignophenol, cross-linked lignocatechol, and cross-linked lignopyrogallol, were prepared by chemical modification of wood lignin by Inoue et al. [104] The adsorption behaviors of these gels for Au(III) ions along with some other metals ions were studied and compared to that of activated carbon. All three gels were found to be more selective for Au(III) than activated carbon in strong hydrochloric acid medium with comparable loading capacities. The loading capacities for Au(III) were evaluated as 1.9, 2.4, 1.9, and 2.5 mol/(kg of dry gel) for cross-linked lignophenol, lignocatechol, lignopyrogallol, and activated carbon, respectively. The high loading capacity of lignin is due in part to polyhydric phenols and other functional groups on the surface. Ion-exchange may also play a role in the adsorption of Au(III) ions by lignin.

1.4.4 Other sorbents

Amino-propyl and thiolpropyl grafted MCM-41 mesoporous silica selectively adsorbed Au(II) ions from gold mining solution and gold spent electroplating wastewater. [105] The NH_2-MCM-41 and SH-MCM-41 displayed strong affinity for Au(III) ions in the binary Au^{3+}/Cu^{2+} and Au^{3+}/Ni^{2+} solutions. The NH_2-MCM-41 is more suitable for the gold mining solution, while SH-MCM-41 is efficient for gold adsorption from the electroplating waste solution containing high amount of organics. The Au(III) ions were recovered as high purity salt solution by elution with mineral acid for NH_2-MCM-41 and thiosulfate for SH-MCM-41. The regenerated adsorbent exhibit the same adsorption capacity as the fresh adsorbent. Also, the regenerated adsorbent performed well even after several reuses.

Lam et al. prepared gold-selective adsorbents, NH_2-MCM-41, NRH-MCM-41, NR_2MCM-41 by grafting the corresponding organic amine groups (i.e. RNH_2, R_2NH and R_3N; R = propyl) onto mesoporous MCM-41 silica. [106] The adsorbents displayed strong affinity for Au(III) ions with loading capacities of 0.40, 0.33 and 0.20 mmol/g of gold, respectively. Adsorption of the Au(III) ions was best described by the Freundlich model. A series of binary adsorption equilibrium

studies with NH_2-MCM-41 containing 2.2 mmol RNH_2/g shows that the adsorbent adsorbs only Au(III) ions from solution containing Cu(II) and Ni(II) ions with a loading capacity of 0.6 mmol of gold/mol of RNH_2 (1.1 mmol of gold/g of NH_2-MCM-41). Copper and nickel were not adsorbed by NH_2-MCM-41 regardless of the solution concentration and pH (i.e. 2 to 4) in the presence of Au(III) ions. The adsorbed Au(III) was completely recovered by a simple acid wash and the recovered Au(III) solution was found to be 99 % pure. The regenerated NH_2-MCM-41 remained 100 % selective for Au(III) ions removal and exhibited the same loading capacity even after several uses.

Interestingly, in a study by Parjuli et al. it was found that Lemon peels adsorb $[AuCl_4]^-$ selectively showing negligible affinity for other precious and base metal ions from aqueous hydrochloric acid solution. The adsorption isotherm study gives the maximum loading capacity of the gel as 6.5 mol/kg of dry gel. [107]

Nano Mn_2O_3 adsorbed gold in the form of metallic nano- to micro-meter size particles from ~100 ppm aqueous solution. A loading capacity of 70 mg of gold/g adsorbent was achieved with good selectivity, recyclability and environmental benignity. Adsorption isotherm studies were carried out, showing a rapid uptake of Au(III) ions from very dilute spent solutions. [108]

1.5 Principles of sorption and ion-exchange processes

1.5.1 Sorption

*Ad*sorption and *Ab*sorption refer to different phenomena. These two terms are often used interchangeably and incorrectly in scientific literature. In the context of metal ions extraction from an aqueous solution, their only commonality is that both involve the physical transfer of metal ions from the aqueous phase to a solid phase as illustrated by the simple representation in Figure 1.2 (a) and (b).

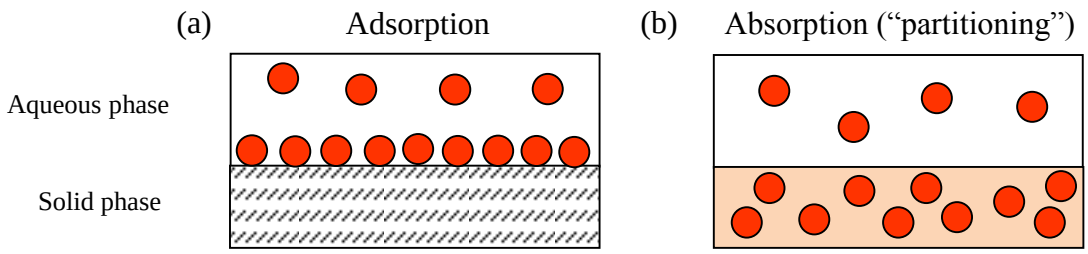

Figure 1.2 Difference between (a) *Ad*sorption and (b) *Ab*sorption processes. The metal ions involved in the sorption process are indicated by the spheres.

*Ad*sorption may be described as enrichment or an accumulation of metal ions, for example from solutions on surfaces of solid state bodies such as sorbent materials (Figure 1.2 (a)). During this accumulation, interactions between the metal ions in the aqueous phase (adsorptive) and the functional groups of the solid phase (sorbent) occur. The solid surface may be regarded as a site with certain electrically charged and steric properties characteristic of the sorbent matrix structure, which induce energetically heterogeneous energy levels based on the degree of the interaction with the adsorptive matrix. In contrast to *Ad*sorption, *Ab*sorption is defined as the permeation or partitioning of metal ions into the solid state body (Figure 1.2 (b)). Sorption is the inclusive term, referring to both processes. Desorption is the inclusive term of opposite meaning, i.e. transfer of the metal ions from the solid phase back into the aqueous phase.

Most sorbents are not only characterized by their exterior surface but also significantly affected by their accessible inner porous surface, which also contributes to sorption. However, there are major differences in the interaction forces and the kinetics of sorption onto the exterior or inner surface. [109,110]

Sorption processes are generally distinguished by two different sorption types depending on the nature of the interactions between the sorbent matrix and the sorptive matrix. Physisorption commonly is a reversible and rapid sorption process, which is mainly based on van der Waals forces, dipole forces, dipole-dipole forces, and dispersion forces as well as induction forces, which are usually below 50 kJ/mol. In contrast, chemisorption relates to a chemical bonding (coordination) between the sorbent and sorptive. Accordingly, the interaction forces are much higher and are reported to be in the range of 60 – 450 kJ/mol. [109,111]

1.5.2 Ion-exchange

Ion-exchange phenomena exhibit numerous similarities to sorption processes, but there are also some differences. Since ion-exchange occurs between ions in solution and charged sites on the internal and outer surface of a solid material it can be viewed as a special type of sorption process. [112] Unlike sorption, ion-exchange requires an interchange of ions (as opposed to a unidirectional transfer) since the electroneutrality of the solution must be maintained. The ion-exchange principle is illustrated by Scheme 1.3. In most cases, sorption and ion-exchange are not differentiated in practical applications, and most theories and models have been developed on the basis of sorbent materials. [113]

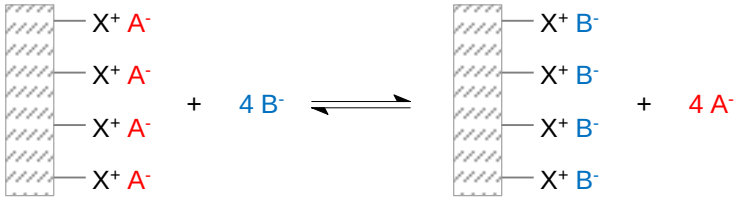

Scheme 1.3 Interchange of A^- and B^- ions in an anion-exchange process to maintain the electroneutrality of the solution. Fixed protonated functional groups located on the solid ion-exchange material are indicated by the X^+ sites.

Ion-exchange is a powerful method to recover metal ions from dilute solutions. Because of the need to maintain electroneutrality, ion-exchange is a reversible stoichiometric process, in contrast to sorption in the sense that every ion removed from the solution is replaced by an equivalent number of another ionic species of the same charge. [38,113] An ion-exchange material is usually an insoluble, three-dimensional network (organic or inorganic matrices) consisting of ionizable functional groups that are chemically bound to this framework. The structure of the network determines the physical properties of the ion-exchange material and the nature of the functional groups largely control the selectivity of the ion-exchange reaction. [37,39] The vast majority of the ion-exchange materials used in industrial wastewater treatment is of synthetic origin. The most common type of synthetic ion-exchange materials are organic resins.

Moreover, there are two major classes of ion-exchange materials: anion-exchangers, whose functional groups can remove the anions of a surrounding solution (*see* Scheme 1.3); and cation-exchangers, whose functional groups can undergo reactions with the cations of a surrounding

solution. [37,39] Depending on the type of functional group, ion-exchange materials can be further divided into several types: strong acidic, strong basic, weak acidic and weak basic. Shown in Table 1.2 are the pK_a values for the most common functional groups present in organic ion-exchangers. [37,39,114] Ion-exchange materials containing sulpho- and phospho-acidic groups and those containing tetraammonium basic groups are strong acidic and strong basic ion-exchangers, respectively, whereas those containing phenolic and primary amino groups are weak acidic and weak basic ion-exchangers, respectively. Ion-exchange materials with carboxy groups and tertiary amino groups take a medium position between strong and weak acidic and basic ion-exchangers, respectively. [37,39,114]

Table 1.2 Typical pK_a values for the most common functional groups of organic ion-exchangers.

Cation-exchangers		Anion-exchangers	
Functional group	pK_a	Functional group	pK_a
$-SO_3H$ (strong acidic)	1 – 2	$-NR_3^+$ (strong basic)	1 – 2
$-PO_3H_2$	2 – 5	$-NR_2H^+$	4 – 6
–COOH	4 – 6	$-NRH_2^+$	6 – 8
–OH (weak acidic)	9 – 10	$-NH_3^+$ (weak basic)	8 – 10

The most common commercially available ion-exchange resins are made from styrene copolymerized with divinylbenzene to produce cross-linkages which generate a rigid, porous structure. Varying degrees of polymer chain cross-linkage can be obtained, which influence the physical and chemical properties of the resin. The resins, in the form of spherical particles, are chemically activated by reacting the polymer matrix with a compound capable of introducing the desired ion-exchange functional group (e.g., with sulfuric acid to introduce sulfonic groups). An example of the preparation of a cation-exchange material *via* polymerization is shown by Scheme 1.4. Ion-exchange resins with very low cross-linking (DVB 1 – 2 %) can have the maximum theoretical concentration of functional groups of 9 mmol/g. Usually, commercial ion-exchange resins contain functional groups at a concentration in the range 2.5 – 5 mmol/g. [37,39]

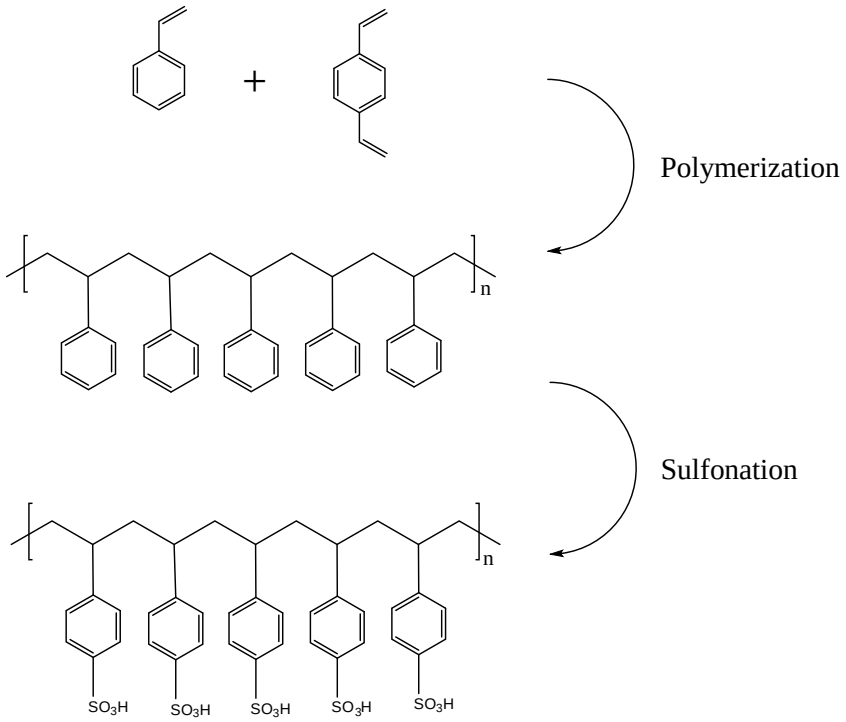

Scheme 1.4 Preparation of a typical sulfonic cation-exchange material.

The selection of the ion-exchange/sorbent material, together with an understanding of its equilibrium properties (i.e., capacity and selectivity as a function of component concentrations) is of primary importance in any application. Comparable to sorption processes, equilibrium isotherms of ion-exchange phenomena describe the distribution of the target metal ions between the solid and aqueous phase at equilibrium. Numerous equilibrium isotherm models exist that describe the sorption of solutes at equilibrium conditions. [109-113] However, the Langmuir and Freundlich models are the most frequently used in the literature. [114-117]

The Langmuir model is based on the assumption of monolayer sorption on the active sites of the sorbent. Furthermore, the Langmuir model assumes that there is no interaction between sorbate species and that once a species occupies a site, no further sorption can take place at that site. Theoretically therefore, a saturation value is reached, beyond which no further sorption can take place. The Langmuir adsorption model is given by Equation 1.5:

$$q_e = \frac{q_{max} k_L C_e}{1 + k_L C_e} \qquad (1.5)$$

which can be linearized and rearranged into

$$\frac{C_e}{q_e} = \frac{1}{q_{max} k_L} + \frac{C_e}{q_{max}} \qquad (1.6)$$

where q_e is the equilibrium loading capacity (mmol/g), C_e is the equilibrium gold concentration in the aqueous phase (mmol/L), q_{max} the maximum loading capacity (mmol/g) on the dry weight of sorbent, and k_L is the Langmuir constant (L/mmol) which is related to the energy of sorption. This constant can be calculated from the intercept and slope of the linear plot, with C_e/q_e versus C_e.

The Freundlich model assumes the sorption on a heterogeneous (multiple layer) surface with uniform energy, but never predicts saturation of the sorbent surface sites. Therefore, infinite surface coverage is predicted mathematically. This model can be represented as follows:

$$q_e = k_F C_e^{\frac{1}{n}} \qquad (1.7)$$

which can be linearized and rearranged into

$$ln\, q_e = ln\, k_F + \frac{1}{n} ln\, C_e \qquad (1.8)$$

where q_e and C_e are the same parameters as described in the Langmuir model, while k_F is the Freundlich constant (L/mmol), and n is the heterogeneity factor associated with the Freundlich model. These two parameters are related to the sorption capacity and intensity, respectively and can be calculated from the slope and intercept of the linear plot, with ln q_e versus ln C_e.

1.5.3 Ion-exchange equilibrium and selectivity

When either an anion- or cation-exchange material is brought into contact with an aqueous solution containing dissolved salts with anions or cations different from that initially bound to the material, an exchange of ions occurs until equilibrium is reached, as illustrated by Equation 1.9 for an ion-exchange process: [37,112,113]

$$a\ XA_{(s)} + b\ B_{(aq)} \rightleftharpoons c\ XB_{(s)} + d\ A_{(aq)} \qquad (1.9)$$

In Equation 1.9 X represents the fixed functional groups of the insoluble polymer network of the ion-exchange material, A is the counter ion and B the ion that takes part in the ion-exchange reaction. Charges of ions are omitted in Equation 1.9 for simplicity.

Quantitative descriptions of the ion-exchange process involve physico-chemical phenomena that fall essentially into two categories. One approximates the ion-exchange process as a sorption phenomenon (physisorption and chemisorption), while the other categorizes it more realistically as a coulombic process where electrostatic forces of the electrolytes are the driving force, such as described by the mass-action law. [37-39,109]

Selectivity is characteristic of an ion-exchange material, which makes the ion-exchanger prefer one ion to another, thus selectively drives the reaction either to the left or right hand side of Equation 1.9. The selectivity coefficient for A/B ion-exchange in the reaction as shown by Equation 1.10 can be written as follows:

$$K_{B/A} = \frac{[XB]^c\,[A]^d}{[XA]^a\,[B]^b} \qquad (1.10)$$

Equation 1.10 is obtained when the mass-action law is applied to the ion-exchanger with activity corrections. The selectivity coefficient depends not only on the functional groups of the ion-exchange material but also on the experimental conditions and the value of the coefficient can vary in the range of a few orders of magnitude. The selectivity coefficient is only applicable over a narrow range of concentrations because the activity coefficients vary with concentrations. In general ion-exchange materials prefers,

(1) ions with high charge, e.g. $Fe^{3+} > Zn^{2+} > Na^{+}$
(2) large ions, e.g. $I^- > Cl^- > F^-$
(3) ions which are poorly solvated by water

There are exceptions to these general trends and data on a specific ion-exchange material should therefore, be consulted before being applied in an application. Most often selectivity is a result of a combination of two or sometimes more factors. [37,39,113] However, the most important factors for selectivity towards ions are:

(i) coulombic interactions between ion and the ion-exchange material – ions with a low charge density (*i.e.* low charge-to-size ratio) have smaller hydration shells associated with them. The smaller the hydration shell, the stronger the coulombic interaction between the ion and ion-exchange material resulting in a higher degree of selectivity.

(ii) pore structure and elasticity of the ion-exchange material – another reason why hydration shells have an effect on selectivity is that macro-reticular pore spaces of ion-exchange resin materials have limited volume as determined by the degree of cross-linkage. Some exchanged ions can cause swelling of the resin. The swelling causes a backpressure that reduces the preference for ions with larger hydration shells.

1.5.4 Ion-exchange capacity

The ion-exchange capacity of an ion-exchange material is the number of moles of ionic species that can be exchanged or taken-up per unit mass of dry material. The ion-exchange capacity is constant for a given ion-exchange material and is a function of the number of available exchange sites (functional groups) in the resin. Because of the need to maintain a charge balance during the ion-exchange process, the ion-exchange capacity is commonly expressed in milli-equivalents or milli-moles of ionic species per gram of dry mass of ion-exchange material. The extent of the use of the total ion-exchange capacity depends on the level of ionization of the functional groups of the ion-exchanger and on the chemical and physical conditions of the process. Operating factors such as solution pH may affect the capacity of the ion-exchanger when the material contains protonable or deprotonable functionality. [37,38,113] The capacity of ion-exchange/sorbent materials quoted in the literature vary widely for different ion-exchange resins. [61-67,79-85,105,106] However, this ion-exchange capacity is used to compare differing ion-exchange resins and to calculate the total amount of resin to be added during a batch sorption process.

1.5.5 Sorption kinetics

The actual rates of ion-exchange sorption can vary over a wide range, requiring a few seconds to several months to reach equilibrium. [38,112,113] In general, ion-exchange sorption processes are fast. From a practical applications oriented point of view, the faster the rate of sorption kinetics,

the better. The ion-exchange reaction occurring between the sorbent/ion-exchange resin particles and the solution containing the ions to be exchanged will involve five distinct steps:

(a) Diffusion of ions through the bulk solution in order to reach the ion-exchange particles,
(b) Diffusion of the ions through the hydrated film surrounding the particles,
(c) Diffusion of the ions across the film-particle interface,
(d) Diffusion of the ions through the particles
(e) The actual chemical reaction involving the exchange of ions.

Provided that the concentration of ions in the solution is not extremely low, steps (a), (c) and (e) are generally fast and do not determine the rate of the reaction. It is only step (b) (diffusion through the hydration film) or step (d) (diffusion through the particle) that controls the kinetics of the overall sorption process, although sometimes both may determine the rate simultaneously. This is a simplified picture of the mechanism of an ion-exchange sorption process and its kinetics. The kinetics may also be affected by a number of parameters, such as the nature of the ion-exchange/sorbent material, the nature of the counter ions, the extent of agitation used in for example batch sorption, the concentration of the counter ions, the solution chemistry of the metal complexes to be recovered from solution, etc. In addition to this, the physical properties of the ion-exchange/sorbent material such as the size of the particles and the degree of porosity (and thus the specific surface area), also plays a significant role on the sorption kinetics.

1.6 The chemistry of gold (III) chloride in aqueous solution

It is known that metal speciation such as the degree (and rate) of chloride ligand substitution (particularly hydrolysis) can strongly affect sorption properties. [118] In aqueous solution, $[AuCl_4]^-$ undergoes acid and alkali hydrolysis (replacement of chlorides in $[AuCl_4]^-$ by H_2O and OH^- ligands, respectively). [119] The extent of hydrolysis depends on the total gold concentration, pH of the solution and chloride ion concentration due to changes in the ionic strength (in the case of anionic chlorido-complexes of gold). In a 1966 paper, the author William Rob reported that the hydrolysis reaction of $[AuCl_4]^-$ can be complex, leading to the formation of no less and perhaps more than five species. [120] This complexity was further illustrated by the work of Baes and Mesmer. [121] The co-existence of hydroxide, chloride and hydroxide – chloride complexes is

what makes gold speciation very complex. At low chloride concentrations (below 10^{-6} M), Baes and Mesmer found that gold is present in the solution in hydroxide forms: $Au(OH)_2^+$ (pH < 1), $Au(OH)_3$ (1 < pH < 12) and $Au(OH)_4^-$ (pH > 12). For higher chloride concentrations (above 0.01 M), $AuCl_4^-$ predominates in acidic solutions, while in alkaline solutions, both $Au(OH)_4^-$ and $Au(OH)_3$, $Au(OH)_3Cl^-$ coexist and/or predominate depending on the value of the constants used for the calculation of the distribution diagrams. In the near neutral region, the existence of $Au(OH)Cl_3^-$ (pH 3.5 – 6.5) and $Au(OH)_2Cl_2^-$ (pH 4.5 – 8) is debatable. In the case of intermediate chloride concentrations (between 0.01 and 10^{-6} M), many species may co-exist depending on the solution pH: In acidic solutions (pH < 5), $AuCl_4^-$, $Au(OH)Cl_3^-$, $Au(OH)_2Cl_2^-$, $Au(OH)_3$, $AuCl_3$, $Au(OH)Cl_2$ and $Au(OH)_2Cl$ may be present in the solution. Under selected experimental conditions corresponding to 25 mM chloride concentration and with pH 1.6, 3.2, 5, 6 and 8, $AuCl_4^-$, $Au(OH)Cl_3^-$, $Au(OH)_2Cl_2^-$ and $Au(OH)_3Cl^-$ (or $Au(OH)_3$) predominate, respectively. [121]

In a more recent work, Ogata and Nakano investigated the hydrolysis of $[AuCl_4]^-$ complexes in aqueous solutions. [122] They calculated the molar fractions of the various gold species as a function of pH with the equilibrium constants at 0.01 M of chloride ion concentration. The equilibrium constants for the hydrolysis reactions are shown in Scheme 1.5 and the obtained distribution diagram is shown in Figure 1.3.

$$Au(OH)_4^- + H^+ + Cl^- \rightleftharpoons AuCl(OH)_3^- + H_2O, \qquad K_1 = 10^{8.51},$$
$$AuCl(OH)_3^- + H^+ + Cl^- \rightleftharpoons AuCl_2(OH)_2^- + H_2O, \qquad K_2 = 10^{8.06},$$
$$AuCl_2(OH)_2^- + H^+ + Cl^- \rightleftharpoons AuCl_3(OH)^- + H_2O, \qquad K_3 = 10^{7.00},$$
$$AuCl_3(OH)^- + H^+ + Cl^- \rightleftharpoons AuCl_4^- + H_2O, \qquad K_4 = 10^{6.07},$$

Scheme 1.5 Distribution constants associated with the hydrolysis reaction of $[AuCl_4]^-$ ions in aqueous solution. [122]

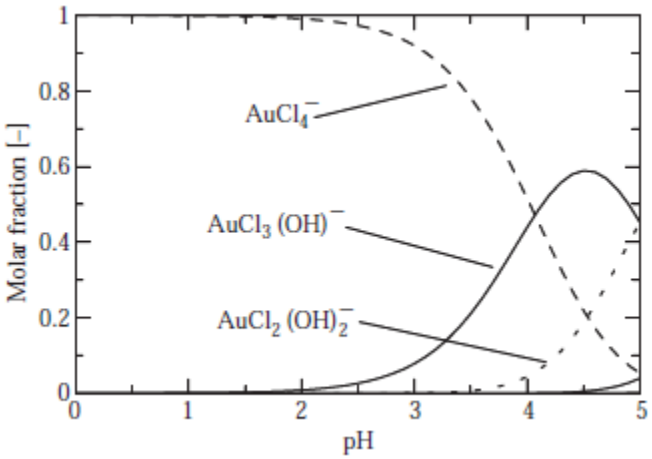

Figure 1.3 Distribution diagram of the hydrolysis reaction of $[AuCl_4]^-$ in aqueous solutions. [122]

From Figure 1.3, it is clear that there is a consecutive exchange of Cl^- by OH^- as the pH value increases forming chlorido-hydroxido gold(III) complexes, $[AuCl_{4-x}(OH)_x]^-$. At a pH value of less than 2, $[AuCl_4]^-$ species are predominantly in solution. For pH values greater than 2, hydrolysis starts to occur with the consequence of chlorido-hydroxido gold (III) complex species formation. The result shows that at a pH of between 4 and 4.2 about 50 % of $[AuCl_4]^-$ and $[AuCl_3(OH)]^-$ species are present in solution. With a further increase in solution pH, $[AuCl_2(OH)]_2^-$ species starts to exist in solution. This result therefore suggests that in order to prevent any hydrolysis of the $[AuCl_4]^-$ complexes, the aqueous solution pH must be below 2 for a relative high chloride concentration.

Similarly, Mironov and Makotchenko also recently studied the hydrolysis of $[AuCl_4]^-$ and the stability of the $[AuCl_{4-x}(OH)_x]^-$ complexes in aqueous solution. [119] On the basis of new and known data, they present a full set of equilibrium constants. Further detailed speciation of $HAuCl_4$ in aqueous solution can be found in the literature. [123-125]

1.7 The redox chemistry of gold (I/III) ions

In the context of anionic gold complex extraction and separation from solution, it is important to understand the redox chemistry of the gold ions. As discussed in section 1.4 of this chapter, $[AuCl_4]^-$ ions are often reduced to colloidal or metallic gold by various sorbent materials used in the extraction process of said complexes. The reduction phenomenon often results in a difficulty

to recover the precious metal from the loaded sorbent material by desorption. This was also a problem encountered in the work presented in this thesis. The standard reduction potential versus the normal hydrogen electrode (NHE) for some gold (I/III) ions along with the respective half reactions is shown in Table 1.3. [126,127]

Table 1.3 Standard reduction potentials for various gold (I/III) ions (V vs. NHE) [126,127]

Half reactions	Potential
Au(III) → Au	
$[AuCl_4]^- + 3\ e^- \rightarrow Au + 4\ Cl^-$	1.0
$Au^{3+} + 3\ e^- \rightarrow Au$	1.71 – 1.85
Au(III) → Au(I)	
$[AuCl_4]^- + 2\ e^- \rightarrow [AuCl_2]^- + 2\ Cl^-$	0.92
$Au^{3+} + 2\ e^- \rightarrow Au^+$	1.40
Au(I) → Au	
$[AuCl_2]^- + e^- \rightarrow Au + 2\ Cl^-$	1.15
$Au^+ + e^- \rightarrow Au$	1.71 – 1.85
$[Au(CN)_2]^- + e^- \rightarrow Au + 2\ CN^-$	-0.61

As can be seen from Table 1.3, with the exception of the $[Au(CN)_2]^-$/Au half reaction, the standard reduction potential values for the other half reactions are relatively high indicating the susceptibility of the gold (I/III) ions towards reduction. Therefore, this may possibly explain the ease with which $[AuCl_4]^-$ ions are reduced by sorbent materials.

1.8 Scope, objectives and outline of this thesis

As follows from the literature overview in this chapter, there is ample research opportunity to investigate the potential of new methods and materials to extract and separate dissolved gold from aqueous solutions such as industrial process effluents and precious metal-rich waste solutions. The need for environmentally friendly processes is of increasing importance. Although

the conventional hydrometallurgical methods such as solvent extraction and ion-exchange for the extraction of $[AuCl_4]^-$ from a range of industrial and mining solutions have been used with a high degree of success, these methods also have significant shortcomings and the use thereof is not always economically competitive for the treatment of smaller volumes of low-concentration precious metal solutions.

Nanometer-size particles are a relatively new type of functional materials that have received much attention in recent years. [128] They possess outstanding physical and chemical properties, such as their high-surface area. They possess inscrutability and are easy to combine with other ions by static electricity, so they have great chemical activities. [129,130] At the same time, nanometer-size materials have very high capacity of sorption of many metal ions. The sorption balances can also be reached quickly. [131] Numerous works exist that discuss the potential of nanoparticles for the sorption of various metal ions. In the literature, for example, the sorption of gold, heavy as well as platinum group metal ions using nano-size particles of iron oxides has been investigated. [108,132-134] A major concern, apart from the excellent properties offered by these said nano-materials, is that they are not very stable under certain experimental conditions especially in solutions of relatively high acidic content which is suitably the matrix for anionic precious metal complexes. Despite the efforts of work previously done in our group, which entailed the silica coating of superparamagnetic iron oxide (magnetite) nanoparticles to increase their stability in acidic solutions, significant sorbent degradation was still evident. [134] We therefore became interested in combining the unique properties of nanoparticles together with increased resistance against acidic chloride solution conditions offered by a robust and functionalized polymer ion-exchange material.

The aim of the research described in this thesis is the development and subsequent use of functionalized poly(styrene-*co*-maleimide) (PSMI) nanoparticles as well as micro- to millimeter size PSMI resin beads for the extraction of dissolved gold in the form of $[AuCl_4]^-$ complexes from aqueous acidic solutions. The choice of using PSMI nanoparticles as an anion-exchange material arise from the fact that (1) the material can be easily synthesized by a simple modification reaction using inexpensive and readily available raw materials, (2) the tertiary amine functionality bound to the polymer backbone is an extremely good ligand/extractant

system to scavenge for $[AuCl_4]^-$ ions from acidic solutions due to its favorable pK_a value (Table 1.1) and (3) the excellent properties offered by the nano-size of the PSMI particles.

In **Chapter 2** the synthesis of functionalized poly(styrene-*co*-maleimide) (PSMI) nanoparticles using a simple, organic solvent free, direct imidization reaction is described. Characterization of the PSMI nanoparticles for their chemical composition (degree of conversion) and physical properties (size-distribution, surface area and porosity) is discussed.

In **Chapter 3**, the PSMI nanoparticles synthesized in Chapter 2 are utilized as novel ion-exchange materials for the extraction of $[AuCl_4]^-$ from aqueous acidic solutions followed by the recovery of the immobilized gold from the PSMI material by desorption. The possible mechanisms involved in the immobilization of $[AuCl_4]^-$ onto the PSMI nanoparticles are also briefly discussed.

As an alternative and for comparison to the PSMI nanoparticles, **Chapter 4** describes the synthesis and characterization of various micro- to millimeter size PSMI resin beads using a *novel* electrospray methodology.

Chapter 5 describes the extraction of $[AuCl_4]^-$ from single as well as multi-metal aqueous acidic solutions using the PSMI resin beads synthesized in Chapter 4.

Chapter 6 describes the encapsulation of superparamagnetic magnetite nanoparticles by the PSMI nanoparticles developed here to yield magnetically responsive nanoparticles that could be used as magnetic ion-exchange materials for $[AuCl_4]^-$ extraction and separation. Preliminary work in this context shows that this is possible in principle, albeit a challenging prospect.

A brief summary of the findings is presented in **Chapter 7** together with some recommendations for further work which includes the encapsulation of the PSMI nanoparticles and the micro- to millimeter diameter PSMI resin beads with superparamagnetic magnetite nanoparticles.

1.9 References

1. W.J. Princeton, C. Van Nostrand, *Gold: Recovery, Properties and Application*, 3rd ed., Harcourt College Publishers, New York, N.Y., **1964.**
2. E.W. Gray, J. Gray, *A History of the Discovery of the Witwatersrand Goldfields*, Sholto Douglas, Johannesburg, **1940**.
3. T.G.H. James, *The British Museum, Gold Technology in Ancient Egypt: Mastery of Metal Working Methods*, Gold Bulletin V., **1972**.
4. V. Ringnes, *Journal of Chemical Education* **1989**, 66 (9), 731.
5. I.M. Holmes, *Great Gold Rushes*, London: Lun, **1947**.
6. E. Rosenthal, *Gold! Gold! Gold!: The Johannesburg Gold Rush*, New York, N.Y.: Macmillan, **1970**.
7. J.G. Cohn, E.W. Stern, *Kirk-Othmer Encyclopedia of Chemical Technology*, John Wiley and Sons Book Co., New York, N.Y, vol. 11, **1980**.
8. R.R. Keays, W.R.H. Ramsay, D.I. Groves, *The Geology of Gold Deposits: The Perspective in 1988*, Economic Geology Pub. Co., U.S.A, 1989.
9. For futher information *see* http://geology.com/minerals/gold.shtml
10. C. Gasparrini, *Gold and Other Precious Metals: From Ore to Market*, Springer-Verlag, **1993**.
11. A.C. Barnicoat, I.H.C. Henderson, R.J. Knipe, B.W.D. Yardley, R.W. Napier, N.P.C. Fox, A.K. Kenyon, D.J. Muntingh, D. Strydom, K.S. Winkler, S.R. Lawrence, C. Cornford, *Nature* **1997**, 386, 820.
12. H.E. Frimmel, *Science* **2002**, 297, 1815.
13. For further information *see* http://minerals.usgs.gov
14. C.Y. Yap, N. Mohamed, *Chemosphere* **2007**, 67, 1502.
15. A. Ramesh, K. Fujiwara, T. Maki, H. Hasegawa, K. Ueda, *Journal of Hazardous Materials* **2007**, 146, 39.
16. A. Ramesh, H. Hasegawa, W. Sugimoto, T. Maki, K. Ueda, *Bioresource Technology* **2008**, 99, 3801.
17. M. Spitzer, B. Rodnei, *Hydrometallurgy* **2004**, 74, 233.

18. R.J. Puddephatt, *The Chemistry of Gold*, Amsterdam: Elsevier Science, **1978**.
19. W.S. Rapson. T. Groenewald, *Gold Usage*, Academic Press, London, **1978**.
20. M. Juliusa, S. Robertsa, J.C.Q. Flethera, *Gold Bulletin* **2010**, 43, 298.
21. J.O. Marsden, I. House, *The Chemistry of Gold Extraction*, Horwood, New York, N.Y., **1992**.
22. M.D. Adams, *Advances in Gold Ore Processing*, Boston:Elsevier, Amsterdam, **2005**.
23. T. Kirke Rose, W.A.C. Newman, *The Metallurgy of Gold*, Charles Griffin and Co., Ltd., London, **1937**.
24. A. King, *Gold Metallurgy on the Witwatersrand*, Johannesburg, **1949**.
25. J.B. Hiskey, X.H. Jiang, *Advances in Gold and Silver Processing*, SME-AIME, Warrendale, **1990**.
26. G.M. Schmid, M.E. Curly-Florina, *in Encyclopedia of Electrochemistry of the Element*, Vol. 4, A.J. Bard (Ed.), Marcel Dekker, New York, N.Y., **1978**.
27. S. Örgül, Ü. Atalay, *Hydrometallurgy* **2002**, 67, 71.
28. H. Gavin, A.J. Monhemius, *Journal of Cleaner Production* **2006**, 14, 1158.
29. G. Korte, F. Coulson, *Ecotoxicology and Environmental Safety* **1998**, 32, 96.
30. S.R. La-Brooy, H.G. Linge, G.S. Walker, *Minerals Engineering* **1994**, 7, 1213.
31. B. Donmez, F. Sevim, S. Colak, *Chemical Engineering and Technology* **2001**, 24, 91.
32. J.C. Yannopoulus, *The Extractive Metallurgy of Gold*, Van Nostrand Reinhold Book Co., New York, N.Y., **1991**.
33. H. Renner, *Ulmann's Encyclopedia of Industrial Chemistry*, Vol. A21, 5th ed., VCH Publishers, **1992**.
34. R. Chand, T. Watari, K. Inoue, H. Kawakita, H.N. Luitel, D. Parajuli, T. Torikai, M. Yada, *Minerals Engineering* **2009**, 22, 1277.
35. M. Cox, *Science and Practice of Liquid-Liquid Extraction*, Clarendon Press, Oxford, **1992**.
36. *Proceedings of the International Solvent Extraction Conference*, Cape Town, South Africa, Volume 2, K.C. Sole, P.M. Cole, J.S. Preston, D.J. Robinson (eds.), **2002**.
37. J.A. Kitchener, *Ion-exchange resins*, Methuen, London, **1957**.
38. J.X. Khym, *Analytical Ion-exchange Procedures in Chemistry and Biology: Theory, Equipment, Techniques*, Prentice-Hall, Inc., Englewood Cliffs, New Jersey, **1974**.

39. K. Dorfner, *Ion-exchangers: Properties and Applications*, 2nd ed., Ann Arbor Science Publishers Inc., Michigan, U.S.A., **1973**.
40. C.W. Ammen, *Recovery and Refining of Precious Metals*, Chapman and Hall Inc., New York, N.Y., **1997**.
41. N. Arbiter, K.N. Han, *Gold: Advances in Precious Metal Recovery*, Gordon and Breach Science Publishers S.A., New York, N.Y., **1990**.
42. C.S. Brooks, *Metal Recovery from Industrial Wastes*, Lewis Publishers, Chelsea, MI
43. L. Barbieri, R. Giovanardi, I. Lancelloti, M. Michelazzi, *Environmental Chemistry Letters* **2010**, 8, 171.
44. J. Cui, L. Zang, *Journal of Hazardous Materials* **2008**, 158, 228.
45. L.E. Macaskie, N.J. Creamer, A.M.M. Essa, N.L. Brown, *Biotechnology and Bioengineering* **2007**, 96, 631.
46. N.J. Creamer, V.S. Baxter-Plant, J. Henderson, M. Potter, L.E. Macaskie, *Biotechnology Letters* **2006**, 28, 1475.
47. I. Villaescusa, V. Salvado, J. De Pablo, *Hydrometallurgy* **1996**, 41, 303.
48. G. Morteani, *Gold: Progress in Chemistry, Biochemistry and Technology*, Wiley and Sons, N.Y., **1999**.
49. X. Sun, Y.C. Guan, K.N. Han, SME, Denver, Colorado, U.S.A, **1995**.
50. M. Cox, *Solvent extraction in hydrometallurgy. Principles and Practices of Solvent Extraction*, In: Rydberg, C. Musikas, G.R. Choppin (Eds.), Marcel Dekker, Inc., New York, N.Y., **1992**.
51. R.I. Edwards, W.A.M. te Riele, *Commercial process for precious metals. Handbook of Solvent Extraction*, John Wiley and Sons, New York, N.Y., **1986**.
52. J. Marsden, L. House, *Chemistry of Gold Extraction*, Ellis Horwood, Hartnoll, U.K., **1993**.
53. C.P. Gomes, *Seperation and Purification Technology* **2001**, 24, 35.
54. P. Navarro, C. Vargas, M. Alonso, F.J. Alguacil, *Gold Bulletin* **2006**, 39, 93.
55. S. Mansooreh, K. Tahereh, *Bioresource Technology* **2008**, 99, 5374.
56. C. Rumi, W. Takanori, I. Katsutoshi, K. Hidetaka, N.L. Hom, P. Durga, T. Toshio, Y. Mitsunori, *Minerals Engineering* **2009**, 22, 1277.
57. M. Cox, A.A. Pichugin, E.I. El-Shafey, Q. Appleton, *Hydrometallurgy* **2005**, 78, 137.

58. L. Zhang, Z. Li, X. Du, X. Chang, *Microchimica Acta* **2011**, 174, 391.
59. D. Li, X.C. Zheng, Z. Hu, Q. Wang, Z. Tu, R. Li, *Microchimica Acta* **2011**, 174, 131.
60. Z. Tu, S. Lu, X. Chang, Z. Li, Z. Hu, L. Zhang, H. Tian, *Microchimica Acta* **2011**, 173, 231.
61. F.J. Alguacil, P. Adera, M. Alonso, *Gold Bulletin* **2005**, 38, 9.
62. E. Latif, D. Sahan, A. Basaran, S. Mustafa, *Environmental Monitoring and Assessment* **2007**, 132, 331.
63. H. Koshima, *Analytical Sciences* **1986**, 2, 255.
64. M. Laatikainen, E. Paatero, *Hydrometallurgy* **2005**, 79, 154.
65. E. Latif Elci, S. Mustafa, E.B. Buyuksekerci, *Analytical Sciences* **2003**, 19, 1621.
66. R. Rajasingam, N.S. Jayasinghe, F.P. Lucien, T. Tran, *Minerals Engineering* **2006**, 19, 896.
67. H. Zhang, D.B. Dreisinger, *Hydrometallurgy* **2002**, 66, 67.
68. J.E. Huheey, E.A. Keiter, R.L. Keiter, *Inorganic Chemistry: Principles of Structure and Reactivity*, 4th Ed., Harper Collins College Publishers, New York, N.Y., **1993**.
69. C. Kantipuly, S. Katragadda, A. Chow, H.D. Gesser, *Talanta* **1990**, 37, 491.
70. E. Antico, A. Masana, V. Salvado, M. Hidalgo, M. Valiente, *Analytica Chimica Acta* **1994**, *296*, 325.
71. J. Polakovicova, J. Medved, V. Stresko, J. Kubova, A. Celkova, *Analytica Chimica Acta* **1996**, *320*, 145.
72. S. Siddhanta, H. R. Das, *Talanta* **1985**, *32*, 457.
73. K. M. Dingman, K.M. Gloss, E. A. Milano, S. Siggia, *Analytical Chemistry* **1974**, *46*, 145.
74. M. Grote, A. Kettrup, *Analytica Chimica Acta* **1985**, *175*, 239.
75. M. Grote, A. Kettrup, *Analytica Chimica Acta* **1987**, *201*, 95.
76. M. A. Congost, D. Salvatierra, G. Marques, J. L. Bourdelande, J. Font, M. Valiente, *Reactive & Functional Polymers* **1996**, *28*, 191.
77. Y. B. Qu, *Analyst (Cambridge, United Kingdom)* **1996**, *121*, 139.
78. D. Morin, A. Lips, T. Pinches, J. Huisman, C. Frias, A. Norberg, E. Forssberg, *Hydrometallurgy* **2006**, 83, 69.

79. Y.N. Mata, E. Torres, M.L. Blázquez, A. Ballester, F. González, J.A. Mu˜noz, *Journal of Hazardous Materials* **2009**, 166, 612.
80. M.E. Romero-Gonz'alez, C.J. Williams, P.H.E. Gardiner, *Environmental Science and Technology* **2003**, 37, 4163.
81. N. Kuyucak, B. Volesky, *Biotechnology Letters* **1988**, 10, 137.
82. D.W. Darnall, B. Greene, M.T. Henzl, *Environmental Science and Technology* **1986**, 20, 206.
83. A.V. Pethkar, S.K. Kulkarni, K.M. Paknikar, *Bioresource Technology* **2001**, 80, 211.
84. Savvaidis, *BioMetals* **1998**, 11, 145.
85. T. Takehiko, *Journal of General and Applied Microbiology* **2004**, 50, 221.
86. E. Gabuil, A. Larkin, T. Vincent, J.M. Tobin, *Industrial and Engineering Chemistry Research* **1999**, 38, 4011.
87. T.-Y. Hsien, G.L. Rorrer, *Industrial and Engineering Chemistry Research* **1997**, 36, 3631.
88. W.S. Wan Ngah, K.H. Liang, *Industrial and Engineering Chemistry Research* **1999**, 38, 1411.
89. K. Inoue, K. Yoshizuka, K. Ohto, *Analitica Chimica Acta* **1999**, 388, 209.
90. M. Ruiz, A. Sastre, E. Gabuil, *Reactive and Functional Polymers* **2000**, 45, 155.
91. R.C.W. Berkeley, *Chitin, Chitosan and Their Degradation Enzymes.* In *Microbial Polysaccharides*, eds. Academic Press, New York, N.Y., **1979**.
92. G.L. Rorrer, T.-Y. Hsien, J.D. Way, *Industrial and Engineering Chemistry Research* **1993**, 32, 2170.
93. E. Onsøyen, G. Skaugrud, *Journal of Chemical Technology and Biotechnology* **1990**, 49, 395.
94. P. Sorlier, A. Denuzière, C. Viton, A. Domard, *Biomacromolecules* **2001**, 2, 765.
95. T.C. Yang, R.R. Zall, *Industrial and Engineering Chemistry Product Research and Development* **1984**, 23, 168.
96. E. Gabuil, C. Milot, J.M. Tobin, *Industrial and Engineering Chemistry Research* **1998**, 37, 1454.
97. A.M. Donia, A.A. Atia, K.Z. Elwakeel, *Hydrometallurgy* **2007**, 87, 197.
98. Y.C. Yang, D.H. Chen, *Gold Bulletin* **2006**, 39, 98.

99. H. Wang, C. Bao, F. Li, X. Kong, J. Xu, *Microchimica Acta* **2010**, 168, 99.
100. D.-H. Chen, Y.-C. Chang, *Gold Bulletin* **2006**, 39, 98.
101. T.-Y. Hsien,G.L. Rorrer, *Seperation Science and Technology* **1995**, 30, 2455.
102. G. Bronow, *Methods to reveal the structure of lignin.* In *Biopolymer: Lignin, Humic Substances and Coal*, M. Hofrider, A. Steinbuchel, Eds. Wiley-VCH: New York, N.Y., **2001**.
103. M. Funaoka, *Polymer International* **1998**, 47, 277.
104. D. Parajuli, C.R. Adhikari, M. Kuriyama, H. Kawakita, K. Ohto, K. Inoue, M. Funaoka, *Industrial and Engineering Chemistry Research* **2006**, 45, 8.
105. F.I. Koon, M.F. Chi, L.Y. King, M. Gordon, *Chemical Engineering Journal* **2008**, 145, 185.
106. K.F. Lam, K.L. Yeung, G. McKay, *Journal of Physical Chemistry B* **2006**, 110, 2187.
107. P. Durga, K. Hidetaka, I. Katsutoshi, O. Keisuke, K. Kumiko, *Hydrometallurgy* **2007**, 87, 133.
108. H. Koyanaka, K. Takeuchi, C.K. Loong, *Seperation and Purification Technology* **2005**, 43, 9.
109. D.M. Ruthven, *Principles of Adsorption and Adsorption Processes*, John Wiley and Sons, New York, N.Y., **1984**.
110. B. Crittenden, W.J. Thomas, *Adsorption Technology and Design*, Elsevier Science and Technology Books, Oxford, U.K., **1998**.
111. M. Suzuki, *Adsorption Engineering*, Elsevier Science and Technology Books, Amsterdam, **1990**.
112. D.D. Do, *Adsorption analysis: Equilibria and Kinetics*, Imperial College Press, London, **1998**.
113. R.X. Grimshaw, C.E. Harland, *Ion-exchange: Introduction to Theory and Practice*, London: Chemical Society, **1998**.
114. Z. Reddad, C. Gerente, Y. Andres, P. Le Cloirec, *Environmental Science and Technology* **2002**, 36, 2067.
115. A.S. Erses, *Journal of Hazardous Materials* **2005**, B121, 223.
116. W. Ngeontae, W. Aeungmaitrepirom, T. Tuntulani, *Talanta* **2007**, 71, 1075.
117. F. Veglio, F. Beolchini, *Hydrometallurgy* **1997**, 44, 301.

118. M.L. Arrascue, H.M. Garcia, O. Horma, E. Gabuil, *Hydrometallurgy* **2003**, 71, 191.
119. I.V. Mironov, E.V. Makotchenko, *Journal of Solution Chemistry* **2009**, 38, 725.
120. W. Rob, *Inorganic Chemistry* **1967**, 6, 382.
121. C.F. Baes Jr., R.E. Mesmer, *Hydrolysis of Cations*, Wiley, New York, **1987**, 490.
122. T. Ogata, Y. Nakano, *Water Research* **2005**, 39, 4281.
123. P.J. Murphy, M.S. LaGrange, *Geochimica Cosmochimica Acta* **1998**, 62, 3515.
124. P.J. Murphy, G. Stevens, M.S. LaGrange, *Geochimica Cosmochimica Acta* **2000**, 64, 479.
125. J.A. Peck, C.D. Tait, B.I. Swanson, G.E. Brown, *Geochimica Cosmochimica Acta* **1991**, 55, 671.
126. A.J. Bard, R. Parsons, J. Jordan (Eds.), *Standard Potentials in Aqueous Solutions*, Marcel Dekker, New York, N.Y., **1985**.
127. M. Pourbaix, *Atlas of Electrochemical Equilibria in Aqueous Solutions*, Pergamon, New York, N.Y., **1966**.
128. A. Henglein, *Chemistry Reviews* **1989**, 89, 1861.
129. Klabunde, K.J., *Nanoscale materials in Chemistry*. 2007, New York: Wiley-Interscience.
130. C.N.R. Rao, A Muller, A.K. Cheetava, *The Chemistry of Nanomaterials*, Vol.1, Wiley-VCH, Weinheim, Germany, **2004**.
131. E. Vassileva, B. Varimezova, K. Hadjiivanov, *Analitica Chimica Acta* **1996**, 336, 141.
132. Y. H. Wang, *Journal of Hazardous Materials* **2003**, *B102*, 291.
133. A. Uheida, M. Iglesias, C. Fontas, M. Hidalgo, V. Salvado, Y. Zhang, M. Muhammed, *Journal of Colloid and Interface Science* **2006**, *301*, 402.
134. L. L. Vatta, J. Kramer, K. R. Koch, *Separation Science and Technology* **2007**, *42*, 1985.

2 Synthesis and characterization of functionalized poly(styrene-*co*-maleimide) nanoparticles

Synopsis

Functionalized poly(styrene-*co*-maleimide) (PSMI) nanoparticles were synthesized by thermal imidization of the poly(styrene-*co*-maleic anhydride) (PSMA) copolymer with 3-*N*,*N*-dimethylaminopropylamine (DMAPA). The functionalized PSMI nanoparticles in dispersion as well at the isolated dried forms were characterized by electron microscopy. In both cases, monodisperse spherically shaped nanoparticles with narrow size-distributions were obtained. The average diameters of the nanoparticles are approximately 50 nm. ^{13}C NMR, FTIR and elemental analyses confirmed the successful and complete conversion of PSMA into the PSMI derivative. The specific surface area of the bulk PSMI nanoparticles was measured by the BET method was found to be 88.1 ± 2.2 m^2/g with an average pore diameter of 82.3 Å.

2.1 Introduction

Poly(styrene-*co*-maleic anhydride) or PSMA is an inexpensive commercially available polymer which can be found in various grades with maleic anhydride contents between 6 and 50 % and molecular weights between 1000 and 300 000 g/mol. The chemical structure of the PSMA copolymer illustrating the styrene and maleic anhydride groups is shown in Figure 2.1.

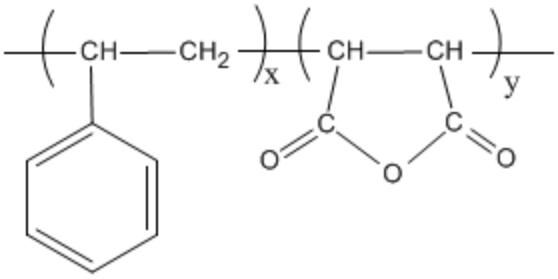

Figure 2.1 Chemical structure of poly(styrene-co-maleic anhydride). The subscripts x and y denotes the styrene and maleic anhydride contents, respectively in the copolymer.

In recent times much research has gone into the development of poly(styrene-*co*-maleimide) or PSMI due to the improved thermal properties offered by the material including higher thermal stability and heat resistance as compared to those of the PSMA copolymer analogue. Moreover, other beneficial properties of this class of polymers include tractability, good chemical stability, high durability, and radiation resistance. [1-4] Current uses of PSMI and PSMA derivatives include the treatment of paper, plastic, glass, nails, textiles and other surfaces in order to improve the characteristics of these surfaces. [5,6]

It has been reported that PSMI was first synthesized in 1982 by the Mitsubishi Monsanto Chemical Company. [1] Since then, numerous methodologies for the preparation of PSMI have been explored. The free radical copolymerization of styrene and maleimide is well documented in scientific literature. [7-9] However, the high cost and complex synthesis of the precursors from the respective monomers, the use of organic solvents such as acetone, methyl ethyl ketone (MEK), tetrahydrofuran (THF) and *N*,*N*-dimethylformamide (DMF) makes this process less attractive. The high reactivity of the maleic anhydride groups in the PSMA copolymer towards nucleophilic reagents enables the manufacturing of *new* PSMI materials with a variety of properties and functionalities using alternative methods. Such a method for the preparation of PSMI derivatives for example, is by reactive extrusion. This is a process in which the PSMA copolymer is reacted in the melt with low molecular weight compounds such as ammonia or a suitable primary amine in an extruder at elevated temperatures. Vermeesch and Groeninckx reported the chemical modification of PSMA with primary *N*-alkylamines by reactive extrusion

to obtain an analogous imide copolymer product. [10,11] Due to the relative ease of synthesis, versatility, total cost-effectiveness and possibility of mass production within an economically feasible reaction time, the most convenient method for the preparation of PSMI is arguably by the direct imidization of PSMA. [6,12] The imidization reaction entails the chemical modification of PSMA *via* the cyclic maleic anhydride groups with functional primary amines of choice to obtain the corresponding imide copolymer PSMI product. Shown in Scheme 2.1 is the general imidization reaction equation of the PSMA copolymer with a primary amine, where R denotes any functional groups other than primary (1°) or secondary (2°) amine moieties. It should be pointed out that the use of primary amines with R end groups of 1° and 2° amine functionality results in cross-linking with the consequence of insoluble reaction product formation.

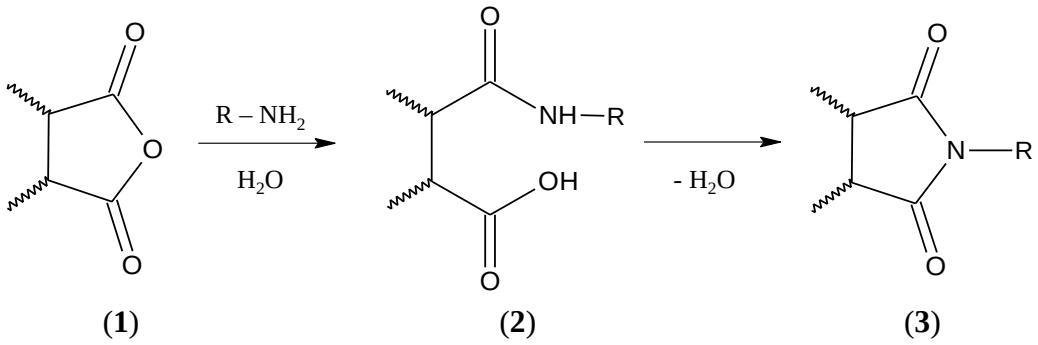

Scheme 2.1 General imidization reaction of the PSMA copolymer with a primary amine to obtain a PSMI derivative. For simplicity only the maleic anhydride moiety is shown.

The first step in the imidization reaction (Scheme 2.1) is the nucleophillic attack of the primary amine moiety of R – NH_2 on a maleic anhydride carbonyl carbon of the PSMA copolymer (**1**) leading to ring-opening (amidation) to give the intermediate adducts (**2**). The second step which involves a dehydration process is ring-closure (cyclization) to obtain the imidized product, PSMI (**3**). The imidization product derived from PSMA may consist of maleic anhydride groups of (**1**), maleamic and carboxylic acid groups of (**2**), and maleimide groups of (**3**), depending on the degree of conversion. The degree of conversion in turn depends on the reaction parameters such as the reaction time, temperature and pressure. Therefore, to optimize the conversion level and to meet the requirements of this thesis, the imidization reactions were performed in an autoclave at

elevated temperatures which also results in the spontaneous formation of nanoparticles. [5,6] The nanoparticles are very specific for the aqueous system.

In this chapter, the synthesis and characterization of functionalized PSMI nanoparticles from the direct imidization of the PSMA copolymer analogue in aqueous media is described. The functionalized PSMI nanoparticles will then be used as a *novel* ion-exchange material for the extraction and separation of $[AuCl_4]^-$ ions from aqueous acidic solutions (Chapter 3). Throughout the rest of this thesis, the functionalized PSMI will simply be referred to as PSMI.

2.2 Experimental

2.2.1 Materials

Poly(styrene-*co*-maleic anhydride) (PSMA) pellets with a weight average molar mass of 80 × 10^3 g/mol and composition of 26 % maleic anhydride and 74 % styrene in the backbone was donated by Polyscope (Geleen, the Netherlands). Prior to use, the PSMA pellets were dissolved in acetone under mild stirring, subsequently the solvent was allowed to evaporate completely at 50 °C resulting in a frail polymer substance. This polymer material was then gently crushed and used as starting reagent as is. Analytical grade 3-*N*,*N*-dimethylaminopropylamine (DMAPA, 99 %) was purchased from Sigma-Aldrich. All other chemicals and solvents were of reagent grade and used without further purification. High purity deionized water (Milli Q, 18 MΩ cm) was used throughout the synthetic work.

2.2.2 Instruments and measurements

Particle size and morphology was determined by Transmission Electron Microscopy (TEM), using a JEM 1200EXII model (JEOL, Japan) microscope. An accelerating voltage of 200 kV was used throughout. A drop of sample was placed on a carbon-coated 200 mesh copper grid, followed by drying at ambient conditions before it was attached to the sample holder on the

microscope. Prior to use, the grids were glow discharged for 30 seconds under air in a vacuum of 10^{-2} mbar. The particle size and morphology of the dried isolated nanoparticles was visualized on nano-scale resolution with Scanning Electron Microscopy (SEM), using a Nova NanoSEM (FEI Company). The mean diameters of the nanoparticles in the dispersion and powder forms were determined with statistical analysis by measuring 100 – 200 individual particles from the micrographs using *Image J*, a public domain image processing program. [13] Elemental analysis was done with an Exeter Analytical CE 440 elemental analyzer. ^{13}C NMR spectra were recorded on a Varian Inova 600 MHz spectrometer operating at 150.586 MHz. A typical sample consists of 250 mg of the polymer dissolved in 1 mL acetone-d_6 and the experiments conducted at an elevated temperate of 44.8 °C. All samples were carefully filtered before any spectroscopic measurement was undertaken. ^{13}C NMR resonances were assigned in conjunction with DEPT and APT techniques. Fourier transform infrared (FTIR) spectra were recorded on a Nexus FTIR spectrophotometer equipped with a Smart Golden Gate attenuated total reflectance (ATR) diamond from Thermo Nicolet, with ZnSe lenses. Each spectrum was scanned 32 times with 4.0 cm^{-1} resolution and data analysis was performed with Omnic Software version 7.2. Surface area measurements were carried out using the Brunauer-Emmet-Teller (BET) method on a Micrometrics ASAP 2010 (Accelerated Surface Area and Porosity System) apparatus using nitrogen as an adsorbent. The samples were degassed at 30 °C for approximately 48 h before use. Each degassed sample (0.1 – 0.4 g) was weighed accurately to four decimal places and placed in a sample tube. Analysis was performed using an automatic multi-point adsorption programme, measuring the volume of nitrogen adsorbed by the sample at a range of N_2 pressures. Thermogravimetric analysis (TGA) was carried out with Q500 TA instrument in the temperature range 0 – 590 °C, using aluminium crucibles with typically 3 – 5 mg dried samples under dynamic N_2 atmosphere (50 mL/min) and heating rate of 10 °C min^{-1}.

2.2.3 Synthesis of PSMI nanoparticles

Poly(styrene-*co*-maleimide) (PSMI) nanoparticles were synthesized by thermal imidization of poly(styrene-*co*-maleic anhydride) (PSMA) with 3-*N*,*N*-dimethylaminopropylamine in a double walled oil heated autoclave equipped with a mechanical agitator using water as solvent. A typical preparation was as follows: 2 × 835 µL DMAPA was added to 5 g crushed PSMA (which is a

1:1 molar ratio between primary amine and maleic anhydride residues) suspended in 50 mL H_2O and allowed to stir at 1000 rpm for 6 h with temperatures between 150 °C – 180 °C and a pressure of 4 – 7 bar. These reaction conditions used were chosen to ensure that complete conversion of starting maleic anhydride moiety into a homogeneous imide product was achieved. It was found that the conversion of PSMA into PSMI as well as the morphology of the nanoparticles is dependent on the reaction time, temperature and agitation rate. (Refer to the supplementary information section for further details). On completion of the imidization reactions using the optimum conditions, stable milky dispersions were obtained.

The obtained water-based dispersions containing the PSMI nanoparticles were purified by dialysis for at least 48 h using dialysis tubing with molecular weight cut-off of 3500 g/mol. Freeze drying for 24 h was used to isolate the PSMI nanoparticles from the dispersions. Subsequently, the resulting off-white fine powdered substance was dried at 50 °C in a vacuo (200 mbar) for a further 6 – 8 h to constant weight before used as an adsorbent material in the extraction experiments.

Shown in Scheme 2.2, is the general imidization reaction illustrating the modification of the PSMA copolymer into the corresponding PSMI derivative and in Figure 2.2 is the autoclave used for the synthesis of the PSMI nanoparticles.

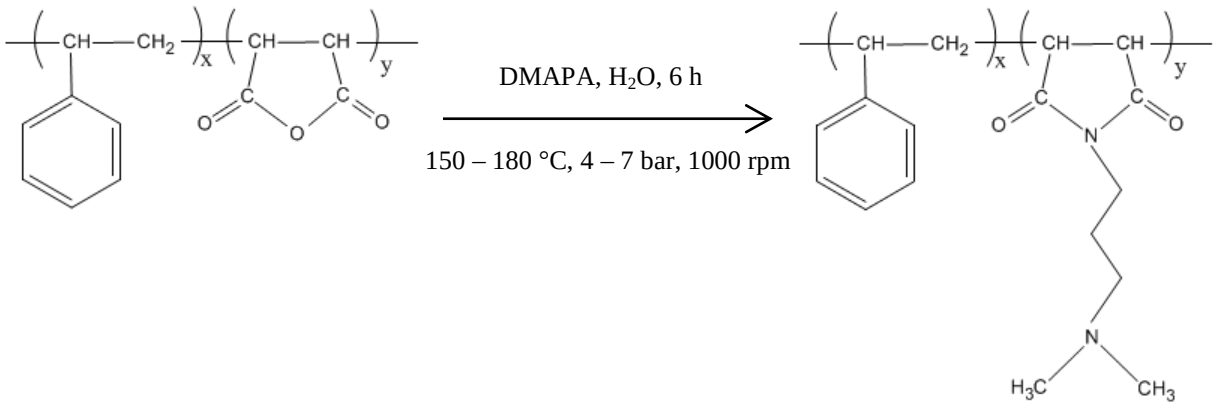

Scheme 2.2 Chemical modification of the PSMA copolymer into the PSMI derivative during the imidization reaction in water. The subscripts x and y denotes the styrene and maleic anhydride contents which are 74 % and 26 %, respectively.

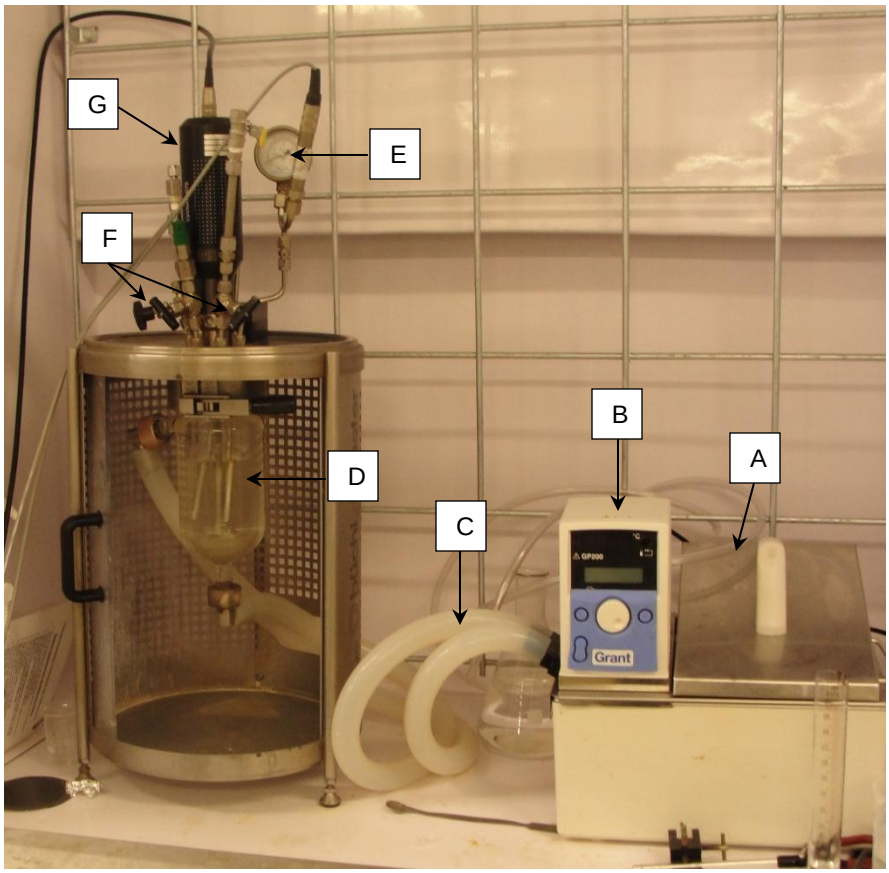

Figure 2.2 The Büchi double walled oil-heated autoclave used for the preparation of the PSMI nanoparticles by the imidization reaction. The components as indicated are identified in Table 2.1.

Table 2.1 Components of the Büchi double walled oil-heated autoclave.

Component	Name
A	Silicon oil reservoir / thermostat bath
B	Temperature control / regulator
C	Silicon oil tubing
D	250 mL glass reactor vessel
E	Pressure gauge
F	Pressure release valves
G	Mechanical rotor for overhead stirrer

2.3 Results and discussion

2.3.1 Elemental analysis

The elemental analyses of PSMA and PSMI are shown in Table 2.2. As expected, the elemental composition of PSMA revealed the presence of C and H only, while the modified PSMI derivate contains C, H and N elements, confirming successful conversion during the imidization reaction (Scheme 2.2). From Table 2.2, it can be seen that there is excellent correlation between experimental and calculated values for the C, H and N elements. The total ligand concentration of PSMI was calculated to be 4.30 ± 0.04 mmol g^{-1} based on the nitrogen content, as is generally done. [14] However, it should be pointed out that the accessible ligand concentration available for interaction with metal species is much smaller due to buried tertiary amines inside the PSMI particles.

Table 2.2 Elemental (C, H and N) analysis of the PSMA copolymer and the PSMI nanoparticles

Polymer	C (%)	H (%)	N (%)	Total ligand concentration (mmol g^{-1})‡
SMA	80.39 (81.50)	6.35 (6.33)	0	-
SMI	78.72 (79.72)	7.73 (7.74)	6.08 (5.85)	4.34

Values in parenthesis are the calculated values

‡ Based on the experimental nitrogen content

2.3.2 ^{13}C nuclear magnetic resonance analysis

The ^{13}C NMR spectra of PSMA and PSMI are shown in Figure 2.3 (a) and (b), respectively. A downfield chemical shift of the carbonyl carbons (C5 and C6) from δ_{PSMA} (^{13}C) = 173 ppm to δ_{PSMI} (^{13}C) = 180 ppm occurred after modification of PSMA into PSMI. The absence of the carbonyl carbon peaks associated with the maleic anhydride moiety of PSMA in the spectrum of PSMI (Figure 2.3 (b)), suggests complete conversion into the maleimide derivative. As expected, no chemical shift changes were observed for the styrene carbons (C12 – C15) after the

modification. Interestingly, the quaternary carbon of the styrene unit (C12) shows multiple peaks which can be ascribed to stereochemical configurations and copolymer sequences. [15,16] The carbon peaks (C1 – C4 and C7 – C11) were unambiguously assigned using an attached proton test (APT) experiment (*see* supplementary information, Figure s2.7) and is indicated in Figure 2.3. Note that the numbering was attributed by the application used for drawing the chemical structures and is arbitrary.

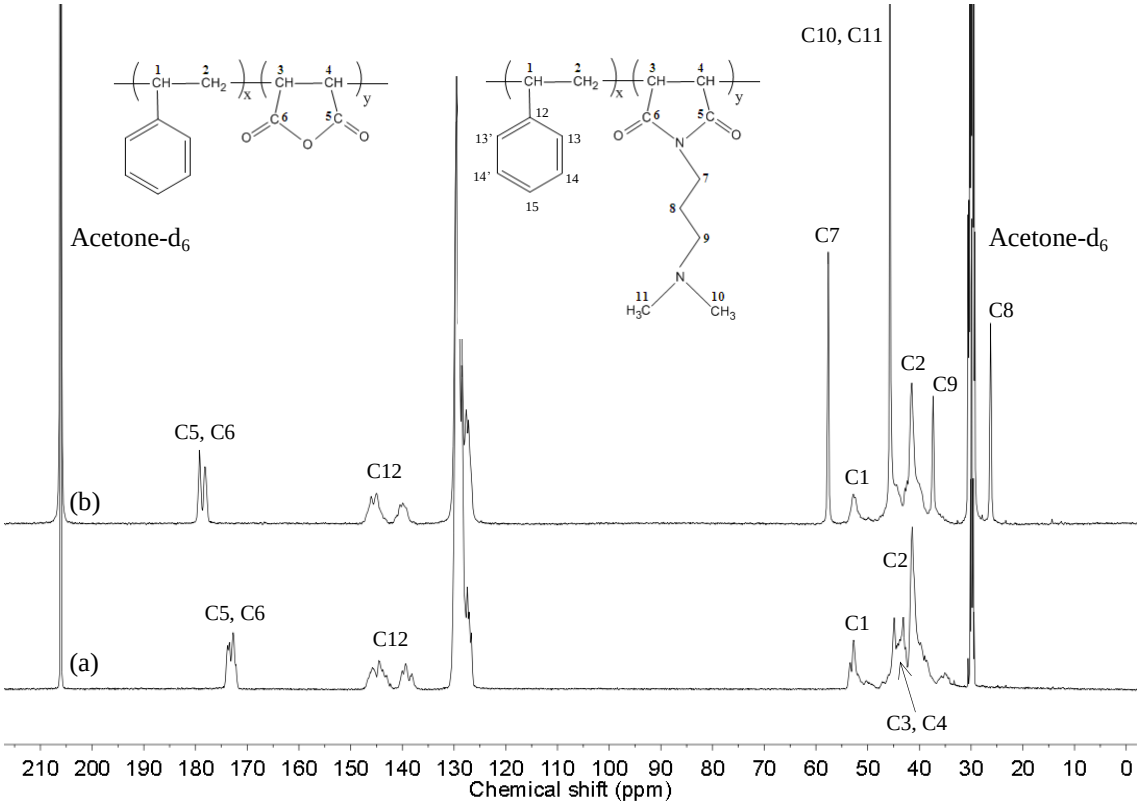

Figure 2.3 ^{13}C NMR spectra of (a) PSMA and (b) PSMI in acetone. The chemical structures of the polymers with the carbon number allocations are shown as insets. Experimental conditions – Frequency: 150.586 MHz; Temperature: 317.9 K; Total acquisition time: 24 h. ^{13}C NMR chemical shifts were quoted relative to the acetone-d_6 resonance at 207 ppm.

2.3.3 ATR-FTIR analysis

The FTIR spectra of PSMA (broken line) and PSMI (solid line) in the region 600 – 2000 cm^{-1} are shown in Figure 2.4. The characteristic C=O stretching vibrations associated with maleic anhydride groups of PSMA are easily distinguished from the maleimide groups of PSMI. A clear shift in the C=O absorption bands from 1848 and 1772 cm^{-1} (corresponding to the anhydride group in the five-membered ring) to 1765 and 1691 cm^{-1} (assigned to the newly formed imide group in the five-membered ring), confirms successful imidization of PSMA into the PSMI derivative. [4,5,17] The absence of the C=O absorption bands of PSMA in the infrared spectrum of PSMI signifies that complete conversion was achieved as substantiated by the ^{13}C NMR results (Figure 2.3). Also shown is the typical overlapping absorption bands in the fingerprint area (1502 – 1418 cm^{-1}) and at 1608 – 1566 cm^{-1}, associated with the C-H bending and C=C stretching vibrations of styrene, respectively.

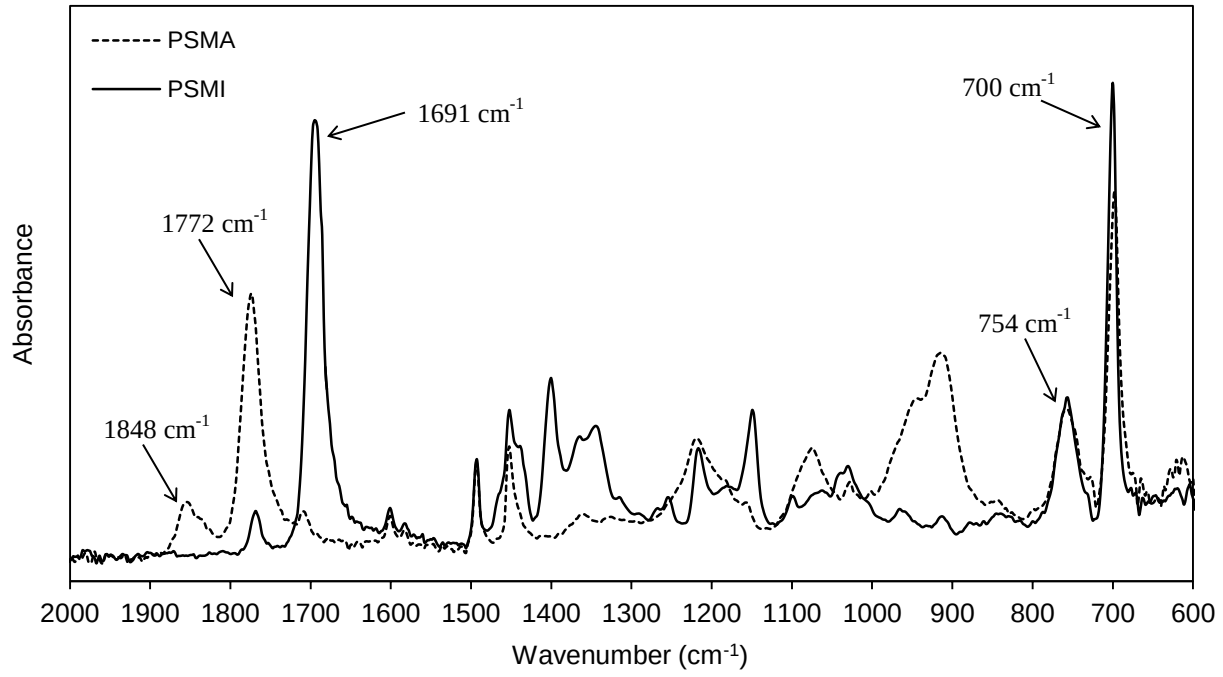

Figure 2.4 FTIR absorption spectra of the PSMA copolymer (broken line) and the corresponding PSMI nanoparticles (solid line) illustrating the complete conversion of PSMA into the PSMI derivative during the imidization reaction.

Other significant differences in the two spectra are summarized in Table 2.3. Most notably, C-H bending and stretching vibrations associated with the terminal tertiary amine (-N(CH_3)$_2$) groups are observed in the spectrum of PSMI in the region 1418 – 1275 cm^{-1} and 2833 – 2692 cm^{-1}, respectively. These prominent peaks were not present in the FTIR spectrum of PSMA.

Table 2.3 Major FTIR absorption bands (cm^{-1}) of the PSMA copolymer and the PSMI nanoparticles

PSMA	PSMI	Assignments of absorption bands
3100 – 2977.6	3100 – 2977.6	aromatic C-H stretching
2977.6 – 2832.9	2977.6 – 2832.9	aliphatic C-H stretching
–	2832.9 – 2692.2	C-H stretching of –N(CH_3)$_2$ (terminal tertiary amine)
1847.5 and 1772.3	–	C=O stretching of cyclo anhydride group
–	1764.6 and 1691.3	C=O stretching of imide group
1608.4 – 1565.9 and 1502.3 – 1417.5	1608.4 – 1565.9 and 1502.3 – 1417.5	C=C stretching and bending of aromatic group(s)
–	1417.5 – 1274.7	C-H bends of –N(CH_3)$_2$ (terminal tertiary amine)
–	1274.7 – 975.8	C-N stretching (multiple bands) of tertiary amine groups
1267 – 831.2	–	C-O stretching (multiple bands) of C-O-C cyclo anhydride group
754.04 – 700.05	754.04 – 700.05	C-H stretching of monosubstituted aromatic ring of styrene

2.3.4 Electron microscopy analysis

The shape and size properties of the PSMI nanoparticles in both the dispersion as well as the isolated dried states were investigated using transmission and scanning electron microscopy. Figure 2.5 shows (a) the TEM micrograph and (b) the corresponding size distribution histogram of the PSMI nanoparticles present in the stable water-based dispersions.

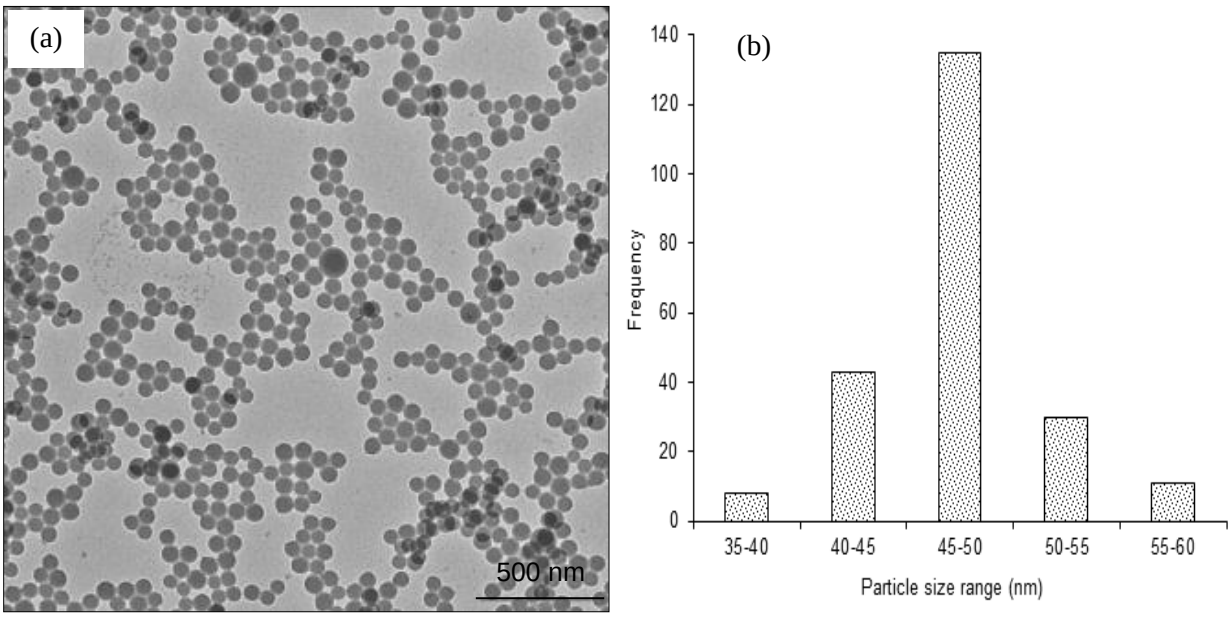

Figure 2.5 (a) TEM micrograph of the PSMI nanoparticles obtained from the imidization reaction and (b) the corresponding size distribution histogram. The average PSMI nanoparticle diameters obtained my measuring about 200 individual particles are 50 ± 4.9 nm.

As can be seen, well disseminated monodispersed nanoparticles with spherical morphology and mean diameters of 50 ± 4.9 nm were attained. No apparent excessive agglomeration was evident in the samples. It was possible to synthesize the PSMI nanoparticles reproducibly with very similar size distributions using the same experimental conditions (Scheme 2.2). Following successful imidization reactions, the PSMI nanoparticles (after purification with a dialysis method) were isolated from the dispersion using freeze drying to obtain a powdered polymer "sponge". The SEM micrographs at different magnifications (viewed on nano-scale resolution) of such a sample are shown in Figure 2.6.

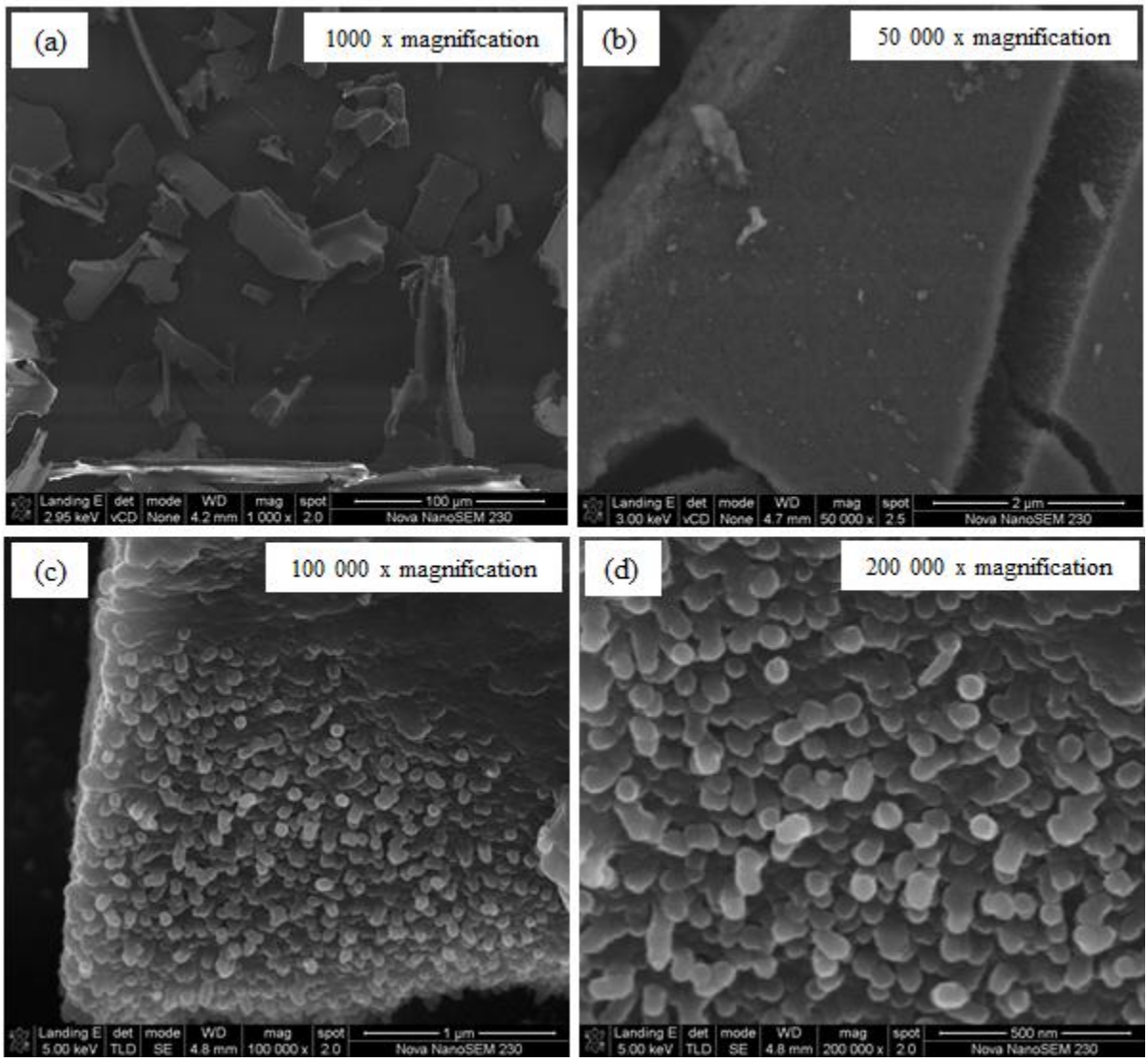

Figure 2.6 SEM micrograph of the dried PSMI nanoparticles isolated from the dispersion by freeze drying. The average PSMI nanoparticle diameters obtained after measuring more than 100 individual nanoparticles are 50.9 ± 6.2 nm.

At 1000 x magnification, it is revealed that the powdered polymer sponge resembles a flake-like structured material. Gradually increasing the magnification (Figure 2.6 (a) – (d)), it becomes clear that the polymer sponge is composed of individual nanoparticles that clustered together during the isolation and freeze drying procedure (refer to experimental section). The polymer sponge however, was further dried in a vacuum oven at 50 °C for 6 h to isolate the bulk PSMI material. The configuration and surface area structures of the dried, bulk desiccated PSMI

nanoparticles used as an adsorbent in the extraction and pre-concentration of gold from solution (Chapter 3) is depicted by the SEM micrographs in Figure 2.7. The presence of spherically shaped nanoparticles is confirmed. This is explicit evidence that the integrity of the PSMI nanoparticles in the stable dispersions were retained after isolation to the dried state. From these SEM micrographs (Figures 2.6 and 2.7) the particles sizes were measured to be 50.9 ± 6.2 nm in diameter, which is in good agreement with the sizes obtained from TEM analysis (Figure 2.5).

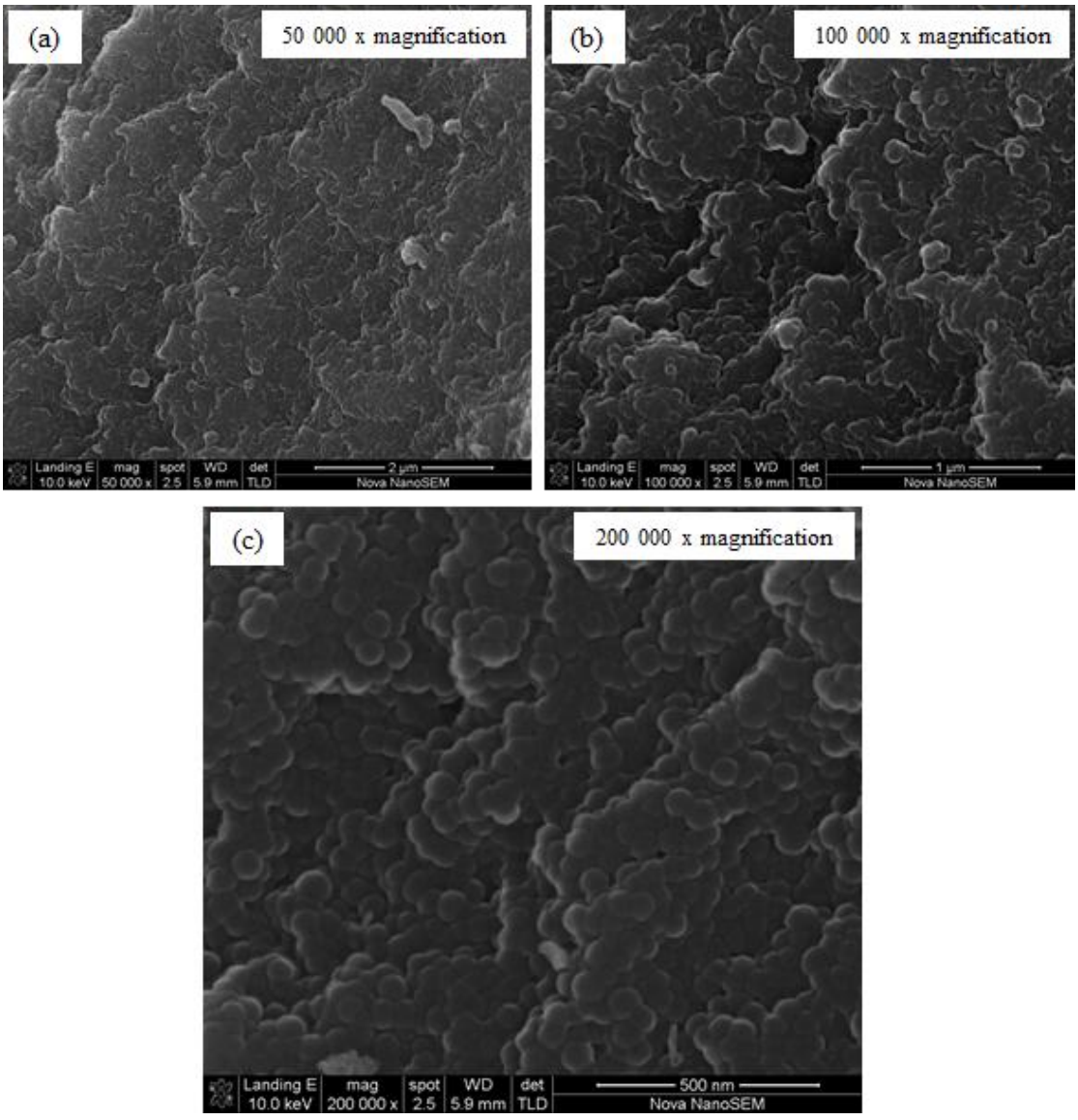

Figure 2.7 SEM micrograph of the dried PSMI nanoparticles isolated from the dispersion by freeze drying followed by oven drying. The average PSMI nanoparticle diameters obtained after measuring more than 100 individual nanoparticles are 50.9 ± 6.2 nm.

2.3.5 Surface area and porosity analysis

The surface area and porosity of bulk PSMI material containing nanoparticles was determined using the BET method. Although the individual PSMI nanoparticles are dense and non-porous, the bulk PSMI material displays clear evidence of features of porosity as illustrated in Figure 2.7 (b) and (c). This observed porosity arises from the packing density of the virtually spherical particles. The N_2 adsorption-desorption isotherm is shown in Figure 2.8. As can be seen from Figure 2.8, the adsorption increases rapidly at low relative pressure, moderately at intermediate relative pressure, and then quite rapidly as the relative pressure approaches unity. Reversing the process by reducing the relative pressure leads to the formation of a slight hysteresis loop. This behaviour is typical of mesoporous materials, i.e. those that have pore sizes larger than 20 Å but less than 500 Å. The BET specific surface area of the PSMI sample was determined as 88.07 ± 2.23 m^2/g with an average pore diameter of 82.30 Å and pore volume of 0.45 cm^3/g.

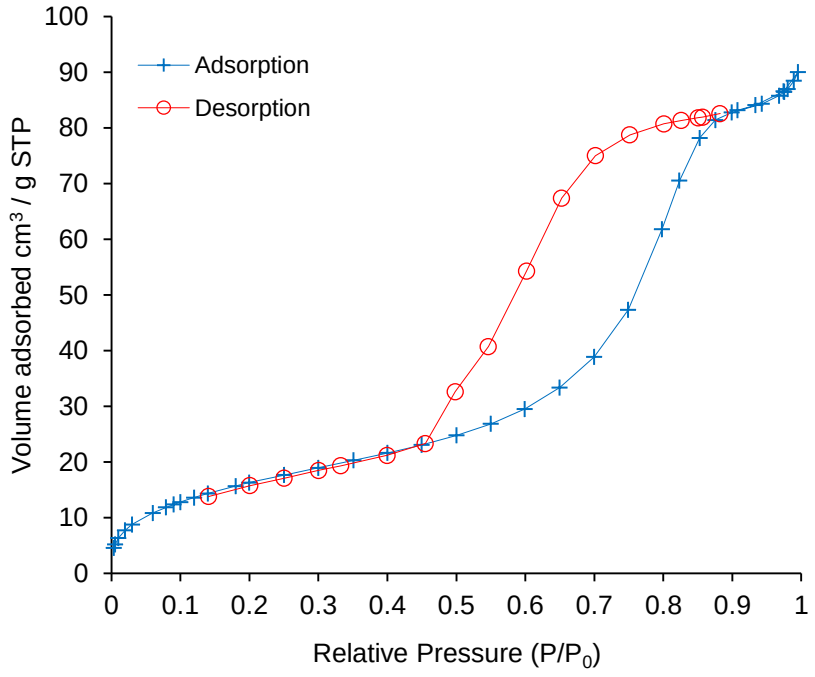

Figure 2.8 BET nitrogen adsorption-desorption isotherms for the bulk PSMI nanoparticles.

Tanev and Pinnavaia defined the term "textural" porosity. [18] Textural porosity represents the porosity which arises from intra-aggregate voids and spaces formed by interparticle contacts such as observed in Figure 2.7. The presence of textural porosity can be verified by the appearance of a well-defined hysteresis loop in the P/P_0 region from 0.5 to 1.0 (Figure 2.8). Therefore, the bulk PSMI material containing individual non-porous nanoparticles can be described as having textural porosity.

2.3.6 Thermal analysis

The TGA thermograms of the PSMA copolymer (broken line) and the PSMI nanoparticles (solid line) are shown in Figure 2.9.

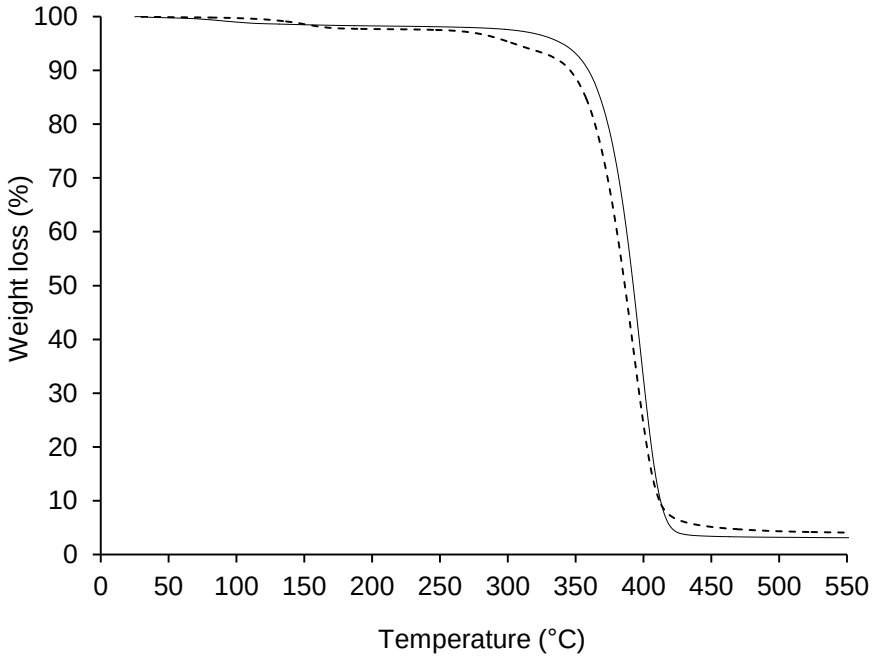

Figure 2.9 TGA thermograms of the PSMA copolymer (broken line) and the PSMI nanoparticles (solid line).

It was found that the thermal stability for both materials is more or less similar before 250 °C with negligible weight loss. Thereafter, a faster rate of weight loss is observed for PSMA compared to PSMI. The onset temperature of decomposition for PSMA is noted as 250 – 260 °C

and for PSMI 285 – 295 °C, indicating enhanced thermal stability after modification. In the latter stages, PSMA and PSMI show the same decomposition patterns with a single step weight loss. The TGA thermograms thus indicate that the PSMI nanoparticles can be safely used and are thermally stable up to about 285 °C. It is believed that PSMI is extremely heat resistant because of the bulky and rigid five-membered maleimide group. [6]

2.4 Conclusions

In this study, stable water-based dispersions were prepared by an imidization reaction in a double walled oil-heated autoclave using an organic solvent free process. The obtained dispersions were purified by dialysis to remove relics such as possible free 3-*N*,*N*-dimethylaminopropylamine (DMAPA). TEM analysis shows that the dispersions are composed of monodisperse spherically shaped PSMI nanoparticles with average diameters of 50 ± 4.9 nm. The PSMI nanoparticles were isolated from the purified dispersion by freeze drying to yield a fine powdered substance. Subsequently, this powder was further dried in a vacuum oven at 50 °C for 6 – 8 h until constant weight. SEM analysis on the powdered PSMI substances reveals that the physical integrity of the individual nanoparticles was retained. Average PSMI nanoparticle diameters of 50.9 ± 2.2 nm were obtained which agrees reasonably well with that estimated by TEM analysis. The specific surface area of the bulk PSMI nanoparticles is 88.1 ± 2.2 m^2/g. The modification of the PSMA copolymer into the PSMI derivative was investigated by ^{13}C NMR and FTIR analysis. The results show that complete conversion of PSMA into the PSMI derivative was possible using an agitation rate of 1000 rpm, a temperature higher than 140 °C and reaction time of 6 h in the imidization reaction. The successful conversion of PSMA into PSMI was validated by elemental analysis which shows a good correlation between experimentally obtained and calculated values for the C, H and N elements. A total ligand concentration of the bulk PSMI nanoparticles was determined as 4.30 ± 0.04 mmol nitrogen per gram PSMI. Thermal analyses show an increase in the thermal stability of PSMI as compared to the PSMA copolymer. The PSMI nanoparticles could be homogenously and reproducibly synthesized with narrow size-distributions using the optimum reaction conditions.

2.5 References

1. H.Y. Liu, K. Cao, Y. Huang, Z. Yao, B.G. Li, G.H. Hu, *Journal of Applied Polymer Science* **2006**, 100, 2744.
2. Y. Aoki, *Macromolecules* **1998**, 21, 1277.
3. Z. Yao, B.G. Li, W.J. Wang, Z.R. Pan, *Journal of Applied Polymer Science* **1999**, 73, 615.
4. H. Fang, F. Mighri, A. Ajji, *Journal of Applied Polymer Science* **2008**, 109, 3938.
5. M. Ahokas, C.E. Wilén, *Polymer Bulletin* **2011**, 66, 491.
6. P. Samyn, M. Deconinck, G. Schoukens, D. Stanssens, L. Vonck, H. Van den Abbeele, *Polymers Advanced Technologies* **2010**, 23, 311.
7. G. H. Kim, C.D. Keun, S.J. Kim, L.S. Park, *Journal of Polymer Science A* **1999**, 37, 3715.
8. H. Winter, G.P.M. van der Velden, *Macromolecules* **1992**, 25, 4285.
9. M.J. Caulfield, D.H. Solomon, *Polymer* **1999**, 40, 1251.
10. I. Vermeesch, G. Groeninckx, *Journal of Applied Polymer Science* **1994**, 53, 1363.
11. I. Vermeesch, G. Groeninckx, *Macromolecules* **1993**, 26, 6643.
12. E. Bortel, M. Styslo, *Macromolecular Chemistry and Physics* **1993**, 191, 2653.
13. W. Rasband, *In Image J: Image processing and analysis in Java* http://rsb.info.nih.gov/ij/, 2006.
14. W. Li, M. Coughlin, R.L. Albright, R.H. Fish, *Reactive and Functional Polymers* **1995**, 28, 89.
15. Y. Inoue, A. Nishioka, R. Chujo, *Makromol Chem* **1972**, 156:207.
16. N.T. Hieu Ha, *Polymer* **1999**, 40, 1081.
17. D.L. Pavia, G.M. Lampman, G.S. Kriz, *Introduction to Spectroscopy*, 3rd ed., Harcourt College Publishers, New York, U.S.A, **2001.**
18. P.T. Tanev, T.J. Pinnavaia, *Chemical Materials* **1996**, 8, 2068.

2.6 Supplementary information

Important parameters that were considered in the modification of maleic anhydride into maleimide included reaction time, temperature, agitation rate, weight percentage of starting copolymer and molar ratio of amine to maleic anhydride moiety. This was done to gain some insight into the formation of the nanoparticles, but most importantly to determine the optimum conditions required to reproducibly synthesize homogeneous and monodisperse nanoparticles with a high degree of conversion and a narrow size distribution. In all cases, an equimolar ratio of amine to maleic anhydride was used for fixed weight percentages of *ca* 10 wt % PSMA copolymer. For PSMA concentrations exceeding 12 wt % in 50 mL aqueous phases, no imidization reactions occurred. The various parameters are summarized by the factorial design in Table s2.1. The internal temperature and pressure reached inside the reaction vessel at the completion of individual experiments as well as the measured viscosities of the reaction mixtures obtained are reported.

Firstly, the effect of reaction temperature was investigated. Figure s2.1 shows the FTIR spectra for the products obtained during the imidization reactions as a function of various reaction temperatures (*see* Table s2.1). The peaks that appear at 697.2 and 747.3 cm^{-1} which are attributed to the C-H stretching vibrations of styrene are present in all of the spectra and as expected remain unchanged throughout the studied temperature range (Figure s.2.1 (a) – (h)). The peaks between 1665 – 1555 cm^{-1} are attributed to the C=O absorption bands of the ring-opened imide rings associated with the intermediate adduct formation **2**. The typical C=O absorption bands of **3** (PSMI) appear at 1764 and 1691 cm^{-1} (*see* Figure 2.4). The absence of the C=O absorption bands at 1851 and 1772 cm^{-1} associated with **1** (PSMA) (Figure s2.1) suggest that DMAPA reacted completely with the starting copolymer. As the temperature is increased from 58.9 – 149.2 °C it is clear that C=O absorption bands associated with **2** steadily diminishes and is accompanied by a simultaneous increase in the C=O absorption bands associated with **3** as more of the PSMI forms. This observation is verified by monitoring the decrease in the relatively broad OH absorption bands (3600 – 3100 cm^{-1}) associated with the carboxylic acid groups of **2** with the rise in temperature. At a temperature of 138.1 °C (Figure s2.1 (f)) significant amounts of PSMI have already formed. At temperatures of 149.2 and 150.9 °C (Figure s2.1 (g) and (h)) complete conversion from **1** to **3** has occurred.

Table s2.1 Factorial design for the imidization of the PSMI nanoparticles as well as the viscosities of the obtained PSMI suspensions and/or dispersions.

Variable reaction time – Set temperature: 180 °C; Set agitation rate: 1000 rpm			
Time (h)	Internal temperature (°C)	Pressure (bar)	Viscosity (MPa.s)
1	121.1	1.26	1.14 ± 0.26
2	136.5	2.42	1.12 ± 0.30
3	147.7	3.21	1.56 ± 0.10
4	142.3	4.07	1.29 ± 0.65
5	146.1	4.29	1.44 ± 0.12
6	152.3	4.10	1.39 ± 0.32
Variable reaction temperature – Set time: 6 h; Set agitation rate: 1000 rpm			
Temperature (°C)	Internal temperature (°C)	Pressure (bar)	Viscosity (Mpa.s)
60	58.9	0.05	17.0 ± 2.31
80	76.9	0.11	26.7 ± 6.02
100	92.5	0.10	2.39 ± 0.40
120	101.5	0.59	1.17 ± 0.12
140	122.9	2.37	1.51 ± 0.32
160	138.1	3.67	1.37 ± 0.45
180	149.2	4.00	1.39 ± 0.32
Variable reaction agitation rate – Set time: 6h; Set temperature: 180 °C			
Agitation rate (rpm)	Internal temperature (°C)	Pressure (bar)	Viscosity (MPa.s)
200	148.0	3.10	1.75 ± 0.13
400	158.1	4.41	1.58 ± 0.17
600	153.3	3.72	1.25 ± 0.43
800	150.0	3.45	1.33 ± 0.38
1000	157.5	4.68	1.39 ± 0.32

Note: Viscosities of obtained reaction mixtures were measured *ca* one week after completion of reactions.

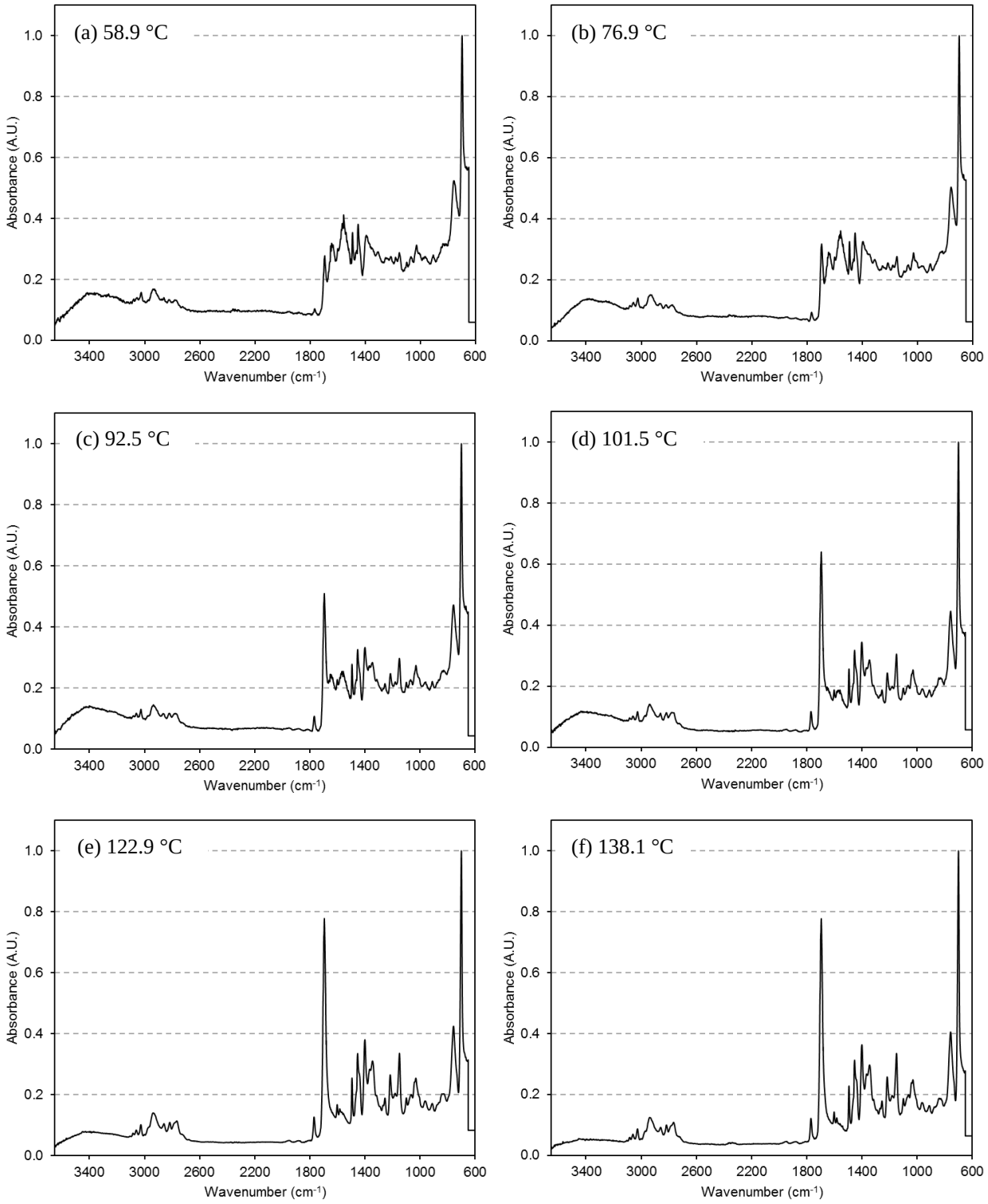

Figure s2.1 FTIR spectra of PSMI formation as a function of temperature.

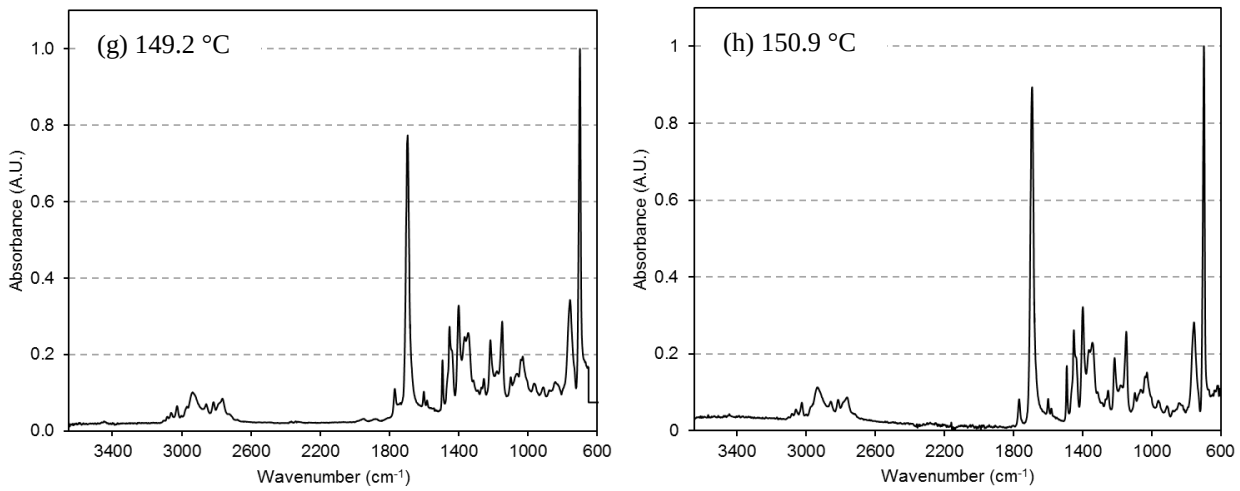

Figure s2.1 FTIR spectra of PSMI formation as a function of temperature (continued).

Shown in Figure s2.2 are the corresponding TEM and cryo-TEM micrographs (at different magnifications) of the products obtained as a function of temperature. At temperatures between 58.9 °C – 76.9 °C no definite structure is observed as the copolymer is dissolved into the ring-opened adduct form. At 92.5 °C it seems as if particle formation is initiated. The appearance of nanoparticles becomes more conspicuous at 101.5 °C. At this latter temperature, ring-closure most probably starts to occur due to the elimination of water *via* hydration. However the particles are not completely shaped. Elevating the temperature to 122.9 °C, a slight improvement in terms of particles formation is observed. Notably the micrograph shows that the density of evolving particles is much higher as compared to lower temperatures. This can most probably be attributed to incomplete conversion of ring-opened adduct and the result of hydrogen bonding. A substantial transformation in terms of particle formation is observed at 138.1 °C. At this stage, the particles are well shaped and it becomes clear that they are in the nano-size regime. At 149.2 °C it becomes unambiguous that the PSMI nanoparticles are completely formed to a fixed spherically-shaped morphology and mean particle size of approximately 50 nm.

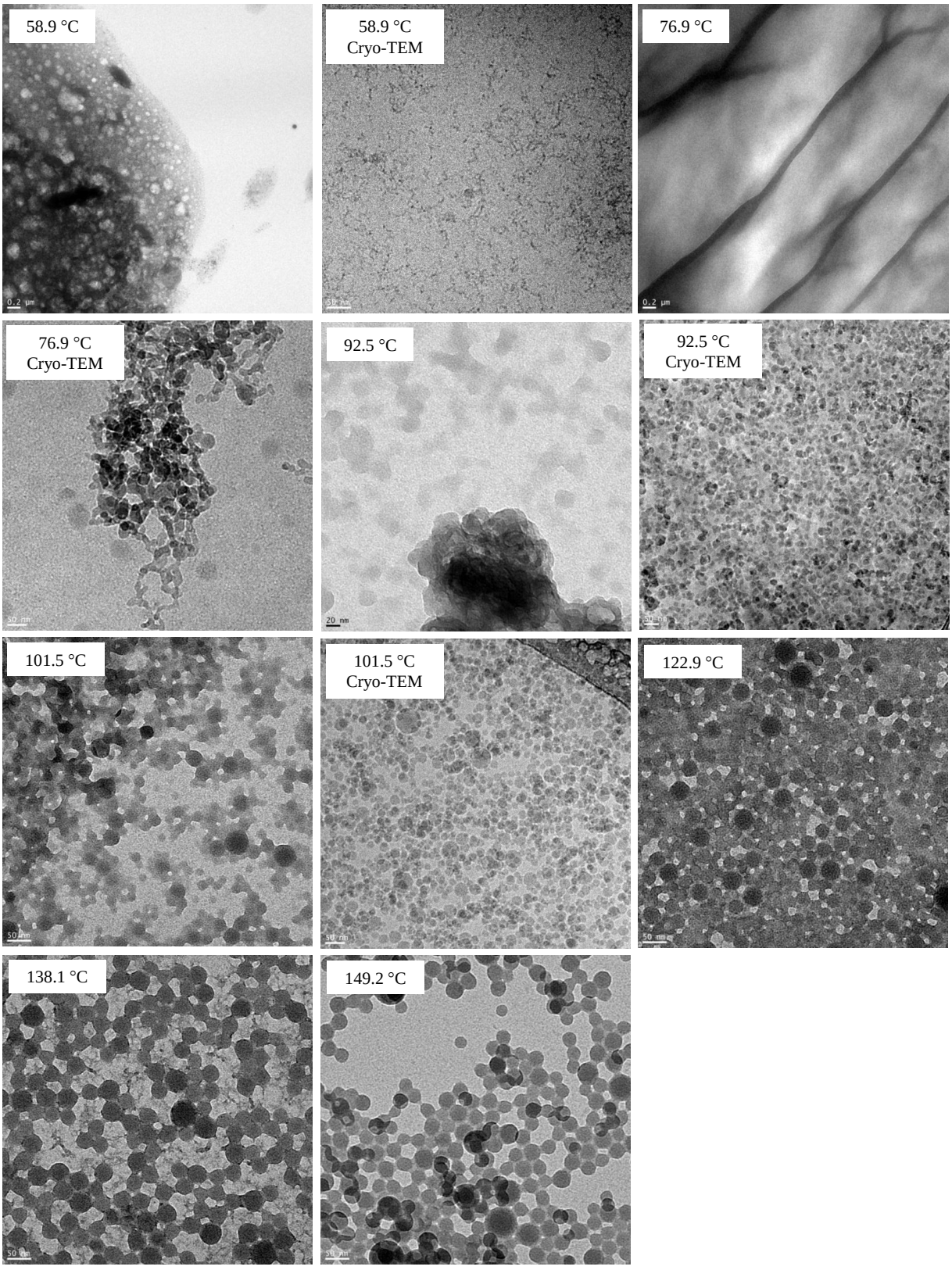

Figure s2.2 TEM micrograph illustrating PSMI nanoparticle formation as a function of temperature.

Secondly, the effect of reaction time on the formation of PSMI nanoparticles was monitored. Figure s2.3 shows the FTIR spectra of the imidization products obtained. A similar trend was observed in the formation of PSMI as was found in the temperature dependence study. An increase in the C=O absorption bands at 1764 and 1691 cm^{-1} associated with the imide group of **3** and accompanied with a simultaneous decrease of the somewhat overlapping C=O absorption bands between 1665 – 1555 cm^{-1} associated with the amide and carboxylic acid groups of **2**, respectively. A decrease in the observed OH groups associated with the carboxylic acid groups was also evident as the reaction time was prolonged, although not as prominent as in the case of the temperature dependence study. From the results in Figure s2.3 it is established that complete conversion was attained for reaction times exceeding 3 h.

Figure s2.4 depicts the TEM micrographs of the formation of PSMI nanoparticles as a function of increasing reaction time. It can be seen that after 1 and 2 h (Figure s2.4 (a) and (b)) the nanoparticles are not completely shaped but after 3 h, homogenous and spherical nanoparticles were obtained. Therefore, a reaction time of 3 h would suffice for the formation of the nanoparticles.

Thirdly, the effect of agitation on the formation of PSMI nanoparticles was monitored. It was found that complete conversion of **1** (PSMA) into **3** (PSMI) was attained irrespective of agitation rate (FTIR spectra not shown). Shown in Figure s2.5 are the TEM micrographs illustrating the PSMI nanoparticles that have been formed using the different agitation rates (*see* Table s2.1). Interestingly, the PSMI nanoparticle formation is dependent on the agitation rate used in the imidization reactions. Spherical nanoparticles were obtained in all cases but with a decrease in agitation rate a drastic increase in mean particle diameters and size distribution was observed as illustrated in Figure s2.6. The smallest particles with a narrow size-distribution were obtained using an agitation rate of 1000 rpm. It is, therefore, evident that the formation of monodisperse nanoparticles with a narrow size-distribution stems from vigorous agitation during the imidization reactions.

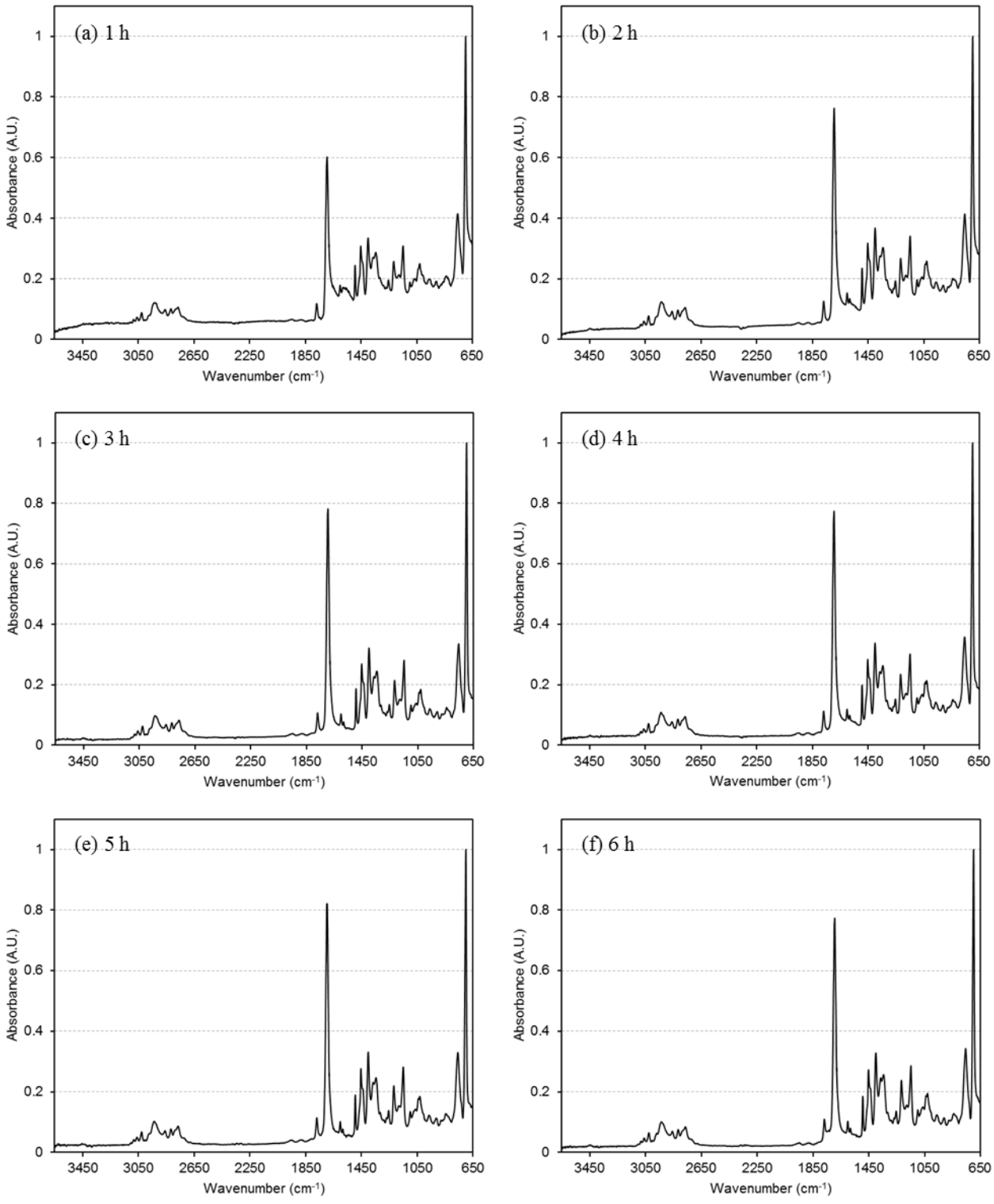

Figure s2.3 FTIR spectra of PSMI formation as a function of reaction time.

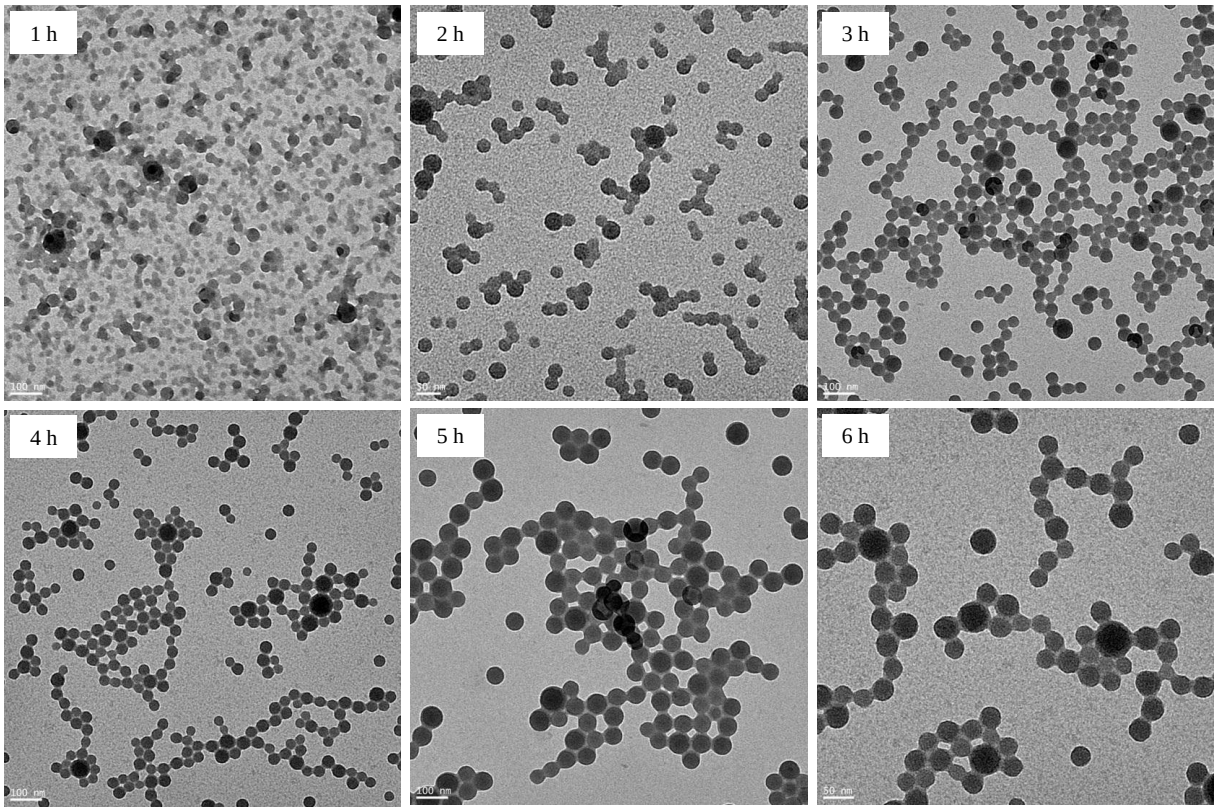

Figure s2.4 TEM micrograph illustrating PSMI nanoparticle formation as a function of reaction time.

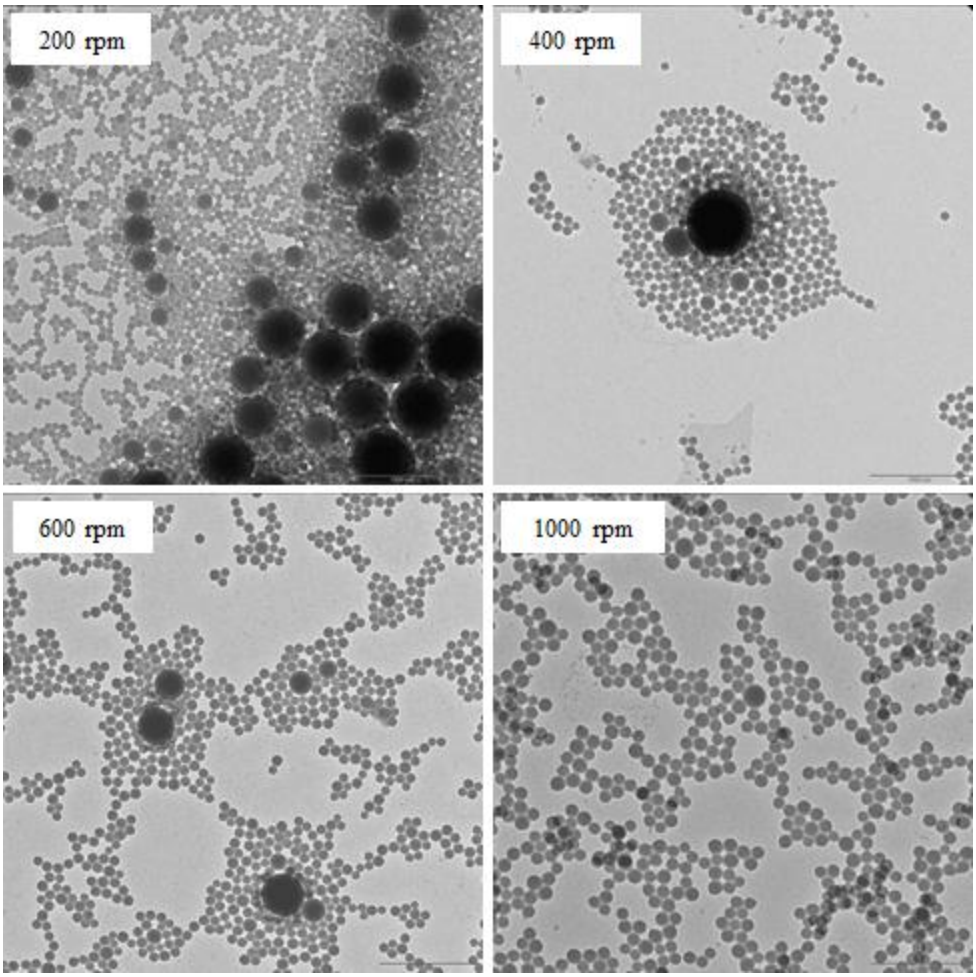

Figure s2.5 TEM micrograph illustrating PSMI nanoparticle formation as a function of agitation rate.

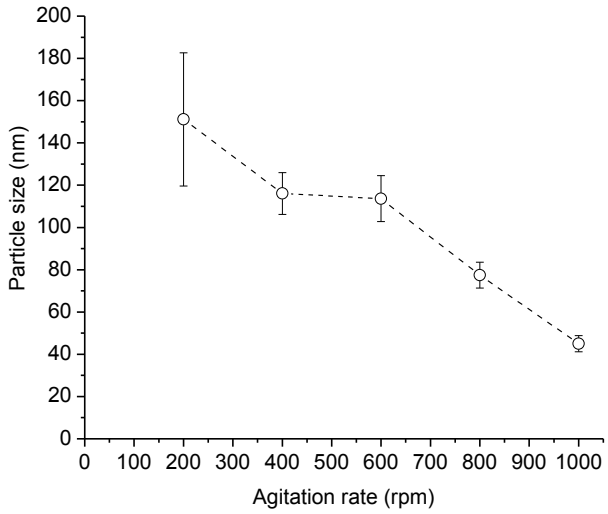

Figure s2.6 PSMI nanoparticle size-dependence on the agitation rate during the imidization reaction.

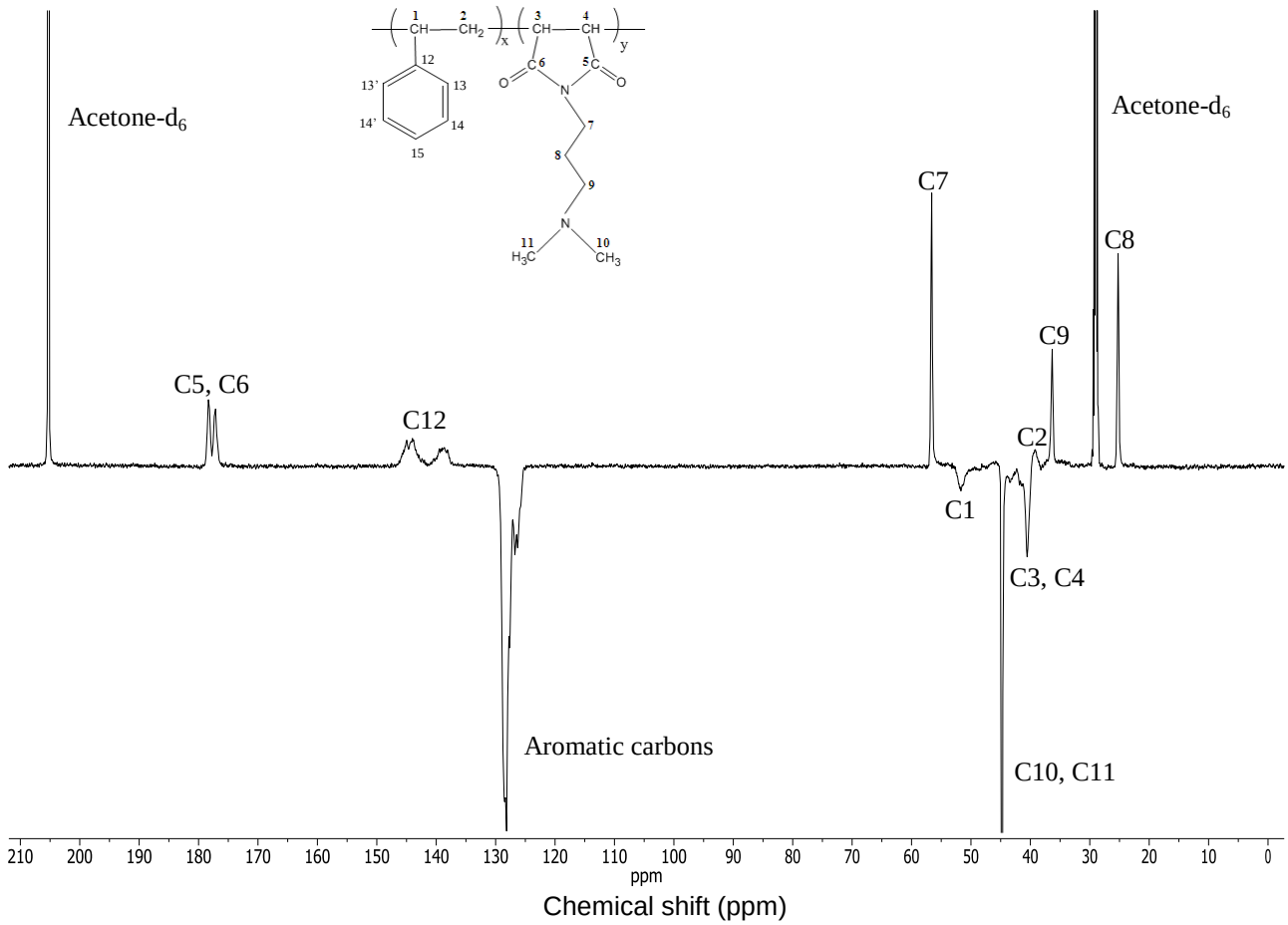

Figure s2.7 ^{13}C NMR attached proton test (APT) spectrum of PSMI in acetone. The chemical structure of PSMI with the carbon number allocations is shown in the inset. Experimental conditions – Frequency: 150.586 MHz; Temperature: 317.9 K; Total acquisition time: 24 h. ^{13}C NMR chemical shifts were quoted relative to the acetone-d_6 resonance at 207 ppm.

3 Extraction of anionic gold (III) chloride complexes from acidic solutions using poly(styrene-*co*-maleimide) nanoparticles

Synopsis

Functionalized poly(styrene-*co*-maleimide) (PSMI) nanoparticles have been investigated as anion-exchange material for the extraction of $[AuCl_4]^-$ from aqueous acidic solutions. Batch sorption studies were carried out as a function of various parameters, such as initial gold ion concentration, PSMI mass, contact time and agitation rate. Langmuir and Freundlich isotherm models were applied to analyze the experimental sorption data. The best model describing the sorption process was given by the Langmuir isotherm and the maximum gold loading capacity was found to be 1.76 mmol/g (347.7 mg/g). PSMI aliquots of 50 mg per 10 mL of a 411.5 mg/L gold feed solution were sufficient for quantitative extraction of $[AuCl_4]^-$ from the solution. The extraction occurred with extremely fast sorption rates, and was dependent on the rate of agitation during the batch sorption process. The immobilized gold ions were successfully eluted from the loaded PSMI material by desorption with up to 93 ± 1.7 % of gold being recoverable. Elemental gold was recovered from a solution of the digested gold-loaded PSMI materials by means of precipitation as a crystalline powder.

3.1 Introduction

In this chapter, the PSMI nanoparticles synthesized as described in Chapter 2 were studied for the extraction of $[AuCl_4]^-$ from aqueous acidic solutions. As shown in Scheme 3.1, PSMI

theoretically consist of two protonable 'sites' A and B which are an imide and tertiary amine functionality, respectively. 'Sites' B are expected to be more readily protonated compared to 'sites' A based on the expectation of a higher pK_b for the tertiary amine. [1] It is not clear to what extent the imide nitrogen atoms will be protonated due to the electron pair delocalization in the imide ring. The tertiary amine functionality of PSMI was specifically incorporated to become protonated in acidic solutions, in order to function as an anion-exchange material (Scheme 3.1). Thus, the design principle was to prepare selective anion-exchange materials suitable for $[AuCl_4]^-$ immobilization.

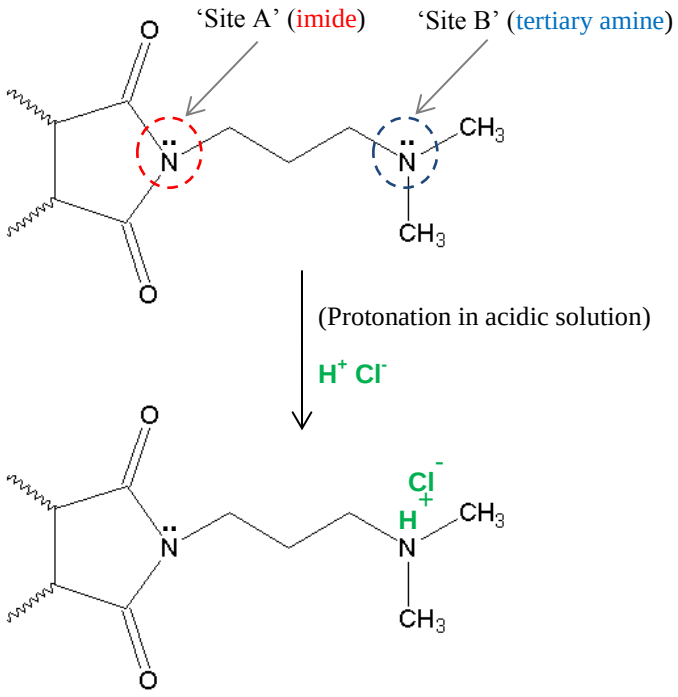

Scheme 3.1 Protonation of the tertiary amine functionality of PSMI in aqueous acidic solution to function as an anion-exchange material.

The interest in investigating functionalized PSMI nanoparticles for the extraction of $[AuCl_4]^-$ ions from acidic solutions is mainly due to the relatively large surface area-to-volume ratio offered by the nano-size anion-exchange material as well as the high affinity of protonated quaternary amines towards anionic precious metal complexes such as gold in this context. [2] The use of PSMI nanoparticles as an anion-exchange material for the extraction of $[AuCl_4]^-$ or any

other anionic metal complexes from solution is unprecedented in the scientific literature. A summary of the basic properties of the PSMI nanoparticles are shown in Table 3.1.

Table 3.1 Characteristic properties of the PSMI nanoparticles used as anion-exchange material for the extraction of $[AuCl_4]^-$ from aqueous acidic solutions.

Matrix	Styrene maleimide copolymer
Functional group	Tertiary amines
Physical form	Fine white powder
Ionic form	H^+
Total ligand concentration	4.3 ± 0.4 mmol/g[(a)]
Mean size of the particles	50 ± 5 nm[(b)] (1000 rpm)
BET specific surface area	88.1 ± 2.2 m^2/g
Average pore diameter (BET)	82.3 Å
BJH pore volume	0.45 cm^3/g
Decomposition temperature	> 290 °C

(a) Ligand concentration as determined by the N content with elemental analysis. It should be noted that not all of the nitrogen moieties will be available for gold immobilization

(b) Mean diameter dependent on agitation rate during synthesis of PSMI nanoparticles.

3.2 General remarks

An important consideration in the $[AuCl_4]^-$ extraction experiments both in view of the protonation of the available functional groups of the PSMI as well as the possible hydrolysis of the $[AuCl_4]^-$ ions is the pH of the aqueous feed solution. As mentioned in Chapter 1, $[AuCl_4]^-$ undergoes aquation to $[AuCl_{4-n}(H_2O)_n]^{n-1}$ (n = 0, 1…) to some extent as well as hydrolysis above a pH of 2 to form anionic chlorido hydroxido gold (III) complexes of the form $[AuCl_{4-x}(OH)_x]^-$, where x represents the number of hydroxide ions exchanged with the chloride ions. The formation of such species is expected to have a significant influence on the extraction efficiency.

In addition to this, another factor is the pK_a of tertiary amine and imide sites of the PSMI nanoparticles. The functional groups associated with the functionalized PSMI nanoparticles are tertiary amine moieties (Scheme 3.1), which are considered to take a medium position between strong and weak basic anion-exchange characteristics, these amine moieties being expected to have pK_a values between 4 – 6 (Table 1.2, Chapter 1). Therefore, in order for these amine moieties to be protonated and thus to be used as an anion-exchange material, the pH of the feed solution containing the $[AuCl_4]^-$ ions, must be below that of the pK_a value of the amine moieties. Hence, in this study all the extraction experiments were performed using 2 M HCl feed solutions in order to suppress any hydrolysis of $[AuCl_4]^-$, as well as to ensure that all the tertiary amine moieties of the PSMI nanoparticles are essentially protonated. In a case where some amine (and imide) moieties of PSMI are not protonated, the nitrogen atoms may coordinate to gold (III) atoms by displacing of one of the chloride ligands in the gold (III) chlorido-complexes and link the metal through the coordination metal-nitrogen bonds as shown by Equation 3.1. (In the Equation 3.1 R_3N = PSMI).

$$R_3N_{(s)} + [AuCl_4]^-_{(aq)} \rightarrow R_3N{-}AuCl_{3(s)} + Cl^-_{(aq)} \qquad (3.1)$$

Alternatively, the protonated nitrogen atoms could form ion pairs by association with the anionic gold (III) chlorido complexes as shown by Equations 3.2 and 3.3.

$$R_3N_{(s)} + (H^+ Cl^-)_{(aq)} \rightarrow R_3NH^+ Cl^-_{(s)} \qquad (3.2)$$

$$R_3NH^+ Cl^-_{(s)} + [AuCl_4]^-_{(aq)} \rightleftharpoons R_3NH^+ [AuCl_4]^-_{(s)} + Cl^-_{(aq)} \qquad (3.3)$$

The two processes could also occur simultaneously, but in strongly acidic solution the extraction mechanism is expected to occur predominantly through electrostatic interaction between protonated sites and $[AuCl_4]^-$ ions in solution to result in an ion pair formation (Equation 3.3).

In order to determine whether the oxygen donor atoms of the unmodified PSMA copolymer do not contribute to the immobilization of $[AuCl_4]^-$, controlled experiments were carried out as follows. The extraction capability of the unmodified PSMA copolymer material was examined by allowing 100 mg PSMA samples (in triplicate) to agitate at 250 rpm with approximately 500 mg/L gold feed solution in 2 M HCl, with a contact time of 24 h. After this, the solid phase was separated from the aqueous phase by centrifugation followed by filtration of the supernatant

solution. The resultant supernatant collected was analyzed with ICP-OES to quantify the amount of $[AuCl_4]^-$ removed from solution and immobilized onto PSMA. The outcome revealed that neglegible quantities of gold (0.9 ± 0.7 %) were lost from the feed solution and thus immobilized onto PSMA. From this, it can be deduced that the oxygen atoms of the PSMI do not result in significant extraction of $[AuCl_4]^-$ from solution. Therefore, the extraction of $[AuCl_4]^-$ is essentially dependant on the protonated tertiary amine sites of the PSMI nanoparticles. This is visually confirmed in Figure 3.1 by images illustrating (a) the insignificant affinity of unmodified PSMA towards $[AuCl_4]^-$, showing no visual color change indicative of $[AuCl_4]^-$ uptake by PSMA even after allowing an equilibration time of 1 week. The feed solution preserved its bright yellow $[AuCl_4]^-$ color, (b) the distribution of $[AuCl_4]^-$ from the feed solution onto the PSMI ion-exchange material. By contrast, a feed solution was completely colorless after only 5 minutes of contact time with PSMI, (c) the isolated and dried characteristic bright yellow PSMI material after $[AuCl_4]^-$ extraction.

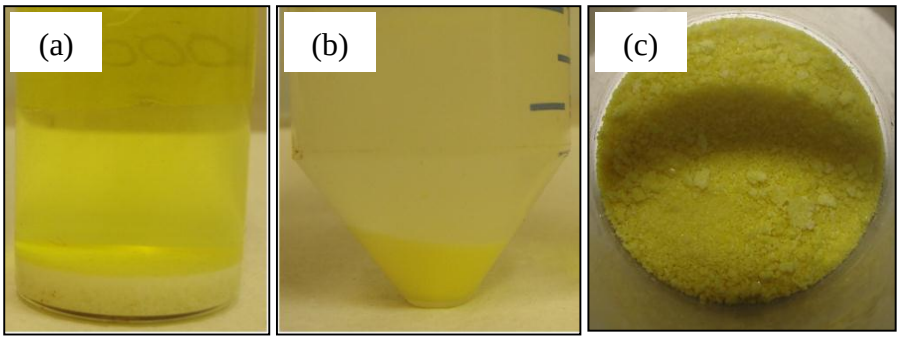

Figure 3.1 Colour changes associated with $[AuCl_4]^-$ extraction from 2 M HCl using (a) PSMA and (b) bulk functionalized PSMI anion-exchange material. The gold-loaded PSMI material is illustrated by the "bright yellow" sample in (c). Experimental conditions – Gold concentration: 500 mg/L; PSMA and PSMI masses: 100 mg and 50 mg, respectively.

3.3 Extraction and desorption methodology

The degree of immobilization or extraction of $[AuCl_4]^-$ ions from hydrochloric acidic solutions using PSMI nanoparticles as an anion-exchange material was investigated using a batch sorption process. Quantities of PSMI were accurately weighed and placed into 20 mL glass stoppered containers. To this, 10 mL aliquots of $[AuCl_4]^-$ aqueous feed solution containing various known

concentrations of gold were introduced and the containers with its contents shaken at 250 rpm (unless otherwise stated) at room temperature (23 ± 1 °C) using a horizontal mechanical shaker for a prescribed length of time to attain equilibrium. At the end of the experiments, the containers were removed from the shaker and the aqueous phase was effortlessly separated from the solid phase by centrifugation at 4500 rpm. Subsequently, the supernatant solutions (effluents) were collected for metal concentration determination by ICP-OES using a linear calibration method. The PSMI anion-exchange material containing the immobilized/loaded gold was washed with deionized H_2O (×3) to eliminate any possible entrained feed solution before desorption of gold compounds was carried out using various elutant solutions. Elution or desorption of immobilized gold was achieved by shaking the gold-loaded PSMI material with 10 mL aliquots of elutant solution for 24 h (unless otherwise stated). All effluents and eluate solutions separated were filtered through 0.45 µm filters prior to gold content analysis. The complete process flow illustrating the extraction, desorption and recovery is summarized by Scheme 3.2.

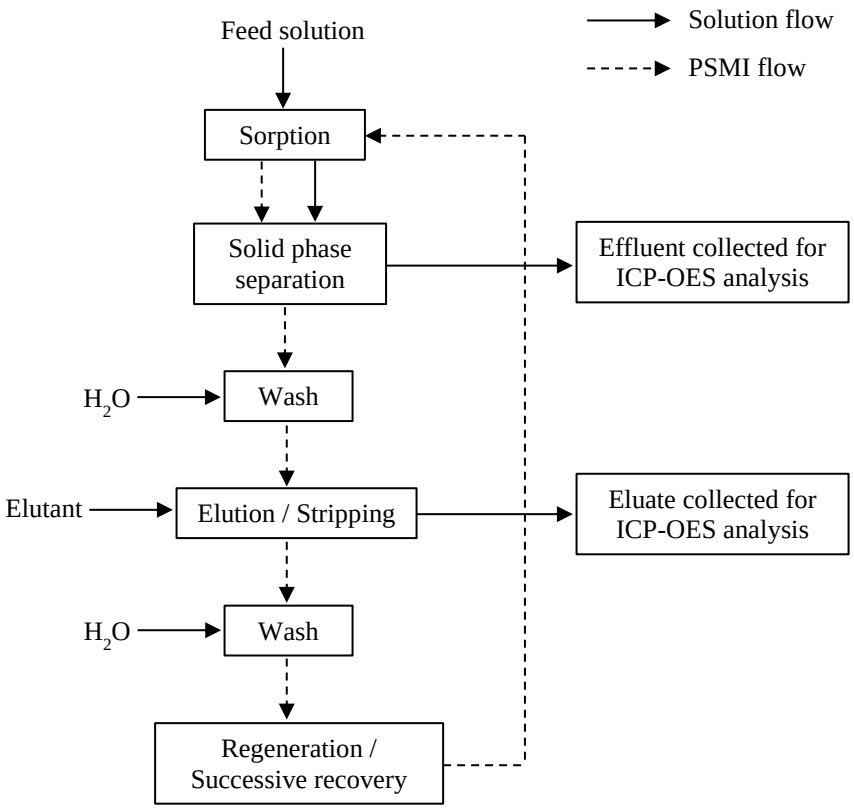

Scheme 3.2 Flow chart illustrating the $[AuCl_4]^-$ extraction from feed solution, desorption and recovery of immobilized gold from loaded PSMI nanoparticles.

The amount of $[AuCl_4]^-$ extracted from solution and immobilized, q was calculated by mass balance of the metals before and after sorption, as illustrated by Equations 3.4 and 3.5. [3,4]

$$q = (C_i - C_{aq})\frac{V}{M} \qquad [mg/g] \qquad (3.4)$$

$$\text{metal ion extraction} = \frac{(C_i - C_{aq})}{C_i} \times 100 \qquad [\%] \qquad (3.5)$$

The amount of immobilized gold eluted from the loaded PSMI was calculated by Equation 3.6 as follows:

$$\text{desorption} = \frac{C_{aq}}{C_{ads}} \times 100 \qquad [\%] \qquad (3.6)$$

In the Equations 3.4 to 3.6, C_i represents initial gold ion concentration (mg/L) in the feed solution, C_{aq} gold ion concentration in the supernatant solution (mg/L) after separation, C_{ads} gold immobilized by the PSMI (mg/L), V volume of the aqueous phase (mL) and M dosage of the PSMI (g) used.

The effect of various parameters such as contact time, the initial gold ion concentration and different dosages of PSMI material on the extent of $[AuCl_4]^-$ extraction was investigated. In addition to this, desorption of the immobilized gold species from the loaded PSMI after extraction is also reported.

3.4 Results and discussion

3.4.1 Loading capacity of PSMI nanoparticles for $[AuCl_4]^-$ ions

The $[AuCl_4]^-$ sorption behavior of various gold concentrations by PSMI nanoparticles was studied to determine the equilibrium loading capacity of the anion-exchange material for the metal ions. Illustrated in Figure 3.2, is the relationship between the equilibrium gold concentration initially present in the solution, C_e, and the equilibrium loading capacity, q_e. PSMI dosages of *ca* 10 mg per 10 mL of gold solution and a contact time of 30 min were used in the equilibrium sorption studies.

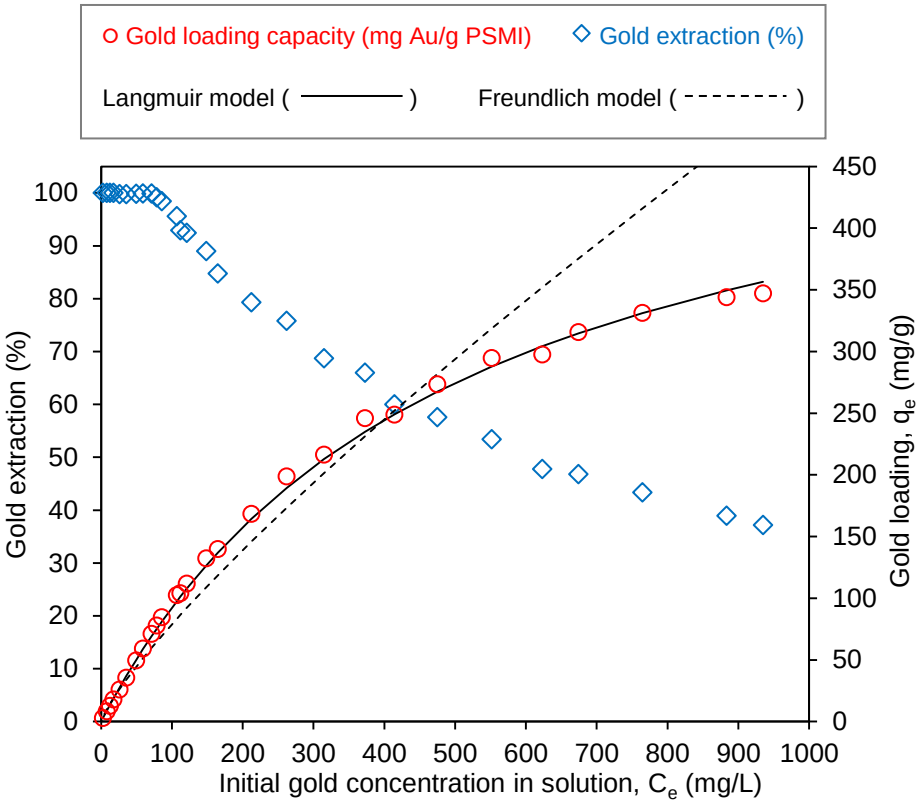

Figure 3.2 Effect of initial gold concentration in solution on the equilibrium gold loading capacity. Experimental conditions – PSMI dosage: 10 ± 0.1 mg; Total aqueous phase: 10 mL; Contact time: 30 min; Agitation rate: 250 rpm, Temperature: 23 ± 1 °C. The Langmuir model is indicated by the solid line and the Freundlich model is indicated by the dotted line.

As can be seen from Figure 3.2, the gold loading capacity increases with an increase in the initial gold concentration in solution up to a point where saturation is approached. At lower initial gold concentrations, the ratio of initial moles of gold in solution to available protonated surface sites is low. However, at higher gold concentrations, the protonated sites available for ion-exchange become fewer compared to moles of gold present; hence, the immobilization of $[AuCl_4]^-$ is strongly dependent upon the initial gold concentration in solution. Figure 3.2 also shows the corresponding extraction efficiency for each of the gold concentrations in solution. From this it can be estimated that quantitative extraction occurs rapidly between the gold concentration ranges of 1 – 100 mg/L using the 10 mg PSMI masses, which would suggest an ion-pairing mechanism. A steady decline in $[AuCl_4]^-$ extraction is observed as the gold concentration in solution is further raised (> 100 mg/L). This is due to the fact that more $[AuCl_4]^-$ ions are predominantly in solution than available protonated nitrogen sites of the PSMI nanoparticles with an increase in the gold concentration.

The Langmuir and Freundlich isotherm models as described by Equations 1.5 and 1.7 in Chapter 1 were fitted to the equilibrium sorption data (Figure 3.2). The corresponding Langmuir and Freundlich parameters along with the coefficients of correlation are listed in Table 3.2.

Table 3.2 Langmuir and Freundlich model parameters for the sorption of $[AuCl_4]^-$ ions by the PSMI nanoparticles (*see* Figure s3.1 for the linearized forms of the Langmuir and Freundlich models).

Langmuir model		Freundlich model	
q_{max} (mmol/g)	2.75	k_F (L/mmol)	0.70
k_L (L/mmol)	0.40	n	1.22
R^2	0.9912	R^2	0.9779

According to the coefficients of correlation and the model fits, the Freundlich model is less adequate for modeling the sorption of $[AuCl_4]^-$ ions by the PSMI nanoparticles. In contrast, the Langmuir model represents a good fit of the experimental data, and therefore better models the sorption isotherm. This observation suggests that sorption is dominated by a monolayer coverage process rather than a multiple layer one, which implies that once a species occupies a sorption site no further interaction takes place at that particular site. From the Langmuir model, it is predicted that the maximum gold loading capacity, q_{max} to be 2.75 mmol/g (541.7 mg/g).

However, the experimentally obtained q_{max} from the sorption data was found to be 1.76 mmol/g (346.7 mg/g), indicating that saturation of the total available protonated nitrogen sites of the PSMI nanoparticles has not been completely attained within the studied gold concentration range. The essential features of the Langmuir isotherm can be expressed in terms of the dimensionless equilibrium parameter R_L, which is defined as $R_L = 1 / (1 + k_L C_0)$, where k_L is the *Langmuir* constant and C_0 is the initial concentration of gold in solution. According to Hall *et al*, R_L values within the range $0 < R_L < 1$, indicate favorable sorption. [5] The present sorption system showed R_L values between 0 and 1 (*see* supplementary information, Table s3.1).

3.4.2 Effect of PSMI dosage at constant gold (III) ion concentration

In order to determine the optimum quantity of PSMI needed for subsequent experiments, the extent of $[AuCl_4]^-$ extraction by PSMI nanoparticles was investigated as a function of PSMI mass at constant gold concentration. A synthetic $[AuCl_4]^-$ feed solution containing 411.5 mg/L gold was used with a prolonged contact time of 24 h to ensure equilibrium sorption in all cases. Figure 3.3 shows the dependence of $[AuCl_4]^-$ extraction on the PSMI mass.

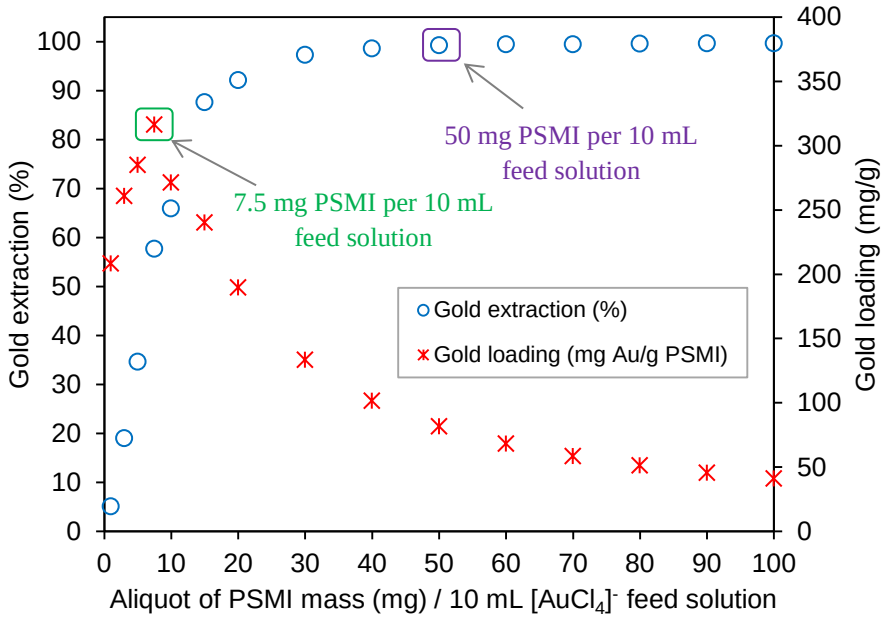

Figure 3.3 Effect of PSMI nanoparticles dosage on the extraction of $[AuCl_4]^-$ from 2 M HCl solution. Experimental conditions – Gold concentration: 411.5 mg/L; Total aqueous phase: 10 mL; Contact time: 24 h; Agitation rate: 250 rpm, Temperature: 23 ± 1 °C.

The results in Figure 3.3 indicate that the degree of $[AuCl_4]^-$ extraction increases steadily with an increase in the PSMI mass, as expected; increasing PSMI masses provides a larger number of ion-exchange sites for a fixed initial gold concentration. [6] An aliquot of 50 mg PSMI per 10 mL gold feed solution could quantitatively extract (99.2 %) the $[AuCl_4]^-$ ions initially present in the synthetic feed solution. For PSMI masses exceeding 50 mg, no significant increase in the extraction efficiency was observed. A maximum amount of about 99.6 % of $[AuCl_4]^-$ was extracted from the solution using a mass of 100 mg PSMI nanoparticles.

Also shown in Figure 3.3 are the corresponding gold loading capacities for each of the PSMI masses per 10 mL feed solution. There is an increase in the gold loading capacity in the initial PSMI mass range up to a point where maximum loading capacity is reached at 7.5 mg PSMI per 10 mL of gold feed solution (Figure 3.3). Thereafter, a gradual decrease in the gold loading capacity is observed with a further increase in the PSMI masses. This can be explained by the total number of protonated nitrogen sites available for ion-pairing. The maximum gold loading capacity, q_{max} predicted by the Langmuir model is 2.75 mmol gold per gram of PSMI (Table 3.2). Based on this estimation, for a PSMI mass of 7.5 mg, the theoretical amount of gold as $[AuCl_4]^-$ expected to be taken-up at equilibrium is about 0.02 mmol. The amount of gold present in 10 mL of feed solution with a gold concentration of 411.5 mg/L as used in this study is also about 0.02 mmol. Therefore, in the 1 – 7.5 mg PSMI per 10 mL gold feed solution range, there is more $[AuCl_4]^-$ present in solution than available protonated nitrogen sites for ion-pair formation to take place. However, within this range an increase in the PSMI mass added results in more $[AuCl_4]^-$ ions being immobilized by the PSMI nanoparticles, hence an increase in gold loading capacity. At a PSMI mass of about 7.5 mg per 10 mL gold feed solution, a more or less equal number of available protonated sites and $[AuCl_4]^-$ ions in solution predominates (0.02 mmol), resulting in the maximum amount of $[AuCl_4]^-$ ions immobilized per gram of PSMI nanoparticles. This suggests that under the experimental conditions for the gold concentration used, 7.5 mg PSMI masses per 10 mL of the gold feed solution are sufficient for complete saturation of all the available protonated sites on the bulk PSMI nanoparticles. This amounts to approximately 57.6 % extraction of the initial $[AuCl_4]^-$ in the synthetic feed solution. Further increases in the PSMI mass however, results in a decrease in gold loading capacity. The decrease in gold loading capacity can be attributed to the fact that more protonated nitrogen sites remain unsaturated upon raising the PSMI mass from 7.5 – 100 mg, at constant gold concentration.

3.4.3 Effect of contact time and agitation rate

The effect of contact time and agitation rate on the extraction of $[AuCl_4]^-$ are shown in Figures 3.4 (a) and (b) for PSMI masses of 10 and 50 mg, respectively at constant gold concentration of 208.2 mg/L.

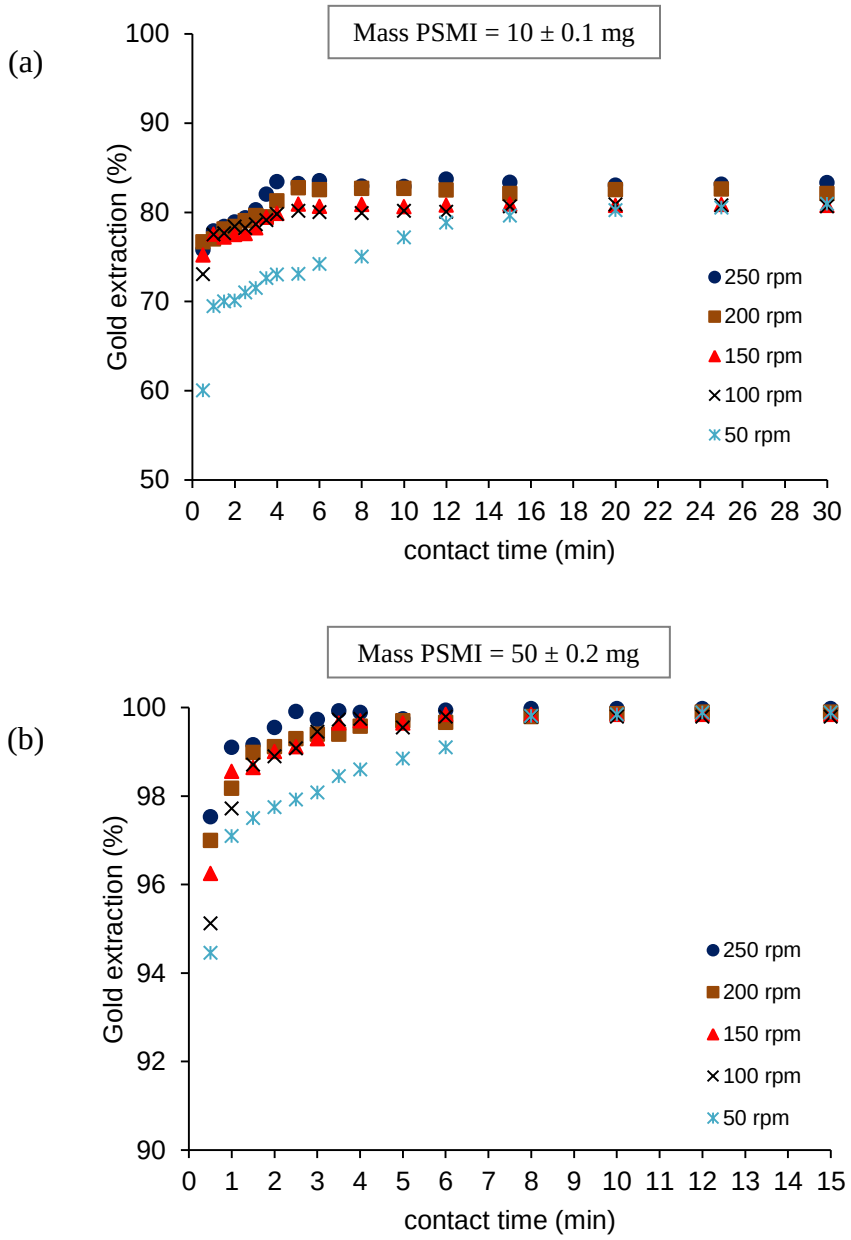

Figure 3.4 Effect of contact time and agitation rate on the extraction of $[AuCl_4]^-$ from 2 M HCl solution using PSMI masses of (a) 10 ± 0.1 mg and (b) 50 ± 0.2 mg. Experimental conditions – Gold concentration: 208.2 mg/L; Total aqueous phase: 10 mL; Temperature: 23 ± 1 °C.

As can be seen from Figure 3.4 (a) and (b), the extraction rate is fast, which suggests that an ion-exchange mechanism is predominantly responsible for the sorption process (Equation 3.3) which is known to display fast extraction kinetics (section 1.5.5, Chapter 1). Also, the extraction of $[AuCl_4]^-$ is dependent on the rate of agitation applied during the batch sorption experiments. For the 100, 150, 200 and 250 rpm agitation rates, it was found that equilibrium sorption was attained in 5 minutes for both the 10 mg and 50 mg PSMI aliquots. For the slowest agitation rate of 50 rpm, equilibrium sorption was attained in 15 minutes and 8 minutes for the 10 mg and 50 mg PSMI aliquots, respectively.

In summary, from the equilibrium sorption study, it was found that within the gold concentration range of 0 – 935 mg/L initially present in solution, a maximum gold loading capacity, q_{max} of 1.76 mmol gold per gram PSMI was obtained. This is less than the predicted q_{max} value of 2.75 mmol gold per gram PSMI as estimated from the Langmuir model (Table 3.2), which indicates that not all of the available protonated nitrogen sites for sorption were occupied, i.e. equilibrium gold loading was not completely reached. The total amount of nitrogen content (mmol) per gram of PSMI as determined from elemental analysis was found to be 4.3 ± 0.4 mmol/g (Table 3.1). The fact that this ligand concentration is much more than the actual and predicted gold loading capacities may be attributed to:

(1) inaccessible nitrogen sites within the non-porous PSMI nanoparticles;
(2) the imide nitrogen atoms which are expected to be less readily protonated than the terminal tertiary amine moieties of PSMI.

Based on a 1:1 stoichiometry, the percentage of potentially available sorption estimated from the Langmuir model is 64 % and the experimental estimate of maximum loading capacity is 40.9 %.

The results presented thus far for the extraction of $[AuCl_4]^-$ ions from acidic solution indicate that the PSMI nanoparticles used as an anion-exchange material have a high affinity for $[AuCl_4]^-$ as evident by the high gold loading capacity and the fast extraction kinetics. The dominant mechanism governing the extraction is expected to be ion pair formation between the available protonated nitrogen moieties and the anionic $[AuCl_4]^-$ ions in solution. For a relatively high gold concentration of 411.5 mg/L, it was found that an aliquot of 50 mg PSMI per 10 mL of feed solution would suffice for almost quantitative extraction of $[AuCl_4]^-$ from solution (Figure 3.3).

3.4.4 Desorption studies

The efficacy and degree of desorption ("stripping") of a precious metal such as gold in this context requires selection of suitable elutants, which strongly depend on the type of sorbent material and the mechanism underlying the sorption of the precious metal. The chosen elutants must preferably be (i) non damaging to the sorbent, (ii) inexpensive, (iii) eco-friendly and (iv) most importantly efficient and of such a nature from which the precious metal may be easily recovered. Various elutants were investigated for the desorption of immobilized $[AuCl_4]^-$ from the loaded PSMI nanoparticles.

3.4.4.1 Desorption using hydrochloric acid

Desorption of immobilized $[AuCl_4]^-$ from the loaded PSMI as a function of HCl concentration is shown in Figure 3.5. A gold loading of 31.5 mg gold/g PSMI was used for these desorption tests.

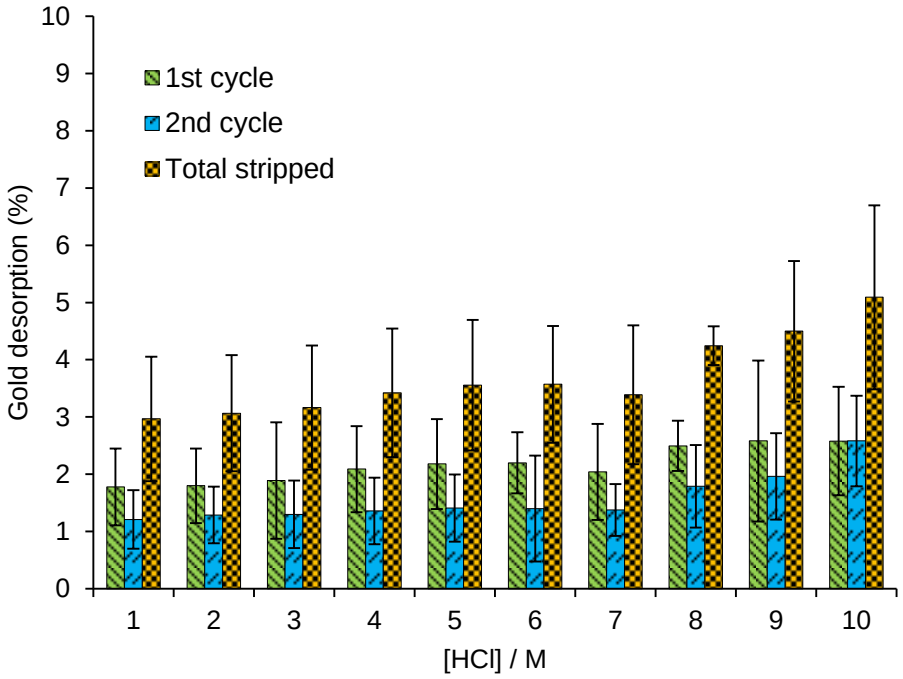

Figure 3.5 Desorption of immobilized $[AuCl_4]^-$ from PSMI nanoparticles as a function of hydrochloric acid concentration. Experimental conditions – Gold loading: 31.5 mg/g; Total elutant aqueous phase: 10 mL; Desorption contact time: 24 h; Agitation rate: 250 rpm; Temperature: 23 ± 1 °C.

From the results, it is clear that HCl is a poor elutant for the desorption of the assumed immobilized $[AuCl_4]^-$, with not more than a total of 5.1 % being eluted even after employing two successive desorption cycles. This suggests 'strong binding' of any gold chlorido-complexes and in particular a combination of immobilization processes other than only ion-exchange. In other words the anticipated 'simple' ion-exchange envisaged by Equation 3.7 does evidently not appear to take place. In Equation 3.7 the protonated nitrogen moieties of PSMI are represented as $PSMI.H^+$ which is charge balanced by either the counter Cl^- ions or the $[AuCl_4]^-$ ions.

$$PSMI.H^+[AuCl_4]^- + Cl^-_{(aq)} \rightleftharpoons PSMI.H^+Cl^- + [AuCl_4]^-_{(aq)} \quad (3.7)$$

In view of the fact that a significant proportion of the immobilized $[AuCl_4]^-$ could not be eluted from the loaded PSMI nanoparticles by desorption with even concentrated HCl, it may be assumed that a significant amount of the $[AuCl_4]^-$ could be reduced to Au(I) chlorido-complexes or even metallic Au(0) on the PSMI nanoparticles. As discussed in section 1.7 of Chapter 1, the reduction potentials for the $[AuCl_4]^-$/Au(0), $[AuCl_4]^-/[AuCl_2]^-$ and $[AuCl_2]^-$/Au(0) half reactions are also relatively high, being 1.002, 0.926 and 1.154 V, respectively. [7]

The poor desorption could be due to a number of different phenomena, for example:

(i) Strong electrostatic interaction between positively charged protonated nitrogen moieties of PSMI and negatively charged $[AuCl_4]^-$ complexes.

(ii) High polarisability of the $[AuCl_4]^-$ complexes.

(iii) Possible Au^{3+} reduction to Au^+ or Au^0 species on the surface of the PSMI nanoparticles after immobilization of $[AuCl_4]^-$.

(iv) Possible coordination of Au^{3+}/Au^+ atoms to non-protonated nitrogen atoms of the PSMI nanoparticles (Equation 3.1).

To identify the most probable causes for the poor desorption efficiency observed using HCl, several other elutans were examined such as H_2SO_4, $NaHCO_3$, dilute NaOH and NH_4OH, acidified thiourea and a mixture of NaCN and NaOH. However, of these elutants it was established that only the strong metal chelating agent, thiourea exhibited potential for eluting gold quantities of any significance from the gold-loaded PSMI nanoparticles.

3.4.4.2 Desorption using thiourea solutions and investigation into the reduction of immobilized $[AuCl_4]^-$ on the surface of the PSMI nanoparticles.

The possible Au^{3+} reduction phenomenon of immobilized $[AuCl_4]^-$ was investigated by conducting extraction-desorption experiments in the presence or absence of chlorate (ClO_3^-) ions which acts as a mild oxidizing agent. This was done in an attempt to stabilize the $[AuCl_4]^-$ ions in solution with the aim of counteracting the possible reduction of said complexes that is suspected to occur on the surface of the PSMI nanoparticles after immobilization. An appropriate amount of the chlorate salt was dissolved in a 411.5 mg/L gold feed solution or corresponding elutants as summarized in Table 3.3.

Table 3.3 Composition of the $[AuCl_4]^-$ feed and corresponding elutant solutions.

Experiment	Feed solution (Extraction)	Elutant solution (Desorption)
A	2 M HCl	0.25 M Thiourea/2 M HCl
B	2 M HCl/0.5 M ClO_3^-	0.25 M Thiourea/2 M HCl/0.1 M ClO_3^-
C	2 M HCl/0.5 M ClO_3^-	0.25 M Thiourea/2 M HCl

In the case of experiment B, for example, the extraction of $[AuCl_4]^-$ was from a feed solution composed of 2 M HCl and 0.5 M ClO_3^- followed by desorption using an elutant solution composed of acidified thiourea and 0.1 M ClO_3^- ions (0.25 M thiourea/2M HCl/0.1 M ClO_3^-). In all cases, the extraction of $[AuCl_4]^-$ from the feed solutions as indicated in Table 3.3 was essentially quantitative (gold loading capacity of more or less 82 mg/g in each case), with the collected effluents containing less than 0.1 mg/L of gold. Due to this minuscule residual gold content remaining in the effluent solutions and the fact that only 50 mg PSMI masses were used in the extraction experiments, no washing of the gold-loaded PSMI materials were employed before desorption in order to minimize mechanical losses.

Shown in Figure 3.6 is the desorption profile for the different elutant solutions as indicated in Table 3.3.

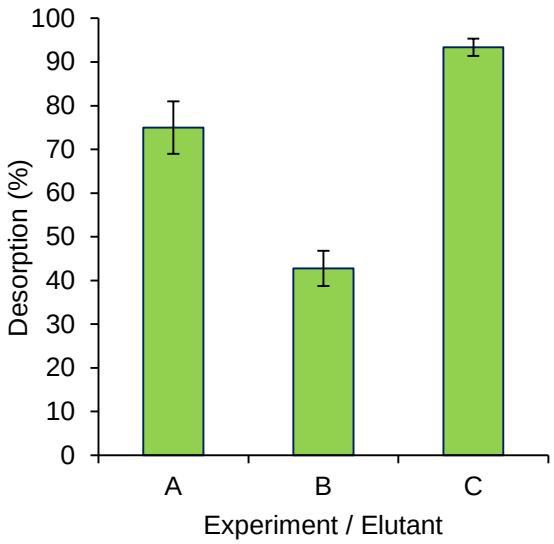

Figure 3.6 Desorption of immobilized gold species from PSMI nanoparticles using various elutant solutions as indicated in Table 3.3. Experimental conditions – Total aqueous phase: 10 mL; Desorption contact time: 24 h; Agitation rate: 250 rpm; Temperature: 23 ± 1 °C.

It is known that the auric ion (Au^{3+}) is not stable in thiourea solution, but rather oxidizes thiourea, itself being reduced to aurous ion (Au^{+}), which complexes as shown below: [8,9]

$$Au^{+} + 2\ SC(NH_2)_2 \rightleftharpoons Au(SC(NH_2)_2)_2^{+} \qquad \beta_2 = 2 \times 10^{32} \qquad (3.8)$$

The suitability of using thiourea as an elutant is emphasized by the high stability constant associated with the gold (I) – thiourea complexes, $Au(SC(NH_2)_2)_2^{+}$ as shown in Equation 3.8.[9,10] Desorption of the immobilized gold species from the loaded PSMI nanoparticles using thiourea was indicated by a color change as the bright yellow color of Au^{3+} disappeared, giving colorless gold (I) – thiourea complex formation ($Au(SC(NH_2)_2)_2^{+}$) almost instantaneously. [11]

From Figure 3.6 it is seen that the efficiency of desorption is in the order C > A > B. Taking into consideration that thiourea readily forms stable gold (I) complexes and the mechanism by which they form these complexes (Equation 3.8), it can be deduced that the *ca* 76 % gold eluted (experiment A) was in the form of Au^{3+} and/or Au^{+} species immobilized on the PSMI nanoparticles. The remaining immobilized gold species (*ca* 24 %) that could not be eluted is postulated to be in a metallic Au^{0} form. The best desorption efficiency of about 93 % (experiment C) was obtained by performing the extraction of $[AuCl_4]^{-}$ from a feed solution containing ClO_3^{-} ions and the subsequent desorption of the immobilized gold species using

acidified thiourea (0.25 M thiourea/2 M HCl) with no ClO_3^- ions present in the elutant solution. The improvement from 76 % (experiment A) to 93 % (experiment C) desorption can clearly be attributed to the presence of the oxidant (ClO_3^- ions) in the $[AuCl_4]^-$ feed solution and thus on the surface of the PSMI particles. The ClO_3^- ions are believed to minimize the Au^{3+} reduction of the immobilized $[AuCl_4]^-$ to Au^0. However, even in the presence of ClO_3^- ions some degree of Au^{3+} reduction to Au^0 may still occur. It has been reported in literature that in the presence of a suitable oxidizing agent, such as O_2, H_2O_2, MnO_2 and Fe, thiourea will solubilize Au^0 to give Au^+ species which complexes as shown by Equation 3.9. [8,11,12]

$$Au^0 + 2\ SC(NH_2)_2 \rightarrow Au(SC(NH_2)_2)^+ + e^- \qquad E^o = 0.352\ V \qquad (3.9)$$

This means that even gold in metallic Au^0 form may be solubilized by thiourea due to the presence of some oxidant ClO_3^- ions on the surface of the PSMI nanoparticles to possibly form complexes as shown by Equation 3.9. Hence, this may have contributed significantly to the excellent desorption efficiency for experiment C. Notably, the least amount of gold species eluted from the loaded PSMI nanoparticles was attained for experiment B with 42 %. This result implies that the 0.1 M ClO_3^- ions present in the acidified thiourea elutant solution most probably interfered with the elution process and thus hampered the desorption effectiveness. The decreased desorption efficiency of experiment B as compared to those obtained for experiments A and C is not surprising considering that chlorate (ClO_3^-) enhance the stability of the Au^{3+} oxidation state of the immobilized gold species. In the case of experiment B, the excess chlorates in the elutant solution may therefore, to a certain degree inhibit the transformation of auric into aurous ions by thiourea during the desorption process (Equation 3.8). Another explanation could be that the excess ClO_3^- ions oxidize the thiourea, resulting in the observed desorption efficiency.

In summary, the results from Figure 3.6 suggest that the $[AuCl_4]^-$ ions initially present in the feed solutions is subject to a reduction of some sort after it has been immobilized by the PSMI nanoparticles. This has a significant effect on the desorption efficiencies. However, it would seem that a significant amount of Au^{3+} reduction is minimized by the presence of ClO_3^- ions in the $[AuCl_4]^-$ feed solution. From these observations, it is therefore clear that in order to attain maximum desorption of immobilized gold species, extraction needs to be performed from a feed solution containing ClO_3^- ions and subsequent desorption using only acidified thiourea as elutant without the presence of the ClO_3^- ions.

3.4.4.3 Desorption using nitric acid/hydrochloric acid solutions

Based on the possible reasons listed for the poor desorption efficiency such as Au^{3+} reduction to Au^{+}/Au^{0}, solutions composed of nitric acid and hydrochloric acid was also investigated as elutants. A mixture HCl and HNO_3 form what is known as aqua regia which is well known to solubilize metallic gold according to the reaction illustrated in Equation 3.10. [13]

$$2\ Au + 11\ HCl + 3\ HNO_3 \rightarrow 2\ HAuCl_4 + 3\ NOCl + 6\ H_2O \qquad (3.10)$$

Therefore, elutant solutions of HNO_3/HCl were chosen to potentially re-dissolve any gold species, even those in reduced oxidation states immobilized on the PSMI nanoparticles. This was done with the aim of improving the desorption without the need for implementing chlorate ions in the initial $[AuCl_4]^-$ feed solution. In these experiments, PSMI samples with gold loading of about 50 mg gold/g PSMI were used in each of the desorption tests. Shown in Figure 3.7, is the desorption efficiencies as a function of various HNO_3 concentrations containing a constant content of 0.5 M HCl in each elutant solution.

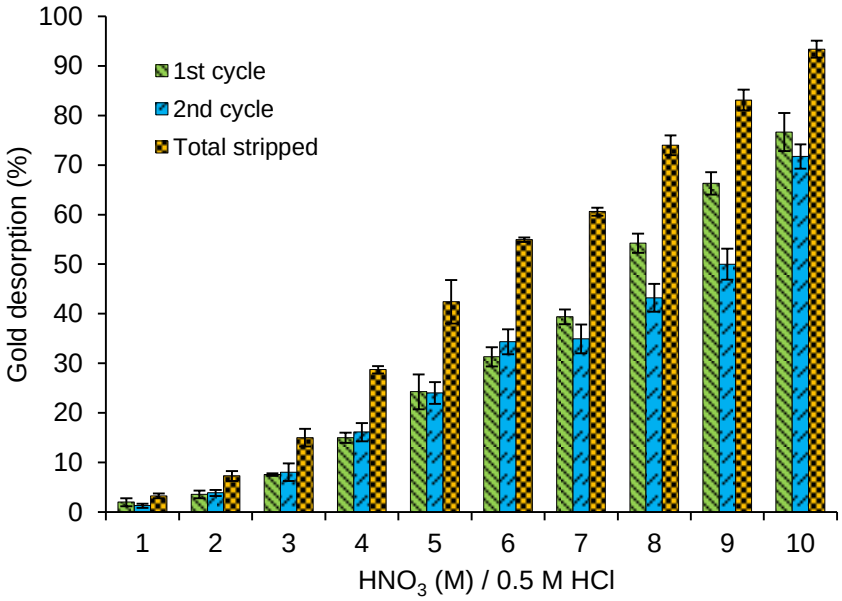

Figure 3.7 Desorption of immobilized gold species from PSMI nanoparticles as a function of nitric acid and hydrochloric acid solutions of varying concentration. Experimental conditions – Gold loading capacity: 50 mg gold/g PSMI; Total aqueous phase: 10 mL; Desorption contact time: 24 h; Agitation rate: 250 rpm; Temperature: 23 ± 1 °C.

The desorption efficiency improved considerably as the concentration of HNO_3 in the elutant solutions was increased from 1 – 10 M (Figure 3.7). A total amount of 93.3 ± 1.7 % immobilized gold species was eluted over two desorption cycles using 10 M HNO_3/0.5 M HCl. Unavoidable material losses as a consequence of washing and separation of solid from aqueous phases during centrifugation and filtration procedures may account for the not completely quantitative gold recovery. The improved desorption for the acidic HNO_3/HCl solution mixtures (Figure 3.7) can be attributed to the oxidizing properties of HNO_3. Any immobilized gold species, especially those in reduced oxidation states of Au^0 and Au^+ could be readily oxidized and re-dissolved resulting in the formation of Au^{3+} ions. The presence of chloride ions in the loaded strip liqour presumably allows complexation with the Au^{3+} ions and thus formation of $[AuCl_4]^-$ anions in solution. Therefore, the increase in HNO_3 concentration is accompanied by an increased desorption as a consequence of excess Au^{3+} ions being formed. From this, it can be concluded that HNO_3/HCl solutions at high concentration are good elutants for desorption of immobilized gold species.

3.4.5 Successive extraction and desorption

An important prerequisite of any desorption route for metals recovery from loaded sorbents is that the elutant should be non-destructive. Although it was ascertained that the chemical integrity of the PSMI nanoparticles used as an anion-exchange material was retained using solutions of HNO_3/HCl, acidified thiourea solution was preferred as elutant in the test for re-usability of the PSMI nanoparticles in continuous extraction and desorption cycles. Figure 3.8 shows the three stage extraction × two stage washing × three stage desorption profiles. It should be noted that the extraction was performed from a $[AuCl_4]^-$ feed solution in 2 M HCl with a gold concentration of 450 mg/L and successive desorption using a 0.25 M thiourea/2 M HCl elutant solution. No chlorate ions were present in either the feed or elutant solutions.

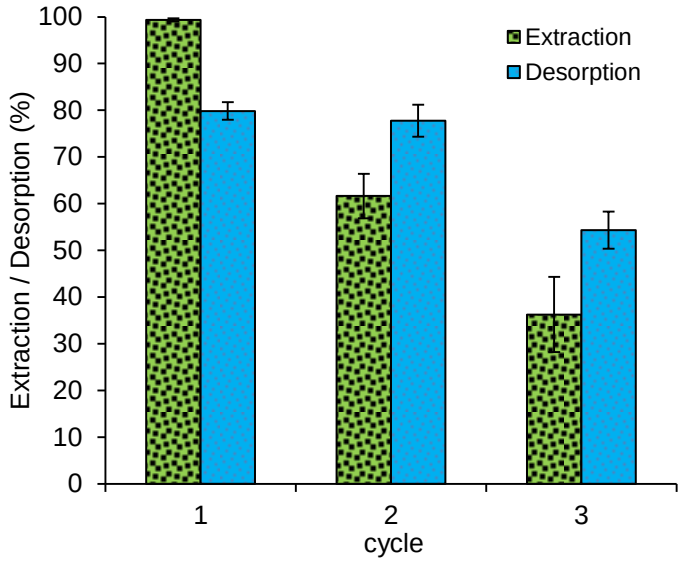

Figure 3.8 Continuous three stage extraction × two stage wash × three stage desorption cycles. Experimental conditions – Gold concentration: 450 mg/L; Total aqueous phases: 10 mL; Extraction contact time: 60 min; Elutant solution: 0.25 M thiourea/2 M HCl; Desorption contact time: 24 h; Agitation rate: 250 rpm; Temperature: 23 ± 1 °C.

From Figure 3.8 it is seen that for both the extraction and desorption a decrease in efficiency is observed over the three continuous cycles, albeit that for the first two cycles desorption is more or less the same. Although the extraction efficiency of about 62 % and 36 % for cycles 2 and 3, respectively is much less than the about 99 % of cycle 1, it is actually still good taking into account that a quite high gold concentration of 450 mg/L was used in these experiments. Lowering the gold concentration of the feed solution would have an adverse effect on the extent of extraction over the three continuous cycles. The decline in the extraction efficiency over the three cycles as shown in Figure 3.8 can be explained by the following:

1) Incomplete desorption of immobilized gold species in preceding cycles resulting in a decrease in available protonated nitrogen sites for successive $[AuCl_4]^-$ immobilization to occur. All the evidence suggests that the incomplete desorption can be due to amongst others reduction of Au^{3+} to Au^+/Au^0 and possibly coordination of the Au^{3+}/Au^+ atoms to the non-protonated nitrogen atoms of PSMI nanoparticles.
2) Mechanical losses as a consequence of washing and regeneration of the PSMI nanoparticles between successive cycles, again possibly decreasing the number of protonated nitrogen sites for successive $[AuCl_4]^-$ immobilization to occur.

3.4.6 XPS measurements

To support the hypothesis of Au(III) reduction on the PSMI nanoparticles a suitable technique for determining the gold oxidation state is X-ray photoelectron spectroscopy (XPS) also known as electron spectroscopy for chemical analysis. XPS is a quantitative surface sensitive chemical analysis technique that measures the elemental composition, chemical and electronic state of the elements that exist within a material.

The basic principle of XPS as illustrated by the photoemission process is shown in Scheme 3.3. In XPS analysis, material surfaces are irradiated with soft X-rays and the emitted photoelectrons kinetic energies analyzed. The difference between the X-ray photon energy (hυ) and the photoelectron kinetic energy, E_k (e^-) gives the binding energies (BEs) of the core level electrons as given by Equation 3.11.

$$BE = h\upsilon - E_k\ (e^-) \qquad (3.11)$$

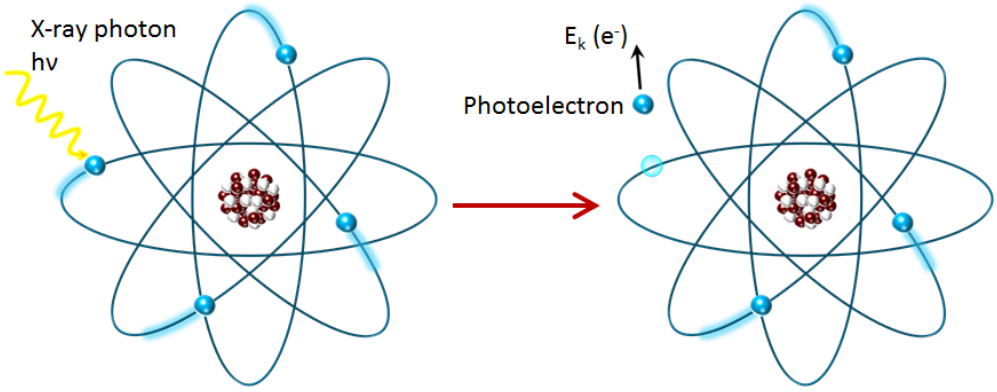

Scheme 3.3 The photoemission process illustrating the use of X-ray photon energy to eject a core level electron from surface atoms of a material.

A typical XPS spectrum is a plot of the number of photoelectrons detected versus the binding energy of the photoelectrons detected. Each element produces a characteristic set of XPS peaks at characteristic binding energy values that directly identify each element that exist in or on the surface of the material being analyzed. These characteristic peaks correspond to the electron configuration of the electrons within the atoms, e.g. 1s, 2s, 2p, 3s etc. Therefore, the binding energies are characteristic of specific electron orbitals in specific atoms. For more information on this technique, the reader is referred to books by Briggs and Beamson. [14-16]

The gold-loaded PSMI material (AuPSMI) was probed using X-ray photoelectron spectroscopy (XPS) to determine the oxidation states of the immobilized gold species to gain insight into the reaction between PSMI nanoparticle surface sites and $[AuCl_4]^-$ anions at the solid-solution interface. The AuPSMI sample was prepared with a batch sorption method by contacting *ca.* 50 mg PSMI nanoparticles with 10 mL of a 450 mg/L gold feed solution in 2 M hydrochloric acid and agitated for 15 min at 250 rpm; therefore simulating the gold extraction process (*see* section 3.2). The gold loading capacity was calculated as 89.6 mg gold per gram PSMI. The 'bright yellow' colored AuPSMI sample obtained (similar to the image as shown in Figure 3.1 (c)) was isolated by centrifugation and subsequently washed (×3) with deionized water to eliminate any residual entrained $[AuCl_4]^-$ and allowed to thoroughly dry at ambient temperature in vacuo (200 mbar) before XPS analysis (*see* section 3.6.2 for XPS analysis experimental details).

Figure 3.9 shows the narrow scan XPS spectrum illustrating the Au 4f peaks of the AuPSMI sample (*see* supplementary section, Figure s3.2 for the survey scan XPS spectrum).

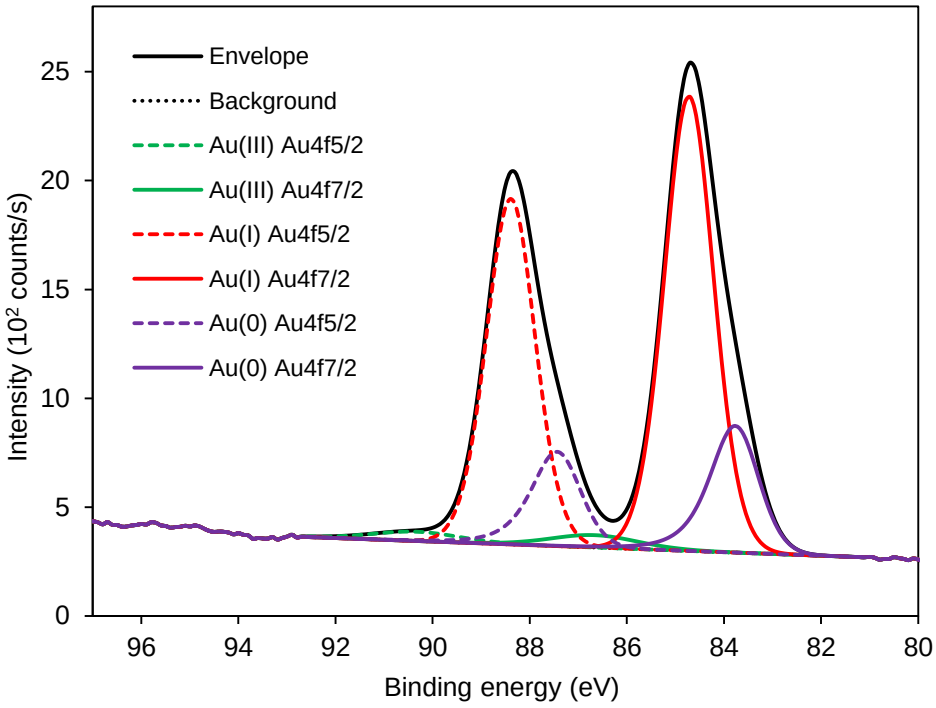

Figure 3.9 Narrow scan XPS spectrum of the gold-loaded PSMI sample (AuPSMI) indicating the contribution from gold species in different oxidation states. (Courtesy: Professor Sophie Hermans, Catholic University of Louvain, Belgium).

The sub-peaks associated with contributions from gold species in different oxidation states of presumably 0, +I, and +III are clearly distinguishable from one another within each region of the envelope (Figure 3.9). Each sub-peak is split into two component peaks or doublets (Au $4f_{7/2}$ and Au $4f_{5/2}$) as a result of spin-orbit coupling. The binding energies (BE) of the Au $4f_{7/2}$ and Au $4f_{5/2}$ core levels together with the full width at half maximum (FWHM) values as well as the quantification data (atomic %) of the immobilized gold species in their corresponding oxidation states are summarized in Table 3.4.

Table 3.4 Summary of the XPS analysis data for the AuPSMI sample.

Oxidation state of gold species	Au $4f_{7/2}$		Au $4f_{5/2}$		Gold content (atomic %)[(a)]
	BE (eV)	FWHM (eV)	BE (eV)	FWHM (eV)	
0	83.8	1.1	87.4	1.1	0.115
+I	84.7	1.2	88.4	1.2	0.439
+III	86.7	2.1	90.3	2.1	0.021

[(a)] Summation of the gold concentration (atomic %) values of the Au $4f_{7/2}$ and Au $4f_{5/2}$ peaks for the corresponding oxidation state

The Au $4f_{7/2}$ binding energy for Au(0) is 83.8 eV that is 0.2 eV lower than the typical value of 84.0 eV for metallic gold. [17] The Au $4f_{7/2}$ binding energy at 84.7 eV is attributed to insoluble polymeric Au(I) chloride, $(AuCl)_n$ surface clusters formation, which agree well with analogous values reported in literature of 84.7 – 85.1 eV for Au(I) sulphur surface species and for gold clusters with binding energy of up to 84.7 eV. [18,19] The peak at 86.7 eV can be attributed to gold species in highest oxidation state within the sample, most probably immobilized trivalent Au(III) in the form of $[AuCl_4]^-$ complexes. The assignments of mixed gold oxidation states present in the AuPSMI sample is verified by comparison with practically identical Au4f peaks associated with Au(0), Au(I) and Au(III) species adsorbed onto solid nanocrystalline cerium oxide supports utilized as catalysts. [20,21] As shown in Table 3.4, the FWHM values of the Au 4f peaks for Au(0) is *ca*. 1.0 eV, which is typical for 'bulk' gold. [17] The much larger FWHM values of 2.1

eV associated with the Au 4f peaks for the Au(III) assignment can be an indication that these immobilized species may be composed of variable sized aggregates. Evidence substantiating this notion is illustrated by the TEM micrograph in Figure 3.10, where it can be seen that the immobilized gold species exist as a combination of highly dispersed 'extremely small' nano-sized particles (almost undetectable with TEM), intermediate sized particles of 8 – 12 nm and larger aggregates of variable sizes between 45 – 55 nm. (Refer to Figure s3.3 in supplementary section for the TEM micrograph at higher magnification) From the atomic % values given in Table 3.4, the different contributions (molar %) of the total gold content on the surface of the AuPSMI sample are 76.35 % Au(I), followed by 20 % Au(0) and 3.65 % Au(III), respectively.

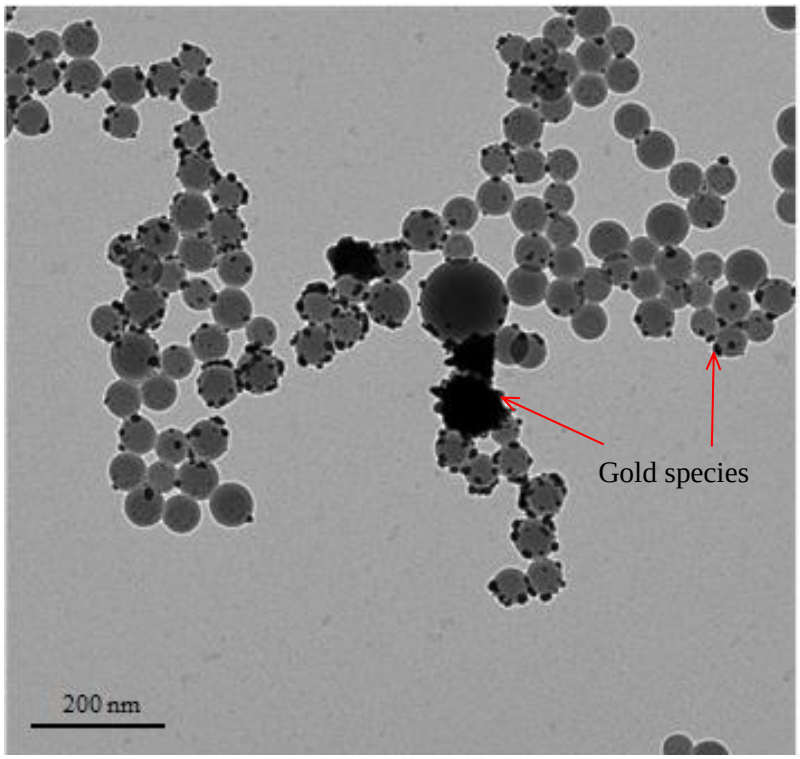

Figure 3.10 TEM micrograph of the AuPSMI sample illustrating the immobilized gold species on the 50 nm PSMI nanoparticles as different sized gold particles and gold aggregates. By XPS analysis, the immobilized gold species are confirmed to be present as various oxidation states of 0, +I and +III. (*See* experimental section 3.6.2 for the preparation of the AuPSMI sample for TEM analysis).

Since the extraction process takes place in a strong acidic medium, it is believed that the dominant mechanism involved in the initial stages of sorption is driven by electrostatic interaction between positively charged sites (protonated nitrogen moieties) and anionic Au(III)

chlorido complexes in solution; hence salt formation. This postulation is supported by the extremely fast kinetics of extraction (Figure 3.4). Once located at the surface, the formation of elemental gold and gold clusters on the PSMI nanoparticles can arise due to a reduction phenomenon.

The reduction of Au(III) ions to elemental gold on sorbents such as polymers, biomaterials and activated carbon has been previously observed and remains a topic of discussion. [22-26] In a study by Kang et al., it was shown that N-containing electroactive polymers such as polypyrrole (PPY) and polyaniline (PAN) could readily reduce and precipitate Au(III) ions as elemental gold by a self-sustained redox and protonation mechanism. It is postulated that in acidic solution, the imine nitrogens of both polymers are readily protonated. In the presence of Au(III) ions, spontaneous deprotonation of either polymer give rise to a more oxidized polymer and reduce the metal ions to a lower oxidation state. The highly oxidized polymer, in turn, is readily reprotonated, allowing the process to be sustained. The reduction of the Au(III) ions to the elemental form was confirmed by XPS analysis data, revealing unambiguously, the presence of a predominantly single Au(0) species with an Au $4f_{7/2}$ binding energy at about 83.8 eV. [22] In a study by Inoue et al., three novel lignin-based adsorption gels as well as activated carbon were found to be efficient in reducing Au(III) to Au(0), as indicated by XRD analysis of the sorbents after adsorption. The reduction was attributed to the fact that Au(III) itself is a good oxidizing agent with a standard reduction potential of + 1.40 V as well as the presence of different functional groups on the surfaces of these sorbent materials such as phenolic and polyphenolic hydroxyl groups along with carbonyl and ether groups which are believed to be oxidized in aqueous media. [23] Gardea-Torresdey et al. have proposed that several possible mechanisms are involved in the binding and reduction of $[AuCl_4]^-$ by the alfalfa biomass. It is reported that the amino and carboxyl containing functional groups on the biomass may be involved in the reduction process. X-ray absorption near edge structure (XANES) and extended X-ray absorption fine structure (EXAFS) spectroscopy studies suggested that Au(III) is initially reduced to Au(I) and is eventually reduced to Au(0). It is also possible that $AuCl_4^-$ is involved in a ligand exchange mechanism and electrostatic interactions between the $AuCl_4^-$ and the biomass to make the electron transfer possible. [24] Based on theories proposed in the literature, the reduction of Au(III) on the surface of the PSMI nanoparticles may be due to any of a number of possibilities such as the different functional groups of PSMI or the high reduction potential of Au(III) itself.

To fully understand the mechanism(s) of Au(III) reduction on the PSMI nanoparticles more in depth experimentation is therefore required. However, this falls outside the scope of this work.

3.4.7 Gold mass balance determinations and the recovery of gold from the bulk gold-loaded PSMI material

Gold mass balance determinations were performed to verify the reliability of our method to determine the $[AuCl_4]^-$ extraction efficiencies by PSMI nanoparticles (*see* experimental section 3.6.2 for details). The % gold mass balance was determined using Equation 3.12 and was found to be around 100 % for replicate samples.

Mass balance (%) = ((amount of gold left in the supernatant solution after extraction (mg) + amount of gold immobilized on the PSMI (mg) / (amount of gold initially present in the $[AuCl_4]^-$ feed solution (mg)) × 100 % (3.12)

The recovery of metals from loaded sorbent materials is often achieved by desorption or by incineration of the loaded sorbent material. In this study, an alternative method for the recovery of gold from the gold-loaded PSMI (AuPSMI) material was investigated. This was done by 'digesting' a weighed aliquot of AuPSMI material by means of microwave digestion using a 10 % suprapure HNO_3 solution without the presence of HCl (*see* experimental section 3.6.2 for details). The completely digested sample obtained was filtered to remove any suspended matter from the solution. Addition of 50 mL deionized H_2O to the yellow coloured filtrate resulted in the precipitation of a fine elemental gold powdered substance as illustrated by the optical micrographs in Figure 3.11. The gold mass balances for duplicate samples are illustrated in Table 3.5. The slight discrepancy in the mass of gold loaded on the PSMI sample and the mass of elemental gold precipitated from the digested sample can be attributed to mechanical losses. Interestingly, this recovered elemental gold has a thin leaf-like morphology as illustrated by the SEM micrograph in Figure 3.12. X-ray diffraction analysis confirms the crystallinity and phase purity consistent with elemental gold (Figure 3.13). [23]

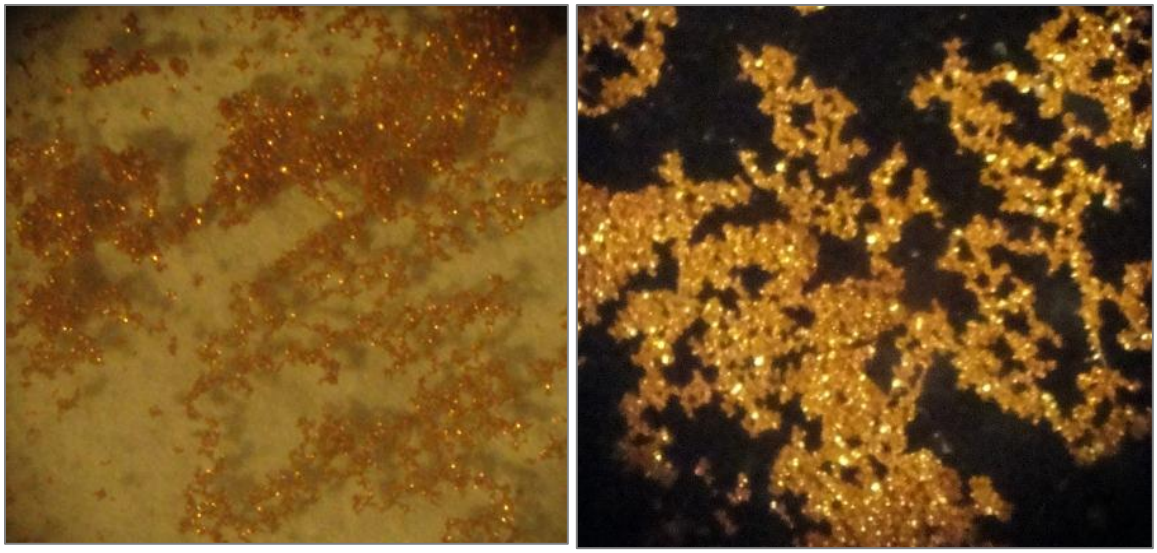

Figure 3.11 Optical micrographs of the precipitated elemental gold obtained by addition of water to a completely digested gold-loaded PSMI sample.

Table 3.5 Gold mass balances for duplicate gold-loaded PSMI and digested samples.

Sample	Gold loaded (mg)	Gold in digested solution (mg)
1	4.29	4.20
2	4.48	4.35

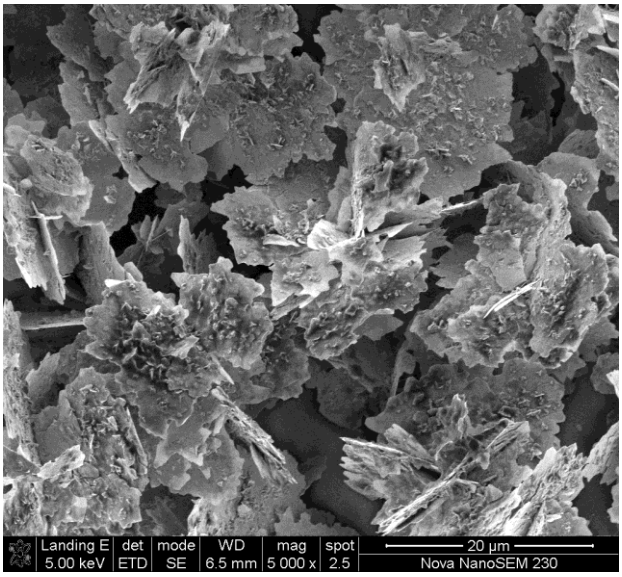

Figure 3.12 SEM micrograph (5000 x magnification) of the precipitated elemental gold sample as shown by the optical micrograph in Figure 3.11.

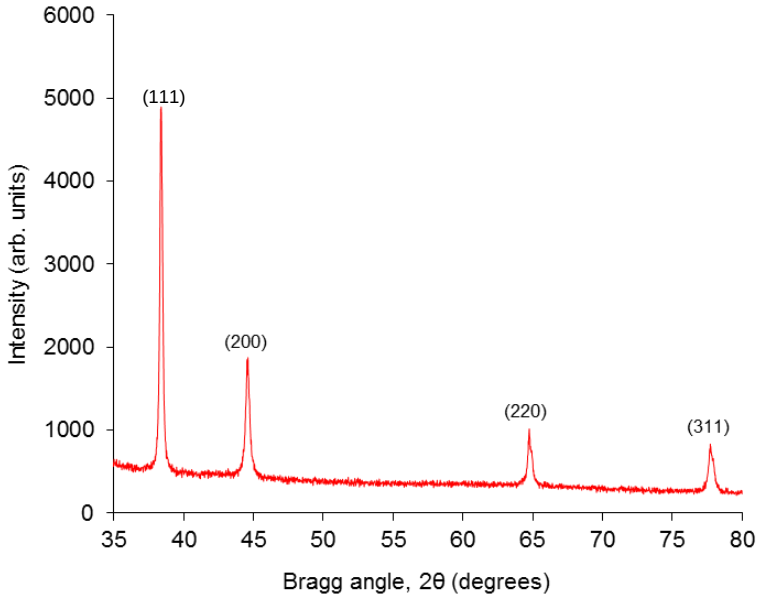

Figure 3.13 Powder x-ray diffraction (PXRD) diffractogram of the precipitated elemental gold sample.

3.5 General discussion and conclusions

A detailed study on the extraction and recovery of $[AuCl_4]^-$ from aqueous acidic solutions using the PSMI nanoparticles as anion-exchange material was undertaken. According to the total ligand concentration as determined by the nitrogen content with elemental analysis, it is estimated that the total number of nitrogen sites available is about 4.3 mmol per gram PSMI. This means that the bulk PSMI material can at most immobilize 4.3 mmol gold per gram PSMI (847 mg/g). From the sorption studies, it was observed that with an increase in initial gold concentration in solution the amount of gold loaded onto the PSMI nanoparticles increased up to a point where saturation was approached. However, equilibrium gold loading was not completely attained within the studied gold concentration range. A maximum gold loading capacity of 1.76 mmol gold per gram of PSMI (346.7 mg/g) was obtained. The equilibrium gold loading capacity predicted by the Langmuir model is 2.75 mmol/g (541.7 mg/g) indicating that the bulk PSMI nanoparticles have a high loading capacity. The fact that the equilibrium gold loading capacity as predicted by the Langmuir model is less than that expected theoretically based on the total nitrogen content (847 mg/g), may be ascribed to:

(1) Some inaccessible nitrogen moieties located within the non-porous PSMI nanoparticles and therefore not taking part in the immobilization of $[AuCl_4]^-$ ions.
(2) Non-protonated nitrogen moieties resulting in lesser sites available for $[AuCl_4]^-$ immobilization to occur *via* ion-exchange. The imide nitrogen atoms are expected to be less readily protonated than the terminal tertiary amine moieties of the PSMI nanoparticles.

From the time-dependent study it was found that $[AuCl_4]^-$ ions could be extracted from solution with fast sorption kinetics. Based on this result, it was assumed that the dominant mechanism of $[AuCl_4]^-$ extraction was by an electrostatic interaction between positively charged protonated nitrogen moieties and the negatively charged anionic gold (III) chloride complexes to form ion pairs.

Desorption of the assumed immobilized $[AuCl_4]^-$ from the PSMI nanoparticles was proven to be difficult. Desorption efficiencies of less than 5 % were obtained using various elutants such as HCl, H_2SO_4, $NaHCO_3$, NaOH, NH_4OH, and mixtures of NaCN and NaOH. The poor desorption efficiencies obtained using these elutants indicates that 'simple' ion-exchange is not the only process involved in the $[AuCl_4]^-$ sorption by the PSMI nanoparticles. Other possible phenomena that most likely contributed to the poor desorption were postulated. These included:

(1) Strong electrostatic interaction between positively charged protonated nitrogen moieties and the negatively charged $[AuCl_4]^-$ ions in the gold feed solution.
(2) High polarisability of the $[AuCl_4]^-$ ions.
(3) Possible reduction of Au^{3+} to Au^+ species and further to Au^0 on the surface of the PSMI nanoparticles after immobilization of $[AuCl_4]^-$ by ion-pair formation.
(4) Coordination between non-protonated nitrogen atoms of the PSMI nanoparticles to Au^{3+}/Au^+ atoms to form covalent bonds.

Desorption efficiency of about 76 % was obtained with a 0.25 M thiourea/2 M HCl solution. Since the desorption mechanism of immobilized gold species using acidified thiourea solution is based on the transformation of auric (Au^{3+}) into aurous (Au^+) ion by thiourea to form extremely stable gold (I) – thiourea complexes, it can be assumed that 76 % of the immobilized gold species were in Au^{3+}/Au^+ oxidation states, presumably as a variety of gold chlorido-complexes.

The remaining 24 % immobilized gold species that could not be eluted are believed to be in the form of Au^0.

The Au^{3+} reduction phenomenon of immobilized $[AuCl_4]^-$ was investigated by conducting the extraction-desorption in the presence of chlorate (ClO_3^-) ions which acts as a mild oxidizing agent. The result shows that the desorption efficiency increased from 76 % to 93 % when the $[AuCl_4]^-$ extraction was performed from a gold feed solution containing 0.5 M ClO_3^- ions and the subsequent desorption using 0.25 M thiourea/2 M HCl solution. This would suggest that the ClO_3^- ions prevent excessive Au^{3+} reduction, hence with the consequence of increased desorption. From these observations it is, therefore, clear that in order to attain maximum desorption of immobilized gold species, extraction needs to be performed from a feed solution containing ClO_3^- ions and the desorption using acidified thiourea as elutant.

The fact that some possible Au^{3+} reduction takes place either to Au^+ and Au^0 was further supported by the fact that an elutant solution mixture of HNO_3/HCl at high concentrations does "re-dissolve" any immobilized gold species. Desorption efficiency of about 93 % was obtained over two cycles using the 10 M HNO_3/0.5 M HCl solution. This was attributed to the strong oxidizing potential of HNO_3 which in the presence of HCl may readily re-oxidize and dissolve immobilized gold species as $[AuCl_4]^-$.

The Au^{3+} auto-reduction phenomenon that is postulated to occur on the surface of the PSMI nanoparticles was unambiguously confirmed by XPS analysis. From the binding energy and the intensity of the XPS photoelectron peaks, the elemental identity, chemical state and the quantity of the different gold species immobilized on the PSMI nanoparticles were determined. The Au 4f photoelectron sub-peaks revealed that the oxidation states of immobilized gold species are 0, +I and +III. The molar percentages of the total gold present in the gold-loaded PSMI material were calculated as 3.65, 20, and 76.35 % for Au(III), Au(0) and Au(I), respectively. The XPS analysis results confirm that the $[AuCl_4]^-$ complexes were reduced on the surface of the PSMI nanoparticles after it had been immobilized.

In summary, the feasibility of using PSMI nanoparticles as an ion-exchange material towards the extraction of $[AuCl_4]^-$ from HCl solutions has been demonstrated. The excellent properties exhibited by PSMI as well as the fact that these polymers are manufactured from inexpensive

raw materials could make the usage thereof viable in a continuous precious metals extraction and recovery process.

3.6 Experimental

3.6.1 Materials

High purity deionized water (Milli Q, 18 MΩ cm) was used throughout this work. All other chemicals and reagents including hydrochloric acid (HCl, 37 %) were used without further purification. For the extraction experiments, synthetic feed solutions of gold were prepared from the $HAuCl_4.xH_2O$ and $NaAuCl_4.2H_2O$ salts in 2M HCl solutions.

3.6.2 Instruments and measurements

A horizontal mechanical shaker (Labcon, BR-30L) was used for constant agitation of the feed solutions with the adsorbent for specified contact times during the batch sorption experiments. A pH meter (Horiba, F-52) was used for pH measurements. For mass balance determinations, samples were digested in a mixture of 10 % HNO_3 and 1% HCl for 30 min at a temperature of 230 °C and pressure 600 PSI with a Mars microwave digester. The concentration of metal ions in the supernatant solutions was determined by Inductively Coupled Plasma Optical Emission Spectroscopy (ICP-OES) with a SPECTRO Arcos spectrometer. Standards were matrix matched to acid concentrations of the samples. After calibration and quality check analysis to verify accuracy of standards, samples were analyzed. The analytical error in the ICP-OES measurements was found to be 5 %. Particle size and morphology was determined by Transmission Electron Microscopy (TEM), using a JEM 1200EXII model (JEOL, Japan) microscope. An accelerating voltage of 200 kV was used throughout. TEM samples were prepared as follows. The dried gold-loaded PSMI sample (AuPSMI) with a gold loading capacity of 89.6 mg/g was re-dispersed in water and sonicated for 15 – 20 minutes. A drop of suspended sample was placed on a carbon-coated 200 mesh copper grid, followed by drying at ambient

conditions before it was attached to the sample holder on the microscope. Prior to use, the grids were glow discharged for 30 seconds under air in a vacuum of 10^{-2} mbar. Powder X-ray diffraction (XRD) analysis was conducted with a Siemens D8 Advance diffractometer using Cu K_α radiation (λ = 1.540 Å) operated at 40 kV and 30 mA. XRD patterns were recorded in the range 10 – 80º (2θ) with a scan step of 0.02° using a prolonged irradiation exposure time of 3 h. The morphology of precipitated gold after recovery was determined by Scanning Electron Microscopy (SEM) using a Nova NanoSEM microscope (FEI Company). The XPS analyses were performed on a Kratos Axis Ultra spectrometer (Kratos Analytical – Manchester – UK) equipped with a monochromatized aluminum X-ray source (powered at 10 mA and 15 kV). The sample powders were pressed onto double-sided adhesive tape mounted on polymer plates fixed on the multi specimen holder. The pressure in the analysis chamber was about 10^{-6} Pa. The angle between the normal to the sample surface and the direction of photoelectrons collection was about 0°. Analyses were performed in the hybrid lens mode, the resulting analyzed area being 700 µm x 300 µm. The pass energy was set at 160 eV for the survey scan and 40 eV for narrow scans. In the latter conditions, the full width at half maximum (FWHM) of the Ag $3d_{5/2}$ peak of a standard silver sample was about 0.9 eV. Charge stabilization was achieved by using the Kratos Axis device. The following sequence of spectra was recorded: survey spectrum, C 1s, O 1s, N 1s, Cl 2p, Au 4f and C 1s again to check for charge stability as a function of time and the absence of degradation of the sample during the analyses. The C1s peak of carbon has been fixed at 284.8 eV to set the binding energy scale. Spectra were decomposed with the CasaXPS program (Casa Software Ltd., UK) with a Gaussian/Lorentzian (70/30) product function and after subtraction of a linear baseline. Atomic percentages were calculated using peak areas normalized on the basis of acquisition parameters, experimental sensitivity factors and transmission factors provided by the manufacturer.

3.7 References

1. J.E. Huheey, E.A. Keiter, R.L. Keiter, *Inorganic Chemistry: Principle of Structure and Reactivity*, 4th ed., Harper Collins College Publishers, N.Y., **1993**.

2. F.J. Alguacil, C. Caravaca, *Hydrometallurgy* **1993**, *34*, 91.
3. A. Uheida, G. Salazar-Alvarez, E. Bjoerkman, Z. Yu, M. Muhammed, *Journal of Colloid and Interface Science* **2006**, *298*, 501.
4. A. Benhammou, A. Yaacoubi, L. Nibou, B. Tanouti, *Journal of Colloid and Interface Science* **2005**, 282, 320.
5. K. R. Hall, L. C. Eagleton, A. Acrivos, T. Vermeulen, *Industrial & Engineering Chemistry Fundamentals* **1966**, *5*, 212.
6. A. Esposito, F. Pagnanelli, A. Lodi, C. Solisio, F. Veglio, *Hydrometallurgy* **2001**, *60*, 129.
7. A.J. Bard, R. Parsons, J. Jordan (Eds.), *Standard Potentials in Aqueous Solutions*, Marcel Dekker, New York, N.Y., **1985**.
8. J. Li, J.D. Miller, *Mineral Processing and Extractive Metallurgy Review* **2006**, 27, 177.
9. J. Marsden, I. House, *The Chemistry of Gold Extraction*, Ellis Horwood, Chichester, **1992**.
10. F.J. Alguacil, P.Adeva, M. Alonso, *Gold Bulletin* **2005**, *38*, 9.
11. I. Savvaidis, *BioMetals* **1998**, 11, 145.
12. S. Örgül, Ü. Atalay, *Hydrometallurgy* **2002**, 67, 71.
13. P.P. Sheng, T.H. Etsell, *Waste Management and Research* **2007**, *25*, 380.
14. D. Briggs, J.C. Rivière, *Spectral Interpretation. In Practical Surface Analysis by Auger and X-ray Photoelectron Spectroscopy*, John Wiley and Sons, N.Y.
15. D. Briggs, J.T. Grant, *Surface Analysis by Auger and X-ray Photoelectron Spectroscopy*, IM Publications, Chichester, **2003**.
16. G. Beamson, D. Briggs, *High Resolution XPS of Organic Polymers*, John Wiley and Sons, N.Y., **1992**.
17. J.F. Moulder, W.F. Stickle, P.E. Sobol, K.D. Bomben, *Handbook of X-ray Photoelectron Spectroscopy. A Reference Book of Standard Spectra for Identification and Interpretation of XPS data*, Perkin-Elmer Corporation, Physical Electronics Division, Eden Prairie, **1992**.
18. M.J. Scaini, G.M. Bancroft, S.W. Knipe, *American Mineralogist* **1998,** 83, 316-322.
19. S.B. DiCenzo, S.D. Berry, E.H. Hartford, Jr., *Physical Review* **1988,** B38 (12), 8465-8468.

20. A. Abad, P. Concepcion, A. Corma and H. Garcia, *Angewandte Chemie, International Edition*, **2005**, 44, 4066-4069.
21. Q.F.H. Saltsburg, M. Stephanopoulus, *Science* **2003**, 301, 935.
22. E.T. Kang, Y.P. Ting, K.G. Neoh, K.L. Tan, *Synthetic Metals* **1995**, 69, 477-478.
23. D. Parajuli, C.R. Adhikari, M. Kuriyama, H. Kawakita, K. Ohto, K. Inoue, M. Funaoka, *Industrial and Engineering Chemistry Research* **2006**, 45, 8.
24. J.L. Gardea-Torresdey, K.J. Tiemann, J.G. Parsons, G. Gamez, I. Herrera, M. Jose-Yacaman, *Microchemical Journal* **2002**, 71, 193-204.
25. Y.N. Mata, E. Torres, M.L. Blazquez, A. Ballester, F. Gonzalez, J.A. Munoz, *Journal of Hazardous Materials* **2009**, 166, 612-618.
26. R. Chand, T. Watari, K. Inoue, H. Kawakita, H.N. Luitel, D. Parajuli, T. Torikai, M. Yada, *Minerals Engineering* **2009**, 22, 1277-1282.

3.8 Supplementary information

Table s3.1 Summary of the equilibrium sorption data and the corresponding R_L values.

C_e (mg/L)	C_e (mmol/L)	Au loaded (mmol/g)	Au loaded (mg/g)	Au extraction (%)	R_L
934.96	4.747	1.763	347.2	37.13	0.343
883.46	4.485	1.746	343.9	38.93	0.356
764.56	3.882	1.682	331.3	43.33	0.390
674.27	3.423	1.602	315.6	46.80	0.420
623.33	3.165	1.510	297.5	47.72	0.439
551.57	2.800	1.496	294.6	53.41	0.470
475.09	2.412	1.388	273.4	57.54	0.507
414.60	2.105	1.263	248.7	60.00	0.541
372.76	1.892	1.248	245.9	65.96	0.567
314.91	1.599	1.099	216.4	68.72	0.608
262.20	1.331	1.009	198.7	75.77	0.651
212.19	1.077	0.854	168.3	79.30	0.697
164.90	0.837	0.709	139.7	84.73	0.748
148.73	0.755	0.672	132.4	89.00	0.767
120.98	0.614	0.568	111.8	92.43	0.801
111.98	0.568	0.528	104.0	92.90	0.813
107.23	0.544	0.520	102.5	95.59	0.820
85.90	0.436	0.429	84.5	98.42	0.850
78.58	0.399	0.395	77.9	99.12	0.861
71.15	0.361	0.361	71.0	99.85	0.873
59.13	0.300	0.300	59.0	99.84	0.892
49.66	0.252	0.252	49.6	99.82	0.908
35.53	0.180	0.180	35.4	99.77	0.932
25.94	0.132	0.131	25.9	99.74	0.950
17.77	0.090	0.090	17.8	100.00	0.965
12.58	0.064	0.064	12.6	100.00	0.975
8.18	0.042	0.042	8.2	100.00	0.984
2.84	0.014	0.014	2.8	100.00	0.994

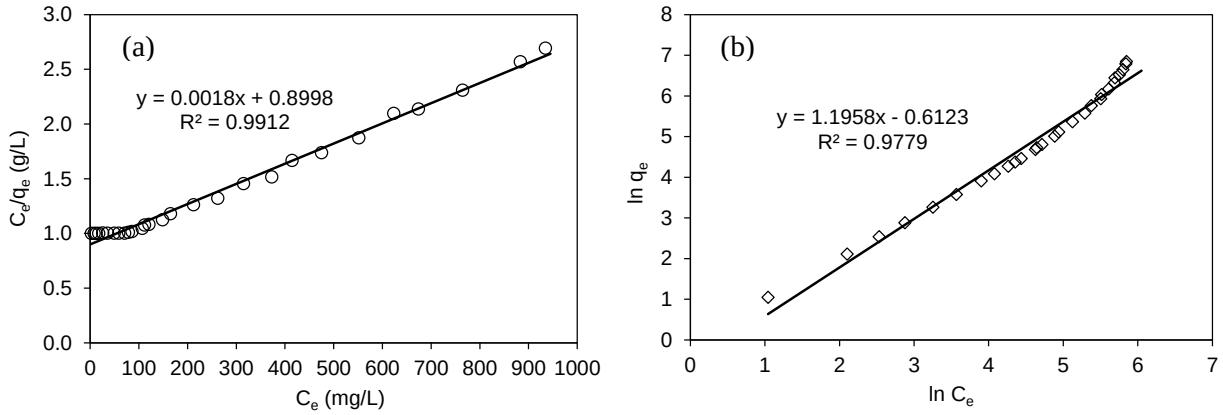

Figure s3.1 Linearized forms of (a) Langmuir and (b) Freundlich models associated with the sorption of $[AuCl_4]^-$ by the PSMI nanoparticles.

Shown in Figure s3.2 is the XPS survey or wide scan spectrum of a typical PSMI sample with adsorbed gold after the extraction process. The characteristic XPS photoelectron peaks of all the elements present in the sample (except hydrogen which is impossible to detect by XPS) is clearly identified. As expected for the polymer sample, the strongest peak is assigned to that of C1s carbon peaks.

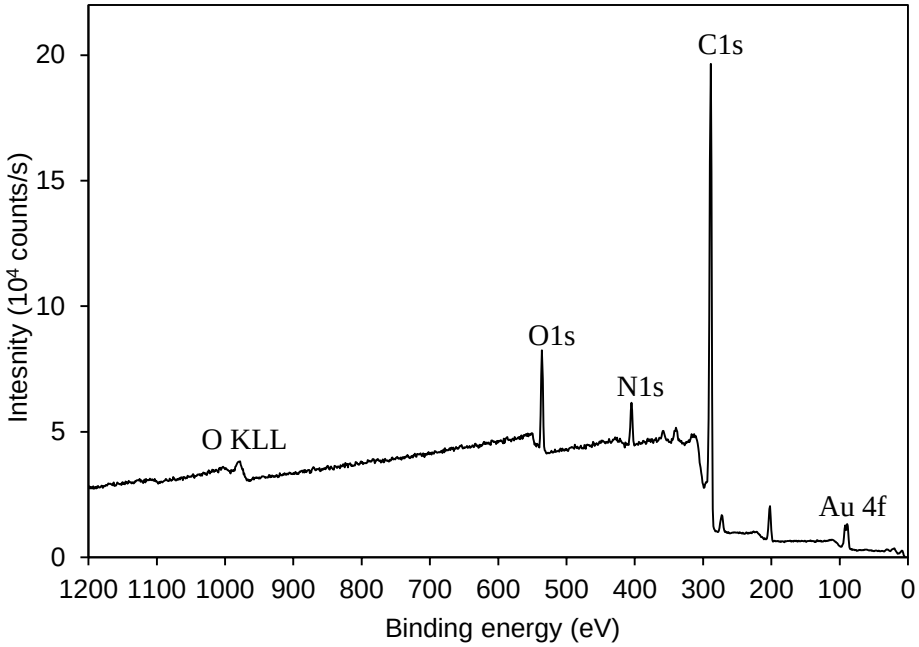

Figure s3.2 Survey or wide scan XPS spectrum of the gold-loaded PSMI sample (AuPSMI) illustrating the presence of all the elements present in the sample. (Courtesy: Professor Sophie Hermans, Catholic University of Louvain, Belgium).

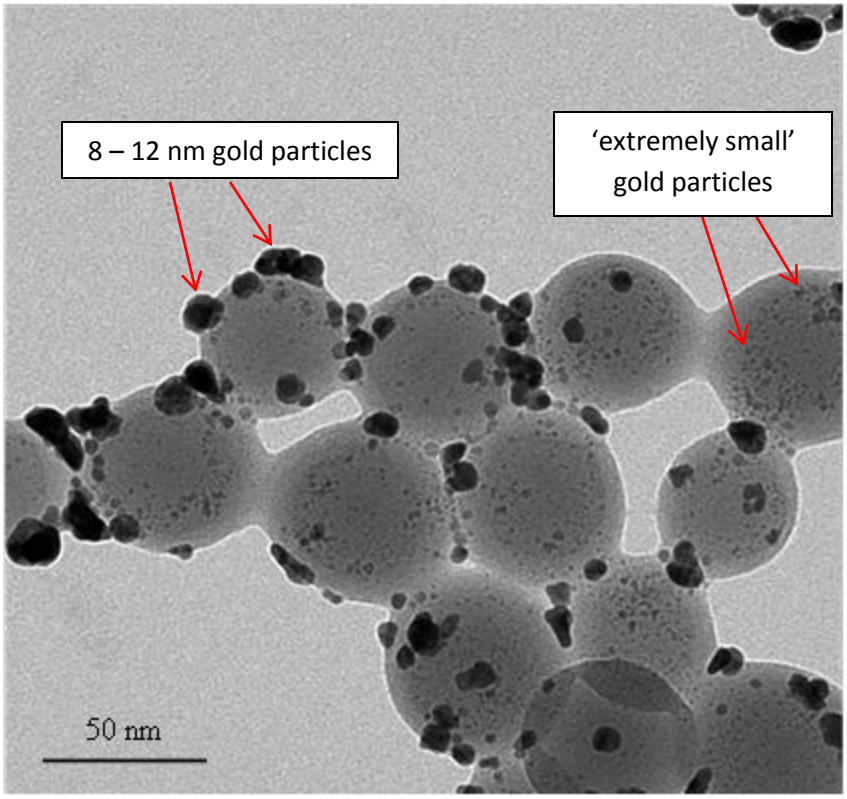

Figure s3.3 TEM micrograph of the AuPSMI sample illustrating the immobilized gold species on the 50 nm PSMI nanoparticles (1000 x magnification). By XPS analysis, the immobilized gold species are confirmed to be present as various oxidation states of 0, +I and +III. (*See* experimental section 3.6.2 for the preparation of the AuPSMI sample for TEM analysis).

Figure s3.4 shows the PXRD diffraction patterns of the PSMI nanoparticle powder as well as the gold-loaded PSMI nanoparticle (AuPSMI) powder samples. No distinctive 'crystalline' diffraction peaks associated with elemental gold could be detected in the AuPSMI sample. This is most probably due to the presence of the amorphous PSMI which is in excess. Therefore, the result indicates that PXRD analysis (even using a long irradiation time of 3 h) is not a sensitive tool to detect the presence of elemental gold on the surface of the PSMI nanoparticles.

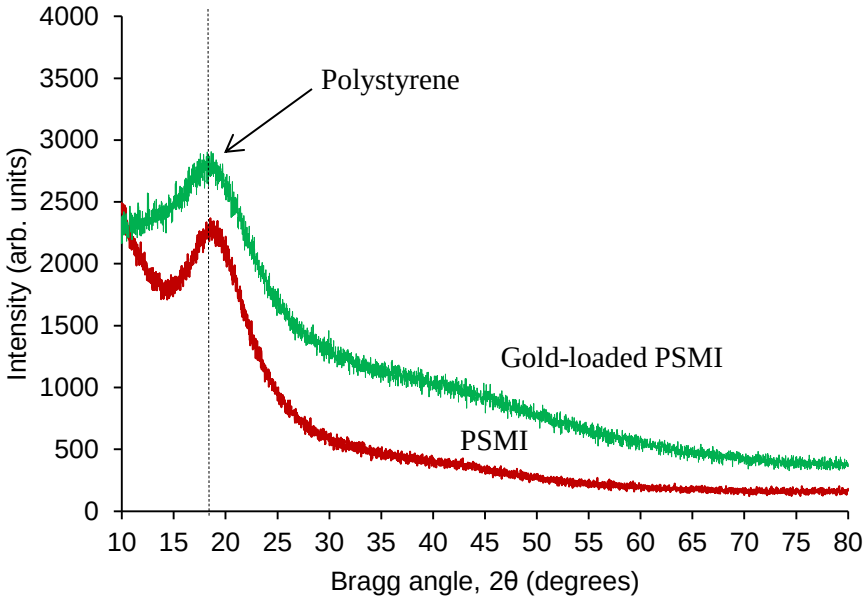

Figure s3.4 PXRD diffraction pattern of PSMI (indicated in red) and the gold-loaded PSMI sample, AuPSMI (indicated in green). The dashed line at about 18 ° indicates the diffraction angle associated with amorphous polystyrene present in PSMI and the gold-loaded PSMI samples.

4 Synthesis and characterization of micro- to millimeter size poly(styrene-*co*-maleimide) beads

Synopsis

In this Chapter, micro- to millimeter size poly(styrene-*co*-maleimide) (PSMI) resin beads were prepared using an electrospray method directly from the PSMI as synthesized in Chapter 2. This novel method allows for a wide range of PSMI spherical and quasi-spherical bead sizes of shape to be prepared by manipulation of the experimental conditions employed during the electrospray process, such as the concentration of the PSMI in solution, the spray distance, flow rate and the applied voltage. Surface area and porosity analysis shows that 450 µm and 1620 µm PSMI resin beads selected for use in the gold extraction experiments (Chapter 5) are microporous and have specific surface areas of 2.8 ± 0.4 m^2/g and 2.0 ± 0.1 m^2/g, respectively.

4.1 Introduction

Most industrial metallurgical processes utilizing sorption and ion-exchange methods for the extraction and separation of metal species from metal-rich solutions make use of functionalized micro- to millimeter (*µm* to *mm*) size particles or beads due to their physico-chemical properties, ease of handling and operation as well as the ability to achieve relatively high fluid flow rates in packed beds or columns. The diameters of such *µm* to *mm* size beads commonly known as resins are typically between 0.3 – 1.2 mm. [1,2] We therefore aimed to synthesize *µm* to *mm* size

poly(styrene-*co*-maleimide) (PSMI) beads to test their ability for the extraction and separation of $[AuCl_4]^-$ ions from single-metal as well as mixed-metal aqueous acidic solutions and compare these results to the PSMI nanoparticles (*ca* 50 nm in diameter) as discussed in Chapters 2 and 3.

The most common techniques utilized for *µm* to *mm* size spherical polymer beads preparation include emulsion polymerization, mini- and microemulsion polymerization, suspension polymerization, dispersion polymerization, precipitation polymerization, membrane emulsification and microfluidics. [3-6] The polymer beads obtained using these techniques cover a wide diameter range, of materials with different functionalities depending on the desired application. In this study, 'electrospraying', also known as electrohydrodynamic spraying was investigated for the preparation of *µm* to *mm* size PSMI beads. [7-9] The general principle of an electrospraying process for the preparation of *µm* to *mm* beads and fibers is shown in Figure 4.1.

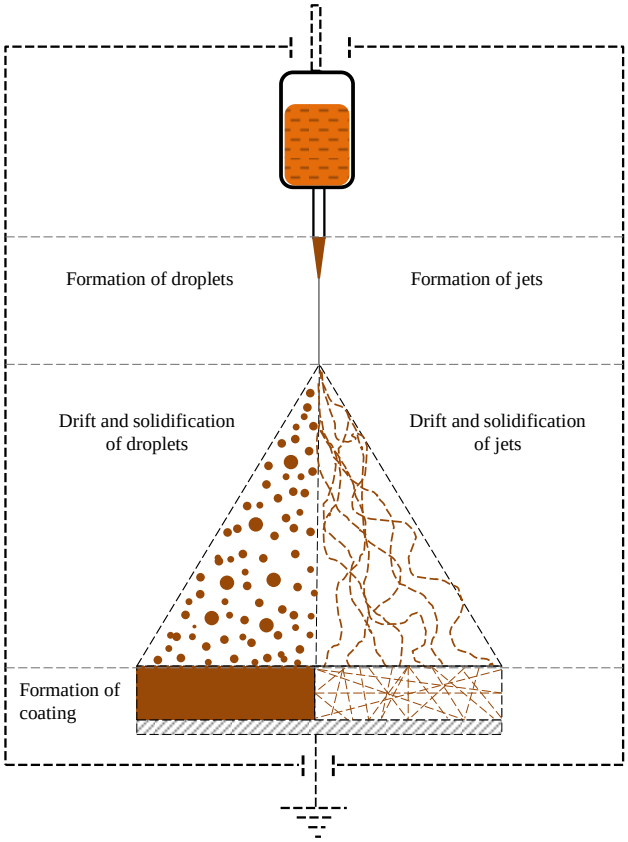

Figure 4.1 Common electrospray system set-up and general principle for the preparation of *µm* to *mm* size polymer beads and nano- to micron-size fibers.

In the electrospray technique, electrical forces are applied to the surface of a solution consisting of a polymer dissolved in a suitable solvent as it flows from the capillary. These forces induce shear stress which makes the solution meniscus at the outlet of the capillary elongate in an electric field and forms solution jets, which upon solvent evaporation and solidification, nano- to micron-size fibers are formed on the grounded collector (Figure 4.1). When the electrical forces overcome the surface tension of the solution, the solution jet can readily break-up into droplets moving toward the collector. With rapid evaporation of the solvent accompanying the newly formed charged droplet, the size of droplets decreases. This leads to a closer aggregation of the electrical charges induced in the droplets and a higher repulsive force between them. At a threshold, the repulsive forces break each droplet down into a group of smaller droplets in a process called 'coulombic explosion'. [10] Coulombic explosion proceeds further for each newly formed droplet until the so formed droplets reaches the grounded collector resulting in loss of its electrical charge to form nano- to micrometer diameter beads. The collector can be either a solid substrate such as aluminium foil or an aqueous solution of various compositions.

As reported in literature, various modes of electrospraying exist. [11] In this study, the process employed for the preparation of *µm* to *mm* size PSMI resin beads is known as dripping mode electrospraying. [11] This mode is characterized by the phenomenon in that droplets of solution are instantaneously formed as the solution flows from the capillary, instead of the formation of a continuous jet stream. Moreover, the dripping mode electrospray process is distinguished by the shape of the solution meniscus (round or cone shaped) as it flows from the capillary tip and is directly dependant on the conditions such as for example applied voltage (electrical forces) and solution flow rate. Upon solvent evaporation and solidification, *µm* to *mm* size beads are formed. For more information on the modes of electrospraying and the general procedures and theory of the technique, the reader is referred to papers by Jaworek and Krupa and the references cited therein. [7,9]

Conceptually it is easy to control the diameter of the polymer beads resulting from this electrospray method ranging from a nanometer to micrometer range by varying critical process parameters such as those summarized in Table 4.1. [8,12]

Table 4.1 Influence of critical parameters on the diameter of polymer beads as prepared by dripping-mode electrospray methodology. [8,12]

Formation of small particle diameters with an increase in the following:	Formation of large particle diameters with an increase in the following:
electric field strength (applied voltage)	polymer concentration
solution conductivity	molecular weight of polymer
solvent volatility	flow rate
surface tension	needle (capillary) diameter
distance to collector	solution density

A wide range of uniform bead diameters can conveniently be obtained by manipulation of the experimental conditions used for the preparation of the beads. The electrospray process employed for the preparation of *μm* to *mm* diameter PSMI resin beads in this work is simple, cheap, flexible, and easy to control which would make the optimization and larger scale production of the beads possible.

4.2 Synthesis of micro- to millimeter size PSMI resin beads

A typical preparation is as follows: The electrospray solution was prepared by dissolving approximately 0.8 g of the purified PSMI nanoparticulate powder (Chapter 2) in 2 g of dimethylformamide (DMF) to a concentration of 28.6 wt. % (w/w). The homogeneous PSMI solution was placed in a 1 mL Hamilton gas-tight glass syringe equipped with a disposable stainless steel needle or capillary tip with an internal diameter of 0.45 µm. An electrode was attached to the capillary tip and connected to a high voltage power supply (Matsuda Precision UNIT AU-80P1.87-LC). The voltages applied in the experiments ranged from 0.1 kV – 20 kV, unless otherwise stated. The feeding flow rate of the PSMI solution was controlled by an automated dosing double syringe pump (Pump 33 model, Harvard apparatus) connected to the

syringe and was set as 0.1 – 1.0 mL/min. An electrically grounded collector bath was positioned 10 or 20 cm below the capillary tip. The collector bath contained an aqueous solution of water/methanol mixture in a ratio of 80:20 (v/v). A vortex was applied to the solution in the collector bath (*via* magnetic stirring at 300 rpm) to ensure that incoming droplets were suspended in solution and to avoid possible aggregation. The resulting PSMI beads were recovered from the collector bath and subsequently dried under vacuum at 80 °C for 6 h to remove any residual solvent that might not have evaporated during the electrospray process. A schematic representation of the electrospray system set-up used in this study is shown in Figure 4.2. As can be seen from Figure 4.2, aluminium foil as well as aqueous solution bath collectors were used in the investigation into the formation of the PSMI resin beads. However, for the preparation of the PSMI resin beads in bulk quantities to be used in the extraction experiments (Chapter 5), only the aqueous solution bath collector system was used.

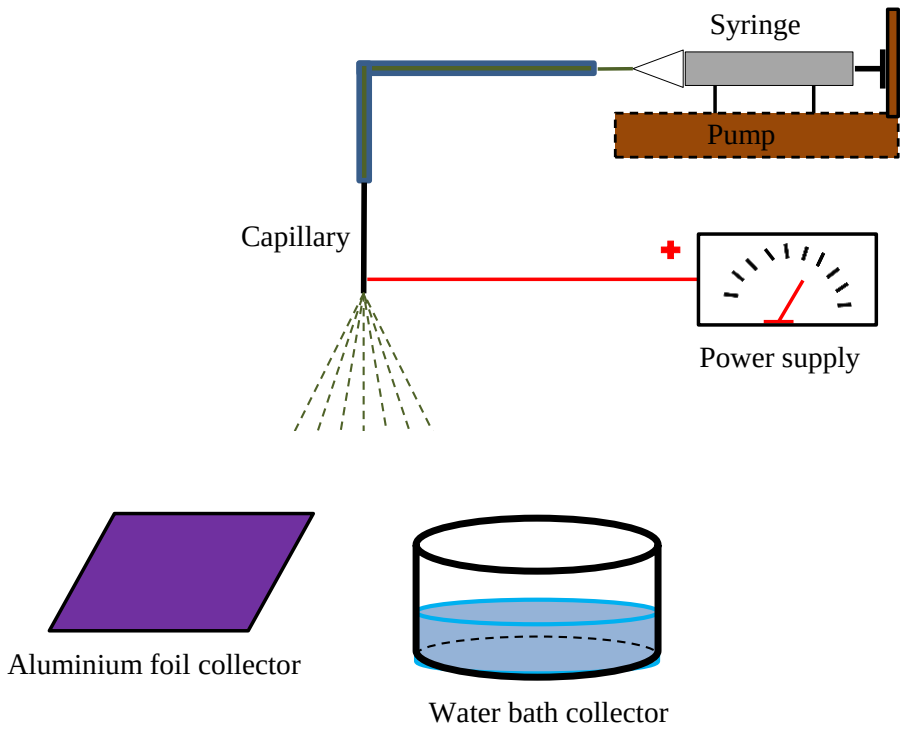

Figure 4.2 Experimental set-up used for the preparation of the *µm* to *mm* size PSMI resin beads by the dripping-mode electrospray methodology.

4.3 Results and discussion

4.3.1 Particle size distribution and SEM analysis

The average diameters and morphology of the *µm* to *mm* size PSMI resin beads obtained with the electrospray methodology was determined by scanning electron microscopy (SEM) analysis. Table 4.2 summarizes the description of the electrospray experimental conditions in the following order: concentration of dissolved PSMI in the spray solution in wt. % (w/w); spray distance in cm (capillary tip-to-collector distance); flow rate of PSMI solution pumped through the capillary in mL/min; and voltage applied on the capillary tip in kV. Also given in Table 4.2 are the average diameters of the PSMI resin beads obtained in each case.

Table 4.2 Electrospray experimental conditions and the corresponding average PSMI resin bead diameters.

Figure 4.3 labelling	Experimental conditions	Bead size (µm)
(a)	28.6 wt.% 10 cm 0.1 mL/min 5 kV	625 ± 65
(b)	28.6 wt.% 10 cm 0.1 mL/min 10 kV	450 ± 30
(c)	28.6 wt.% 10 cm 0.1 mL/min 20 kV	8 ± 4
(d)	28.6 wt.% 10 cm 0.5 mL/min 5 kV	950 ± 110
(e)	28.6 wt.% 10 cm 0.5 mL/min 10 kV	700 ± 39
(f)	28.6 wt.% 10 cm 0.5 mL/min 20 kV	19 ± 10.5
(g)	28.6 wt.% 10 cm 1.0 mL/min 5 kV	1620 ± 200
(h)	28.6 wt.% 10 cm 1.0 mL/min 10 kV	870 ± 90
(i)	28.6 wt.% 10 cm 1.0 mL/min 20 kV	360 ± 85
(j)	28.6 wt.% 20 cm 0.1 mL/min 10 kV	405 ± 15
(k)	9.10 wt.% 10 cm 0.1 mL/min 10 kV	160 ± 10*
(l)	37.5 wt.% 10 cm 0.1 mL/min 10 kV	2.4 ± 0.2#

Note: * Irregular shape PSMI beads obtained

PSMI fibers obtained

Figure 4.3 shows the corresponding SEM micrographs at different magnifications of the PSMI resin beads obtained. The beads could be reproducibly prepared depending on the set of experimental conditions used. From Table 4.2 and the SEM micrographs (Figure 4.3 (a) – (i)), it can be seen that an increase in applied voltage from 5 – 20 kV results in a significant decrease in average PSMI resin bead diameter. This can be explained by the fact that with higher applied voltages, overcoming the surface tension of the electrospray PSMI solution (as it flows through the capillary) becomes easier, leading to efficient atomization and break-up into smaller droplets and thus smaller PSMI resin beads formation in electrospraying.

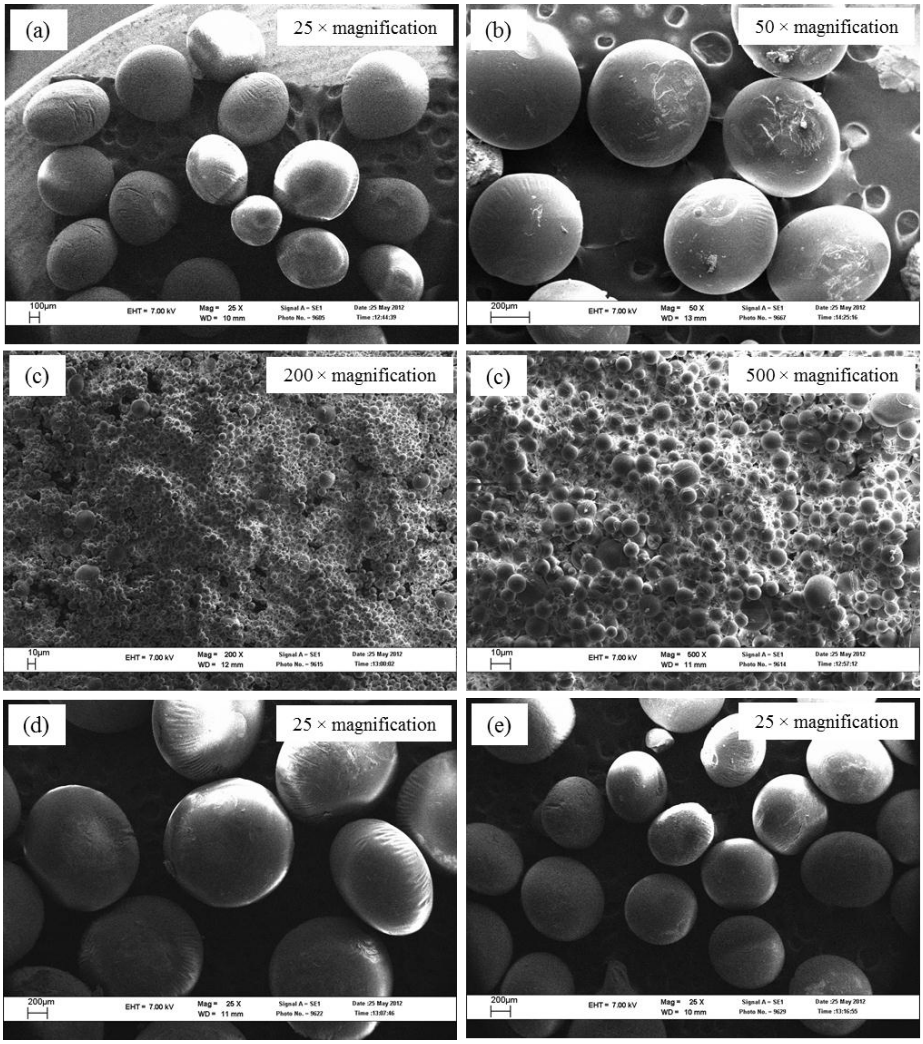

Figure 4.3 SEM micrographs of the *μm* to *mm* size PSMI resin beads obtained for different electrospray experimental conditions: (a) 28.6 wt. %, 10 cm, 0.1 mL/min, 5 kV (625 ± 65 μm); (b) 28.6 wt. %, 10 cm, 0.1 mL/min, 10 kV (450 ± 30 μm); (c) 28.6 wt. %, 10 cm, 0.1 mL/min, 20 kV (8 ± 4 μm); (d) 28.6 wt. %, 10 cm, 0.5 mL/min, 5 kV (950 ± 110 μm); (e) 28.6 wt. %, 10 cm, 0.5 mL/min, 10 kV (700 ± 39 μm).

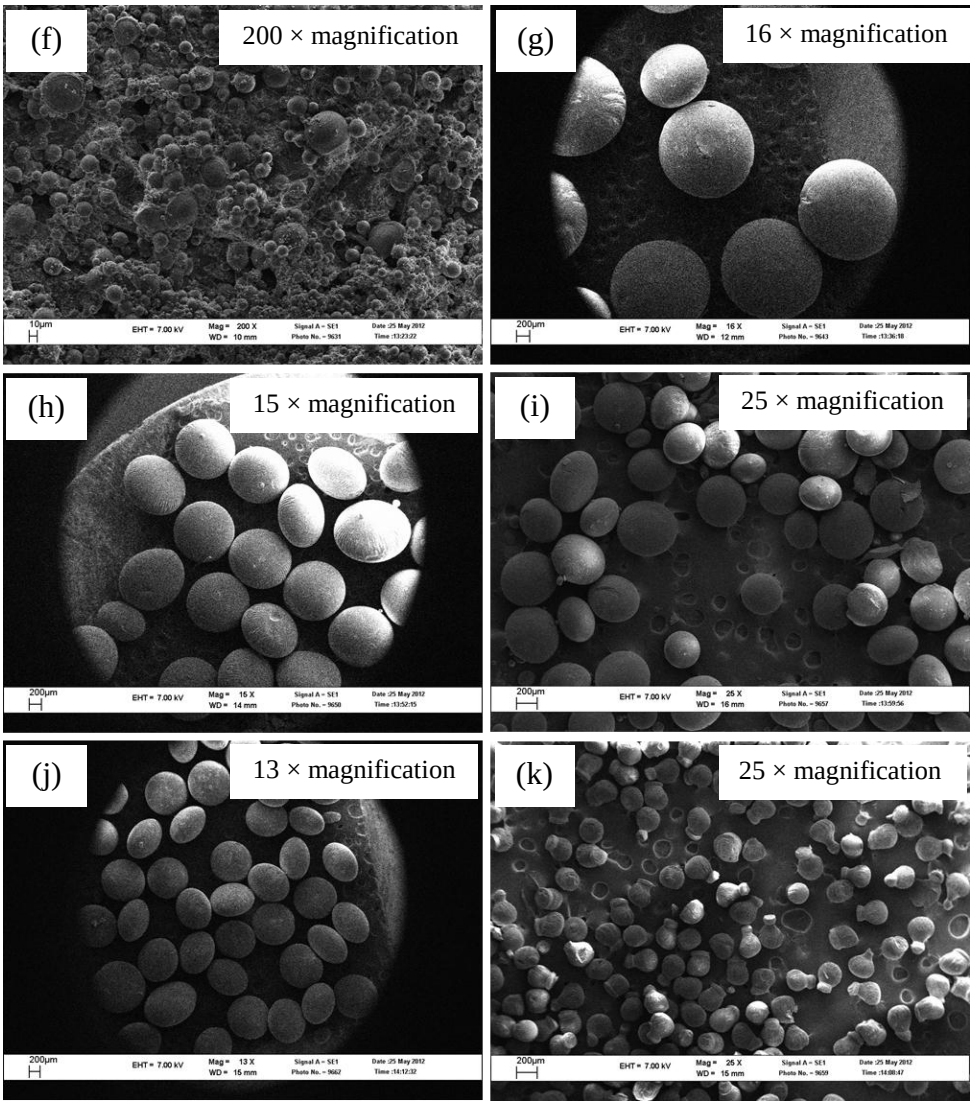

Figure 4.3 SEM micrographs of the *μm* to *mm* size PSMI resin beads obtained for different electrospray experimental conditions (continued): (f) 28.6 wt. %, 10 cm, 0.5 mL/min, 20 kV (19 ± 10.5 μm); (g) 28.6 wt. %, 10 cm, 1.0 mL/min, 5 kV (1620 ± 200 μm); (h) 28.6 wt. %, 10 cm, 1.0 mL/min, 10 kV (870 ± 90 μm); (i) 28.6 wt. %, 10 cm, 1.0 mL/min, 20 kV (360 ± 85 μm); (j) 28.6 wt. %, 20 cm, 0.1 mL/min, 10 kV (405 ± 15 μm); (k) 9.10 wt. %, 10 cm, 0.1 mL/min, 10 kV (160 ± 10 μm).

In contrast with the applied voltage, increasing the flow rate at which the PSMI solution is pumped through the capillary from 0.1 – 1.0 mL/min results in an increase in average PSMI resin bead diameters (Table 4.2). This can be attributed to the fact that increasing flow rate results in an increase in mass flow, i.e. more PSMI solution flows through the capillary per second. This causes the droplets at the capillary tip to be less sufficiently charged and form too quickly to be atomized and larger charged spherical droplets travel towards the collector. These larger droplets

results in the formation of *μm* to *mm* size PSMI resin beads upon solvent evaporation and solidification.

On direct comparison of the PSMI resin bead diameters obtained using different capillary tip-to-collector spray distances of 10 and 20 cm (Figure 4.3 (b) and (j)) for similar PSMI concentrations of 28.6 wt. %, flow rate of 0.1 mL/min and applied voltage of 10 kV, a decrease in average PSMI resin bead diameters were observed with the increase in capillary tip-to-collector distance from 10 to 20 cm (Table 4.2). The formation of smaller average PSMI resin bead diameters with longer capillary tip-to-collector distances are expected as the trajectory of the droplets increases; hence there exists more time for the coloumbic explosions to act on the electrospray droplets before reaching the collector.

For lower PSMI solution concentrations of 9.10 wt. %, beads with an irregular morphology were formed as shown in Figure 4.3 (k). This is most probably related to a lower degree of PSMI molecular chains entanglement in the solution, thus indicating the importance of concentration in such an electrospray methodology. Interestingly, it was found that for higher PSMI solution concentrations of 37.5 wt. %, monodisperse fibers with narrow size-distributions were obtained with diameters of 2.4 ± 0.2 μm (Figure 4.3 (l)).

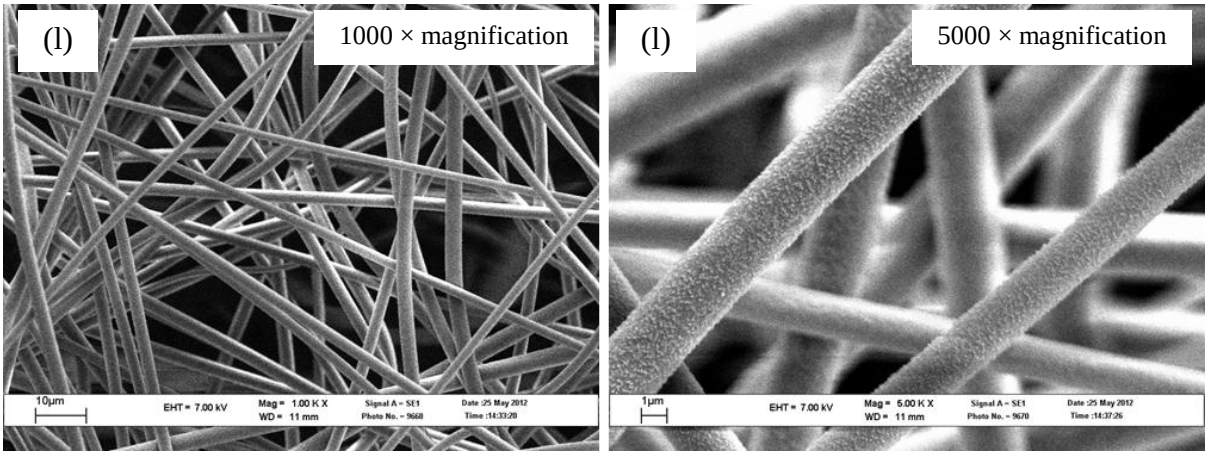

Figure 4.3 SEM micrographs of the *μm*-size PSMI fibers obtained for different electrospray experimental conditions (continued): (l) 37.5 wt. %, 10 cm, 0.1 mL/min, 10 kV (2.4 ± 0.2 μm).

The formation of the fibers as a result of the relatively higher PSMI concentration in DMF (electrospray solution) is most probably related to greater degree of entanglement of the polymer

molecular chains in the solution, leading to electrospinning, rather than electrospraying observed when lower concentration PSMI solutions are used.

The influence of an alternative collector on the PSMI resin beads size and morphology was also briefly investigated. Figure 4.4 shows the PSMI resin beads obtained with the electrospray methodology using aluminium foil as a collector instead of an aqueous water/methanol solution bath. The experimental conditions were similar to that of the beads obtained as shown in Figure 4.3 (c) (Table 4.2), but using an applied voltage of 25 kV. It was found that monodisperse spherically shaped µm-size PSMI resin beads with a narrow size-distribution were attained as shown by the SEM micrographs (at different magnifications) in Figure 4.4.

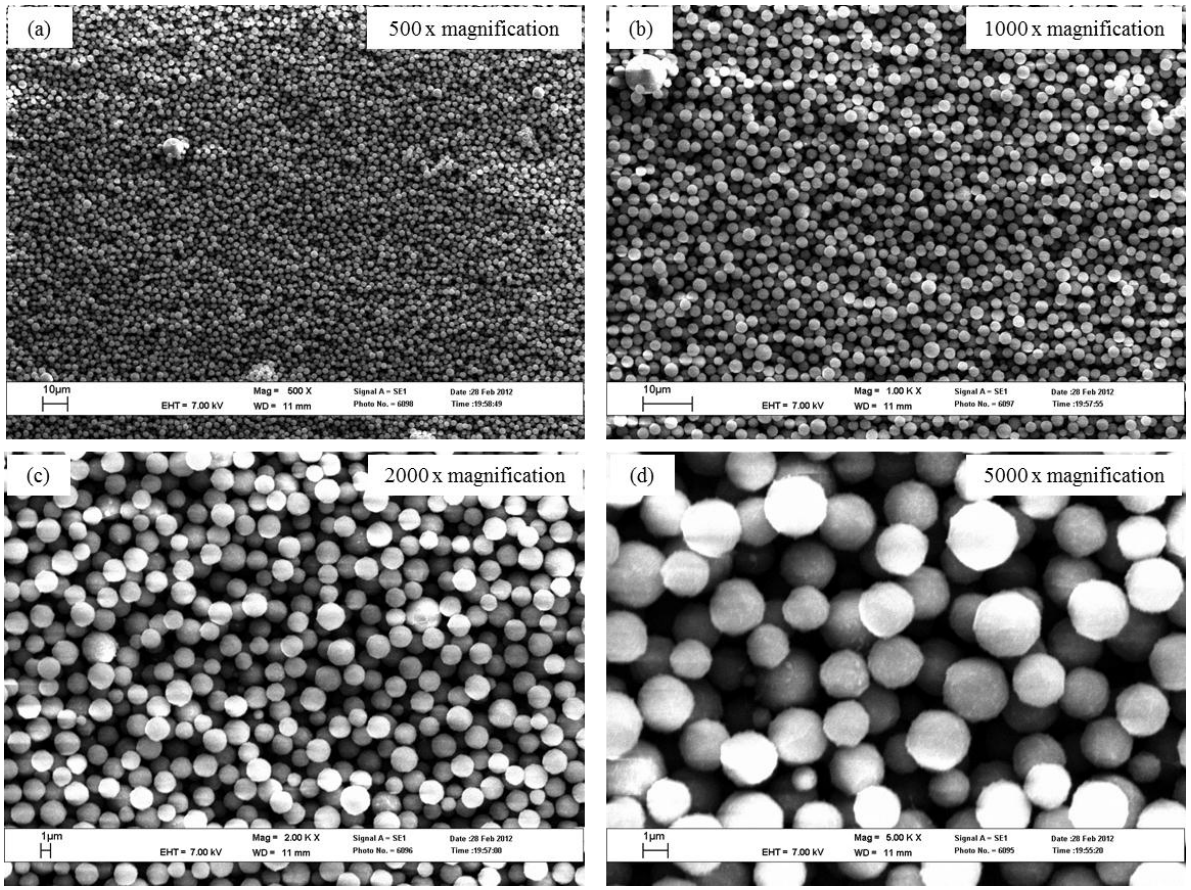

Figure 4.4 SEM micrographs at different magnifications of the *µm*-size PSMI resin beads obtained by electrospraying on aluminium foil. Experimental conditions: 28.6 wt. %, 10 cm, 0.1 mL/min, 25 kV (2.1 ± 0.2 µm).

Due to the relatively higher applied voltage of 25 kV to the capillary, smaller average PSMI bead diameters of 2.1 ± 0.2 µm were attained as a result of increased atomization of the droplets into finer aerosols.

The observed trends for the different diameter PSMI resin beads obtained are in accordance with that expected and predicted by Table 5.1. [8] Preliminary studies have shown that the solvents used to prepare the electrospray solution and also the surface tension of the aqueous solutions used as collector has an influence to some extent on the diameter but more specifically on the morphology of the PSMI resin beads obtained. For the preparation of the PSMI beads as shown in Figures 4.3 (a) – (k) and described in Table 4.2, an aqueous water/methanol solution bath (in a ratio of 80:20 (v/v)) with a surface tension of about 47 $mN.m^{-1}$ was used. For a water bath collector without any methanol, the surface tension was about 72 $mN.m^{-1}$. These surface tension values measured for the aqueous water/methanol solutions coincide well with that reported in literature at 25 °C. [13] When using a water bath as collector (without methanol), quasi-spherical PSMI beads with average diameters of 800 ± 20 µm were obtained with a peculiar morphology as shown in Figure 4.5. The experimental conditions used in the electrospray process for the preparation of these beads are as shown in the figure caption.

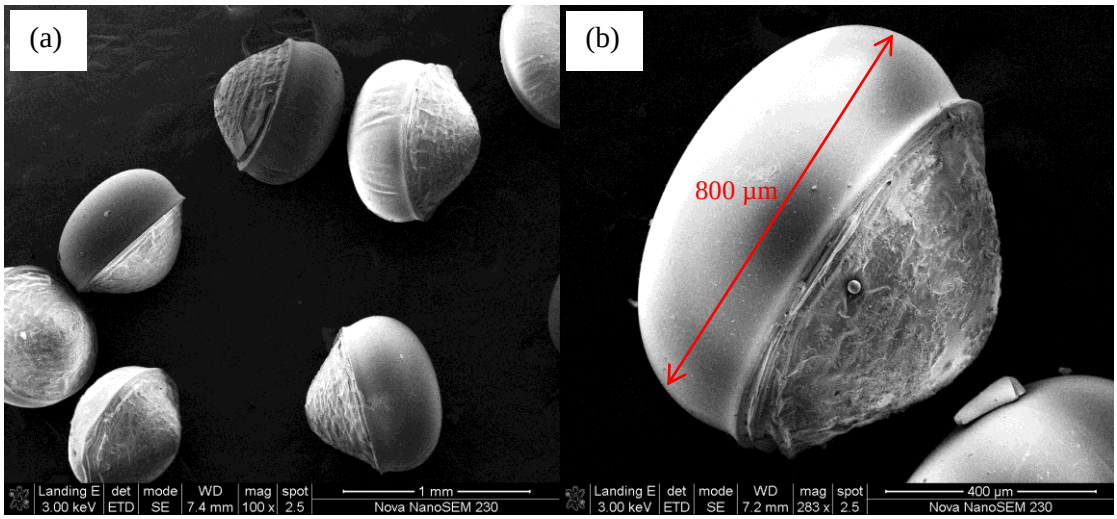

Figure 4.5 SEM micrographs the *µm* to *mm* size PSMI resin beads obtained by electrospraying using a water bath collector (without methanol). Experimental conditions: 40 wt. %, 10 cm, 0.1 mL/min, 5 kV (800 ± 20 µm).

By increasing the ratio of methanol to water, and thus decreasing the surface tension of the aqueous solution of the collector bath, more regular shaped beads were formed. The best results were obtained for the water/methanol ratio of 80:20 (v/v). The result, therefore suggests that the surface tension of the water bath collector has a significant effect on the formation of the beads. The main interest in this study was the preparation of spherical PSMI resin beads with regular morphology as shown in Figure 4.3 (a) – (j).

4.3.2 ^{13}C NMR and FTIR analysis

The chemical composition of the 450 µm and 1620 µm PSMI resin beads obtained by the electrospray methodology after drying in vacuo to remove any residual solvent and water was checked by means of ^{13}C NMR and FTIR spectroscopy analysis on powdered samples after crushing of the PSMI resin beads in a mortar with a pestle. Figure 4.6 shows a digital camera picture and corresponding optical microscope pictures of the 450 µm PSMI resin beads.

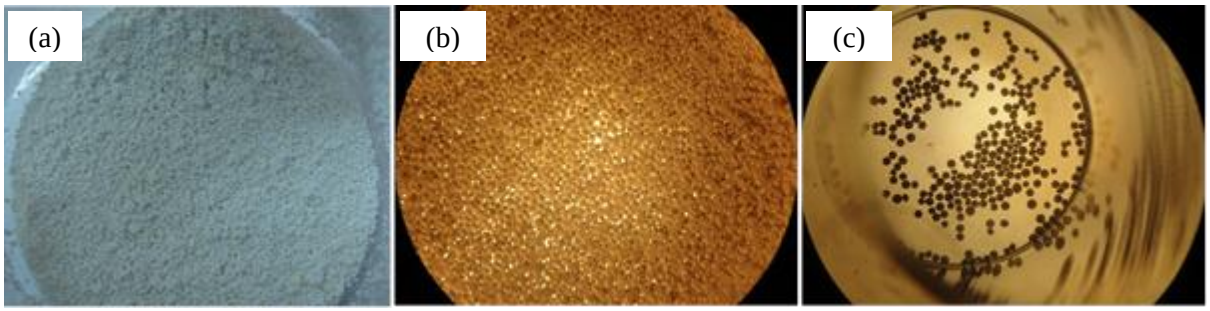

Figure 4.6 Digital camera picture (a) and corresponding optical microscope pictures (b), (c) of the 450 µm PSMI resin beads crushed to a powdered substance for ^{13}C NMR and FTIR analysis.

The ^{13}C NMR and FTIR spectra for the 450 µm PSMI sample shown in Figure 4.7 (a) and (b), respectively are identical to those as shown in Figures 2.3 and 2.4 for the analogous PSMI nanoparticles (Chapter 2). This indicates that the chemical composition of the prepared PSMI resin beads remains unchanged after electrospray beads formation. Similar ^{13}C NMR and FTIR spectra were obtained for the 1620 µm PSMI sample. This result supports the belief that electrospraying allows *µm* to *mm* size PSMI resin beads preparation without any change in chemical composition of the PSMI material to be sprayed.

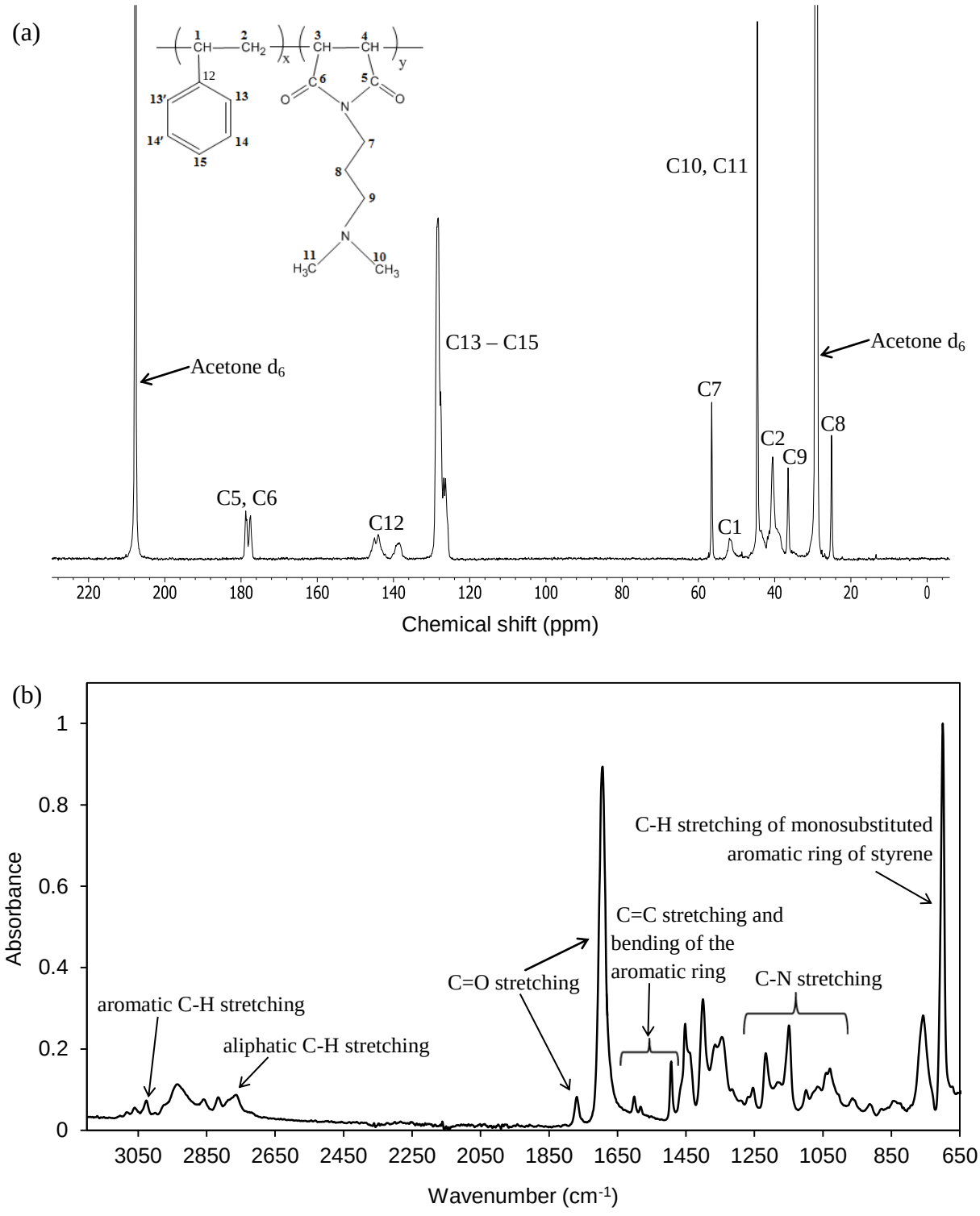

Figure 4.7 (a) ^{13}C NMR and (b) ATR-FTIR spectra of the 450 µm PSMI sample indicating that the chemical composition of the PSMI remains unchanged after electrospray bead formation. NMR experimental conditions – Solvent: Acetone; Frequency: 150.586 MHz; Total acquisition time: 24 h; Temperature: 317.9 K. ^{13}C NMR chemical shifts were quoted relative to the acetone-d_6 resonance at 207 ppm.

4.3.3 Thermal analysis

In order to determine whether the 450 µm and 1620 µm PSMI resin beads contained any traces of residual solvent, thermogravimetric analysis was done on samples obtained by crushing the respective PSMI resin beads in a mortar with a pestle to finer fragments. It is important to point out that the PSMI resin beads were dried under vacuum at 80 °C for 6 h prior to being used in the $[AuCl_4]^-$ extraction experiments (Chapter 5). The TGA thermogram and TGA derivative curve of the crushed 450 µm PSMI samples are shown in Figure 4.8. A similar TGA thermogram was obtained for the 1620 µm PSMI samples (result not shown).

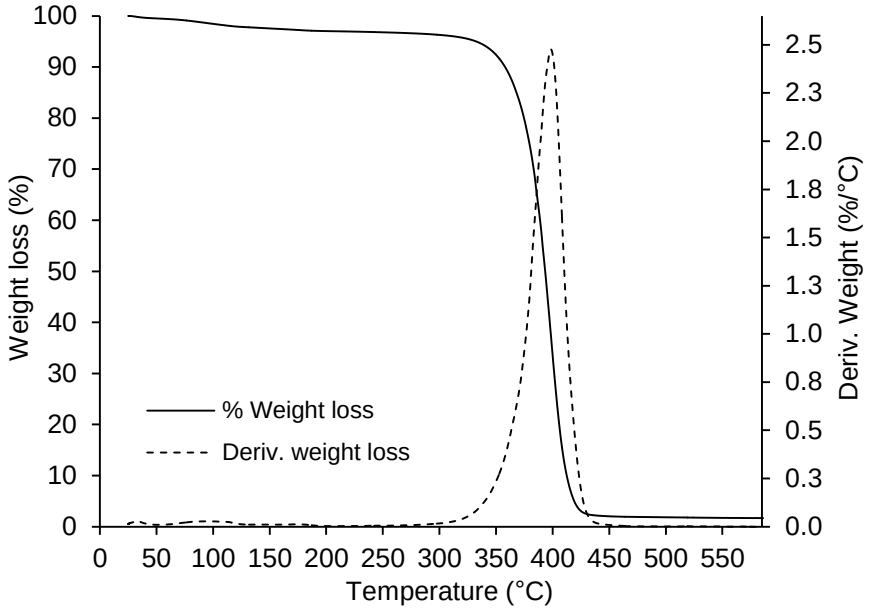

Figure 4.8 TGA thermogram (solid line) and corresponding first-derivative TGA curve (dotted line) of the 450 µm PSMI sample. A similar TGA thermogram was obtained for the 1620 µm PSMI sample.

As can be seen from the TGA thermogram in Figure 4.8, no clear trace of any residual solvent was left within the PSMI sample. This verifies that the solvent was completely evaporated from the PSMI resin beads used in the extraction experiments. The onset temperature of decomposition for the PSMI sample is about 285 – 295 ˚C, which is similar to the TGA thermogram obtained from the PSMI nanoparticles (Figure 2.9, Chapter 2). This suggests that the PSMI resin beads are thermally stable up to about 285 ˚C. The temperature at which the maximum decomposition rate occurs as estimated by the TGA derivative curve is approximately 395 ˚C.

4.3.4 Surface area and porosity analysis

The surface area and porosity of the 450 µm and the 1620 µm PSMI resin beads used in the gold extraction studies (Chapter 5) were characterized using the Brunauer-Emmet-Teller (BET) method. [14,15] The N_2 adsorption – desorption isotherms for the 450 µm and 1620 µm PSMI resin beads are shown in Figure 4.9 (a) and (b), respectively.

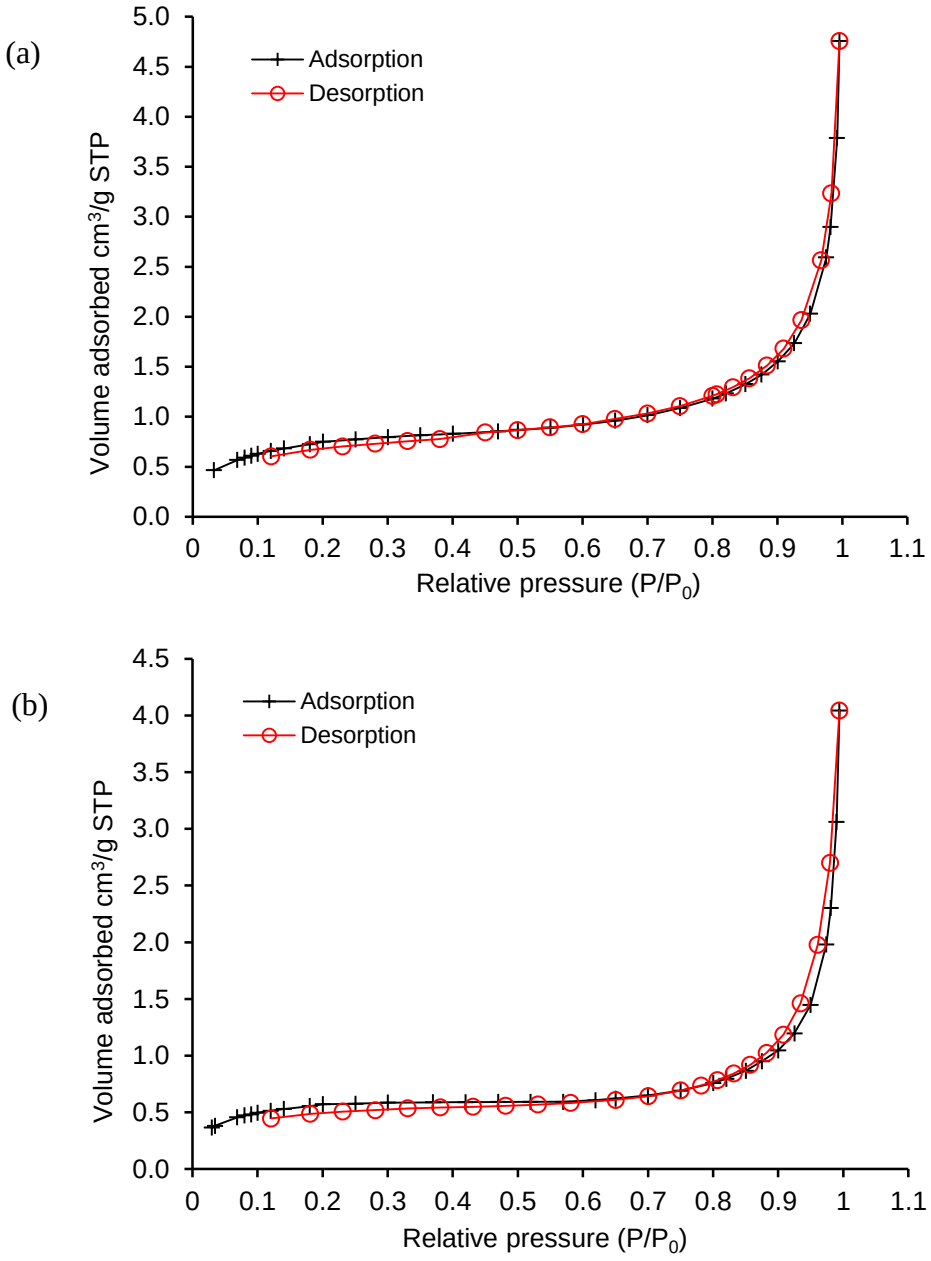

Figure 4.9 BET nitrogen adsorption-desorption isotherms for (a) the 450 µm and (b) the 1620 µm PSMI resin beads obtained by the electrospray methodology.

From the shape of the isotherms it is clear that the degree of porosity is very small (Figure 4.9). Based on the International Union of Pure and Applied Chemistry (IUPAC) classification, the pores can be divided into broad terms according to diameter (d) into macropores (d > 500 Å), mesopores (20 Å < d < 500 Å) and micropores (d < 20 Å). [14-16] As listed in Table 4.3, both the 450 µm and the 1620 µm PSMI resin beads predominantly contains micropores.

Table 4.3. BET specific surface area and porosity analysis of the 450 µm/1620 µm PSMI resin beads and the analogous 50 nm PSMI nanoparticles.

PSMI particle diameter	BET surface area (m^2/g)	Average pore diameter (Å)
1620 ± 200 µm	2.0 ± 0.1	15.1
450 ± 30 µm	2.8 ± 0.4	18.8
50 ± 5 nm	88.1 ± 2.2	82.3[#]

Note: [#] Textural porosity due to packing density of non-porous PSMI nanoparticles (Figure 2.8, Chapter 2).

As can be seen in Table 4.3 for the 450 µm and 1620 µm PSMI resin beads selected, there is not a large variation in the specific surface areas between the two physically different diameter beads. This is due to the fact the both the 450 µm and 1620 µm PSMI resin beads are relatively large, resulting in the similar range specific surface areas obtained by the BET method. [13,14] The specific surface area is not only dependent on the size of the beads but also the degree of porosity. However, as in this case when the porosity is small, there is an inverse relationship between the physical diameter and the specific surface area. Larger beads generally results in smaller specific surface area.

For comparison, the specific surface area obtained for the PSMI nanoparticles as synthesized in Chapter 2 was found to be 88.1 ± 2.2 m^2/g. This relatively larger specific surface area as compared to the 450 µm and 1620 µm PSMI beads can be attributed to the 'smaller' nano-sized particles. Smaller particles exhibit a larger surface area-to-volume ratio.

Figure 4.10 shows the SEM micrograph illustrating the cross-section of a 450 µm PSMI resin bead. Interestingly, the internal structure of the beads is completely different from the surface morphology. Compared to the overall porous microstructure as determined by BET analysis (Table 4.3), the internal structure of the bead appears to contain an array of macropores of

different diameters. These pores were most likely generated by the evaporation and migration of the solvent during the electrospray process. The bead appears to have a distinctive dense outer crust, which most probably prevented sufficient N_2 adsorption or diffusion to reach the internal structure, hence resulting in the moderate specific surface areas.

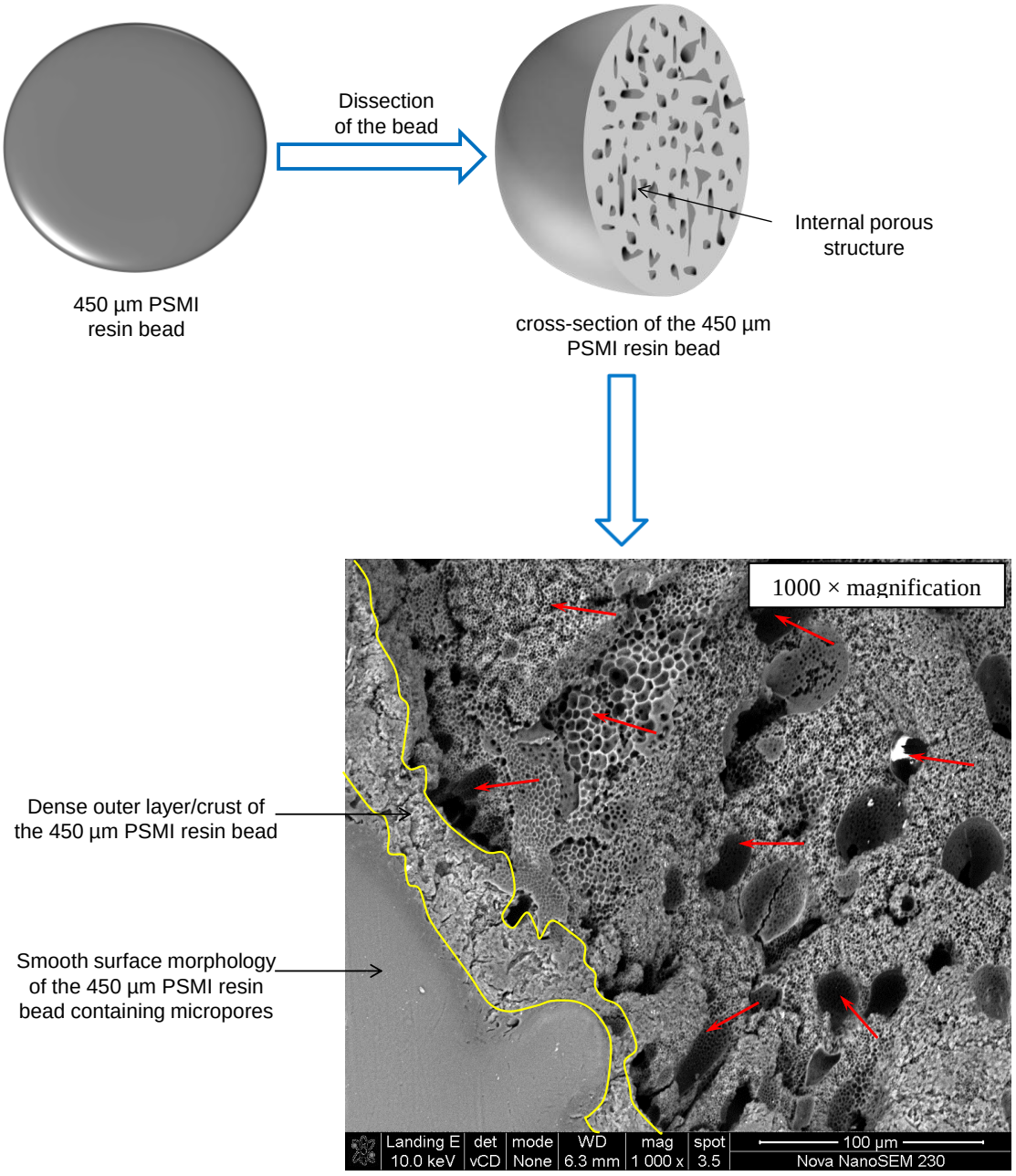

Figure 4.10 Graphic representation and the corresponding SEM micrograph (1000 × magnification) illustrating the cross-section of a 450 µm PSMI resin bead. The dense outer layer/edge of the bead is outlined by the yellow lines and the various internal porous structures inside the bead are indicated by the red arrows.

4.4 Conclusions

A novel electrospray methodology was used for the preparation of *µm* to *mm* size PSMI resin beads of spherical and quasi-spherical shape. The electrospray solutions were prepared by dissolving the PSMI prepared in Chapter 2 in dimethylformamide (DMF) to known concentrations. It was found that the diameters of the PSMI resin beads obtained are dependent on the experimental conditions employed in the electrospray process such as the concentration of PSMI in solution, the flow rate at which the PSMI solution is pumped through the capillary, the capillary tip-to-collector distance (spray distance), and the applied voltage at the capillary tip.

For fixed PSMI concentrations in solution of 28.6 wt. % (w/w), the average PSMI resin bead diameters were found to decrease with increases in the applied voltage from 5 – 20 kV and capillary-tip-to-collector distance from 10 cm to 20 cm. For a similar PSMI concentration in solution (28.6 wt. %), the average PSMI resin bead diameters increased with an increase in the flow rate from 0.1 – 1.0 mL/min. The formation of the physically different diameter beads may be attributed to the atomization process in the electrospray methodology. A more efficient atomization process results in smaller droplets formed during electrospraying and thus smaller beads upon solvent evaporation and solidification. For a relatively lower PSMI concentration of 9.1 wt. % (w/w), irregular PSMI resin beads were obtained. Interestingly, for higher PSMI concentration of 37.5 wt. % (w/w), micron-sized PSMI fibers were obtained with diameters of 2.4 ± 0.2 µm. This clearly indicates that the PSMI concentration in solution significantly affects the morphology of the PSMI resin beads.

^{13}C NMR and FTIR spectroscopy analyses show that the electrospray methodology allows for *µm* to *mm* diameter PSMI resin beads preparation without any change in chemical composition of the PSMI material. Thermal analysis verified that the 450 µm and 1620 µm PSMI resin beads dried under vacuum at 80 °C for 6 h contained no residual solvent. The specific surface areas of the 450 µm and 1620 µm PSMI resin beads to be used for $[AuCl_4]^-$ extractions, were found to be 2.8 ± 0.4 m^2/g and 2.0 ± 0.1 m^2/g, respectively. Both the 450 µm and 1620 µm PSMI resin beads are classified as being microporous with average pore diameters of less than 20 Å.

The electrospray methodology used for the preparation of the PSMI resin beads is simple, inexpensive, flexible, and easy to control. This means that PSMI resin beads with desired diameters and narrow-size distributions could be produced in larger scale for potential use in applications such as for example separation and preconcentration of metals species using packed bed column systems.

4.5 Experimental

4.5.1 Materials

The poly(styrene-*co*-maleimide) (PSMI) synthesized in Chapter 2 was used as precursors for the preparation of the *µm* to *mm* size PSMI beads. Reagent grade dimethylformamide (DMF) (Sigma-Aldrich, 99 %) was used without further purification. All other chemicals and reagents such as methanol used were of analytical reagent grade. High purity deionized water (Milli Q, 18 MΩ cm) was used throughout this work.

4.5.2 Instruments and measurements

Particle size and morphology was determined by Scanning Electron Microscopy (SEM), using a Leo® 1430VP and Nova NanoSEM 430 (FEI Company) microscopes. The samples were deposited onto double sided carbon tape mounted on a SEM stub and gold coated before analysis. The average PSMI bead diameter was estimated by statistical analysis of the SEM images using *ImageJ*, a public domain software program. [17] This was done by measuring 50 – 100 individual beads using different SEM images. ^{13}C NMR spectra were recorded on a Varian Inova 600 MHz spectrometer operating at 150.586 MHz. A typical sample consists of 250 mg of the PSMI dissolved in 1 mL acetone-d_6 and the experiments conducted at an elevated temperate of 44.8 °C. All samples were carefully filtered before any spectroscopic measurement was undertaken. Fourier transform infrared (FTIR) spectra were recorded on a Nexus FTIR spectrophotometer equipped with a Smart Golden Gate attenuated total reflectance (ATR)

diamond from Thermo Nicolet, with ZnSe lenses. Each spectrum was scanned 32 times with 4.0 cm^{-1} resolution and data analysis was performed with Omnic Software version 7.2. Surface area measurements were carried out using the Brunauer-Emmet-Teller (BET) method on a Micrometrics ASAP 2010 (Accelerated Surface Area and Porosity System) apparatus using nitrogen as an adsorbate. The samples were degassed at 30 °C for approximately 48 h before use. Each degassed sample (0.1 – 0.4 g) was weighed accurately to four decimal places and placed in a sample tube. Analysis was performed using an automatic multi-point adsorption programme, measuring the volume of nitrogen adsorbed by the sample at a range of N_2 pressures. Thermogravimetric analysis (TGA) was carried out with Q500 TA instrument in the temperature range 0 – 590 °C, using aluminium crucibles with typically 3 – 5 mg dried PSMI samples under dynamic N_2 atmosphere (50 mL/min) and heating rate of 10 °C min^{-1}.

4.6 References

1. K. Dorfner, Ion-exchangers: Propertie and Applications, 2nd Ed., Ann Arbor Science Publishers Inc., Michigan, U.S.A., 1973.
2. F. De Dardel, T.V. Arden, Ion Exchangers, 5th Ed., VCH Verlagsgesellschaft mbH: Weinheim, Germany.
3. M.T. Gokmen, F.E. Du Prez, *Progress in Polymer Science* **2012**, 37, 365.
4. C.Y. Yang, L.L. Yu, X.Y. Dong, Y. Sun, *Reactive and Functional Polymers* **2012**, 72, 889.
5. J.S. Song, M.A. Winnik, *Macromolecules* **2006**, 39, 8318.
6. R.S. Frank, J.S. Downey, H.D.H. Stöver, *Journal of Polymer Science: Part A: Polymer Chemistry* **1998**, 36, 2223.
7. A. Jaworek, A.T. Sobczyk, *Journal of Electrostatics* **2008**, 66, 197.
8. S. Chakraborty, I.C. Liao, A. Adler, K.W. Leong, *Advanced Drug Delivery Reviews* **2009**, 61, 1043.
9. A. Jaworek, A. Krupa, *Experimental Fluids* **1999**, 27, 43.
10. J.F. de la Mora, *Analytica Chimica Acta* **2000**, 406, 93.

11. D.R. Chen, D.Y.H. Pui, S. Kaufman, *Journal of Aerosol Science* **1995**, 26, 963.
12. D.R. Chen, Y.H.P. David, *Journal of Aerosol Science* **1996**, 27, 646.
13. G. Vásquez, E. Alvarez, J.M. Navaza, *J. Chem. Eng. Data* **1995**, 40, 611.
14. S. Lowell, J.E. Shields, *Powder Surface Area and Porosity*, Chapman and Hall, London, **1984**.
15. P.A. Webb, C. Orr, *Analytical Methods in Fine Particle Technology*, Micromeritics, Instrument Corporation, **1997**.
16. J.E. Huheey, E.A. Keiter, R.L. Keiter, *Inorganic Chemistry: Principles of Structure and Reactivity*, 4th Ed., Harper Collins College Publishers, New York, N.Y., **1993**.
17. W. Rasband, *In Image J: Image processing and analysis in Java* http://rsb.info.nih.gov/ij/, 2006.

5 Extraction of anionic gold (III) chloride complexes from acidic solutions using micro- to millimeter size poly(styrene-*co*-maleimide) resin beads

Synopsis

Micro- to millimeter size poly(styrene-*co*-maleimide) (PSMI) beads of 450 µm and 1620 µm diameter were tested as potential anion-exchange resins for the extraction of $[AuCl_4]^-$ from aqueous acidic solutions. The time-dependent studies reveal that the extent of gold uptake increases with an increase in contact time and is dependent on the gold concentration of the $[AuCl_4]^-$ feed solutions. A maximum gold loading capacity of 120.7 mg/g and 98.2 mg/g was attained for the 450 µm and 1620 µm PSMI resin beads, respectively. The experimental sorption data followed a linear trend consistent with the Freundlich equation. This sorption trend for $[AuCl_4]^-$ suggests that a multi-layer sorption process predominates. Desorption of immobilized gold from loaded PSMI resin beads was investigated using various elutants such as HCl, HNO_3, thiourea, NaCN and NaOH solutions. The best results were obtained using a mixture of 10 M HNO_3/0.5 M HCl as elutant with a desorption efficiency of about 97%.

5.1 Introduction

There is a large number of papers describing the use of an assortment of laboratory prepared synthetic anion-exchange resins and/or sorbent materials in various forms and with different functionalities for the extraction of precious metals from aqueous solutions. [1-5] The papers published revolving around the preparation of such materials translate the scope available for

research and development in this area. Surprisingly, few of these studies illustrate the complete physical characterization (such as particle size distribution determination from electron microscopy) of prepared polymeric ion-exchange resins used for the application of metal preconcentration. [6] Recently, most studies concerning micro- to millimeter size polymeric anion-exchange resins used for the extraction of $[AuCl_4]^-$ and other precious metal complexes from acidic solutions make use of resins obtained from commercial sources. [7-11] Commercial ion-exchange resins often include the very effective, classical cross-linked divinylbenzene polystyrene matrix containing various weak, medium and strong base functional (typically amine) ion-exchange groups. As discussed in Chapter 1, the ion-exchange capacity of such commercial anion-exchange resins is typically 2.5 – 5 mmol/g and has sizes between 0.3 to 1.2 mm depending on the application. [12-14] Commercially available ion-exchange resins are however less competitive with activated carbon, mainly due to the high cost involved in resin preparation, sometimes poor selectivity, mechanical breakdown of the beads, and the necessity for easy precious metal complex elution and regeneration capability. [15] Yet, ion-exchange resins offer some chemical advantages over activated carbon and have excellent technical potential for application in gold extraction systems.

In this study, the efficacy of the novel PSMI resin materials prepared as 450 µm and for comparison 1620 µm spherical beads as described in Chapter 4 is examined for the extraction of $[AuCl_4]^-$ from single-metal solutions in some detail. Additionally, a preliminary assessment concerning the selectivity of the PSMI resin beads toward $[AuCl_4]^-$ in the presence of members of the platinum group metal (PGM) chlorido-anions in HCl solution have been carried out. This is of interest since $[AuCl_4]^-$ often co-exist with these PGM anions as part of industrial process streams as discussed in Chapter 1. Having similar protonated ion-exchange functional groups as those of the analogous nanoparticles (Scheme 3.1, Chapter 3), the PSMI resins beads are expected to also exhibit large ability towards the uptake of $[AuCl_4]^-$ ions. Of interest in this work was the use of the 450 µm and 1620 µm PSMI resin beads to:

1) Compare the $[AuCl_4]^-$ extraction and desorption efficiency to that of the PSMI nanoparticles used in Chapter 3.
2) Test for $[AuCl_4]^-$ extraction selectivity in the presence of co-existing PGM anions.

3) Preliminary test the ability of the PSMI resin beads to preconcentrate $[AuCl_4]^-$ by a continuous loading process using a mini-column operation set-up.

5.2 Extraction and desorption methodology

The degree of immobilization or extraction of $[AuCl_4]^-$ from 2 M HCl solution and subsequent desorption processes adopted in this study is similar to that employed and described by the batch sorption method in Chapter 3. The 450 µm and 1620 µm PSMI resin beads were contacted with 200 mL of a 0.5 M HCl solution and agitated on the horizontal mechanical shaker at 250 rpm for 6 h. Subsequently, the PSMI resin beads now in the protonated salt form (Scheme 3.1) were thoroughly washed with deionized H_2O (×3) and dried in a vacuum oven at 60 °C for 6 h. The conditioned PSMI resin beads were then allowed to stand overnight at room temperature in the fume cupboard. The amount of $[AuCl_4]^-$ ions immobilized on the PSMI resin beads were calculated based on the difference of the gold concentration in aqueous solution before and after extraction, the volume of the aqueous solution (10 mL) and the weight of the PSMI resin beads used (30 ± 0.2 mg) according to Equation 3.4. The percentage extraction and desorption was calculated by using Equations 3.5 and 3.6, respectively.

In addition to the batch sorption experiments, fixed-bed sorption or column loading experiments were also carried out to test for the continuous loading of $[AuCl_4]^-$ ions by the PSMI resin beads from a feed solution. A typical column loading experiment was as follows: Approximately 1 g of the dry pre-conditioned 450 µm PSMI resin beads were tightly packed in a designed Teflon column (10 cm length and 1 cm internal diameter) connected at one end to a peristaltic pump (Perimax 12, Spetec) through 1 mm diameter tubing and at the other end to a UV-Vis flow cell. Prior to the $[AuCl_4]^-$ loading tests, the PSMI resin bed was allowed to thoroughly wet by flowing 2 M HCl solution through the packed column at a flow rate of 0.5 mL/min for 2 h and then at a flow rate of 0.3 mL/min for a further 3 h. Subsequently, a 2 M HCl $[AuCl_4]^-$ feed solution was pumped through the packed column at a flow rate of 0.3 mL/min and the $[AuCl_4]^-$ loading process monitored by continuously recording the UV-Vis absorbance of the down flow solution (supernatant) at a wavelength of 391 nm. The acquisition time between each absorbance reading

was 300 s for 24 h. After the successful loading of gold ions, presumably in the form of $[AuCl_4]^-$, the gold-loaded PSMI resin bed was washed to remove any $[AuCl_4]^-$ ions that may be present in the interstitial voids of the packed column and not retained by the protonated sites of the PSMI resin beads. This was done by pumping deionized H_2O through the column at a flow rate of 0.3 mL/min for 8 h. Directly after this rinsing procedure, elution was initiated by pumping an elutant solution consisting of 10 M HNO_3/0.5 M HCl through the gold-loaded PSMI resin column bed at a flow rate of 0.3 mL/min until elution was completed. The elution process was monitored by continuously recording the UV-Vis absorbance of the down flow solution (aqueous eluate) at a wavelength of 391 nm. The 10 M HNO_3/0.5 M HCl solution was chosen as elutant as it has shown significant promise in batch desorption experiments. A schematic representation of the fixed-bed column system set-up used for the preconcentration of $[AuCl_4]^-$ ions from aqueous acidic solution is shown in Figure 5.1.

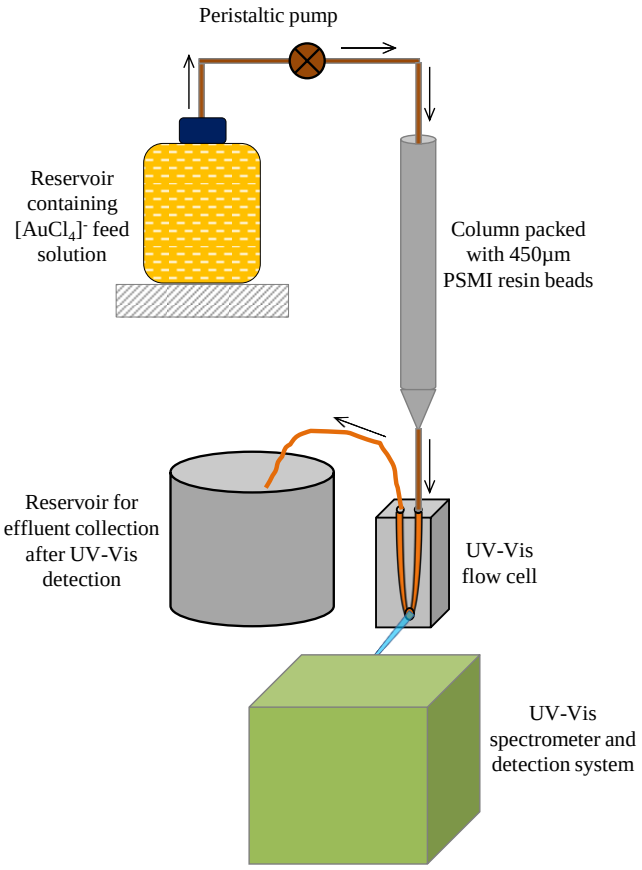

Figure 5.1 Fixed-bed column set-up used for the preconcentration of $[AuCl_4]^-$ ions from a gold feed solution in a continuous process. Teflon column dimensions: 10 cm length, 1 cm internal diameter. (Note: Picture not drawn to scale).

5.3 Results and discussion

5.3.1 Effect of contact time on the uptake of $[AuCl_4]^-$ ions by the PSMI resin beads

For practical applications, the sorption kinetics is very important. [16] The residence time of a sorbate at the solid-solution interface controls the kinetics of uptake. [17] The rate of the sorption process can be influenced by a number of factors as described in section 1.5.5, Chapter 1. To examine the contact time required for $[AuCl_4]^-$ to reach the equilibrium loading state, time-dependent experiments were carried out using approximately 30 mg of the 450 µm and 1620 µm PSMI resin beads for three different gold concentrations in 2 M HCl solutions. The effect of contact time on the uptake of $[AuCl_4]^-$ are shown in Figures 5.2 (a) and (b) for the 450 µm and 1620 µm PSMI resin beads, respectively. As expected, the results in Figures 5.2 (a) and (b) indicate that with an increase in contact time there is an increase in the extent of $[AuCl_4]^-$ uptake as equilibrium loading is approached. Interestingly, for both the 450 µm and 1620 µm PSMI resin beads, the rate of $[AuCl_4]^-$ uptake is fast for the first 5 – 10 minutes as evidenced by the steep slope in this time interval range. This observation would suggest that the uptake is by means of an anion-exchange mechanism between $[AuCl_4]^-$ ions and the protonated sites on the surface of the PSMI resin beads (Equation 3.3, Chapter 3). For contact times exceeding 10 minutes, the uptake of $[AuCl_4]^-$ increases steadily but at a relatively slower rate as compared to the initial stages. This may be due to $[AuCl_4]^-$ ions diffusion through the PSMI resin beads to reach the protonated sites located inside the micro-porous channels, since it is believed that the available protonated sites on the surface of the beads have already been occupied in the first 10 minutes. Hence, diffusion of $[AuCl_4]^-$ ions results in the slower rate of uptake.

For the 450 µm PSMI resin beads, maximum gold loading capacities of about 17.0, 54.3 and 112.9 mg/g were attained for the 51, 170 and 401 mg/L gold concentrations in the $[AuCl_4]^-$ feed solutions, respectively. For the 1620 µm PSMI resin beads, maximum gold loading capacities of about 18.9, 47.8 and 91.4 mg/g were attained for the 57, 169 and 395 mg/L gold concentrations in the $[AuCl_4]^-$ feed solutions, respectively. Comparatively, the rate at which $[AuCl_4]^-$ is taken-up by the 450 µm PSMI resin beads appears to be slightly faster than that of the 1620 µm PSMI resin beads. This can most probably be attributed to the slight difference in the specific surface

areas and the accessibility of the protonated functional groups on the surface and within the porous channels of the respective physically different PSMI resin bead diameters. It was established that the 450 µm and 1620 µm PSMI resin beads have modest specific surface areas of about 2.8 ± 0.4 m^2/g and 2.0 ± 0.1 m^2/g, respectively (Table 4.3, Chapter 4).

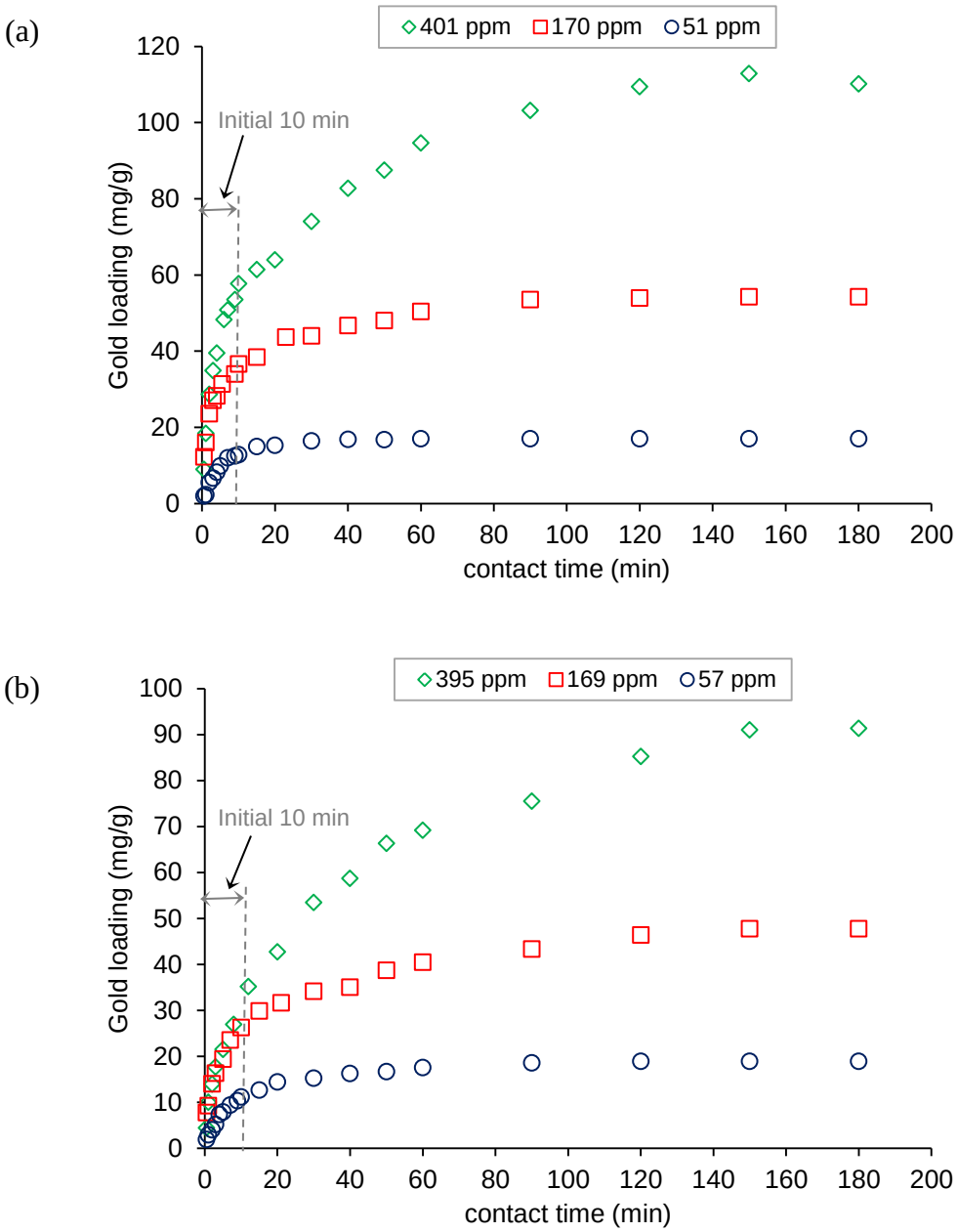

Figure 5.2 Effect of contact time on the uptake of $[AuCl_4]^-$ from 2 M HCl solution using (a) 450 µm and (b) 1620 µm PSMI resin beads. Experimental conditions – PSMI masses: 30 ± 0.2 mg; Total aqueous phase: 10 mL; Agitation rate: 250 rpm; Temperature: 23 ± 1 °C.

5.3.2 Loading capacity of PSMI resin beads for $[AuCl_4]^-$ ions

As was done in Chapter 3 with the PSMI nanoparticles, it was important to determine the maximum loading capacity of the PSMI resin beads for $[AuCl_4]^-$ ions since the total number of available protonated nitrogen sites for ion-exchange to occur is unknown for these novel materials. This was done by determining the amount of $[AuCl_4]^-$ ions taken-up by the 450 µm and 1620 µm PSMI resin beads at equilibrium for varying initial gold concentrations in solution in the range of 0 – 600 mg/L, while maintaining the PSMI resin aliquots at a constant mass of 30 ± 0.2 mg per 10 mL of the $[AuCl_4]^-$ feed solution. A prolonged contact time of 6 h was employed during the batch sorption experiments to ensure that equilibrium is attained. Figure 5.3 illustrates the relationship between the gold concentration initially present in solution, C_e, and the equilibrium gold loading capacity, q_e for the 450 µm and 1620 µm PSMI resin beads. It should be pointed out that the solid lines that connect the data points in Figure 5.3 are for better illustration of the gold loading trends and are not model fits to the experimental data.

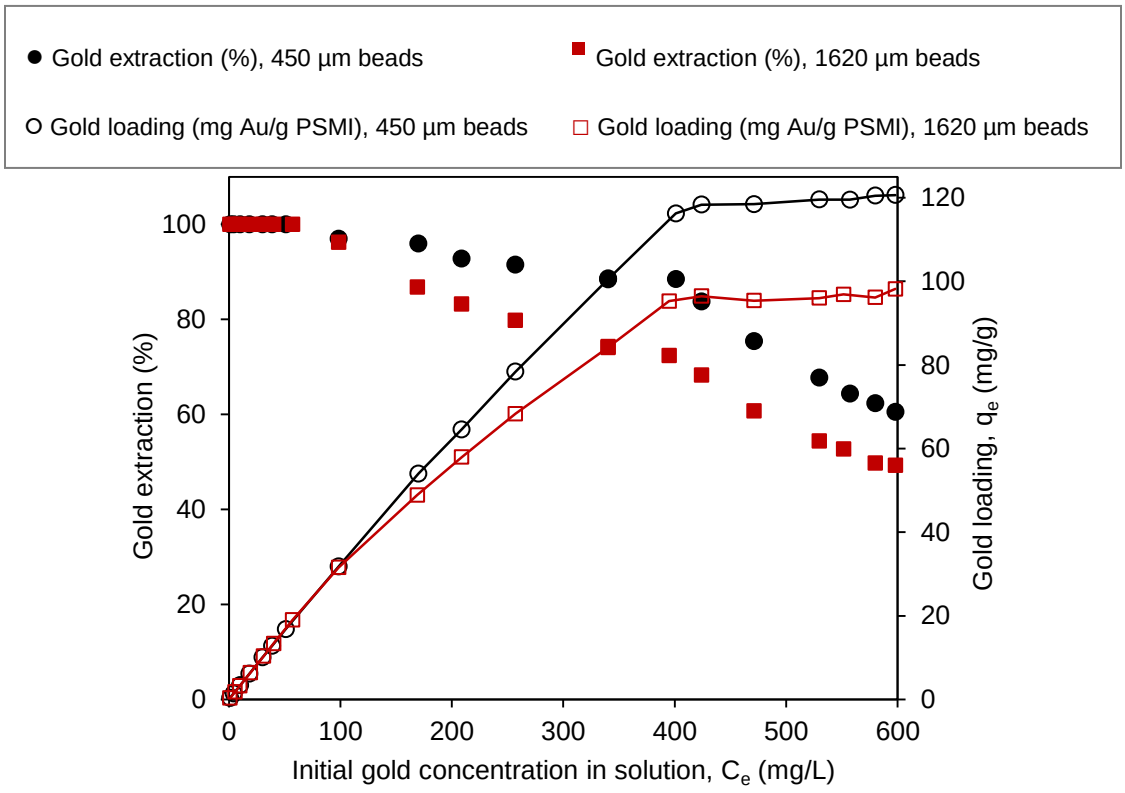

Figure 5.3 Effect of initial gold concentration in solution on the equilibrium gold loading capacity. Experimental conditions – PSMI resin beads mass: 30 ± 0.2 mg; Total aqueous phase: 10 mL; Contact time: 6 h; Agitation rate: 250 rpm, Temperature: 23 ± 1 °C.

From Figure 5.3, it is clear that the gold loading capacity increases as the initial gold concentration in solution is increased up to a point where saturation is approached. For the studied gold concentration range, the maximum gold loading capacity, q_{max} was found to be 120.7 mg/g and 98.2 mg/g for the 450 µm and 1620 µm PSMI resin beads, respectively. Interestingly, the gold loading capacity for the 450 µm PSMI resin beads at a gold concentration of about 401 mg/L was found to be 116.2 mg/g. Likewise, the gold loading capacity for the 1620 µm PSMI resin beads at a gold concentration of about 395 mg/L was found to be 95.3 mg/g. These gold loading capacity values obtained from Figure 5.3 correspond reasonably well with those obtained after 3 h from the time-dependant study at similar gold concentrations which were 112.9 mg/g and 91.4 mg/g for the 450 µm and 1620 µm PSMI resin beads, respectively (Figure 5.2). The slight discrepancy in the comparative gold loading capacity values for the physically different diameter PSMI resin beads in the two independent studies can be attributed to:

1) In the case of the time-dependence study (Figure 5.2), equilibrium gold loading capacity was not completely reached after 3 h of contact time between the available protonated sites of the PSMI resin beads and the $[AuCl_4]^-$ ions initially in the feed solution.
2) In the equilibrium sorption study (Figure 5.3), it seems as if more diffusion of $[AuCl_4]^-$ ions into the PSMI resin beads have occurred due to the longer contact time of 6 h that were used during batch sorption; hence $[AuCl_4]^-$ ions reaching possible protonated ion-exchange sites located in the internal microporous structure of the PSMI resin beads and thus allowing equilibrium gold loading to be attained.

Figure 5.3 also shows the corresponding $[AuCl_4]^-$ extraction efficiency for each of the gold concentrations initially in solution. For both the different diameter PSMI resin beads, it can be estimated that quantitative extraction occurs rapidly between the gold concentration ranges of about 1 – 60 mg/L for the 30 mg PSMI masses per 10 mL feed solution, which is consistent with ion-pairing formation. The $[AuCl_4]^-$ extraction efficiency decreases as the gold concentration in solution is further raised (> 60 mg/L). This is attributed to the fact that more $[AuCl_4]^-$ ions are predominantly in solution than available protonated ion-exchange sites with an increase in the gold concentration.

The Langmuir and Freundlich isotherm models, expressed by Equations 1.5 and 1.7 (Chapter 1) have been fitted to the gold loading data in Figure 5.3. The corresponding Langmuir and

Freundlich parameters along with the coefficients of correlation are shown in Tables 5.1 and 5.2 for the 450 µm and 1620 µm PSMI resin beads, respectively. The model fits associated with the gold loading data is shown in Figure s5.1 and Figure s5.2 (*see* supplementary section).

Table 5.1 Langmuir and Freundlich parameters for the sorption of $[AuCl_4]^-$ by the 450 µm beads.

Langmuir model		Freundlich model	
q_{max} (mg/g)	357.1	k_F (L/mmol)	0.39
k_L (L/mg)	1.0×10^{-3}	n	1.07
R^2	0.847	R^2	0.9948

Table 5.2 Langmuir and Freundlich parameters for the sorption of $[AuCl_4]^-$ by the 1620 µm beads.

Langmuir model		Freundlich model	
q_{max} (mmol/g)	204.1	k_F (L/mmol)	0.24
k_L (L/mmol)	1.8×10^{-3}	n	1.13
R^2	0.9397	R^2	0.9902

According to the coefficients of correlation and the model fits, the Langmuir model is less adequate for modeling the sorption of $[AuCl_4]^-$ ions by the PSMI resin beads. In contrast, the Freundlich model represents a good fit of the experimental data and, therefore is adequate for modeling the sorption isotherm. In general, the Freundlich model assumes the sorption on a heterogeneous (multi-layer) surface with uniform energy, but never predicts saturation of the sorbent surface sites. Therefore, infinite surface coverage is predicted mathematically.

5.3.3 Desorption studies

Exhaustive desorption experiments have been conducted to identify appropriate elutants for the desorption of the assumed immobilized $[AuCl_4]^-$ ions from the 450 µm PSMI resin beads. In all cases, gold loading capacities of about 28.3 mg gold per gram of the 450 µm PSMI resin beads were used in the desorption tests. As was done in Chapter 3 prior to desorption, the gold-loaded PSMI resin beads were washed with deionized H_2O (×3) to remove any 'unbound' $[AuCl_4]^-$ ions and possible as Cl^- ions. An extended desorption contact time of 24 h was used to ensure that the maximum amount of gold ions could be eluted from the gold-loaded PSMI resin beads. Various elutants investigated and their effectiveness expressed in terms of percentage desorption are summarized in Table 5.3.

Table 5.3 Desorption of immobilized gold species from the gold-loaded 450 µm PSMI resin beads for different elutants. Experimental conditions – PSMI resin beads mass: 30 ± 0.2 mg; Total aqueous phase: 10 mL; Contact time: 24 h; Agitation rate: 250 rpm, Temperature: 23 ± 1 °C.

Elutant	Desorption (%)
0.5 M HCl	0.7 ± 0.1
6 M HCl	2.9 ± 0.6
0.05 M thiourea / 2 M HCl	80.4 ± 2.4
0.5 M HNO_3 / 0.5 M HCl	1.1 ± 0.6
6 M HNO_3 / 0.5 M HCl	32.8 ± 3.0
10 M HNO_3 / 0.5 M HCl	96.8 ± 1.3
0.025 M NaOH/0.01 M NaCN	26.2 ± 7.0

For the elutants as shown in Table 5.3, insignificant quantities of gold were eluted from the gold-loaded PSMI resin beads with the exception of the acidified thiourea solution (0.05 M thiourea/2 M HCl) with desorption efficiency of about 80 % and also the mixture of nitric acid/hydrochloric acid solution (10 M HNO_3/0.5 M HCl) with an excellent desorption efficiency of about 97 %. As was the case with the PSMI nanoparticles (Chapter 3), it would appear that additional processes

other than only 'simple' anion-exchange are also involved in the $[AuCl_4]^-$ sorption by the PSMI resin beads. Similar to the possible phenomena proposed in Chapter 3, in this study the poor desorption efficiencies of the assumed immobilized $[AuCl_4]^-$ from the PSMI resin beads using elutants other than acidified thiourea and 10 M HNO_3/0.5 M HCl may be due to:

1) Strong electrostatic interaction between protonated sites of the PSMI resin beads and the $[AuCl_4]^-$ ions in the feed solution, i.e. ion-pair formation [18] (Equation 3.3, Chapter 3)
2) Possible reduction of Au^{3+} ions to Au^+ species and Au^0 on the surface and in the micropores of the PSMI resin beads after initial $[AuCl_4]^-$ immobilization by ion-pair formation. As discussed in section 1.7 of Chapter 1, the reduction potentials associated with the $[AuCl_4]^-/Au^0$, $[AuCl_4]^-/[AuCl_2]^-$ and $[AuCl_2]^-/Au^0$ half reactions are relatively high, indicating the relative ease for possible reduction to occur. [19]
3) Coordination of the Au^{3+}/Au^+ atoms of the respective gold chlorido-complexes to non-protonated nitrogen atoms of the PSMI resin beads (Equation 3.1, Chapter 3).

The excellent desorption efficiency obtained by using the 10 M HNO_3/0.5 M HCl solution as elutant can be ascribed to the strong oxidizing potential of HNO_3, since it is known that aqua regia (HNO_3/HCl) readily dissolves elemental gold to form $[AuCl_4]^-$ ions. [20] Moreover, in this study, desorption using other elutant solutions such as 0.028 M NH_4OH, 0.5 M $NaHCO_3$ and 0.025 M NaOH were also investigated (result not shown). It was established that less than 0.2 % of the immobilized gold species could be eluted from the gold-loaded PSMI resin beads using these elutants.

5.3.4 Successive extraction and desorption

The 450 µm PSMI resin beads were tested for their re-usability in continuous extraction and desorption cycles. Shown in Figure 5.4 is the three stage extraction × two stage washing × three stage desorption profiles using 30 mg of the PSMI resin beads and a $[AuCl_4]^-$ feed solution with a gold concentration of 84 mg/L. The extraction was performed from this feed solution composed of 2 M HCl and 0.5 M ClO_3^- ions. The successive desorption was done using an acidified thiourea solution containing 0.1 M ClO_3^- ions (0.05 M thiourea/2M HCl/0.1 M ClO_3^-) as elutant. The presence of the ClO_3^- ions in the feed and elutant solutions which acts as a mild

oxidizing agent were employed for the prevention of any possible reduction of the $[AuCl_4]^-$ ions that might hamper the desorption and thus the consecutive extraction processes in the repeated cycles. Although excellent desorption efficiencies were obtained using 10 M HNO_3/0.5 M HCl solution (*see* Table 5.3), acidified thiourea solution was used as elutant since it is milder than the mentioned acid mixture solution and is more practical.

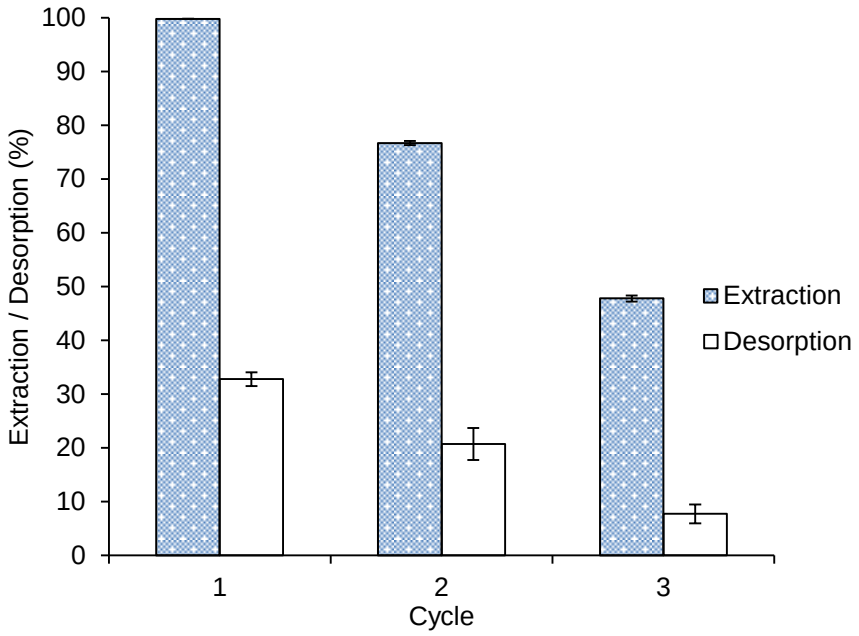

Figure 5.4 Continuous three stage extraction × two stage wash × three stage desorption cycles. Extraction performed from a 2 M HCl/0.5 M ClO_3^- solution and desorption using a 0.05 M thiourea/2 M HCl/0.1 M ClO_3^- elutant solution. Experimental conditions – PSMI resin beads mass: 30 ± 0.2 mg; Gold concentration in feed solution: 84 mg/L; Total aqueous phase: 10 mL; Extraction contact time: 60 min; Desorption contact time: 24 h; Agitation rate: 250 rpm, Temperature: 23 ± 1 °C.

As can be seen from Figure 5.4, the extent of extraction and desorption decreased considerably over the three consecutive cycles. In particular, the poor desorption efficiencies most likely contributed significantly in the observed trends in the second and third cycles of extraction.

As discussed in Chapter 3, the decreased desorption in the three stages may also be attributed to the presence of ClO_3^- ions in the elutant solution, probably impeding with the transformation of auric (Au^{3+}) into aurous (Au^+) ion by thiourea and thus inhibiting the formation of the stable gold(I) – thiourea complexes, ($Au(SC(NH_2)_2)_2^+$) (Equation 3.8, Chapter 3). Another plausible

explanation could be that the oxidizing potential of the ClO_3^- ions in the elutant solution cause the destruction of the thiourea itself resulting in the inefficient desorption ability of the elutant.

In order to test and verify the influence of the ClO_3^- ions in the elutant solution, desorption experiments were conducted using an acidified thiourea solution without any chlorate ions. In contrast to the results in Figure 5.4, as shown in Figure 5.5, when performing the extraction of $[AuCl_4]^-$ from a 2 M HCl feed solution containing 0.5 M ClO_3^- ions and the subsequent desorption using 0.05 M thiourea/2M HCl (no chlorates present in the elutant solution), a significant improvement in both the extent of extraction and desorption are found over the three respective cycles. As shown in Figure 5.5, the increased desorption efficiency over the three stages resulted in an enhancement in the extractions in the successive cycles probably due to the fact that more protonated sites are made available for ion-exchange to occur. This result indicates that the PSMI resin beads have good durability as well as good efficiency for repeated use.

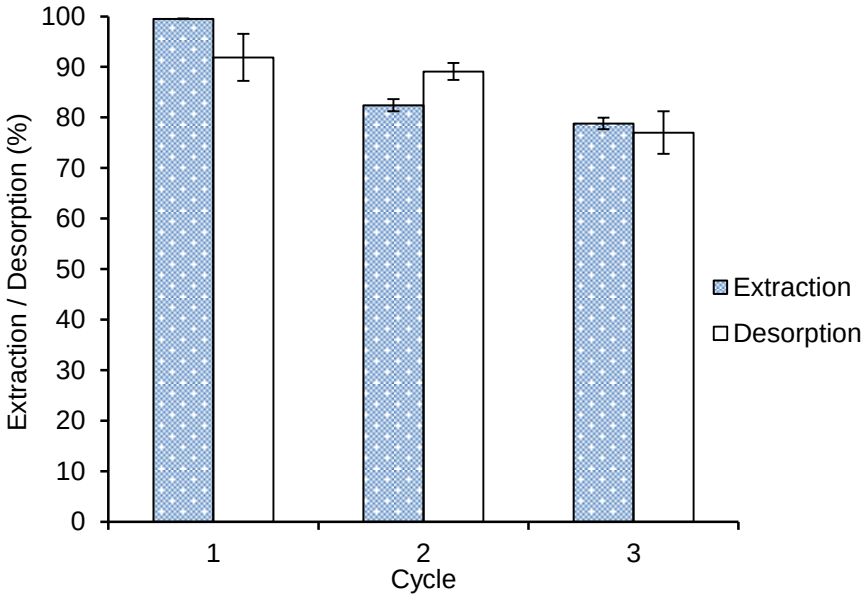

Figure 5.5 Continuous three stage extraction × two stage wash × three stage desorption cycles. Extraction performed from a 2 M HCl/0.5 M ClO_3^- solution and desorption using a 0.05 M thiourea/2 M HCl elutant solution. Experimental conditions – PSMI resin beads mass: 30 ± 0.2 mg; Gold concentration in feed solution: 65.9 mg/L; Total aqueous phases: 10 mL; Extraction contact time: 60 min; Desorption contact time: 24 h; Agitation rate: 250 rpm, Temperature: 23 ± 1 °C.

5.3.5 Comparison between PSMI resin beads and PSMI nanoparticles used for $[AuCl_4]^-$ uptake

Table 5.4 shows correlation between the anion-exchange PSMI particles of different diameters investigated in Chapter 3 and in the present work for the uptake of $[AuCl_4]^-$ ions.

Table 5.4 Comparison between the PSMI nanoparticles and the 450 µm/1620 µm PSMI resin beads

Anion-exchange material	Average diameter	BET surface area	Maximum gold loading capacity
PSMI nanoparticles	50 ± 5 nm	88.1 ± 2.2 m^2/g	541.7 mg/g ǂ
PSMI resin beads	450 ± 30 µm	2.8 ± 0.4 m^2/g	120.7 mg/g
PSMI resin beads	1620 ± 200 µm	2.0 ± 0.1 m^2/g	98.2 mg/g

ǂNote: Equilibrium loading capacity predicted by the Langmuir model.

From the time-dependent studies it was observed that the rate of $[AuCl_4]^-$ uptake using the PSMI nanoparticles was much faster than the PSMI resin bead counterparts. This is most probably related in part to the much larger surface area-to-volume ratio offered by the nanoparticles suspended in the gold feed solutions during batch sorption (Table 5.4). Another important factor that may have contributed to the relative differences in the $[AuCl_4]^-$ uptake kinetics is the degree of porosity. Although the bulk PSMI nanoparticles in dry powder form exhibit textural porosity due to the packing density, the individual nanoparticles are believed to be dense and non-porous. In contrast, the 450 µm and 1620 µm PSMI resin beads were found to be microporous (Figure 4.9, Chapter 4). The degree of porosity has a significant effect on the rate of uptake; diffusion of $[AuCl_4]^-$ ions through the PSMI resin beads to reach the protonated sites located inside the microporous channels results in a slower rate of uptake kinetics as compared to the faster rate observed for the non-porous PSMI nanoparticles. The PSMI nanoparticles have a higher concentration of available protonated sites on their surface than the PSMI resin beads for ion-exchange to occur more readily.

As can be seen from Table 5.4, the maximum gold loading capacity of the PSMI nanoparticles are much larger than the 450 µm and 1620 µm PSMI resin beads. It should be pointed out the gold loading capacity given in Table 5.4 for the 50 nm diameter PSMI nanoparticles is that predicted by the Langmuir model. The maximum gold loading capacity obtained experimentally

from the sorption study was 346.7 mg/g (Figure 3.2, Chapter 3). This is attributed to the fact that within the studied initial gold concentration range, complete saturation of all the available protonated sites for ion-exchange has not occurred, i.e. equilibrium gold loading has not been reached. In the case of the sorption studies for the PSMI resin beads, it appears as if equilibrium has been attained. The maximum gold loading capacities for the bulk PSMI nanoparticles are compatible with commercial ion-exchange resins which have loading capacities in the range of 2.5 – 5 mmol/g (492 – 985 mg/g). [12,13]

Desorption of the immobilized gold from the gold-loaded PSMI nanoparticles as well as from the PSMI resin beads proved to be more difficult than initially expected. Interestingly, only elutant solutions of acidified thiourea and 10 M HNO_3/0.5 M HCl were effective in eluting significant quantities of the immobilized gold.

The results show that both the PSMI nanoparticles and the PSMI resin beads can be used for the uptake and preconcentration of $[AuCl_4]^-$ with above average gold loading capacities. The immobilized gold species can be successfully recovered from the loaded PSMI materials by improvised, yet simple desorption methods.

5.3.6 Assessment of $[AuCl_4]^-$ extraction selectivity from a mixed-metal PGM solution

As mentioned in Chapter 1, $[AuCl_4]^-$ is present in industrial process effluents and acidic waste liquors generated by gold recycling such as for example, from electronic scrap materials or electroplating solutions. These solutions often contain PGM metal ions as well as base metal ions. In principle, the extraction and separation of $[AuCl_4]^-$ from the base metals are easily achieved due to the fact that base metals such as Zn^{2+}, Co^{2+} and Ni^{2+} readily form cationic species of the form $[M(H_2O)_6]^{2+}$ (where M is the base metal ion) in aqueous solution. [21,22] Therefore, anion-exchange resins could easily be applied for the selective extraction and separation of $[AuCl_4]^-$ from the dissolved base metal ions. The challenge, however, is to be able to selectively separate $[AuCl_4]^-$ from the PGM metal ions which readily form anionic chlorido-complexes of the form $[MCl_x]^{n-x}$ in acidic solutions (where x is the number of chloride ligands bound to the metal center and n is the oxidation state of the metal ion). These PGM metal complexes will often compete with the metal of interest for binding sites or lower the specificity

of the ion-exchange material by binding to sites which the metal ions of interest do not bind. Industrially (Scheme 1.2), the separation of $[AuCl_4]^-$ from the PGMs and silver is achieved by a solvent extraction process, which has numerous disadvantages. Also mentioned in Chapter 1, is that some anion-exchange materials often have difficulty in discriminating between the various anionic precious metal chlorido-complexes and in this regard is an area of intense research.

In this study, the efficiency and selectivity of $[AuCl_4]^-$ extraction from acidic solution in the presence of PGMs was investigated by conducting batch sorption experiments using 30 ± 0.2 mg 450 µm PSMI resin beads and a contact time of 24 hours. The synthetic precious metal feed solution containing $[AuCl_4]^-$, $[PdCl_4]^{2-}$, $[PtCl_6]^{2-}$, $[IrCl_6]^{2-}$ and $[RhCl_6]^{3-}$ ions was prepared by dissolving a certain amount of the precious metal salts in 2 M HCl to metal concentrations of 65.9 mg/L, 84.60 mg/L, 77.04 mg/L, 76.50 mg/L and 86.59 mg/L, respectively. The feed solution was allowed to equilibrate for 48 h prior to use. The degree of extraction obtained for each metal chlorido-complex is shown in Figure 5.6.

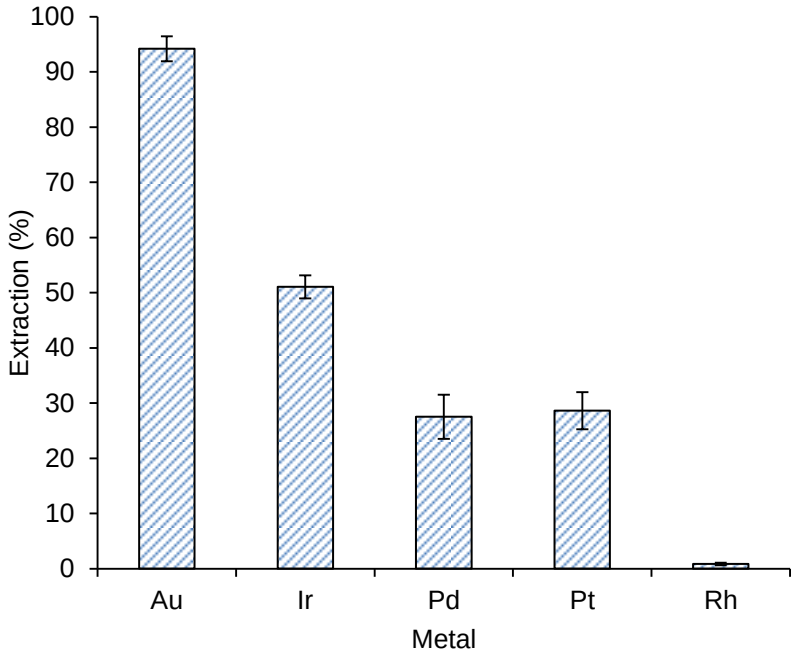

Figure 5.6 Extraction selectivity of $[AuCl_4]^-$ from a mixed-metal PGM solution in 2 M HCl solution. Experimental conditions – PSMI resin beads mass: 30 ± 0.2 mg; Total aqueous phase: 10 mL; Contact time: 24 h; Agitation rate: 250 rpm, Temperature: 23 ± 1 °C.

From Figure 5.6, it is clear that the $[AuCl_4]^-$ ions are most favorably extracted from the mixed-metal solution by the PSMI resin beads. The tendency for the metal chlorido-complexes to form ion pairs with an anion-exchange material, in this particular case the PSMI resin beads, is $[MCl_4]^- > [MCl_6]^{2-} > [MCl_4]^{2-} > [MCl_6]^{3-}$ > aqua species. This order is determined by the charge to size ratio or charge density of the species. Species with low charge density are more easily paired than species with higher charge density. This is a consequence of the size of the hydration shell surrounding the ions; densely charged species having larger hydration shells exhibit lower coulombic interaction with their counterions than those with smaller hydration shells. [23]

The ratio of gold to total metal concentration ([M]) on the loaded PSMI resin beads, which is a measurement of selectivity, is shown in Table 5.5. From Table 5.5 and Figure 5.6 it is clear that the PSMI resin beads are moderately selective for $[AuCl_4]^-$ over the $[IrCl_6]^{2-}$, $[PtCl_6]^{2-}$ and $[PdCl_4]^{2-}$ ions. However, it was found that the PSMI resin beads were highly selective for $[AuCl_4]^-$ over $[RhCl_6]^{3-}$. The reason for the latter observation can most likely be attributed to the fact that $[RhCl_6]^{3-}$ complexes hydrate extensively to form aquated complexes, $[RhCl_{6-n}(H_2O)_n]^{3-n}$ (with n = 0, 1, 2 and 3), even under the acidic solution conditions used in these extraction experiments. [24] The values for the stability constants of Rh(III) and Ru(III) (not present in the synthetic feed solution) chlorido-complexes are much more lower in comparison to those corresponding to the chlorido-complexes of Au(III), Ir(IV), Pt(IV) and Pd(II), and thus, in the case of Rh (and Ru), formation of aqua-complexes are highly probable. [25] The intricate chemistry of rhodium in solution is, therefore, responsible for the poor extraction efficiency of this metal. The extraction is in the order $[AuCl_4]^- >> [IrCl_6]^{2-} > [PtCl_6]^{2-} > [PdCl_4]^{2-} >> [RhCl_6]^{3-}$, which is in accordance to what is expected based on the charge density of the precious metal chlorido-complexes. [23] The results show that the PSMI resin beads have gold loading capacities significantly greater than those of the other co-existing PGM metal complex anions.

Table 5.5 Ratio of gold concentration to precious metal concentration, the extraction efficiency and loading capacity of the 450 µm PSMI resin beads for the various anionic precious metal complexes.

Metal complex ion	Extraction (%)	Loading capacity (mg/g)	$\frac{[Au]}{[M]}$
$[AuCl_4]^-$	94.18 ± 1.25	39.12 ± 0.52	0.580 ± 0.008
$[IrCl_6]^{2-}$	51.03 ± 2.09	13.01 ± 0.53	0.193 ± 0.008
$[PdCl_4]^{2-}$	27.53 ± 4.01	7.76 ± 1.13	0.115 ± 0.017
$[PtCl_6]^{2-}$	28.65 ± 3.36	7.36 ± 0.86	0.109 ± 0.013
$[RhCl_6]^{3-}$	0.83 ± 0.23	0.24 ± 0.07	0.004 ± 0.001

‡ [M] represents the total precious metal (Au, Ir, Pd, Pt, Rh) concentration in the feed solution

5.3.7 Preliminary study of $[AuCl_4]^-$ ions preconcentration using a packed bed column method

From the batch sorption tests it was established that the 450 µm and 1620 µm PSMI resin beads are good anion-exchange materials for the extraction $[AuCl_4]^-$ ions from acidic solutions based on their high affinity and high loading capacity. From a practical point of view, it was of interest to investigate the potential of the PSMI resin beads for the preconcentration of $[AuCl_4]^-$ ions in a continuous process, since precious metal complexes such as gold in this context are industrially often separated from solutions using column-type preconcentration methods. The packed bed column set-up used in this study is shown in Figure 5.1 (*see* section 5.2 for experimental details). The column was efficiently packed with a resin bed consisting of 1.02 g 450 µm pre-conditioned PSMI beads. The gold concentration in the 2 M HCl $[AuCl_4]^-$ feed solution pumped through the column was *ca* 250 mg/L. The loading of the $[AuCl_4]^-$ ions and the subsequent elution profiles are shown in Figure 5.7.

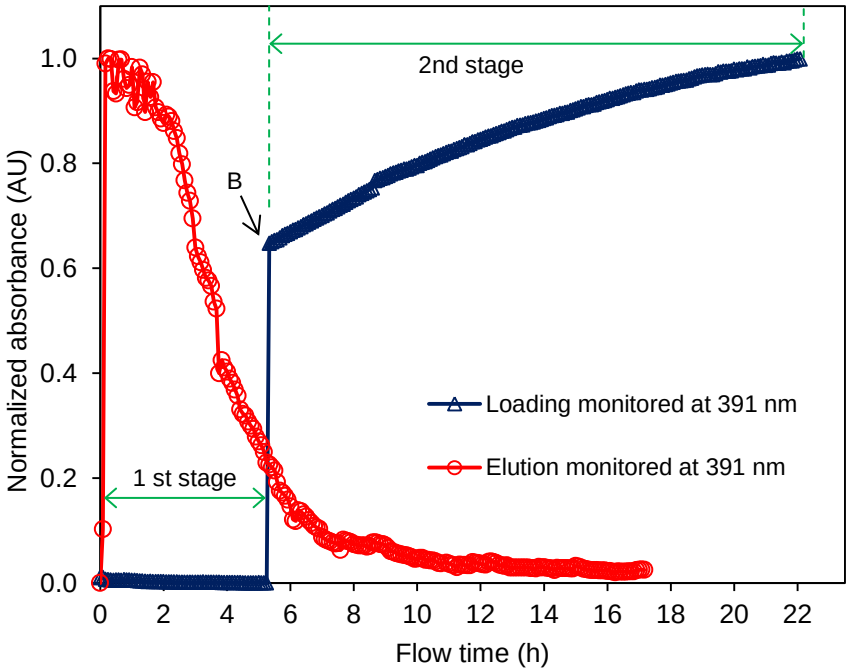

Figure 5.7 Breakthrough and elution curves for $[AuCl_4]^-$ ions using 450 µm PSMI resin beads packed in a column (10 cm length × 1 cm internal diameter). Experimental conditions – Gold concentration: 250 mg/L; PSMI resin mass: 1.02 g; Elutant: 10 M HNO_3/0.5 M HCl; Feed and elutant solution flow rates: 0.3 mL/min; Temperature: 23 ± 1 °C.

As can be seen from Figure 5.7 in the initial stages of the $[AuCl_4]^-$ loading process (0 – 5 h), the down flow/supernatant solution contained no traces of $[AuCl_4]^-$ ions with absorbance values of zero. Therefore, it can be estimated that in the first stage quantitative gold preconcentration has occurred on the PSMI resin bed in the column. This suggest that sufficient interaction occurs between the $[AuCl_4]^-$ ions and the protonated surface sites of the anion-exchange PSMI resin beads as the gold feed solution percolates through the packed column. As indicated in Figure 5.7 at point B, an instantaneous breakthrough is attained after about 5 h, indicating that all the available protonated surface sites on the PSMI resin beads are occupied.

In the second stage of the $[AuCl_4]^-$ loading process, an appreciable amount of $[AuCl_4]^-$ ions passed through the packed PSMI resin bed in the column as indicated by the higher concentrations of gold in the down flow solution with the increase in flow time. In this stage (5 – 22 h), there is a relatively slow increase in the $[AuCl_4]^-$ loading onto the PSMI resin beads packed in the column as saturation is approached. This observed trend may be attributed to:

1) slow diffusion of $[AuCl_4]^-$ ions through the micropores of the PSMI resin beads to reach the protonated sites located in the internal structure of the beads,
2) a change in the molar extinction coefficient of the $[AuCl_4]^-$ ions present in the down flow solution as a result of a possible reduction phenomenon on the surface or in the pores of the PSMI resin beads as the gold feed solution percolates through the packed column.

Clearly, complete saturation of all the available protonated anion-exchange sites has not been reached after about 22 h, indicated that the PSMI resin beads packed in the column have a fairly high loading capacity for $[AuCl_4]^-$ ions in solution.

Following the $[AuCl_4]^-$ loading process, the gold-loaded PSMI resin bed was immediately flushed with deionized water to remove $[AuCl_4]^-$ ions not retained on the packed column. Subsequently, a solution of 10 M HNO_3/0.5 M HCl was pumped through the packed bed to elute the preconcentrated gold from the loaded PSMI resin beads. The corresponding elution profile is also shown in Figure 5.7. The 10 M HNO_3/0.5 M HCl solution is an excellent elutant for the gold loaded onto the PSMI resin beads since it has the ability to solubilize elemental gold or any other possible gold species in reduced oxidation states to form $[AuCl_4]^-$ ions; hence resulting in a good elution process. As can be seen from Figure 5.7, the elution profile is accompanied by a decline in the absorbance indicative of elution of the loaded gold species as $[AuCl_4]^-$ ions. After 16 h almost no $[AuCl_4]^-$ ions were detected in the down flow solution signifying successful and complete elution. This result indicates that the 450 µm PSMI resin beads packed in a column can be used for the preconcentration of $[AuCl_4]^-$ from aqueous acidic solutions in a continuous process and the loaded gold species can be readily recovered by elution.

5.4 Conclusions

The 450 µm and 1620 µm PSMI resin beads demonstrated excellent capability towards the uptake of $[AuCl_4]^-$ ions from aqueous acidic solutions. The rate of uptake was fast within the first 5 – 10 minutes indicating that in this time interval range interaction between $[AuCl_4]^-$ ions in the

feed solution and available protonated nitrogen sites on the surface of the PSMI resin beads occurs until all the sites are occupied. This rapid uptake process is consistent with an anion-exchange mechanism. For contact times exceeding 10 minutes, the rate of uptake is slower which can most probably be attributed to the diffusion of $[AuCl_4]^-$ ions through the microporous PSMI resin beads to reach the available protonated nitrogen sites located inside the microporous channels. Due to the slightly larger specific surface area, larger average pore diameters and thus perhaps better accessibility of available protonated sites for ion-exchange to occur, the 450 µm PSMI resin beads exhibit a relatively faster rate of $[AuCl_4]^-$ uptake than that of the 1620 µm PSMI resin beads. After 3 h of contact time during batch sorption gold loading capacities of 17.0, 54.3, 112.9 mg/g were obtained for 51, 170 and 401 mg/L gold concentrations, respectively using the 450 µm PSMI resin beads. At a similar stage, gold loading capacities of 18.9, 47.8, 91.4 mg/g were obtained for 57, 169 and 395 mg/L gold concentrations, respectively using the 1620 µm PSMI resin beads.

From the equilibrium sorption studies, an increase in the gold loading capacity was observed with an increase in the initial gold concentration in solution. For the 450 µm and 1620 µm PSMI resin beads at gold concentrations of about 400 mg/L, equilibrium appears to have been attained. The equilibrium gold loading capacities were found to be 120.7 and 98.2 mg/g for the 450 µm and 1620 µm PSMI resin beads, respectively. This indicates that the 450 µm PSMI resin beads have a higher concentration of functional groups available for ion-exchange or perhaps coordination to occur.

Desorption of the immobilized gold species from the gold-loaded PSMI resin beads were investigated using various elutants. With the exception of the 0.05 M thiourea/2 M HCl and the 10 M HNO_3/0.5 M HCl solutions, poor desorption efficiencies were obtained indicating that processes other than only ‘simple’ ion-exchange were involved in the uptake of $[AuCl_4]^-$ from solution. The poor to incomplete desorption efficiencies may be attributed to:

1) Strong electrostatic interaction between protonated sites of the PSMI resin beads and the $[AuCl_4]^-$ ions in the feed solution, i.e. strong ion-pair formation.
2) Possible reduction of Au^{3+} ions to Au^+ ions and Au^0 on the surface and in the micropores of the PSMI resin beads after initial $[AuCl_4]^-$ immobilization by ion-pair formation.

3) Coordination of the Au^{3+}/Au^{+} atoms of the respective gold chlorido-complexes to non-protonated nitrogen atoms of the PSMI resin beads.

Desorption of about 80 % was obtained with the 0.05 M thiourea/2 M HCl solution. Since the desorption of immobilized gold species using acidified thiourea is based on the transformation of auric (Au^{3+}) into aurous (Au^{+}) ion by thiourea to form stable gold (I) – thiourea complexes, it can be assumed that 80 % of the immobilized gold species were in Au^{3+}/Au^{+} oxidation states, presumably in a variety of gold chlorido-complexes. The other 20 % gold species that could not be eluted are believed to be in the form of Au^{0}. The best desorption efficiency of about 97 % was obtained using the 10 M HNO_3/0.5 M HCl solution. This was attributed to the strong oxidizing potential of HNO_3 which in the presence of HCl may readily re-oxidize and dissolve immobilized gold species as $[AuCl_4]^-$.

The 450 µm PSMI resin beads could be used in successive extraction and desorption processes indicating that the beads have good durability as well as good efficiency for repeated use. The best results were obtained when performing the $[AuCl_4]^-$ extraction in the presence of ClO_3^- ions and the subsequent desorption using a 0.05 M thiourea/2 M HCl solution without ClO_3^- ions. This suggests that the ClO_3^- ions to some extent inhibit the reduction of $[AuCl_4]^-$ ions which results in good extraction and desorption efficiencies over the 3 consecutive cycles.

The preconcentration of $[AuCl_4]^-$ ions onto a mini-column packed with a bed of 450 µm PSMI resin beads as well as the subsequent elution of the loaded gold illustrate the viability of using the resin in a continuous process.

5.5 Experimental

5.5.1 Materials

High purity deionized water (Milli Q, 18 MΩ cm) was used throughout this work. All other chemicals and reagents including hydrochloric acid (HCl, 37 %) were used without further purification. For the extraction experiments, synthetic feed solutions of gold were prepared from

the $HAuCl_4.xH_2O$ and $NaAuCl_4.2H_2O$ salts in 2M HCl solutions. Similarly, for the mixed-metal extraction experiments, synthetic feed solutions were prepared from the respective precious metal salts.

5.5.2 Instruments and measurements

A horizontal mechanical shaker (Labcon, BR-30L) was used for constant agitation of the feed and elutant solutions with the PSMI resin beads for specified contact times during the experiments. A pH meter (Horiba, F-52) was used for pH measurements. The concentration of metal ions in the effluent (supernatant) and eluate solutions was determined by Inductively Coupled Plasma Optical Emission Spectroscopy (ICP-OES) with a SPECTRO Arcos spectrometer. Standards were matrix matched to acid concentrations of the samples. After calibration and quality check analysis to verify accuracy of standards, samples were analysed. The analytical error in the ICP-OES measurements was found to be 5 %.

5.6 References

1. A.M. Donia, A.A. Atia, K.W. Elwakeel, *Separation and Purification Technology* **2005**, 42, 111.
2. J. Kramer, W.L. Driessen, K.R. Koch, J. Reedijk, *Hydrometallurgy* **2002**, 64, 59.
3. K.F. Lam, K.L. Yeung, G. McKay, *Journal of Physical Chemistry B* **2006**, 110, 2187.
4. D. Jermakowicz-Bartkowiak, B.N. Kolarz, *European Polymer Journal* **2002**, 38, 2239.
5. J.H. Hodgkin, R. Eibi, *Reactive Polymers* **1988**, 9, 285.
6. J.-S. Park, C. Han, J.-Y Lee, S.-D. Kim, J-S. Kim, J.-H. Wee, *Separation and Purification Technology* **2005**, 43, 111.
7. F.J. Alguacil, P. Adera, M. Alonso, *Gold Bulletin* **2005**, 38, 9.
8. E. Latif, D. Sahan, A. Basaran, S. Mustafa, *Environmental Monitoring and Assessment* **2007**, 132, 331.
9. M. Laatikainen, E. Paatero, *Hydrometallurgy* **2005**, 79, 154.

10. E. Latif Elci, S. Mustafa, E.B. Buyuksekerci, *Analytical Sciences* **2003**, 19, 1621.
11. R. Rajasingam, N.S. Jayasinghe, F.P. Lucien, T. Tran, *Minerals Engineering* **2006**, 19, 896.
12. J.A. Kitchener, *Ion-exchange resins*, Methuen, London, **1957**.
13. K. Dorfner, *Ion-exchangers: Properties and Applications*, 2nd Ed., Ann Arbor Science Publishers Inc., Michigan, U.S.A., **1973**.
14. F. De Dardel, T.V. Arden, Ion Exchangers, 5th Ed.; VCH Verlagsgesellschaft mbH: Weinheim, Germany.
15. A. Warshawsky, N. Kahana, B. Kampel, *Macromol. Mater. Eng.* **2000**, 283, 103.
16. S. Azizian, *Journal of Colloid and Interface Science* **2004**, 276, 47.
17. Y.S. Ho, G. McKay, *Chemical Engineering Journal* **1998**, 70, 115.
18. F.J. Alguacil, P. Adera, M. Alonso, *Gold Bulletin* **2005**, 38, 9.
19. A.J. Bard, R. Parsons, J. Jordan (Eds.), *Standard Potentials in Aqueous Solutions*, Marcel Dekker, New York, N.Y., **1985**.
20. P.P. Sheng, T.H. Etsell, *Waste Management and Research* **2007**, 25, 380.
21. L.L. Vatta, J. Kramer, K.R. Koch, *Separation Science and Technology* **2007**, 42, 1985.
22. B. Kar-On Leung, M.J. Hudson, *Solvent Extraction and Ion Exchange* **1992**, 10, 173.
23. F.L. Bernardis, R.A. Grant, D.C. Sherrington, *Reactive and Functional Polymers* **2005**, 65, 205.
24. T.M. Buslaeva, S.A. Simanova, *Russian Journal of Coordination Chemistry* **1999**, 25, 151.
25. E. Hogfeldt, *Stability Constants of Metal-ion Complexes. Part A. Inorganic Ligands*, Pergamon Press Ltd., Headington Hill Hall, Oxford, **1982**.

5.7 Supplementary information

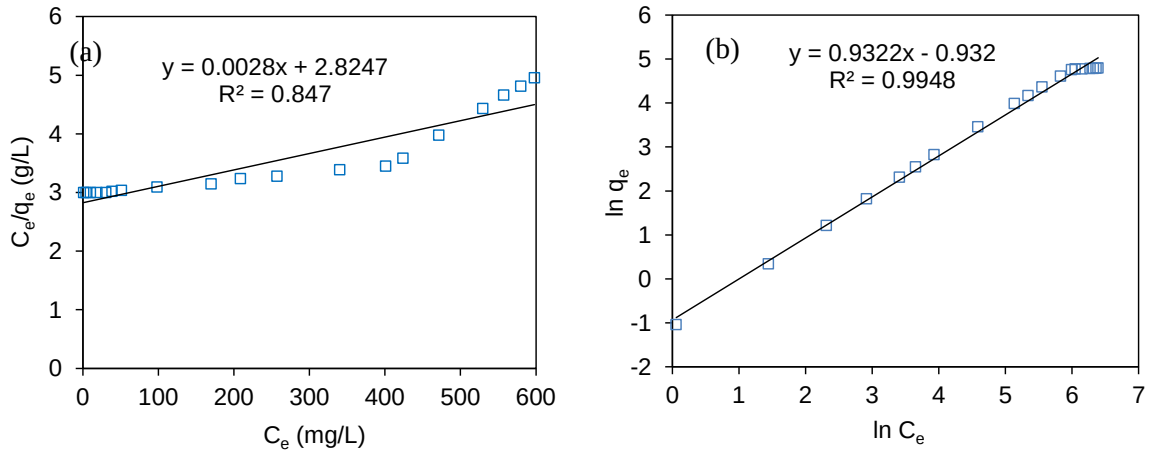

Figure s5.1 Linearized forms of (a) Langmuir and (b) Freundlich model fits for the 450 µm PSMI resin beads.

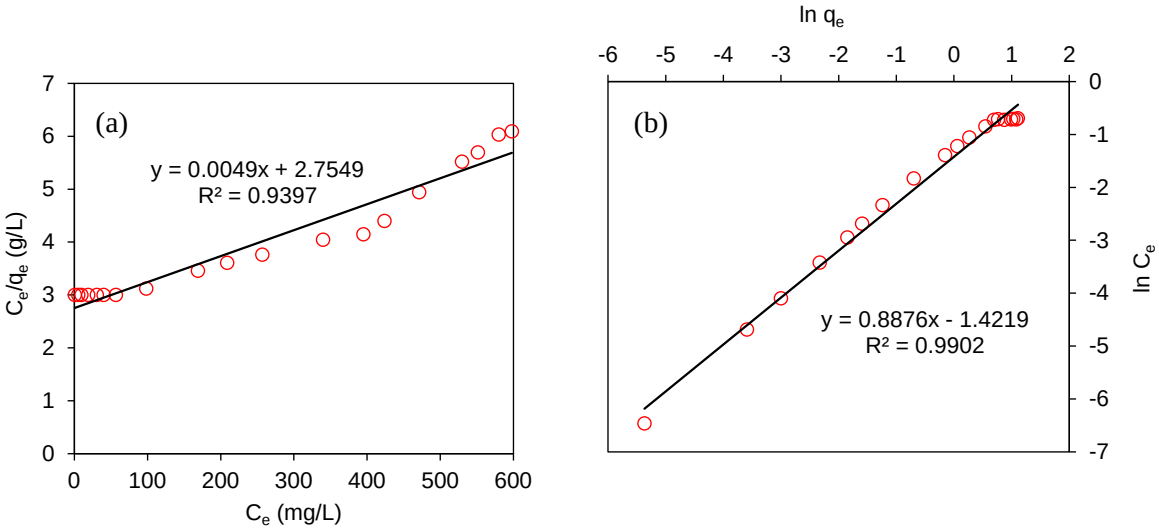

Figure s5.2 Linearized forms of (a) Langmuir and (b) Freundlich model fits for the 1620 µm PSMI resin beads.

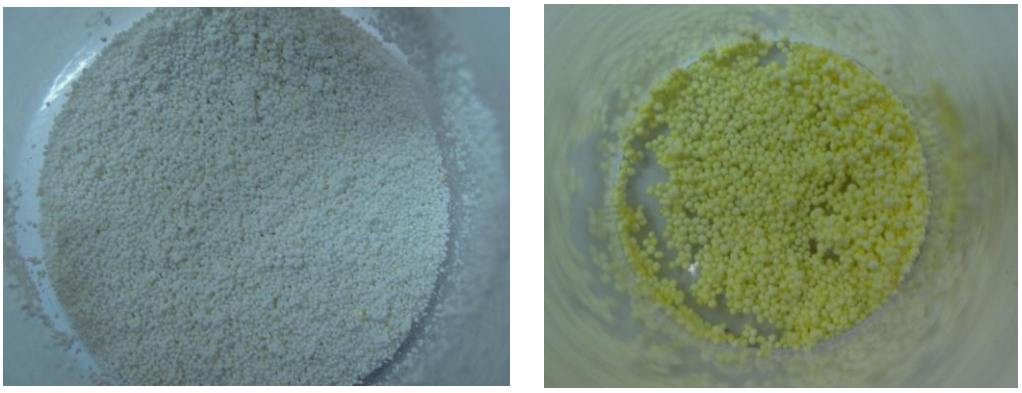

Figure s5.3 Optical microscope picture of the 450 µm PSMI resin beads (a) before and (b) after gold loading.

6 Synthesis and characterization of magnetic poly(styrene-*co*-maleimide) nanoparticles

Synopsis

Magnetically responsive poly(styrene-*co*-maleimide) (PSMI) nanoparticles were prepared by an *in situ* imidization reaction in the presence of oleic acid-coated superparamagnetic magnetite (Fe_3O_4) nanoparticles. The superparamagnetic Fe_3O_4 nanoparticles were prepared by a chemical co-precipitation method with a high degree of crystallinity and phase purity. The Fe_3O_4 nanoparticles coated with oleic acid surfactant molecules were used as seeds for the preparation of the magnetic PSMI nanoparticles. Stable magnetic dispersions containing the oleic acid-coated Fe_3O_4 nanoparticles encapsulated by the PSMI nanoparticles were obtained. TEM analysis confirms that the magnetic PSMI nanoparticles have magnetite core-polymer shell morphology. The average size of the magnetic PSMI nanoparticles is about 50 nm in diameter.

6.1 Introduction

Since their introduction in the mid-1970's, several kinds of magnetic polymer nanoparticles have been produced from both natural and synthetic polymers with the intention to incorporate groups on the surface or to treat their surface to perform, for instance, selective separation. [1] These particles have an ability to interact with various biological molecules in different ways due to high specific surface area and wide choice of surface functionalization. In this regard, magnetic

polymer particles have been increasingly used in the area of biosciences and medicine, in particular for biomolecule/cell separation, targeted drug delivery, protein and enzyme purification, nucleic acid sequencing and medical therapy. [1-4] Such magnetic polymer nanoparticles are often encapsulated by relatively smaller magnetite nanoparticles or clusters thereof due to their low levels of toxicity.

Magnetite (Fe_3O_4) nanoparticles have been well studied and are known in particular to be useful due to their unique magnetic properties. [5] Various synthetic methods have been reported in literature to prepare Fe_3O_4 nanoparticles which include ball milling, [6] chemical co-precipitation, [7] thermal decomposition [8] and mechanical grinding. [9] Among these, chemical co-precipitation may be the most promising one because of its simplicity, productivity and low cost in the production process. Large-scale production using this method is also possible. [10] Magnetite can be readily synthesized by a co-precipitation that is effected by addition of a strong base to an aqueous mixture of Fe^{2+} and Fe^{3+} at a 1:2 molar ratio. [9,11-13] The precipitated Fe_3O_4 is black in colour. The overall chemical reaction may be written as:

$$Fe^{2+} + 2\ Fe^{3+} + 8\ OH^- \rightarrow Fe_3O_4 + 4\ H_2O \qquad (6.1)$$

A complete precipitation of Fe_3O_4 is expected between pH 9 and 14, while maintaining a molar ratio of Fe^{3+}: Fe^{2+} (2:1) under a non-oxidizing oxygen-free environment. Otherwise, Fe_3O_4 might be oxidized to other iron oxides such as for example maghemite (γ- Fe_2O_3) or $Fe(OH)_3$. [5,6] This would critically affect the chemical and physical properties of the nano-sized magnetic particles.

If the size of the Fe_3O_4 nanoparticles is reduced to below a critical size (< 10 nm), they become superparamagnetic. This is a phenomenon where the thermal energy is sufficient to overcome the magnetic coupling forces, causing the magnetic moments to fluctuate randomly. When a magnetic field is applied, the particles acquire a certain magnetization but because of the high thermal energy, the long range order is lost when the field is removed, and the particles have no permanent magnetization. [5,14,15] This essentially means that nanoparticles exhibiting superparamagnetic behaviour could be attracted into an external magnetic field gradient but would retain no residual magnetism after the field is removed.

Magnetic polymer particles have been produced by *in situ* precipitation of magnetic particles in the presence of water soluble polymers that act as surfactants to stabilize the particles. Examples of such polymers that have been used are dextran, [16] poly(vinyl alcohol) (PVA), [17] poly(ethylene glycol) (PEG), [18] sodium poly(oxyalkylene diphosphonates), [19] and amylose starch. [20] In all cases, the magnetic polymer particles thus produced had a hydrophilic outer shell. It is also possible to use a strategy comprising the polymerization in the heterophase in the presence of magnetic particles. The magnetic particles preferably have a surfactant coating to stabilize the particles and are encapsulated into a polymer using processes such as suspension, emulsion or precipitation polymerization. Magnetic particles were encapsulated in hydrophilic polyglutaraldehyde by suspension polymerization resulting in particles with an average diameter of 100 nm. [21] Magnetic nanoparticles of 150 – 200 nm were synthesized by seed precipitation polymerization of methacrylic acid and hydroxylethyl methacrylate in the presence of magnetite particles containing tris(hydroxymethyl)aminomethane hydroxide in ethyl acetate medium. [22] In a paper by Antonietti et al. it was shown that the synthesis of magnetic polymer nanoparticles with magnetic core and polymeric shell is also possible using an emulsion polymerization. Prior to the miniemulsification, the magnetite were hydrophobized by dispersing it in the styrene monomer phase. A mixture of magnetite in styrene was miniemulsified in water and after polymerization, polymer-encapsulated magnetite particles were obtained. [23] Also, polystyrene coating of Fe_3O_4 particles was obtained using a dispersion polymerization method with poly(*N*-vinylpyrrolidone) as stabilizer. In that study, a continuous and dense polymer coating was formed on the Fe_3O_4 particles. [24]

Besides using magnetic polymer particles in biology-related fields, the potential of using such materials in the application to separate or preconcentrate metal species from their solutions has gained interest. Chen et al. have investigated the recovery of gold (III) ions from solutions using a chitosan coated magnetic nano-adsorbent. [25] It was found that the gold (III) ions could be fast and efficiently adsorbed, and the adsorption capacity increased with a decrease in solution pH due to the protonation of the amino groups of the chitosan biopolymer. In another example, Takafuji et al. prepared poly(1-vinylimidazole)-grafted magnetic nanoparticles. [26] The material showed a selective binding of divalent base metal ions. Selective separation of Cu^{2+} ions from a

mixture of Cu^{2+}/Co^{2+} aqueous solution was demonstrated. Numerous other examples of such processes are available in scientific literature.

The basic procedure in a magnetic separation process using magnetic polymer particles would comprise of (i) targeted and selective binding or interaction of metal species of interest in solution with the functional groups of the magnetic polymer particles through coordination or ion-exchange, (ii) separation of the particles from the surrounding solution by application of an external magnetic field, and (iii) recovery of the bound metal species by desorption. The morphology, surface area, surface functionality and the magnetic susceptibility of the functionalized magnetic polymer particles would contribute in a major fashion to the efficiency of the separation process.

In this chapter, work is presented that illustrate the encapsulation of Fe_3O_4 nanoparticles by PSMI nanoparticles to produce a potential magnetic ion-exchange material. In order to obtain the hydrophilic, magnetic PSMI nanoparticles, a three-step strategy is proposed:

1) Synthesis of superparamagnetic Fe_3O_4 nanoparticles.
2) Adsorption or surface coating of the Fe_3O_4 nanoparticles with oleic acid surfactant molecules to stabilize the nanoparticles in solution. The oleic acid-coated Fe_3O_4 nanoparticles are then used as seeds for the synthesis of the magnetic PSMI nanoparticles.
3) *In situ* imidization of PSMI nanoparticles in the presence of oleic acid-coated Fe_3O_4 nanoparticles. This step is intended to encapsulate the oleic acid-coated Fe_3O_4 by the PSMI nanoparticles to obtain magnetite core-polymer shell structures.

Preliminary $[AuCl_4]^-$ extraction from aqueous acidic solutions and the subsequent magnetic separation were tested and show significant promise. However, this will not be discussed as part of this work. During the rest of this chapter, magnetic PSMI nanoparticles will refer to the oleic acid-coated Fe_3O_4 encapsulated by the PSMI nanoparticles.

6.2 Experimental

6.2.1 Materials

Analytical grade ferric chloride hexahydrate ($FeCl_3.6H_2O$, 99 %), ferrous sulphate ($FeSO_4.7H_2O$, 99 %), ammonium hydroxide (NH_4OH, 25 % in H_2O) and 3-*N*,*N*-dimethylaminopropylamine (DMAPA, 99 %) were purchased from Sigma-Aldrich. Poly(styrene-*co*-maleic anhydride) (PSMA) pellets with a weight average molar mass of 80×10^3 g/mol and composition of 26 % maleic anhydride and 74 % styrene in the backbone was donated by Polyscope (Geleen, the Netherlands). Prior to use, the PSMA pellets were dissolved in acetone under mild stirring, subsequently the solvent was allowed to completely evaporate at 50 °C resulting in a frail polymer substance. This polymer material was then gently crushed and used as starting reagent as is. All other chemicals and solvents were of reagent grade and used without further purification. High purity deionized water (Milli Q, 18 MΩ cm) was used throughout the synthetic work.

6.2.2 Instruments and measurements

Powder X-ray diffraction (PXRD) analysis was conducted with a Siemens D8 Advance diffractometer using Cu K_α radiation (λ = 1.540 Å) operated at 40 kV and 30 mA. XRD patterns were recorded in the range 20 – 80º (2θ) with a scan step of 0.02° using a prolonged irradiation exposure time of 3 h. Fourier transform infrared (FTIR) spectra were recorded on a Nexus FTIR spectrophotometer equipped with a Smart Golden Gate attenuated total reflectance (ATR) diamond from Thermo Nicolet, with ZnSe lenses. Each spectrum was scanned 32 times with 4.0 cm^{-1} resolution and data analysis was performed with Omnic Software version 7.2. Particle size and morphology was determined by Transmission Electron Microscopy (TEM), using a JEM 1200EXII model (JEOL, Japan) microscope. An accelerating voltage of 200 kV was used throughout. A drop of sample was placed on a carbon-coated 200 mesh copper grid, followed by drying at ambient conditions before it was attached to the sample holder on the microscope. Prior to use, the grids were glow discharged for 30 seconds under air in a vacuum of 10^{-2} mbar. The mean diameters of the nanoparticles in the suspensions were determined with statistical analysis by measuring 100 – 150 individual particles from the micrographs using *Image J*, a public domain image processing program. [27]

6.2.3 Synthesis of magnetic magnetite nanoparticles

Magnetite (Fe_3O_4) nanoparticles were prepared with a chemical co-precipitation method under anaerobic conditions. A typical preparation was as follows: 11.61 g $FeCl_3.6H_2O$ (42.95 mmol) and 5.97 g $FeSO_4.7H_2O$ (21.47 mmol) were dissolved in 150 mL deionized H_2O and stirred in a 250 mL beaker until completely dissolved. This mixture was transferred to a 250 mL round-bottom flask equipped with a magnetic stirrer bar and stirred under reflux and nitrogen at 40 °C for about 30 minutes. Subsequently, 15 mL 25 % NH_4OH solution was rapidly added to the mixture, which immediately resulted in the precipitation of Fe_3O_4 nanoparticles. After vigorous stirring of the black suspension containing the Fe_3O_4 nanoparticles at 60 – 70 °C for 20 minutes, 9 mL oleic acid was added drop wise into the suspension at about 2 mL/min. This mixture was allowed to stir for a further 30 min whilst keeping the temperature at 80 – 90 °C. The upper solution became colourless after 10 min and a 'tarlike' black magnetic magnetite gel formed at the bottom of the reaction flask. The obtained magnetic gel consisting of oleic acid-coated magnetite nanoparticles was thoroughly washed with deionized H_2O (×3) and with absolute ethanol (×5) *via* magnetic decantation to remove any suspended matter and excess oleic acid that may not be bound to the surface of the magnetic Fe_3O_4 nanoparticles. The mass of the final magnetic gel containing the oleic acid-coated Fe_3O_4 nanoparticles was about 9.80 g.

6.2.4 Synthesis of magnetic PSMI nanoparticles

The magnetic PSMI nanoparticles were synthesized using an imidization reaction (as described in section 2.2.3, Chapter 2) in the presence of oleic acid-coated Fe_3O_4 nanoparticles. A typical preparation was as follows: 2 × 835 µL DMAPA was added to 5 g crushed PSMA (which is a 1:1 molar ratio between primary amine and maleic anhydride residues) suspended in 50 mL H_2O together with about 8 g of the oleic acid coated Fe_3O_4 nanoparticles (~15.5 wt. %). The mixture was allowed to agitate at 1000 rpm for 3 h with temperatures between 150 °C – 180 °C and a pressure of 4 – 7 bar. On completion of the imidization reactions in the presence of the oleic acid-coated Fe_3O_4 nanoparticles, stable black dispersions were obtained as illustrated in Figure 6.1 (a). The isolated dispersions containing the Fe_3O_4 encapsulated PSMI nanoparticles had a strong magnetic behaviour at room temperature in the presence of an external magnetic field gradient (~0.35 T) as shown by Figure 6.1 (b). The dried magnetic PSMI nanoparticles isolated from the dispersion and re-suspended in H_2O is shown in Figure 6.1 (c). It should be pointed out

that after drying at ambient temperature, the Fe_3O_4 nanoparticles formed a crystalline substance whereas the magnetic PSMI nanoparticles appeared as an amorphous powdered substance.

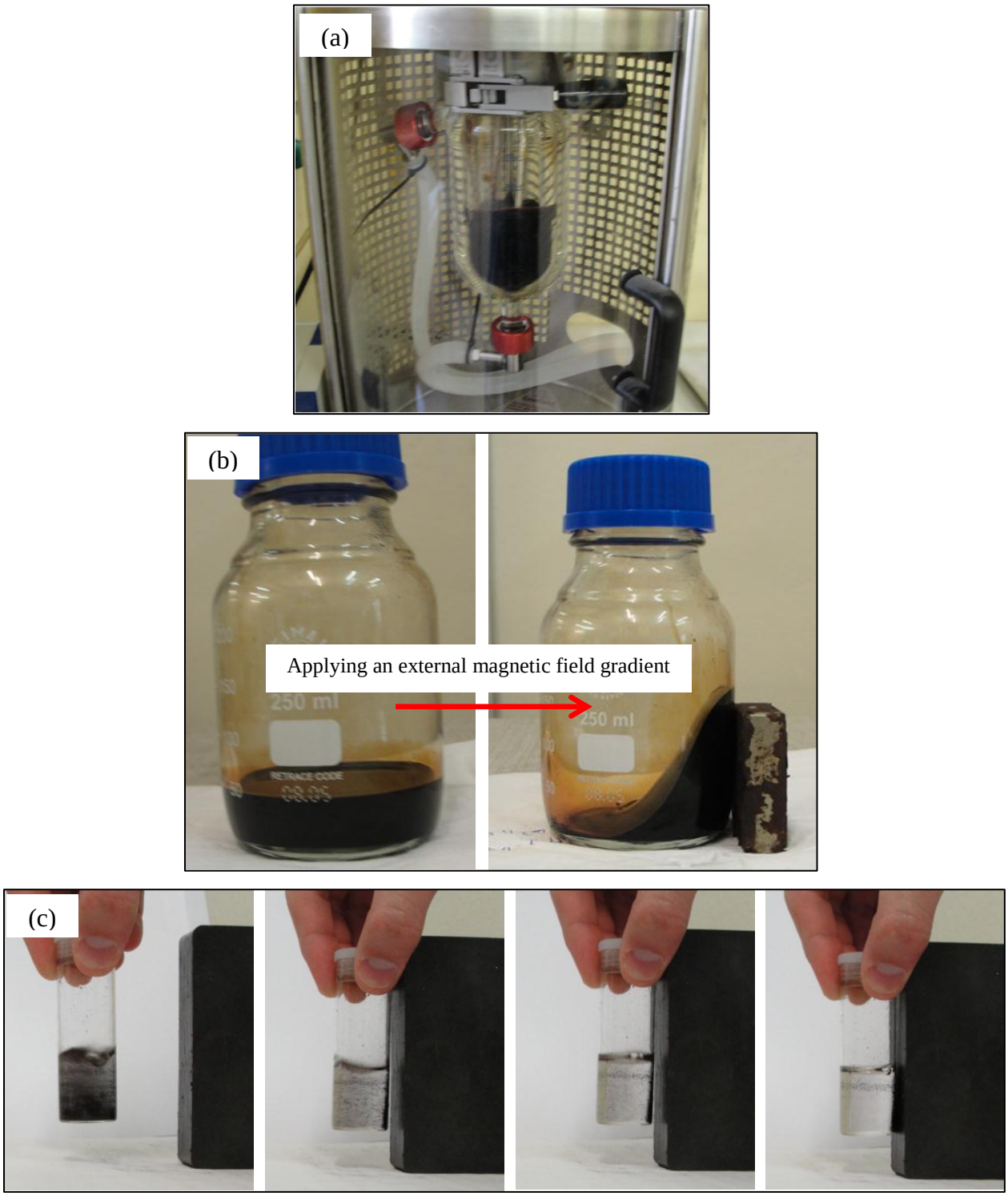

Figure 6.1 (a) Magnetic PSMI dispersion; Application of an external magnetic field gradient to (b) the isolated magnetic PSMI dispersion, and (c) magnetic PSMI nanoparticles re-suspended in water.

6.3 Results and discussion

6.3.1 PXRD analysis

Figure 6.2 shows the PXRD diffactogram of the synthesized superparamagnetic Fe_3O_4 nanoparticles. As can be seen from the diffractogram, a high degree of crystallinity and phase purity was obtained. The positions and the relative intensities of the diffraction peaks are consistent with the expected composition of Fe_3O_4 as evidenced by the good agreement with diffractograms and data in literature. [5,28,29] The diffraction peaks could be indexed into a spinel cubic lattice type with lattice parameter of 8.69 Å. Although it is clear that the bulk of the precipitate consist of Fe_3O_4 phase, there is some evidence of small amounts of maghemite phase (γ-Fe_2O_3) present (indicated by the 'asterisk' in Figure 6.2). This is most probably as a result of slight oxidation that may have occurred during the synthesis of the Fe_3O_4 nanoparticles. It cannot be ascertained from the diffactogram to what extend the γ-Fe_2O_3 phase (which also has magnetic characteristics) exist in the precipitate because of similar lattice type and lattice parameters. [5,9] The average crystallite size as calculated from line broadening analysis using the Debye-Scherrer equation was found to be 7.10 ± 0.26 nm. [30] No crystalline diffraction peaks were obtained for the magnetic PSMI nanoparticles (result not shown). This is most probably due to the amorphous PSMI polymer, which is in excess.

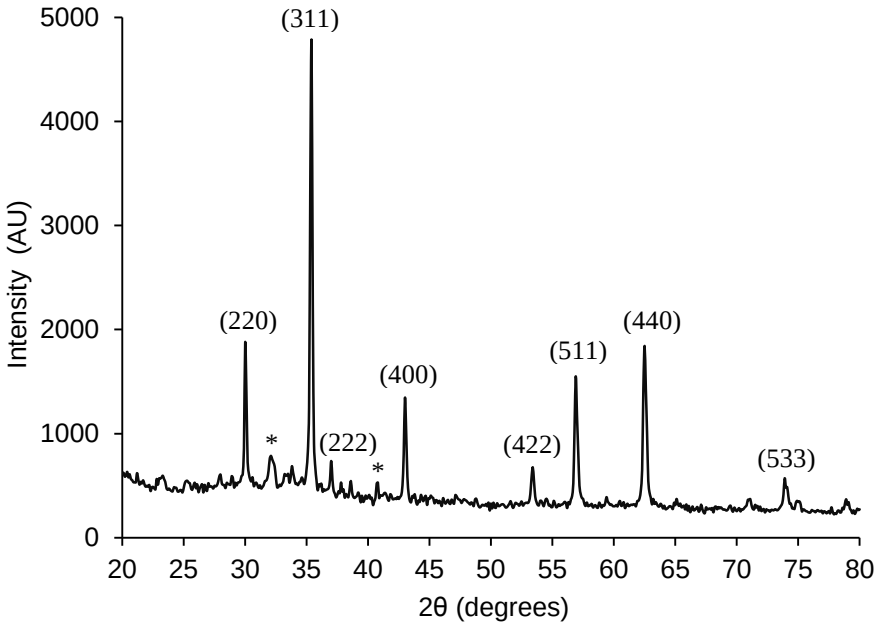

Figure 6.2 PXRD diffractogram of the superparamagnetic Fe_3O_4 nanoparticles prepared by the chemical co-precipitation of Fe^{2+} and Fe^{3+} (1:2 ratio) with ammonium hydroxide solution.

6.3.2 ATR-FTIR analysis

Figure 6.3 shows the typical FTIR spectrum of (a) pure oleic acid used as surfactant molecules, (b) the Fe_3O_4 nanoparticles coated with oleic acid and (c) the magnetic PSMI nanoparticles.

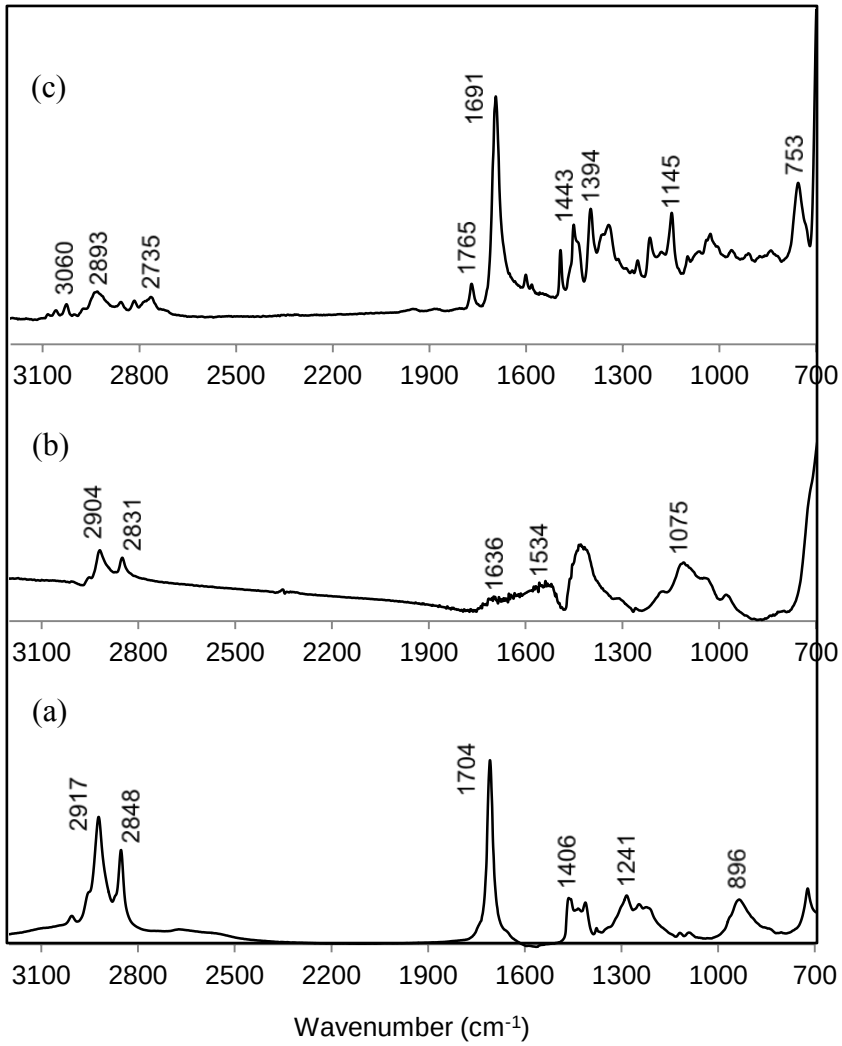

Figure 6.3 FTIR spectra of (a) pure oleic acid, (b) oleic acid-coated Fe_3O_4 nanoparticles and (c) magnetic PSMI nanoparticles.

In Figure 6.3 (a), two sharp bands at 2917 and 2848 cm^{-1} are attributed to the asymmetric and the symmetric CH_2 stretches, respectively. The intense peak at 1704 cm^{-1} is derived from the existence of the C=O stretch and the band at 1241 cm^{-1} exhibited the presence of the C-O stretch. The O-H in-plane and out-of-plane bands appeared at 1406 and 896 cm^{-1}, respectively. In Figure

6.3 (b), the asymmetric and the symmetric CH_2 stretches shifted to a lower frequency region which indicated that the hydrocarbon chains in the monolayer surrounding the Fe_3O_4 nanoparticles were in a closed-packed crystalline state. [31] It is worth to note that the C=O stretch band of the oleic acid carbonyl group, which was present at 1704 cm^{-1} in Figure 6.3 (a), spectrum of the pure oleic acid, was absent in Figure 6.3 (b), spectrum of the oleic acid coated Fe_3O_4 nanoparticles. Two broad new bands appeared at 1636 and 1534 cm^{-1}, which are characteristic of the asymmetric υ_{as} (COO^-) and the symmetric υ_s (COO^-) stretches. [32] Moreover, a strong absorption at 1075 cm^{-1} arises from the C-O single bond stretching. These results reveal that the oleic acid used as surfactant was chemisorbed onto the surfaces of the Fe_3O_4 nanoparticles as carboxylates.

Combined with previous studies of carboxylates, the interaction between the carboxylate head and the metal atom can be categorized as four types: monodentate, bridging (bidentate), chelating (bidentate), and ionic interaction. [31-33] The wavenumber separation, Δ, between the υ_{as} (COO^-) and υ_s (COO^-) IR bands can be used to distinguish the type of interaction between the carboxylate heads and the iron atoms on the surface of the Fe_3O_4 nanoparticles. The largest Δ (200 – 320 cm^{-1}) generally corresponds to monodentate interaction, medium range Δ (140 – 190 cm^{-1}) bridging bidentate, and the smallest Δ (< 110 cm^{-1}) chelating bidentate. In this work, Δ was found to be 102 cm^{-1} (1636 – 1534 = 102 cm^{-1}). This indicates that the carboxylate (of the oleic acid) is bound *via* a chelating bidentate interaction with the surface of the Fe_3O_4 nanoparticles as illustrated by Scheme 6.1.

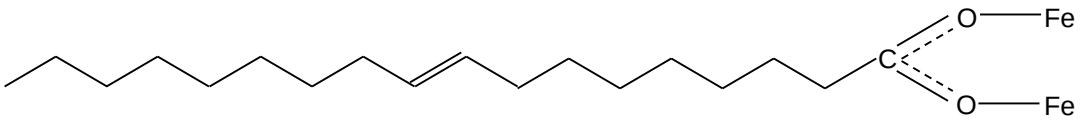

Scheme 6.1 Chelating bidentate interaction between the carboxylate (COO^-) group of the oleic acid and the iron atoms on the surface of the superparamagnetic Fe_3O_4 nanoparticles.

Also shown in Figure 6.3 (c) is the FTIR spectrum of the magnetic PSMI nanoparticles. As can be seen from Figure 6.3 (c), the characteristic peaks of PSMI are present in the bulk magnetic material (*see* Figure 2.4 and Table 2.3). This indicates successful and complete conversion of PSMA into the PSMI derivative during the simultaneous encapsulation and imidization reaction.

6.3.3 TEM analysis

The particle size and morphology of the magnetic PSMI nanoparticles was determined by TEM analysis. The TEM micrographs of the superparamagnetic Fe_3O_4 nanoparticles and the oleic acid-coated Fe_3O_4 nanoparticles are shown in Figure 6.4 (a) and (b), respectively. As can be seen from Figure 6.4 (a), excessive agglomeration of the Fe_3O_4 nanoparticles occurred. This can be attributed to strong, short range inter-particle dipole-dipole forces between individual Fe_3O_4 nanoparticles. [1,5,15] In comparison, Figure 6.4 (b) shows that the agglomeration is significantly minimized by coating the Fe_3O_4 nanoparticles with oleic acid surfactant molecules which provides steric stabilization of the nanoparticles in suspension. This result proves that most nanoparticles are separated from their neighbours by the oleic acid surfactant molecules physically adsorbed onto the Fe_3O_4 surfaces and as was shown by FTIR analysis (Figure 6.3). The nanoparticles are somewhat irregular in morphology ranging from oval to spherical in shape. The corresponding narrow size-distribution histogram is shown in Figure 6.5. Monodispersed nanoparticles with an average diameter of 8.31 ± 0.70 nm were obtained and compare reasonably well with the Fe_3O_4 crystallite size determined from PXRD analysis (Figure 6.2).

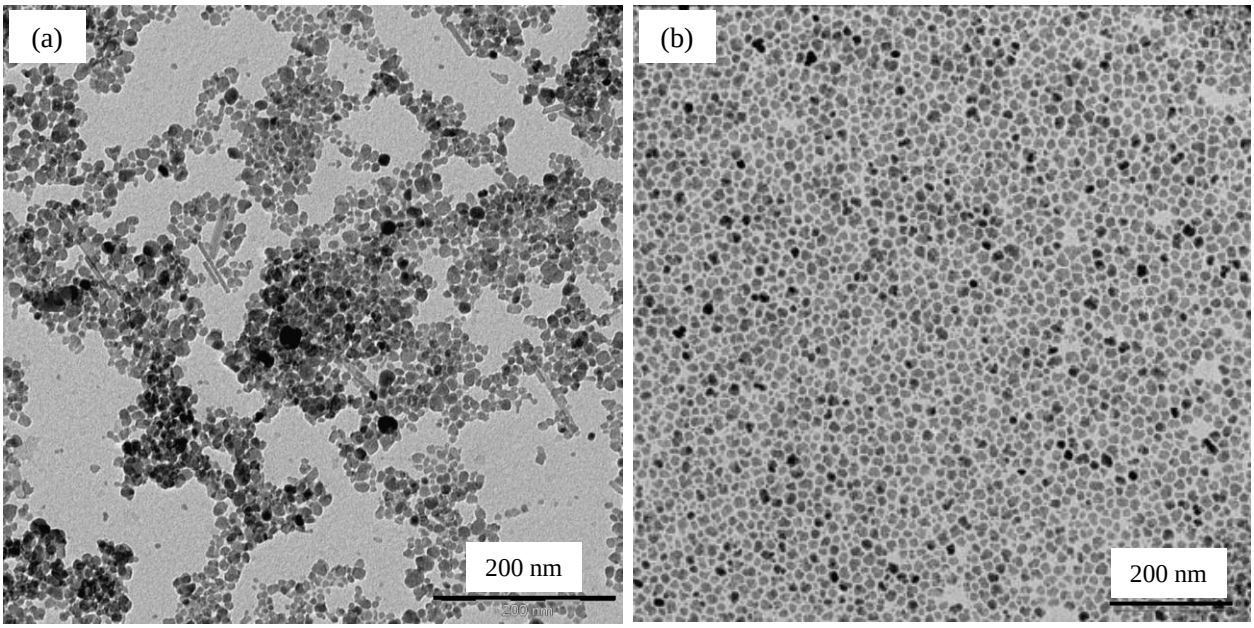

Figure 6.4 TEM micrograph of (a) the superparamagnetic Fe_3O_4 nanoparticles and (b) oleic acid-coated Fe_3O_4 nanoparticles. The average Fe_3O_4 nanoparticle diameter is 8.31 ± 0.70 nm.

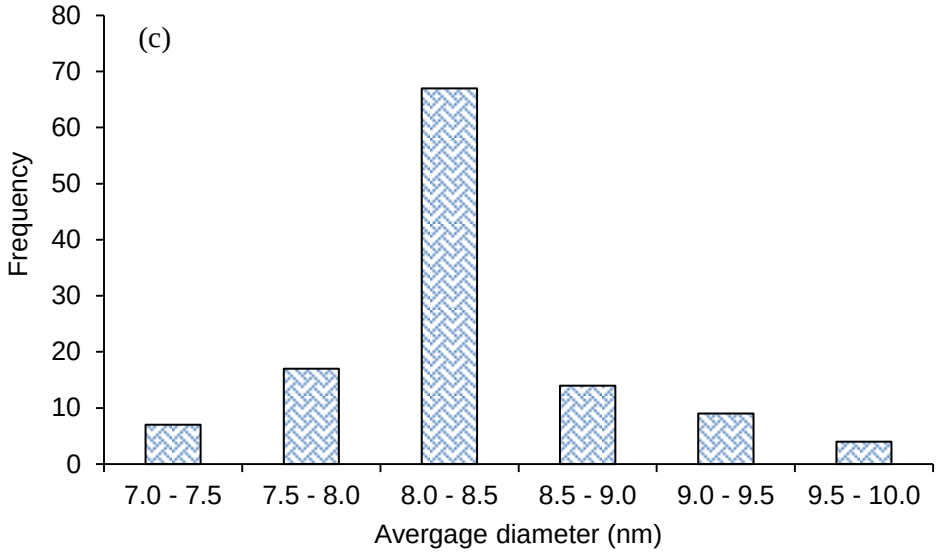

Figure 6.5 Size-distribution histogram of the oleic acid-coated Fe_3O_4 nanoparticles. The average Fe_3O_4 nanoparticle diameter is 8.31 ± 0.70 nm.

Figure 6.6 shows the TEM micrograph of the magnetic PSMI nanoparticles present in the black stable dispersion (Figure 6.1). Magnetic PSMI nanoparticles with average diameters of about 50 nm were obtained. Based on the evidence presented, they are not as well dispersed as in the case of the milky PSMI nanoparticle dispersions synthesized in Chapter 2 (refer to TEM micrograph, Figure 2.5). Rather, it appears that individual magnetic PSMI nanoparticles are slightly linked together to almost form composite materials. Nonetheless, magnetite core-polymer shell structures are identified indicating successful encapsulation of the oleic acid-coated Fe_3O_4 nanoparticles inside the relatively larger PSMI nanoparticles. This was also confirmed by EDX analysis. It is highly likely that the magnetite core is constituted of more than one oleic acid-coated Fe_3O_4 nanoparticle. From Figure 6.6, there is also some evidence of Fe_3O_4 not encapsulated by the PSMI nanoparticles. The Fe_3O_4 not encapsulated by PSMI may be attributed to partial or incomplete coating of oleic acid which resulted in an excessive aggregation to form larger clusters. As a consequence they could not be encapsulated due to their size. Another reason could be that the concentration (~15.5 wt. %) of oleic acid-coated Fe_3O_4 used in the preparation of the magnetic PSMI nanoparticles was too high (*see* section 6.2.4). A simplified reaction illustrating a model for the encapsulation of the oleic acid-coated Fe_3O_4 by the PSMI nanoparticles is shown in Scheme 6.2.

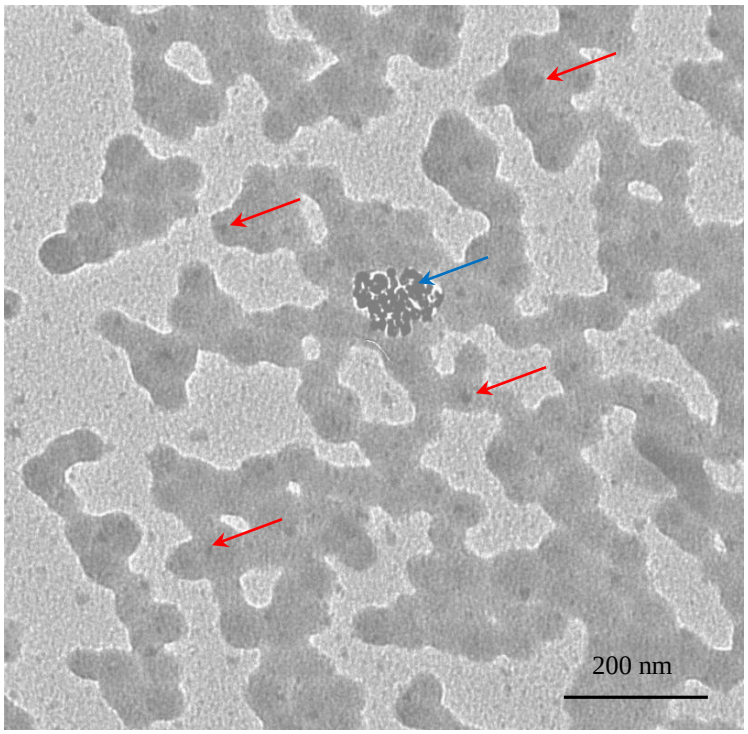

Figure 6.6 TEM micrograph of the magnetic PSMI nanoparticles illustrating the magnetite core-polymer shell structure. The red arrows indicate the presence of the oleic acid-coated Fe_3O_4 nanoparticles encapsulated by the PSMI nanoparticles and the blue arrow indicates the oleic acid-coated Fe_3O_4 nanoparticles not encapsulated. The average PSMI nanoparticle diameter is about 50 nm.

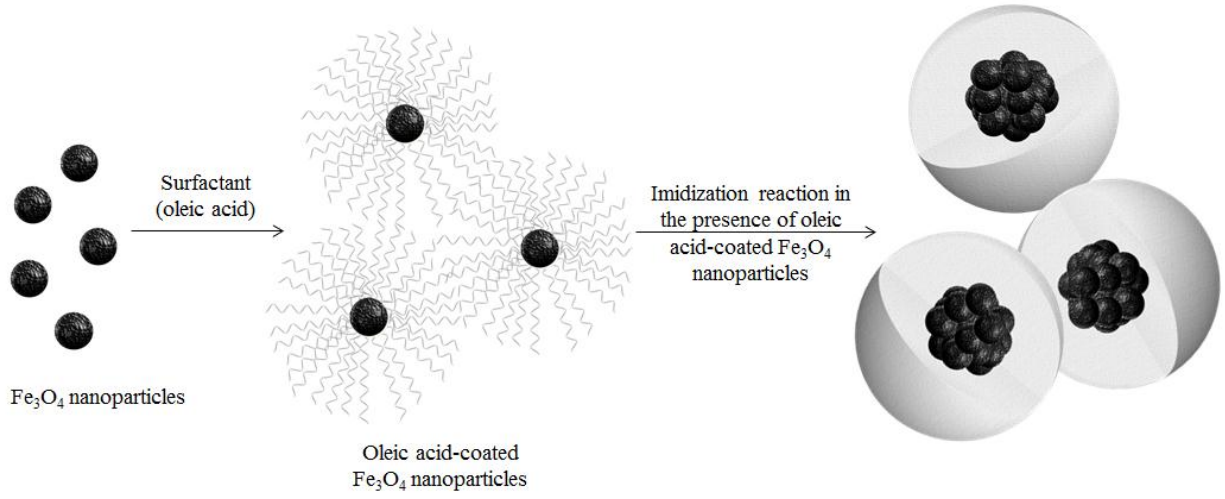

Scheme 6.2 Surface coating of the superparamagnetic Fe_3O_4 nanoparticles with oleic acid and the formation of the magnetic PSMI nanoparticles by an *in situ* imidization reaction. The obtained magnetic PSMI nanoparticles have a magnetite core-polymer shell structure as represented by the cross-section of the particles.

6.4 Conclusions

The preparation of magnetic PSMI nanoparticles was carried out by a three-step process. First superparamagnetic Fe_3O_4 nanoparticles were prepared by a co-precipitation of iron salt solutions, Fe^{3+} and Fe^{2+} in a ratio of 2:1 with concentrated NH_4OH solution. PXRD analysis identified the formation of mainly Fe_3O_4 phase in the black magnetic precipitate. TEM analysis shows that the superparamagnetic Fe_3O_4 nanoparticles agglomerate significantly in solution due to strong, short range inter-particle dipole-dipole forces between individual particles.

In the second step, the formed superparamagnetic Fe_3O_4 nanoparticles were coated with oleic acid to enhance their stability in solution and thus to prevent excessive agglomeration. FTIR analysis confirms that the oleic acid is bound *via* a chelating bidentate interaction with the surface of the Fe_3O_4 nanoparticles. TEM analysis clearly shows that most nanoparticles are separated from their neighbours by the oleic acid surfactant molecules which are physically adsorbed onto the Fe_3O_4 surfaces. Monodispersed Fe_3O_4 nanoparticles with average diameters of 8.31 ± 0.70 nm were obtained and compare reasonably well with the Fe_3O_4 crystallite size determined from PXRD analysis. The nanoparticles are somewhat irregular in morphology ranging from oval to spherical in shape.

The third step entailed the imidization reaction of the PSMA copolymer with 3-*N*,*N*-dimethylaminopropylamine in the presence of the oleic acid-coated Fe_3O_4 nanoparticles to obtain stable, black dispersions containing the magnetic PSMI nanoparticles. FTIR analysis of the isolated bulk magnetic PSMI nanoparticles confirms successful and complete conversion of PSMA into the PSMI derivative during the simultaneous encapsulation and imidization reaction. The magnetic PSMI nanoparticles were shown to consist of magnetite core-polymer shell morphology, hence indicating successful encapsulation of the superparamagnetic Fe_3O_4 nanoparticles by the PSMI nanoparticles. The average diameters of the magnetic PSMI nanoparticles are about 50 nm, which are similar to the PSMI nanoparticles synthesized in Chapter 2 under similar imidization reaction conditions.

6.5 References

1. U. Häfeli, et al., *Scientific and Clinical Applications of Magnetic Carriers*, Plenum Press, New York, **1997**.
2. G.M. Whitesides, R.J. Kazlauskas et al., *Trends Biotechnology* **1983**, 1, 144.
3. J. Chomoucka et al., *Pharmacological Research* **2010**, 62, 144.
4. G. Mistlberger, K. Koren, E. Scheucher, D. Aigner, S.M. Borisov, A. Zankel, P. Pölt, I. Klimant, *Advanced Functional Materials* **2010**, 20, 1842.
5. R.M. Cornell, U. Schwertmann, *The Iron Oxides: Structure, Properties, Reactions, Occurences and Uses*, Wiley-VCH, Weinham, Germany, **1996**.
6. G.F. Goya, *Solid State Communications* **2004**, 130, 783.
7. A.M. Schmidt, *Journal of Magnetism and Magnetic Materials* **2005**, 289, 5.
8. K. Woo, J. Hong, S. Choi, H.-W. Lee, J.-P. Ahn, C.S. Kim, S.W. Lee, *Chemistry of Materials* **2004**, 16, 2814.
9. R.M. Cornell, U. Schwertmann, *Iron Oxides in the Laboratory*, VCH Verlagsgesellschaft, Weinham, Germany, **1991**.
10. L.L. Vatta, R.D. Sanderson, K,R. Koch, *Journal of Magnetism and Magnetic Materials* **2007**, 311, 114.
11. P.A. Dresco, V.S. Zaitsev, R.J. Gambino, B. Chu, *Langmuir* **1999**, 15, 1945.
12. M. Mikhaylova, D.K. Kim, N. Bobrysheva, M. Osmolowsky, V. Semenov, T. Tsakalakos, M. Muhammed, *Langmuir* **2004**, 20, 2472.
13. J. Yang, S.-B. Park, H.-G. Yoon, Y.-M. Huh, S. Haan, *International Journal of Pharmaceutics* **2006**, 324, 185.
14. B.D. Cullity, *Introduction to Magnetic Materials*, Addison-Wesley Publishing Company, San Fransisco, C.A., **1972**.
15. K.J. Klabunde, *Nanoscale Materials in Chemistry*, Wiley-Interscience, New York, **2007**.
16. S. Dutz, W. Andrä, et al., *Journal of Magnetism and Magnetic Materials* **2007**, 311, 51.
17. J. Lee, T. Isobe, M. Senna, *Colloids and Surfaces A* **1996**, 109, 121.
18. M. Suzuki, M. Shinkai, M. Kamihira, T. Kobayashi, *Biotechnology Applied Biochemistry* **1995**, 21, 335.
19. I. Dumazet-Bonnamour, P. Le Perchec, *Colloids and Surfaces A* **2000**, 173, 61.

20. V. Veiga, D.H. Ryan, E. Sourty, F. Llanes, R.H. Marchessault, *Carbohydrate Polymers* **2000**, 42, 353.
21. A. Rembaum, US. Patent No. 4, 267,234, **1981**.
22. V.S. Zaitsev, D.S. Filimonov, I.A. Presnyakov, R.J. Gambino, B. Chu, *Journal of Colloid and Interface Science* **1999**, 212, 49.
23. D. Hoffman, K. Landfester, M. Antonietti, *Magnetohydrodynamics* **2001**, 37, 217.
24. L. Guo, G.-L. Pei, T.-J. Wang, Z.-W. Wang, Y. Jin, *Colloids and Surfaces A* **2007**, 293, 58.
25. Y.-C. Chang, D.-H. Chen, *Gold Bulletin* **2006**, 39, 98.
26. M. Takafuji, S. Ide, H. Ihara, Z. Xu, *Chemistry of Materials* **2004**, 16, 1977.
27. W. Rasband, *In Image J: Image processing and analysis in Java* http://rsb.info.nih.gov/ij/, 2006.
28. M. Ma, Y. Zhang, W. Yu, H.-Y. Shen, H.-Q. Zhang, N. Gu, *Colloids and Surfaces A* **2003**, 212, 219.
29. Y.-H. Deng, C.-C. Wang, J.-H. Hu, W.-L. Yang, S.-K. Fu, *Colloids and Surfaces A* **2005**, 262, 87.
30. H.P. Klug, L.E. Alexander, *X-Ray Diffraction Procedures for Polycrystalline and Amorphous Materials*, Wiley, New York, **1974**.
31. K. Nakamoto, *Infrared and Raman spectra of inorganic and coordination compounds*, John Wiley and Son, New York, **1997**.
32. D.L. Pavia, G.M. Lampman, G.S. Kriz, *Introduction to Spectroscopy*, 3rd. ed., Harcourt College Publishers, New York, **2001**.
33. Y. Ren, K. Iimura, T. Kato, *Langmuir* **2001**, 17, 2688.

7 General conclusions and recommendations for further study

7.1 Summary

In **Chapter 2**, functionalized poly(styrene-*co*-maleimide) (PSMI) nanoparticles were prepared by an imidization reaction of commercially available poly(styrene-*co*-maleic anhydride) (PSMA) with 3-*N*,*N*-dimethylaminopropylamine (DMAPA). The imidization reactions were performed in a double-walled oil-heated autoclave in an organic solvent-free process, using water as the solvent. The degree of conversion, the particle size distribution and their morphology were dependant on the reaction parameters such as the reaction time, temperature, agitation rate as well as the amount (wt. %) of initial PSMA copolymer used in the imidization reactions. The best results were obtained by agitating the mixture containing the crushed PSMA copolymer with DMAPA in H_2O (in a 1:1 molar ratio between primary amine and maleic anhydride residues) at 1000 rpm for 6 h using reaction temperatures exceeding 140 °C. Under these optimum conditions, stable water-based dispersions were reproducibly and homogenously obtained containing the PSMI nanoparticles of about 50 nm in diameter.

In **Chapter 3**, the PSMI nanoparticles synthesized were tested as a *novel* ion-exchange material for the extraction and separation of dissolved $[AuCl_4]^-$ from aqueous acidic chloride-rich solutions using a batch sorption method. The extraction mechanism is based on an ion-pair formation as a result of the electrostatic interaction between the positively charged protonated

nitrogen moieties of the PSMI nanoparticles and the anionic chlorido-complexes of $[AuCl_4]^-$ ions. Typical characteristics of the sorption process were extremely fast extraction kinetics and a good loading capacity of $[AuCl_4]^-$ indicating high affinity of the PSMI nanoparticles for these precious metal ions. The $[AuCl_4]^-$ ions were strongly associated to the surface of the PSMI nanoparticles and have been partly reduced to inaccessible Au^+ and Au^0 species illustrating the complexity of elucidating the precise sorption process at the solid-solution interface. Desorption of the immobilized gold species of any significance required the use of the strong chelating agent thiourea (0.25 M thiourea/2 M HCl) as well as a mixture of 10 M HNO_3/0.5 M HCl as elutant solutions. The immobilized gold species could be recovered from the gold-loaded PSMI nanoparticles due to the fact that extremely stable gold (I) – thiourea complexes are formed using thiourea as elutant. In the case of the 10 M HNO_3/0.5 M HCl solutions, successful desorption was attributed to the strong oxidizing properties of HNO_3 resulting in the oxidation of any lower oxidation state immobilized gold species and the subsequent formation of $[AuCl_4]^-$ ions in the strip liquor due to the presence of chloride ions in the elutant solution. Besides the high thermal stability of the PSMI nanoparticles, they have been shown to be quite robust against degradation in acidic solutions. Due to this property, they could be used in successive extraction and desorption cycles with reasonably good effect.

As an alternative to the nanoparticles, micro- to millimeter size PSMI resin beads were prepared in **Chapter 4** by an electrospray methodology directly from the PSMI polymer synthesized in Chapter 2. The chemical composition of the PSMI polymer was retained during this process. The PSMI resin bead diameters and shapes were dependent on the conditions employed such as the PSMI concentration in the spray solution, flow rate at which the PSMI solution was pumped through the capillary, the capillary tip-to-collector distance and the applied voltage. It was shown that under a specific set of experimental conditions micrometer-size monodisperse PSMI fibers with a narrow size-distribution was obtained.

In **Chapter 5**, PSMI resin beads of 450 µm and 1620 µm diameter prepared in Chapter 4 were tested as potential anion-exchange resin materials for the extraction and separation of dissolved $[AuCl_4]^-$ from single as well as multi-metal aqueous acidic chloride-rich solutions using a batch sorption method. Fast uptake kinetics was observed, once again indicating that an electrostatic

interaction mechanism is dominant in the sorption process. As was the case with the PSMI nanoparticles, the best elutants for desorption of immobilized gold species were acidified thiourea and a mixture of 10 M HNO_3/0.5 M HCl solutions. The PSMI resin beads were successfully used in successive extraction and desorption experiments, indicating that the resin has good durability as well as good efficiency for repeated use. It was illustrated that the PSMI resin beads are highly selective for $[AuCl_4]^-$ ions over $[RhCl_6]^{3-}$ ions and moderately selective over the other anionic PGM chlorido-complexes. The PSMI resin beads packed in a column have shown excellent capability towards the preconcentration of $[AuCl_4]^-$ ions indicating the versatility and potential of applying the resin in such a larger-scale continuous process.

In **Chapter 6**, preliminary results have been presented for the preparation of magnetically responsive PSMI nanoparticles. It was shown that oleic acid-coated magnetite nanoparticles were encapsulated by the PSMI nanoparticles to form magnetite core-polymer shell structures.

The objectives of this thesis as stated in **Chapter 1** have mainly been met. Therefore, in this thesis, the feasibility of using poly(styrene-*co*-maleimide) (PSMI) nanoparticles and micro- to millimeter size PSMI resin beads as anion-exchange materials for the extraction and recovery of $[AuCl_4]^-$ from aqueous acidic chloride-rich solutions have been demonstrated.

7.2 Future recommendations

7.2.1 Preparation of magnetic PSMI nanoparticles

An important factor in the formation of the magnetite core-polymer shell structures of the magnetic PSMI nanoparticles during the imidization reaction was the use of stabilized oleic acid-coated magnetite nanoparticles. In the absence of any surfactant coating, unstable brown suspensions were formed rather than black stable dispersions as illustrated in Figure 6.1. Shown in Figure 7.1 is a TEM micrograph illustrating the magnetic PSMI composite material that was formed when performing the imidization reaction in the presence of magnetite nanoparticles without an oleic acid coating.

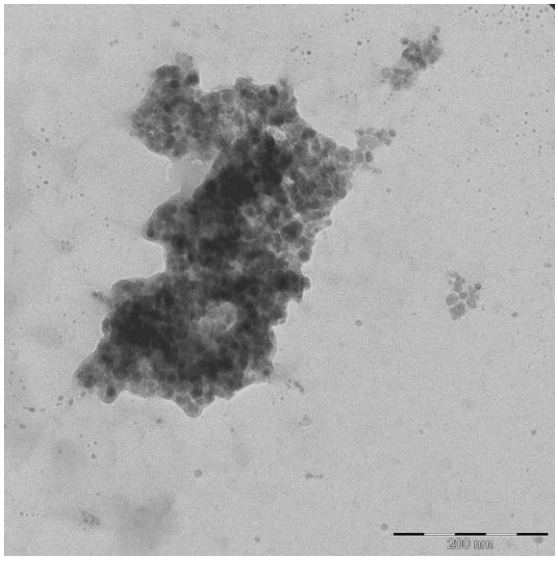

Figure 7.1. TEM micrograph of the magnetic PSMI composite obtained from the imidization reaction in the presence of uncoated Fe_3O_4 nanoparticles.

From this study, it is clear that the role of a surfactant is important to obtain stable dispersions. In this regard, it would therefore be worthwhile to study the formation of the magnetic PSMI nanoparticles in more detail using different surfactant molecules or perhaps other stabilizers prior to imidization. In particular, factors influencing the dispersion stability should be investigated since this could lead to the formation of more homogenous dispersions. Another interesting avenue of investigation would be to determine the amount of oleic acid-coated magnetite nanoparticles encapsulated inside the PSMI particles. This would be important since the degree of magnetite encapsulation would directly affect the magnetic susceptibility of the magnetic PSMI nanoparticles – more oleic acid coated magnetite nanoparticles encapsulated would inevitably lead to higher magnetic susceptibility which in turn would enable easier manipulation by an external magnetic field gradient. Also, the use of the magnetic PSMI nanoparticles as an ion-exchange material for the extraction of precious metal species from solution needs to be investigated further. Due to their magnetic behaviour, large surface area and high surface reactivity, these materials are excellent candidates for combining metal sorption with ease of phase separation. This could lead to a rapid, efficient and cheap way of metals recovery and the utility of magnetic separation would mean that centrifugation and filtration which is used in the aqueous from solid separation could be dispensed of.

7.2.2 Preparation of magnetic micro- to milli-meter size PSMI resin beads

In addition to the encapsulation of the magnetite nanoparticles by the PSMI nanoparticles, preliminary work was done to prepare magnetic micro- to milli-meter size PSMI resin beads. In this brief investigation, magnetite nanoparticles were prepared by the co-precipitation methods as described in section 6.2.1, Chapter 6. The black magnetic precipitate obtained was thoroughly washed and used as seeds as is without coating with oleic acid. The magnetic micro- to milli-meter size PSMI resin beads were obtained by an electrospray methodology similar to that described in Chapter 4. The electrospray solution was composed of *ca* 10 wt. % (w/w) magnetite dispersed in a 28.6 wt. % (w/w) homogeneous PSMI solution in DMF. The particles were prepared using a capillary tip-to-collector distance of 10 cm, a flow rate of 0.5 mL/min and an applied voltage of 5 kV.

The SEM micrograph obtained of the magnetic PSMI resin beads are shown in Figure 7.2 (a). As can be seen, the morphology was approximately spherical shape and the average diameter (by measuring the diameters of 35 beads) is 1020 ± 80 µm.

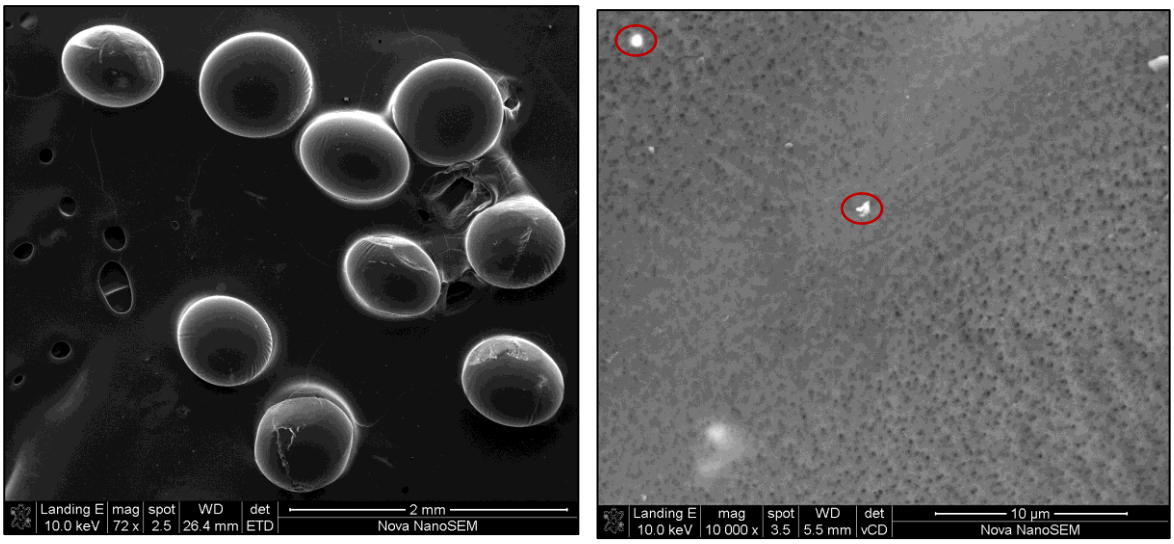

Figure 7.2. (a) SEM micrograph of the magnetic micron-sized PSMI particles and (b) presence of Fe_3O_4 clusters on the surface of the particles.

By increasing the magnification (10 000 x), the presence of magnetite clusters are observed on the surface of the PSMI resin (Figure 7.2 (b)). The formation of the magnetite clusters are most

probably due to agglomeration of individual Fe_3O_4 nanoparticles. Shown in Figure 7.2 (c) is a SEM micrograph of the cross-section of one magnetic PSMI resin bead that had been dissected by micro-toming. It becomes clear that some of the Fe_3O_4 clusters are embedded inside the PSMI resin beads and others are physisorbed on the surface of the particles.

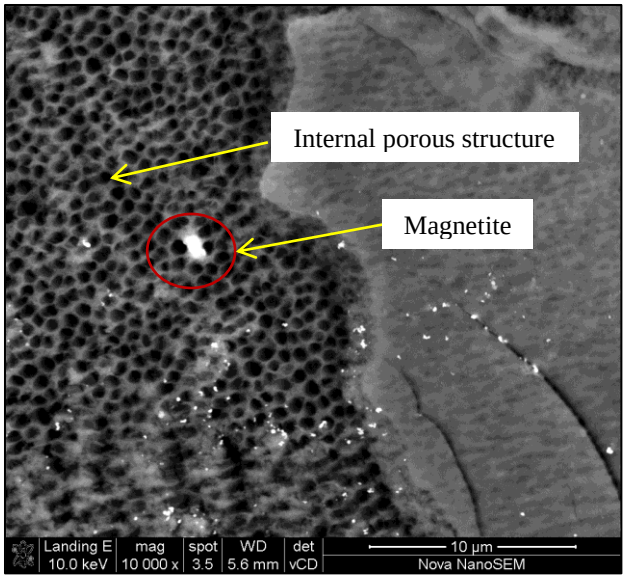

Figure 7.2. (c) SEM micrograph illustrating the cross-section of a magnetic PSMI resin bead.

In view of this it would be interesting to investigate whether the stabilized oleic acid-coated Fe_3O_4 nanoparticles could be completely embedded inside the magnetic PSMI resin beads compared to the uncoated Fe_3O_4 nanoparticles. Also, the influences of other factors such as for example variations in the concentrations of Fe_3O_4 relative to dissolved PSMI polymer prior to electrospraying needs to be investigated in an attempt to encapsulate more magnetite nanoparticles inside the PSMI resin beads.